

**Stimuli-Responsive Janus Particles:
Design and Investigation of their Self-Assembly
in Bulk and at Interfaces**

DISSERTATION

zur Erlangung des akademischen Grades

**Doctor rerum naturalium
(Dr. rer. nat.)**

vorgelegt

**der Fakultät Mathematik und Naturwissenschaften
der Technischen Universität Dresden**

von

Alina Kirillova

geboren am 31.01.1989 in Riga, Lettland

Eingereicht am _____

Die Dissertation wurde in der Zeit von Juli 2012 bis Dezember 2015
in der Professur für Physikalische Chemie polymerer Materialien am
Leibniz-Institut für Polymerforschung Dresden e.V. angefertigt.

Preface

This work was carried out at the Leibniz Institute of Polymer Research Dresden (Leibniz-Institut für Polymerforschung Dresden e.V.), in the Institute of Physical Chemistry and Polymer Physics, Department of Polymer Interfaces, in the years 2012 – 2015 under the supervision of Prof. Dr. Manfred Stamm and Dr. Alla Synytska. All the experiments and analyses were carried out in the institute. The research was made possible by funding from the Leibniz Institute of Polymer Research Dresden, which is gratefully acknowledged.

Outline

The present thesis is divided into four major parts. In Chapter I, a general introduction into the topic of Janus particles is provided, highlighting the importance of their investigation, and their potential in various research fields. The motivation and goals of the present work are also emphasized.

In Chapter II, an extensive theoretical background is provided, covering the topics of the Janus particle synthesis, their (self-) assembly, and potential applications. Recent literature is reviewed and discussed, providing the state-of-the-art on the topic of Janus particles.

In Chapter III, synthetic and modification approaches used for the experiments in the present work are summarized. A description of the used characterization techniques is also provided.

In Chapter IV, the results on each part of the work are presented and discussed. A short motivation is included for each part, as well as additional experimental procedures used. A summary providing the conclusions drawn from the results is presented at the end of each part. The Chapter starts from the synthesis and characterization of two geometries of Janus particles – spherical and platelet-like, passes through two different studies of the Janus particle assembly behavior, and results in three types of applications offered for hybrid hairy Janus particles.

Finally, Chapter V provides the summary and conclusions of the present work as well as ideas for further exploration.

Table of Contents

Preface	3
Outline.....	5
Table of Contents	7
CHAPTER I	11
Abstract.....	11
Motivation & Goals.....	13
CHAPTER II	15
Theoretical Background & State-of-the-Art	15
2.1. INTRODUCTION.....	15
2.1.1. Concepts of Symmetry and Asymmetry.....	15
2.1.2. Concept of Janus Particles.....	15
2.2. SYNTHETIC STRATEGIES FOR THE DESIGN OF JANUS PARTICLES.....	17
2.2.1. Soft Organic Janus Particles.....	17
2.2.2. Hard Inorganic Janus Particles.....	29
2.2.3. Hybrid Organic / Inorganic Janus Particles	33
2.3. INTERFACIAL ACTIVITY & (SELF-) ASSEMBLY OF JANUS PARTICLES.....	37
2.3.1. Interfacial Activity of Homogeneously Decorated Particles.....	37
2.3.2. Interfacial Activity of Janus Particles.....	37
2.3.3. (Self-) Assembly of Janus Particles in Continuous Media	40
2.4. APPLICATIONS OF JANUS PARTICLES.....	47
2.4.1. Modification of Interfaces.....	47
2.4.2. Applications of Individual Janus Particles	50
2.4.3. Janus Particles for Biological Applications.....	54
2.4.4. (Multi-) Functional Surfaces.....	55
2.5. SUMMARY	56
CHAPTER III	59
Materials & Methods	59
3.1. MATERIALS	59
3.2. SYNTHETIC & MODIFICATION APPROACHES.....	63
3.2.1. Preparation of Reference “Flat” Surfaces Using Silicon Wafers	63
3.2.2. Synthesis of Homogeneously Decorated Silica Particles.....	64
3.2.3. Synthesis of Spherical Silica-Based Janus Particles	66

3.2.4.	Synthesis of Homogeneously Decorated Kaolinite Particles.....	67
3.2.5.	Synthesis of Platelet-like Kaolinite-Based Janus Particles	69
3.2.6.	Preparation of Structured Functional Surfaces	69
3.3.	CHARACTERIZATION TECHNIQUES.....	70
3.3.1.	Scanning Electron Microscopy (SEM) & Cryo-SEM.....	70
3.3.2.	Transmission Electron Microscopy (TEM) & Cryo-TEM	72
3.3.3.	Atomic Force Microscopy	74
3.3.4.	Visible Light & Fluorescence Microscopy.....	76
3.3.5.	Electrokinetic Measurements.....	78
3.3.6.	Dynamic Light Scattering.....	79
3.3.7.	Contact Angle Measurements	79
3.3.8.	Null-Ellipsometry.....	80
3.3.9.	Thermogravimetric Analysis and Gel Permeation Chromatography.....	80
3.3.10.	Attenuated Total Reflectance Fourier Transform Infrared Spectroscopy	81
	CHAPTER IV.....	83
	Results & Discussion.....	83
4.1.	SPHERICAL HYBRID HAIRY JANUS PARTICLES	83
4.1.1.	Motivation.....	83
4.1.2.	Experimental Part	84
4.1.3.	Results and Discussion	85
4.1.4.	Summary.....	90
4.2.	PLATELET-LIKE HYBRID HAIRY JANUS PARTICLES	91
4.2.1.	Motivation.....	91
4.2.2.	Experimental Part	91
4.2.3.	Results and Discussion	92
4.2.4.	Summary.....	100
4.3.	(SELF-) ASSEMBLY OF SPHERICAL HYBRID HAIRY JANUS PARTICLES..	101
4.3.1.	Motivation.....	101
4.3.2.	Experimental Part	101
4.3.3.	Results and Discussion	102
4.3.4.	Summary.....	112
4.4.	MATERIALS BASED ON HYBRID HAIRY JANUS PARTICLES	113
4.4.1.	Janus Particles for Catalytic Applications	113
4.4.1.1.	Motivation.....	113
4.4.1.2.	Experimental Part	114

4.4.1.3.	Results and Discussion	115
4.4.1.4.	Summary.....	123
4.4.2.	Janus Particles as Building Blocks for (Multi-) Functional Coatings.....	123
4.4.2.1.	Anti-Icing / Deicing Coatings.....	123
4.4.2.1.1.	Motivation.....	123
4.4.2.1.2.	Experimental Part	124
4.4.2.1.3.	Results and Discussion	125
4.4.2.1.4.	Summary.....	134
4.4.2.2.	Anti-Fouling / Fouling-Release Coatings.....	134
4.4.2.2.1.	Motivation.....	134
4.4.2.2.2.	Experimental Part	136
4.4.2.2.3.	Results and Discussion	137
4.4.2.2.4.	Summary.....	149
CHAPTER V	151
	Summary & Conclusions	151
	Outlook	153
	References	155
	Table of Abbreviations	163
	Table of Symbols	165
	List of Publications	167
	Acknowledgements	169
	Versicherung	171
	Erklärung.....	171

CHAPTER I

Abstract

Janus particles, named after the two faced Roman god Janus, possess unique asymmetry and combine two distinct functions at their opposite sides, allowing them to target complex self-assembled architectures and materials inaccessible for homogeneous building blocks. In this study, three areas regarding the topic of Janus particles were explored: the synthesis of Janus particles, their (self-) assembly, and applications. Despite the growing number of contributions on the topic of Janus particles, a potential for improvement lies in all three of the aforementioned areas.

In the first part of the work, we have drawn our attention to the optimization of the synthetic procedures concerning the preparation of Janus particles and to the extending of the current Janus particle library by adding new geometries to the list. In the case of spherical Janus particles, we have developed an easy approach to tailor the Janus ratio of the resulting particles, thus, extending the possibilities of the Pickering emulsion approach for the creation of a variety of Janus particle architectures. The resulting hybrid Janus particles comprised a silica core and two kinds of polymer shells covering the surface of the core in different ratios. Additionally, a new methodology was employed to measure directly and *in situ* the position/contact angle of the prepared Janus particles with different Janus ratios at a water-oil interface. It was further concluded that having simply two different functionalities on a particle surface does not necessarily imply amphiphilic behavior: only in the case of large wettability contrasts our particles were in a true Janus regime. In the case of platelet-like Janus particles, we have developed a completely new approach for their large-scale synthesis, which involved a reduced number of steps compared to the spherical Janus particles. For this purpose, we used a natural clay mineral kaolinite as a core material and grafted two distinct polymer shells from the opposite sides of the core via simultaneous surface-initiated ATRPs in an emulsion. The initiator-modified kaolinite particles assembled at the interfaces between the oil and water phases, stabilizing the emulsion, while two different monomers were located in the respective phases, leading to simultaneous polymerizations from the opposite sides of the particles. Up to several grams of amphiphilic hybrid Janus particles could be synthesized in one batch, making this system relevant for technological applications.

In the second part of the work, the assembly behavior of various kinds of functional spherical Janus particles was investigated depending on the nature of the Janus particles and the surrounding media conditions. Oppositely charged, uncharged amphiphilic, and charged amphiphilic Janus particles were fabricated comprising different responsive polymers on their surface, and their assembly was investigated depending on the pH value of the dispersion, the ionic strength, or the solvent. It was found that, under specific conditions, the Janus particles formed hierarchical chain-like structures in solutions, which were not observed in the case of

the homogeneous particle mixtures. Such linear structures could be formed in a programmed manner and altered simply through changing the conditions of the surrounding media, such as pH or salt concentration. Therefore, the advantage of the Janus particle hairy polymer shells is the responsiveness and functionality of the utilized polymers, which leads to responsive structures that can be assembled or disassembled upon external stimuli. Moreover, the unique asymmetry of the Janus particles allows the formation of such structures that are not formed in the case of homogeneous particles. The obtained results indicate that the fundamental understanding of the Janus particle assembly mechanisms is crucial for the programmed formation of desired structures.

In the third part of the work, we have focused on the applications of our developed hybrid hairy Janus particles and proposed two main directions that would benefit from the unique properties or architecture of the Janus particles. The first direction is based on the exploitation of the superior interfacial activity of the Janus particles and their use for interfacial catalysis. We have demonstrated successful selective functionalization of amphiphilic hairy Janus particles with metallic nanoparticles, which were selectively located in one hemisphere of the Janus particles. The resulting Janus catalyst showed high interfacial activity and efficient stabilization of oil-water emulsions, which can be tuned by pH. Further, we have conducted a successful and effective reduction of two dyes, and a nitro compound with extremely low amounts of catalyst. The potential of the modified Janus particles for interfacial catalysis was demonstrated by successfully performing a catalyzed reduction of a dye in the water phase of an oil-water emulsion stabilized by the Janus particles. Moreover, the Janus catalyst can be easily recovered after the reaction by centrifugation and reused again.

The second proposed direction for the application of Janus particles is based on their use as building blocks for functional structured surfaces. The prepared surfaces were thoroughly characterized and tested for their performance toward anti-icing as well as anti-fouling applications. In the case of the anti-icing testing, it was found that the ice formation mechanism on the Janus particle-based surfaces is different compared to the surfaces formed from homogeneous particles covered with the same polymers, leading to a considerable ice-free area of the surface. Moreover, the ice adhesion to the Janus particle-based layers was extremely low, indicating on their potential for advanced anti-icing coatings. In the case of the anti-fouling testing, we performed a systematic investigation of the anti-fouling performance of the Janus particle-based layers and compared them to the layers of homogeneous particles covered with the same polymers and flat polymer-modified surfaces as well as unmodified particle layers and silicon wafers. Ultimately, we found that the Janus particle-based surfaces are robust under application-relevant conditions, and a significant reduction of the bacterial adhesion under various shear stress conditions was observed independent of their geometry: spherical or platelet-like. Therefore, the developed functional surfaces based on Janus particles as building blocks are very promising for their future application in the coating technology.

Motivation & Goals

Molecular asymmetry is the key point in the design of synthetic molecules, surfactants, liquid crystals, or block copolymers for their further self-assembly processes into micelles, vesicles, polymersomes, as well as sophisticated block copolymer, and liquid crystalline bulk phases. Asymmetry on the building block level may lead to complex superstructures and hierarchical architectures favorable for various fields of applications. Similarly to atoms being the bricks of molecules, macromolecules, and crystals, colloidal particles may be considered as building blocks for advanced materials. They provide the engineered materials with rich functionality, such as optical activity, mechanical strength, conductivity, etc.

Among these particles, Janus particles are a unique class of multifunctional building blocks, combining two distinct functionalities at their opposite sides. The unique asymmetry of the Janus particles offers the possibility to target complex self-assembled architectures and materials inaccessible for homogeneous building blocks. Significant progress has been made in the past two decades concerning the fabrication of Janus particles through the development of new synthetic methods, understanding their new physical properties, and potential fields of applications. Nevertheless, despite the numerous synthetic methods for the production of Janus particles, their truly large-scale synthesis still remains a challenge. Moreover, by far fewer studies are devoted to the investigation of the properties and assembly of Janus particles, and even fewer – to their potential applications and the design of materials based on the Janus particles.

Real applications of Janus particles have been assessed by several research groups. For instance, the group of Müller addressed technologically relevant application possibilities of the Janus particles through utilizing their enhanced surface activity, and demonstrated examples of successful emulsion polymerization using Janus particles as stabilizers, as well as efficient polymer blend compatibilization employing Janus particles as compatibilizers on a multigram scale.^{1, 2} In terms of biological applications, the group of Lahann developed a new type of bio-hybrid material based on Janus particles with spatially-controlled affinity toward human endothelial cells.³ A potential application of the Janus particles in electronics was demonstrated by Nisisako et al., who used bicolored Janus particles for the E-paper display technology.⁴ Additionally, individual Janus particles have been used as modulated optical nanoprobe or self-propelled nanomotors.^{5, 6} However, compared to the number of contributions regarding the Janus particle synthesis, the number of proposed applications is significantly lower, which is mostly due to the limitations present during the synthesis of the Janus particles. Moreover, most of the studies on the synthesis, assembly, and applications utilize either soft polymeric Janus particles, or very large several micrometer-sized hard Janus particles, whereas the combination of both organic and inorganic compartments in one particle could lead to novel beneficial properties of the particle itself as well as of the resulting assembled material.

Therefore, three main goals were pursued in the present work: (1) to optimize the synthetic strategies of the Janus particle preparation toward new geometries and a large-scale synthesis; (2) to investigate and understand the assembly of the hybrid hairy Janus particles in bulk depending on their different functionalities and media conditions; (3) to test the developed hybrid hairy Janus particles as building blocks for different types of applications, including interfacial catalysis and the development of structured surfaces toward the production of functional coatings.

The main advantage of the systems designed in this work arises from their hybrid structure: the designed hybrid Janus particles combine an inorganic core for improved mechanical stability and functional hairy polymer shells, providing the particles with stimuli-responsive properties. As a result, they are robust, multi-functional, and surface-active. Such Janus particles can be prepared on a large scale, thus opening new perspectives for their technological applications.

CHAPTER II

Theoretical Background & State-of-the-Art

2.1. INTRODUCTION

2.1.1. Concepts of Symmetry and Asymmetry

Symmetry is a term that refers to a sense of harmonious and beautiful proportion and balance. Humans and certain other species typically find symmetrical patterns more attractive than asymmetrical ones. Such preferences of symmetry may arise in response to biological signals or in the exploratory behavior and human aesthetic response to pattern.⁷ For instance, this makes symmetrical human faces more preferred.⁸ This can be explained by the fact that symmetrical stimuli are more easily processed by the visual system.

On the other hand, asymmetry is much more widely seen in nature, having evolved in many organisms and at many levels of organization from individual cells to entire body shapes. Going deeper onto the molecular level, one can identify that many organic molecules, including glucose and most biological amino acids, are ‘chiral’, which means that they are different than their mirror-image molecules, or, in other words, asymmetric. The asymmetrical nature of amino acids, in turn, determines the asymmetrical architectures of proteins. Furthermore, lipids are another kind of asymmetric structures, the amphiphilic nature of which results in their self-organization into bilayers, yielding vesicles, liposomes, or membranes for cells and bacteria.

Molecular asymmetry is the key point in the design of synthetic molecules, surfactants, liquid crystals, or block copolymers for their further self-assembly processes into micelles, vesicles, polymersomes, as well as sophisticated block copolymer, and liquid crystalline bulk phases.⁹ Therefore, asymmetry on the building block level may lead to complex superstructures and hierarchical architectures favorable for various fields of applications.

2.1.2. Concept of Janus Particles

Colloidal particles are small objects, which sizes at least in one dimension are in the range from several nanometers to a few micrometers, suspended in continuous medium in particulate form.¹⁰ They have found widespread technical applications in pigment, coating, food, and pharmaceutical industries. Analogous to atoms being the bricks of molecules, macromolecules, and crystals, colloidal particles may be considered as building blocks for advanced materials. They provide the engineered materials with rich functionality, such as optical activity, mechanical strength, conductivity, etc. For instance, periodic arrays of homogeneous colloids (colloidal crystals) have unique photonic properties.¹¹

Furthermore, an emerging field of research gaining significant attention in the recent years is the area of patchy particles. The breakthroughs in the particle synthesis have led to a spectacular variety of building blocks with different shapes, compositions, patterns, and functionalities.¹² The interactions through chemical patchiness have become powerful tools for engineering smart structured micro-objects. Moreover, the unique anisotropy of patchy particles significantly contrasts with the isotropic spherical colloids, providing the assembled materials with different macroscopic properties.¹³

Janus particles (JPs) are a unique class among homogeneous and multi-functional patchy particles, combining two distinct functionalities at their opposite sides, thus, having a block copolymer character. These particles were named after the two faced Roman god Janus, the god of beginnings and transitions, of gates, doors, passages, and endings. The term “Janus beads” was first coined by Casagrande et al. in 1988, describing glass spherical particles with one hydrophilic and one hydrophobic hemisphere.¹⁴ In 1991, Pierre-Gilles de Gennes addressed the Janus particles in his Nobel lecture, pointing out their potential and significance.¹⁵ Indeed, the unique asymmetry of Janus particles offers the possibility to target complex self-assembled architectures and materials inaccessible for homogeneous building blocks. Significant progress has been made in the past two decades concerning the fabrication of Janus particles through the development of new synthetic methods, understanding their new physical properties and potential fields of applications. As a result, the number of contributions on the topic of “Janus particles” is rapidly growing (**Figure T1**).

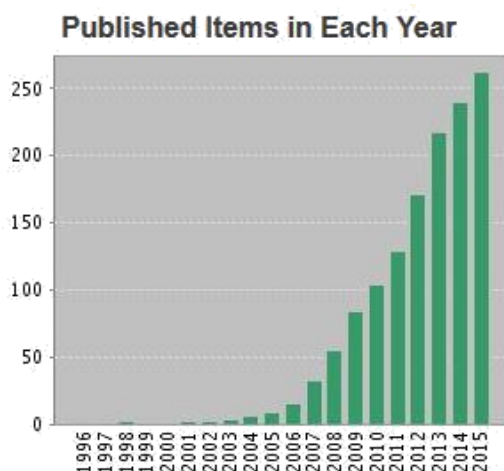


Figure T1. Number of articles concerning the topic „Janus particles” published each year over the last 20 years (03.12.2015).¹⁶

Originally, the main challenge to be overcome in the topic of Janus particles is the advancement of synthetic procedures to break the symmetry of existing particles, or to directly synthesize the Janus particles with a high yield and monodispersity. However, major progress has been made to attain various types of Janus particles, ranging from spherical, disc-shaped, or cylindrical to dumbbell-like Janus particles, and Janus capsules/vesicles (**Figure T2**).⁹ There are three different types of Janus particle functionalization: the compartmentalization of the particle can occur throughout the whole particle core (core-

compartmentalized), only at the surface through different surface modifiers (surface-compartmentalized), or the whole particle including its surface and the core can be compartmentalized.⁹ Along with better ways to synthesize Janus particles, increasing interest has been focused on their physical properties, their unusual self-assembly behavior, as well as on possible fields of applications, such as solid surfactants, sensors, elements for electronic paper, or biomedical applications.

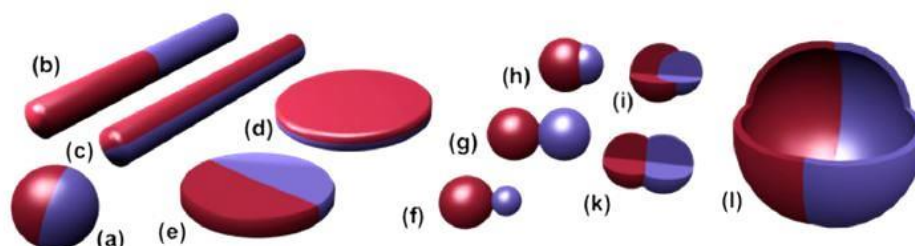


Figure T2. Janus particles of different types: spherical (a), two types of cylindrical (b, c), and disc-shaped (d, e) JPs; various kinds of dumbbell-shaped (f–k) JPs with asymmetric or snowman character (f), symmetric appearance (g, k), attached nodes (h), and eccentric encapsulation (i); Janus vesicles or capsules (l).⁹

In the following sections, all of the abovementioned topics will be discussed separately, starting from the synthetic strategies for the design of Janus particles, going through their physical properties and self-assembly behavior, and coming to the applications of Janus particles in various research fields.

2.2. SYNTHETIC STRATEGIES FOR THE DESIGN OF JANUS PARTICLES

Tremendous progress has been made in the past decade concerning the fabrication of Janus particles with diverse functionalities, well-defined shapes, and various architectures. Nowadays, JPs are known throughout the nano- to microscopic length scale. Although there are numerous routes to construct different kinds of JPs, the successful preparation of well-defined multifunctional JPs with advanced physical properties on a large scale is still an important issue in the field.

The synthetic approaches discussed below have been classified depending on the physical properties of the Janus particles into soft (organic, polymer-based), hard (inorganic, metallic), and hybrid organic/inorganic Janus particles.

2.2.1. Soft Organic Janus Particles

Biological and Biomimetic Janus Particles

Most proteins are asymmetric, thus having a Janus character; however, the most pronounced separation into different domains is present in the so-called hydrophobins (HFBs), which are proteins produced by filamentous fungi.¹⁷ Hydrophobins are amphiphiles having hydrophilic and hydrophobic parts and are among the most surface active proteins

known. Based on the patterns of clustering of hydrophobic and hydrophilic groups, HFBs can be divided into two groups called class I and class II. For instance, class II HFB of *T. reesei* is able to reduce the surface tension of water to 28 mJ/m² at a concentration of 0.02 mg/ml, which is in the range that aqueous solutions of surfactants typically exhibit.¹⁸ Furthermore, the advancements in protein engineering allow the preparation of biological Janus proteins through the precise and selective modification of the hydrophobins. For instance, Kostinen et al. used the free thiol group of a genetically engineered cysteine mutant of class II HFBs to couple spermine dendrons with high DNA binding affinity onto the protein, which yielded a surface active DNA-Janus protein after complexation with DNA that could be used for the intracellular delivery and expression of genes.¹⁹

A second way to fabricate Janus proteins or biphasic capsids is based on controlled masking and modification steps, which involves a temporary shielding of one hemisphere at an interface. This symmetry-breaking method has gained huge importance in the creation of a wide variety of JPs. It typically involves three to four steps: (1) the particles are reversibly immobilized at an interface through physical or chemical interactions; (2) the solvent-exposed surface is modified creating asymmetric particles; (3) the modified JPs are removed from the interface and separated; (4) an optional modification of the previously masked site can be performed.⁹

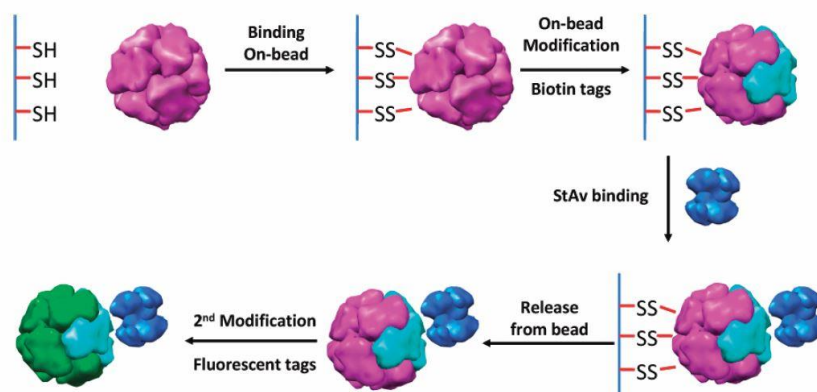


Figure T3. Surface-masking approach used to toposelectively biotinylate the KLFC LiDps construct and couple StAv to the Janus particle (purple subunits, free sulfhydryl; blue subunits, biotinylated; green subunits, fluorescently tagged).²⁰

The first toposelective surface modification of symmetric protein cages through the masking/unmasking technique on solid supports was reported by Young and Douglas et al.²⁰ Protein cages are nanoplatfoms, which can be used as reactors or cargo transporters. More specifically, they used a protein cage, LiDps (the DNA-binding protein from *Listeria innocua*), as a template for the fabrication of the streptavidin (StAv)-functionalized nanoplatfom through toposelective biotinylation (**Figure T3**). Further, they have used the StAv-functionalized fluorescent Janus protein cages for the optical detection of the microbial pathogen *S. aureus*.

Going to a larger length scale, phase separated giant unilamellar vesicles (GUVs) serve as a suitable model system to study lipid membranes. Depending on the composition and

temperature, a ternary lipid system consisting of unsaturated phospholipids, fully saturated sphingolipids (sphingomyelin), and cholesterol demonstrates a coexistence of two liquid lipid phases. In a synthetic system, phase separation can be induced through quenching of a homogeneous vesicle into the coexistence region of the two lipid phases. Completely biphasic Janus vesicles then form via nucleation and growth process or spinodal decomposition.²¹ This concept was taken further by Discher and co-workers, who managed to create synthetic Janus vesicles based on block copolymers.²²

Unimolecular Janus Particles

The smallest Janus particles may be found at the molecular level, given that the respective asymmetric molecule has a particulate character as well as significant branching around a focal point or a cage-like structure.

Dendrimers are technologically advanced synthetic compounds produced by classical organic synthesis, which possess monodisperse and precisely branched molecular architectures. Depending on their generation, dendrimers can reach sizes of several nanometers. The spherical symmetry of the dendrimers can be broken by linking two chemically distinct dendritic building blocks, thus creating Janus dendrimers. Some of the earliest reports describing the synthesis of Janus dendrimers were published by Frechet, Hawker, and Wooley.^{23, 24} They synthesized amphiphilic dendritic polyether macromolecules having hydrophobic benzyl ether end groups on one side and hydrophilic carboxylate groups as chain-ends on the other side.²³ Similarly, strongly dipolar Janus dendrimers were prepared through the placement of electron-withdrawing cyano groups and electron-donating benzyloxy groups at segmentally opposed regions of the dendrimer chain ends.²⁴ Further large progress in the direction of Janus dendrimers was reported by Percec and co-workers, who prepared libraries of amphiphilic Janus dendrimers by facile coupling of tailored hydrophilic and hydrophobic branched segments, and studied their self-assembly in water, which revealed a rich palette of different morphologies.^{25, 26} Recently, they extended their approach towards Janus glycodendrimers with D-mannose, D-galactose, and D-lactose in the hydrophilic part, synthesized through an accelerated modular strategy.²⁷ The resulting Janus compounds self-assembled into uniform, soft unilamellar vesicles, named glycodendrimersomes, which mimic biological membranes (**Figure T4**).

On the other hand, the main challenge in the area of dendrimers is their laborious synthesis and limitations to the overall size of the resulting molecules. To overcome these problems, Janus-type dendrimer-like polymers were synthesized. For instance, Feng et al. has shown a straightforward methodology to synthesize Janus-type dendrimer-like poly(ethylene oxide)s (PEOs) carrying orthogonal functional groups on their surface.²⁸ Repetition of living anionic polymerization of EO and chain-end functionalization/branching reactions afforded Janus-type dendrimer-like PEOs up to the sixth generation.

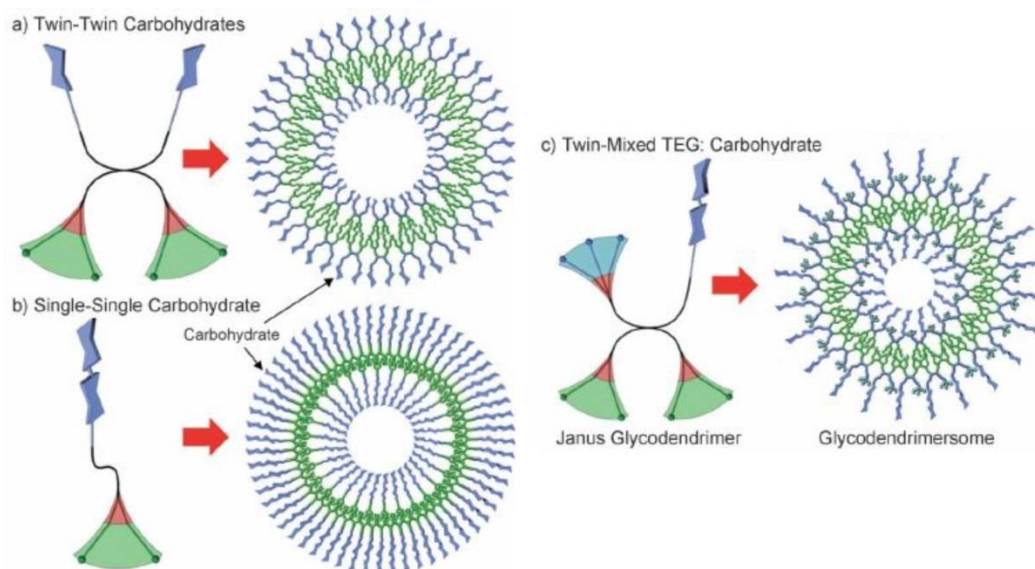


Figure T4. Three different topologies of amphiphilic Janus glycodendrimers and the structure of the corresponding multivalent glycodendrimersomes: a) twin-twin carbohydrates, b) single-single carbohydrate, and c) twin-mixed TEG:carbohydrate. Color code: hydrophilic blue, hydrophobic green, aromatic red.²⁷

Another and synthetically much easier way to produce unimolecular JPs utilizes heterografting of polymers. Both heteroarm star polymers and cylindrical brushes grafted with two polymers can lead to phase-separated spherical and cylindrical JPs, respectively, if the polymer arms or side-chains undergo phase separation in solution. There are five main parameters, which determine the extent of phase separation: (a) the incompatibility of the two polymers (expressed by the Flory-Huggins interaction parameter, χ); (b) the quality of the solvent with respect to the two polymers; (c) the degree of polymerization of the two polymers; (d) local chain crowding (grafting density, branching) at the point of attachment; (e) the influence of the system's entropy (e.g., polymer conformations).⁹ High polymer incompatibility is necessary to accomplish successful phase separation. An example of Janus-type heteroarm star copolymers was reported by Liu et al.²⁹ Janus-type A_7B_{14} star copolymers of *N*-isopropylacrylamide (NIPAAm) and 2-diethylaminoethyl methacrylate (DEA), $(PDEA)_7-CD-(PNIPAAm)_{14}$, were synthesized by coupling atom transfer radical polymerization (ATRP) and click chemistry techniques. On the other hand, cylindrical Janus brushes can be synthesized, if the two different types of brush arms are segregated in a block-wise manner. For instance, Deffieux et al. reported on the synthesis of Janus-like comb copolymers consisting of polystyrene and poly(methyl vinyl ether) branches attached to a diblock backbone, which was achieved by using living/controlled cationic and anionic polymerization techniques via “grafting from” and “grafting onto” approaches.³⁰ Another example was shown by Rzyayev et al., who produced asymmetric polystyrene-poly(lactide) (PS-PLA) bottlebrush block copolymers with long PS branches and shorter PLA branches through a combination of controlled radical and ring-opening polymerizations.³¹ However, one of the main problems in the field of dynamic, unimolecular polymer-based JPs is the challenge to give a solid in situ proof for the existence of the Janus character in solution, especially if self-assembly is involved during the process.

Block copolymer self-assembly is a very useful tool to create precisely defined Janus micelles. There are two strategies in the case of diblock copolymers that allow the preparation of Janus micelles: (a) a combination of AB and BC diblock copolymers, in which the B segments are insoluble in a given solvent and form the micellar core, and (b) a mixture of AB and CD diblock copolymers, where B and C have an attractive interaction resulting in a forced co-assembly of the two polymers.⁹ In the case of ABC triblock terpolymers, Janus micelles can be prepared from two outer soluble end blocks, A and C, and an inner insoluble block, B. Similarly to the case of heteroarm star polymers, the two corona-forming blocks of the Janus micelles must undergo phase separation.⁹ As for unimolecular JPs, the main challenge here is the direct proof of the formed micelle Janus character. There are only few suitable techniques to overcome this challenge, including direct imaging methods (electron microscopy), and small-angle neutron scattering (SANS) with contrast variation of selectively deuterated corona blocks.⁹ Another obstacle to be overcome is the synthesis of purely Janus micelle populations in solution, excluding the other simultaneously formed patchy micelles.

For the case of AB and CD diblock copolymers, Stuart and co-workers reported on the co-assembly of two double hydrophilic block copolymers, poly(acrylic acid)-*block*-poly(acrylamide) (PAA-*b*-PAAm) and poly(*N*-methyl-2-vinyl pyridinium iodide)-*block*-poly(ethylene oxide) (P2MVP-*b*-PEO), through electrostatic interactions (complex coacervation), resulting in Janus-type micelles having a complex coacervate core formed by an interpolyelectrolyte complex of P2MVP and PAA, and an asymmetric water-swollen corona consisting of PAAm and PEO.^{32, 33}

For the case of ABC triblock terpolymers, the formation of micelles with compartmentalized Janus-type corona was reported by the group of Müller.³⁴ They designed a special block terpolymer, poly(4-*tert*-butoxystyrene)-*block*-polybutadiene-*block*-poly(*tert*-butyl methacrylate) (PtBS-PB-PtBMA), where the central PB block was modified with a fluorinated side group. The fluorinated block acted as a micellar core, and micelles with patchy coronas could be obtained in dioxane, a common solvent for both outer blocks.

Another challenge faced in the block copolymer approach is the generation of Janus micelles purely via self-assembly. However, the often resulting patchy multicompartment micelles can be transformed into Janus ones through subsequent modifications. For instance, the group of Müller recently proposed a simple solution-based routine to produce soft, nanosized Janus micelles with tunable properties based on the cross-linking of compartments within precisely defined multicompartment micelles (MCMs).³⁵ The MCMs themselves are formed by the self-assembly of ABC triblock terpolymers and consist of cores of the A block, carrying compartments of the B block, and corona chains of the C block emanating from the B compartments. Cross-linking of the B compartments permanently fixates the phase-separated state and, after dissolution of the MCMs in a non-selective solvent, JPs are obtained (**Figure T5**).

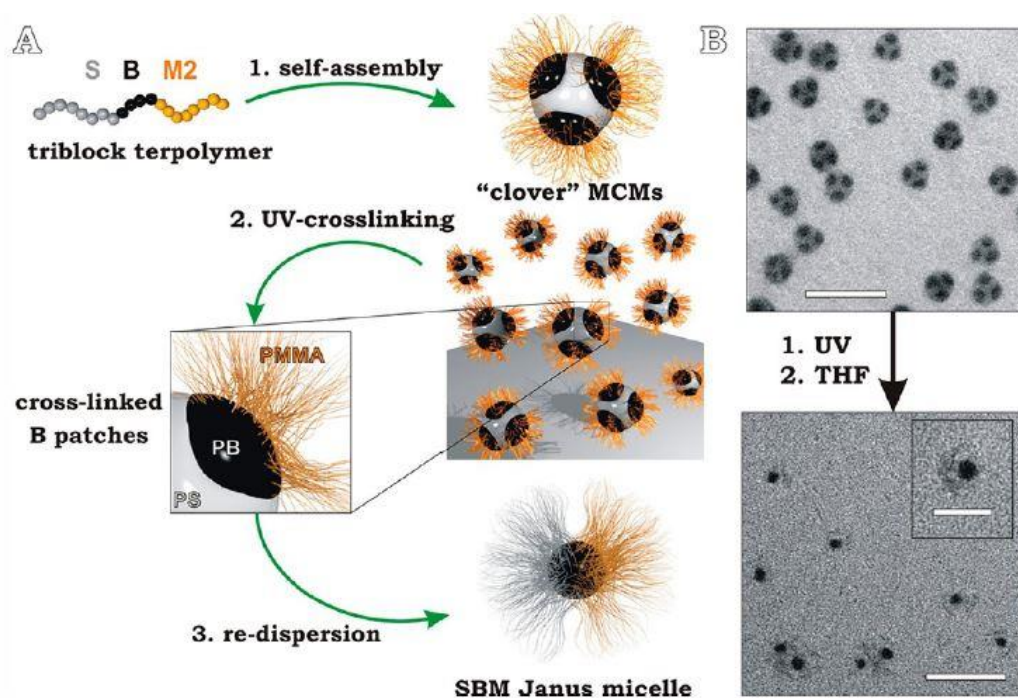


Figure T5. (A) JP synthesis via self-assembly of multicompart ment micelles, subsequent cross-linking of the compartments and redispersion in THF. (B) Corresponding TEM images of SBM2 “clover” MCMs and derived JPs. OsO_4 staining: PS gray, PB black, and PMMA is not visible due to electron beam degradation. Scale bars are 200 and 50 nm in the inset.³⁵

Janus Particles via Self-Assembled Block Terpolymer Bulk Structures

Block terpolymers are able to form a variety of well-defined self-assembled structures in the solid state. Microphase-segregated structures evolve due to the incompatibilities of different polymers (χ_{AB} , χ_{BC} , χ_{AC}), as well as the volume fractions of each block. Therefore, the appearance of certain morphologies can be tuned by changing the chemical composition of triblock terpolymers. The most widely studied triblock terpolymer system is polystyrene-*block*-polybutadiene-*block*-poly(methyl methacrylate) (SBM); its phase diagram is displayed in **Figure T6** (left).⁹ Suitable bulk morphologies for the fabrication of Janus micelles were determined by the groups of Ishizu and Müller.³⁶⁻³⁸ In both cases, spherical Janus micelles were fabricated based on the selective crosslinking of spherical domains (B) located at the interface between two lamellar domains of A and C in the so-called lamella-sphere morphology of ABC block terpolymers. Diverse chemical crosslinking methods are available for the bulk phases, such as radical crosslinking, thermally or photo-induced dimerization, or chemical crosslinking with additives. Likewise, there is a wide variety of crosslinkable polymer segments, including polydienes, cinnamoyl groups, polyacids/-bases, or gelable groups based on alkoxy-silane motifs.⁹

In detail, the Janus micelles proposed by Ishizu et al. were synthesized through the crosslinking of P2VP spherical domains in polystyrene-*block*-poly(2-vinyl pyridine)-*block*-poly(*tert*-butyl methacrylate) ABC triblock terpolymer film with PS/PtBMA lamellae-P2VP spherical structures.³⁸ Toluene was used for the formation of lamellae-sphere structures,

whereas 1,4-diiodobutane gas was used for the crosslinking of the P2VP spheres. As a result, spherical Janus micelles composed of P2VP cores and PS/PtBMA shells were formed.

Janus micelles based on SBM block terpolymers, having a polybutadiene (PB) crosslinked core surrounded by PS and poly(methyl methacrylate) (PMMA) shells, were prepared and investigated by the group of Müller.³⁷ Spherical domains of the middle PB block in well-ordered bulk morphology were crosslinked via cold vulcanization using S₂Cl₂ or via radical crosslinking with a co-cast initiator. In a further contribution, these SBM Janus micelles were transformed into strongly amphiphilic ones by alkaline hydrolysis of the PMMA ester groups, yielding Janus micelles with hydrophilic poly(methacrylic acid) (PMAA) and hydrophobic PS shells surrounding a crosslinked PB core.³⁶

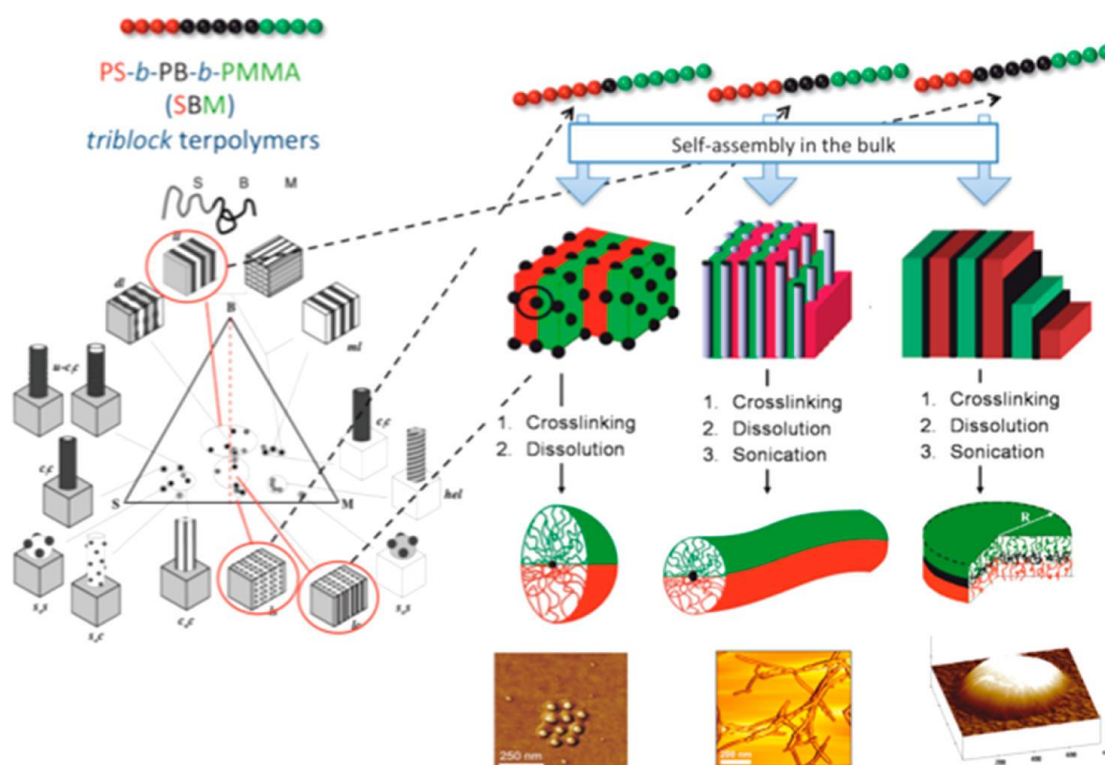


Figure T6. JPs of different architectures prepared via the selective crosslinking of the middle block of triblock terpolymer bulk phases and subsequent dissolution. Left: Phase diagram of SBM. Right: Synthetic strategy toward Janus micelles, Janus cylinders, and Janus discs.⁹

The spherical Janus micelle preparation approach was further extended by the group of Müller by transforming the central B domains of ABC block terpolymers from spherical to cylindrical and then to lamellar to yield Janus cylinders and Janus discs respectively (**Figure T6**, right). In particular, Janus cylinders were prepared in a similar way as the Janus spheres, using the SBM block terpolymer forming the lamellae-cylinder morphology in bulk and subsequent crosslinking of the PB, and dispersion.³⁹ The formed Janus cylinders had PB cores with PS and PMMA hemicylinders, and lengths up to several micrometers. In the case of the Janus discs, lamella-lamella morphology of a microphase-segregated bulk template of polystyrene-*block*-polybutadiene-*block*-poly(*tert*-butyl methacrylate) (SBT) block terpolymer was used.⁴⁰ After crosslinking the PB lamella and subsequent acid catalyzed hydrolysis of the PtBMA into PMAA, amphiphilic Janus discs with hydrophilic PMAA and hydrophobic PS

sides were obtained with thickness in the range of 30-35 nm. Moreover, the same group has recently demonstrated how one single poly(*tert*-butoxystyrene)-*block*-polybutadiene-*block*-poly(*tert*-butyl methacrylate) triblock terpolymer can be used to synthesize three different Janus topologies - Janus cylinders, sheets, and previously unknown Janus ribbons.⁴¹

In summary, JPs produced via triblock terpolymer self-assembly in bulk exhibit precise dimensions and near monodisperse sizes, typically ranging between 5 and 50 nm for their cross sections. Considering the challenges faced in the preparation of nanoscale JPs, this approach has proven to be particularly useful regarding the chemical composition and the scalability of the synthesis.⁹

Janus particles via Phase Separation in (Mini)emulsions

As already mentioned above, phase separation of polymer mixtures on the micrometer-scale occurs due to the incompatibility of two homopolymers in polymer blends. If this system is placed into an object below this length scale, a complete phase separation can be expected. Emulsions and miniemulsions can provide this suitable size regime, and can therefore be used for the fabrication of soft JPs.⁹

For instance, Okubo and co-workers examined the phase behavior of PS/PMMA homopolymer mixtures confined in micrometer-sized emulsion droplets.⁴² Composite PS/PMMA particles were prepared by evaporation of toluene from PS/PMMA/toluene droplets dispersed in an aqueous solution of a stabilizer. It was found that in the case of sodium dodecyl sulfate (SDS) as a stabilizer, the shapes of the composite particles changed from dimple, via acorn, to spherical with increasing SDS concentration. Higher SDS concentration promoted the formation of JPs with symmetric hemispheres.

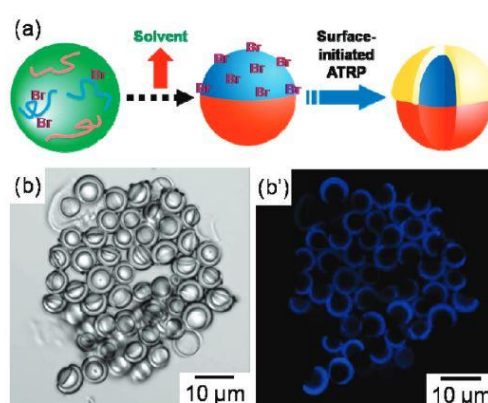


Figure T7. (a) Schematic representation of the synthesis of “mushroom-like” Janus polymer particles by the solvent evaporation method, followed by surface-initiated ATRP. (b) Optical and (b’) confocal laser scanning micrographs of labeled PMMA/P(S-BIEM)-g-PDMAEMA Janus particles dispersed in an aqueous medium on the same visual field. PDMAEMA phases appear as bright in (b’).⁴³

The same group has further extended their approach to prepare micrometer-sized amphiphilic “mushroom-like” Janus particles (**Figure T7**).⁴³ Instead of plain PS, modified PS with immobilized ATRP-initiator molecules was used to prepare spherical PMMA/poly(styrene-2-(2-bromoisobutyryloxy)ethyl methacrylate) (P(S-BIEM)) Janus

particles based on the internal phase separation induced by toluene evaporation in an aqueous medium. Surface-initiated ATRP of 2-dimethylaminoethyl methacrylate (DMAEMA) was then performed using the macroinitiator Janus particles, resulting in the formation of mushroom-like PMMA/P(S-BIEM)-*graft*-PDMAEMA JPs.

Janus Particles via Phase Inversion

In the case of the phase inversion strategy to prepare soft JPs, the same concept applies, that is, the polymers must also be spatially confined below the length scale of the bulk phase separation. However, typically a solvent that is miscible with water is used and no surfactant is needed.

For instance, Higuchi and co-workers developed a self-organized precipitation method to produce JPs based on the dissolution of polymers in a water-miscible solvent such as THF, to which a certain amount of water is added.⁴⁴ THF is then gradually evaporated, which leads to the nucleation of the phase-separated polymer particles at the air-solution interface and their subsequent precipitation. Using this strategy, well-defined JPs with PS and polyisoprene (PI) hemispheres were produced with sizes in the range of 100-300 nm depending on the preparation conditions (**Figure T8**). Another strategy to produce JPs as well as a variety of particles with different microphase separation structures developed by the same group was based on using block copolymers instead of a homopolymer mixture.⁴⁵ The effect of the PS-*block*-PI block copolymer molecular weight on the resulting particle structures was studied.

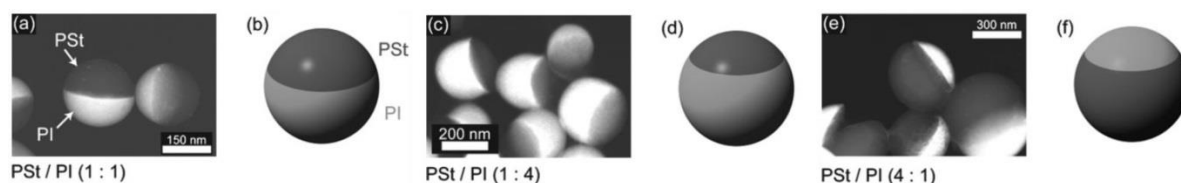


Figure T8. Dark field TEM mode images of polymer blend particles containing PS and PI [PS : PI = (a) 1 : 1, (c) 1 : 4, (e) 4 : 1]. Schematic models of polymer blend particles [PS : PI = (b) 1 : 1, (d) 1 : 4, (f) 4 : 1], respectively.⁴⁴

Janus Particles via Seeded Emulsion Polymerization

Seeded emulsion polymerization is the most technologically relevant approach for the production of Janus latex particles. First, conventional emulsion polymerization is used to prepare the initial latex seeds. Afterward, the second monomer is added and its polymerization on the latex seeds leads to a phase separation and, as a result, to completely bi-phasic Janus latex particles.⁹

For instance, Misra and Urban reported on a two-step emulsion polymerization approach to yield acorn-shaped JPs with two distinct PMMA/*n*-butylacrylate (nBA) and poly(nBA)/pentafluorostyrene (PFS) phases, their size being around 100 nm.⁴⁶ They have also indicated that it is essential to provide desirable interfacial energetic conditions during polymerization and to utilize monomers that have similar glass transition temperatures (T_g) in order to get stable phase-separated morphologies.

Dufresne et al. presented a high-yield method to produce highly monodisperse dumbbell-shaped polymer JPs with tunable aspect ratios as high as 1.8 based on a two-step seeded emulsion polymerization.⁴⁷ In the first step, core-shell nanoparticles were prepared comprising a PS core and a shell of a random copolymer of styrene and trimethoxysilylpropylacrylate (TMSPA). In the next step, the core-shell particles were swelled with styrene and polymerized, resulting in Janus particles with highly uniform dumbbell shapes on the scale of 250 to 500 nm (**Figure T9**).

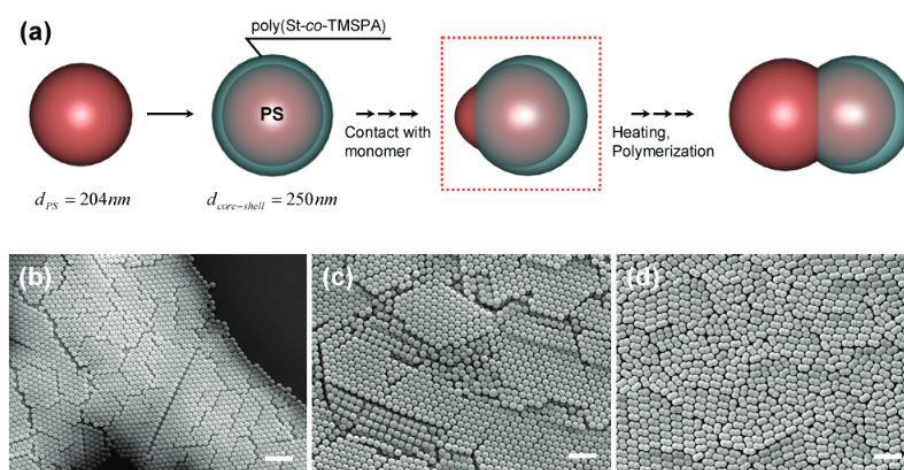


Figure T9. Synthesis of dumbbell-shaped polymer nanoparticles: (a) Schematic representation of the two-step seeded emulsion polymerization. (b-d) Scanning electron micrographs of (b) PS nanoparticles, (c) PS/poly(St-co-TMSPA) core-shell nanoparticles, and (d) symmetric dumbbell-shaped nanoparticles.⁴⁷

Janus Particles via Electrohydrodynamic Jetting

Electrohydrodynamic approaches are a powerful tool to create polymer-based or hybrid materials as well as core-shell particles or fibres. They are based on the formation of an electrohydrodynamic jet from a droplet at the tip of an electrically charged needle and a collecting counter electrode. Using this method, the biphasic geometry of the Janus particles can be induced by the simultaneous electrohydrodynamic jetting of parallel polymer solutions under the influence of an electrical field.⁴⁸

Lahann and co-workers developed this concept for the production of diverse structures, such as multicompartiment or biphasic particles with spherical or cylindrical shapes (**Figure T10 a**).⁴⁸⁻⁵⁰ For instance, biphasic Janus particles with sub-micrometer diameters were fabricated using a laminar flow of two distinct polymer solutions, which was pumped at suitable flow rates through a modified nozzle with side-by-side geometry.⁴⁸ The bipolar polymer/polymer interface was maintained between the two jetting fluids throughout the nozzle until electrified jetting occurred.

In another contribution, they have reported on the fabrication of cylindrical JPs, which were prepared through the production of multicompartimental microfiber bundles using electrohydrodynamic co-spinning, followed by an automated microsectioning step to convert the microfiber bundles into multifunctional microcylinders.⁴⁹ Electrohydrodynamic co-jetting of poly(lactide-co-glycolide) (PLGA) from organic solvents was utilized to yield cylinders

with average diameters of 14 μm and an average length of 5 μm . In a similar contribution, selective surface modification of individual compartments via click chemistry could also be demonstrated, yielding a novel type of spatioselectively modified particles and fibers (**Figure T10 b, c**).⁵⁰

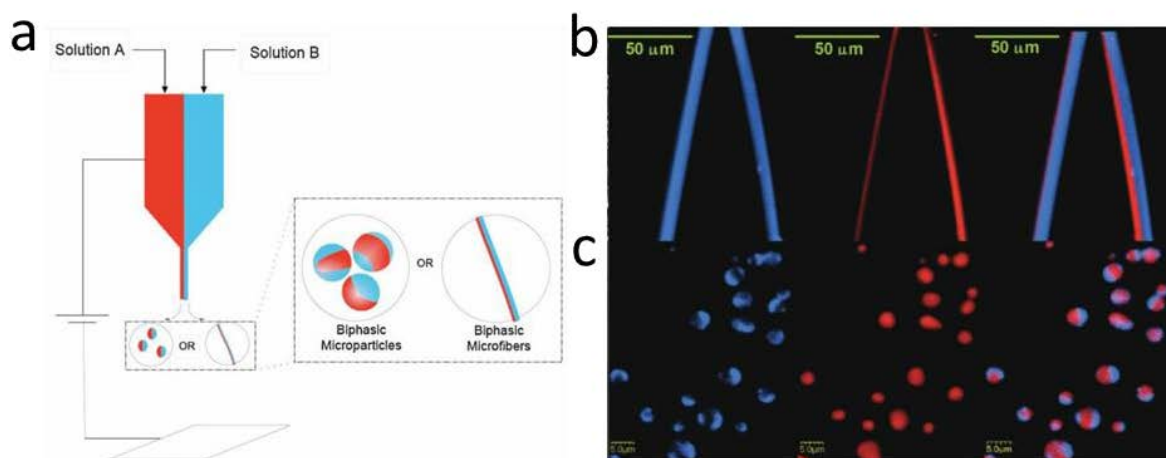


Figure T10. (a) Scheme depicting the electrified jetting process to produce biphasic microparticles or microfibers. Confocal laser scanning microscopy images of (b) biphasic microfibers, and (c) biphasic microparticles made from PLGA 85:15 (red) and PLGA 50:50 (blue).⁵⁰

Janus Particles via Microfluidics

Microfluidic techniques have proven to be a very effective tool to produce micrometer-sized particles as well as Janus particles with precise control over their shape and functionality. Two types of microfluidic setups can be used for the preparation of JPs: (a) droplet-based production via side-by-side emulsification, and (b) lithographic exposure of parallel streams.⁹

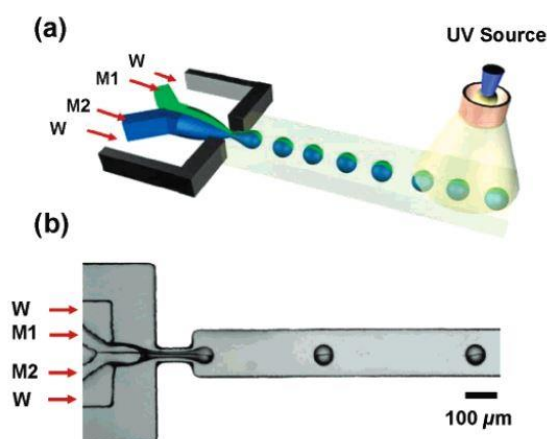


Figure T11. (a) Schematic of the Janus droplet generation from immiscible monomers $M1$ and $M2$, emulsified in an aqueous solution of SDS (W). The droplets are irradiated with UV light in the downstream channel. (b) Optical microscopy image of the Janus droplet formation.⁵¹

Using the first approach, Kumacheva et al. generated Janus droplets in a microfluidic flow-focusing device (MFFD) using side-by-side emulsification of two liquid monomers ($M1$ and $M2$), each mixed with a photoinitiator and supplied to two central channels of the MFFD (**Figure T11**).⁵¹ Methacryloxypropyl dimethylsiloxane was used as $M1$, and a mixture of

pentaerythritol triacrylate (45.0 wt %), poly(ethylene glycol) diacrylate (45.0 wt %) and acrylic acid (5.0 wt %) was used as M2. An aqueous solution of SDS served as a continuous phase. The droplets were subsequently polymerized by exposing them to UV-irradiation. The Janus ratio of the resulting particles could be tailored by changing the ratio of the flow rates.

An interesting strategy was proposed by Weitz and co-workers, who prepared JPs with one side composed of a hydrogel and the other side composed of aggregated microgel nanoparticles.⁵² For this purpose, they used polyacrylamide (PAAm) as the hydrogel and poly(*N*-isopropylacrylamide) (PNIPAAm) microgels as the nanoparticles. PNIPAAm microgels were modified with reactive amine groups, and a small amount of PAA was added to induce clustering of the microgels by electrostatic interactions. Additionally, acrylamide along with a crosslinker and a photoinitiator were dissolved in the microgel suspension. The microfluidics approach was then used to prepare emulsion droplets of the suspension in a surfactant-containing silicon oil phase. Upon heating the emulsion, the PNIPAAm microgels shrank and compacted on one side of the droplets, forming polyelectrolyte complexes with the PAA and pushing the acrylamide containing water to the other side. The acrylamide monomer was then polymerized and cross-linked by UV-exposure, forming Janus particles with a PNIPAAm microgel-rich side and a PAAm-rich side.

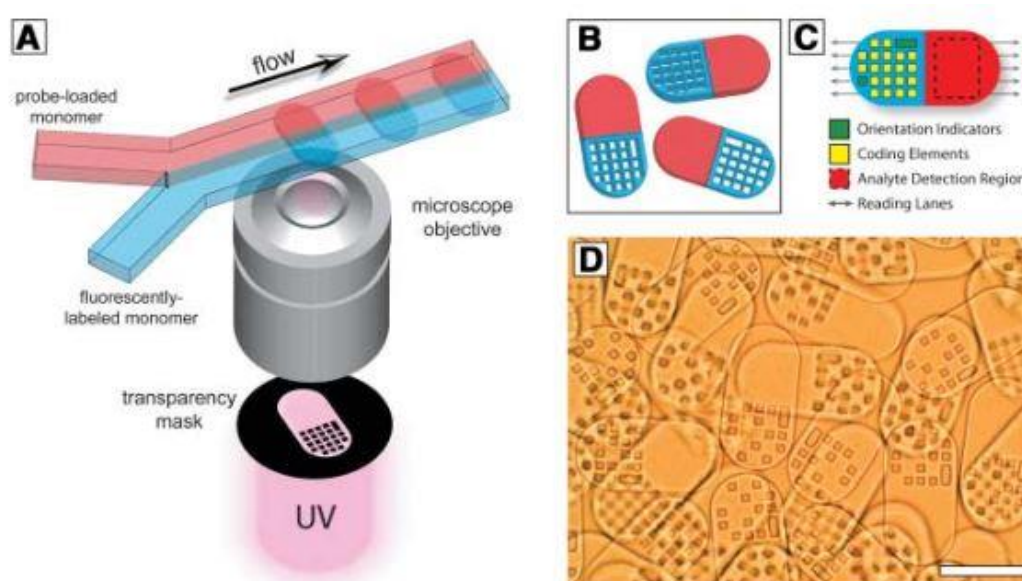


Figure T12. (A) Schematic diagram of the dot-coded particle synthesis, showing polymerization across two adjacent laminar streams to make single-probe, half-fluorescent particles shown in (B). (C) Diagrammatic representation of particle features for encoding and analyte detection. (D) Differential interference contrast image of the particles generated by using the scheme shown in (A).⁵³

The second microfluidic approach developed to create well-defined submillimeter-sized JPs with sophisticated microstructures and patterns is based on the combination of lithography and co-continuous flow microfluidics. For instance, Doyle and co-workers combined microscope projection photolithography and microfluidics to continuously form particles with diverse shapes as well as Janus particles down to the colloidal length scale.⁵⁴ In the developed approach, a mask containing the desired features is inserted in the field-stop plane of the

microscope. The co-flowing monomer streams are passed through the all-polydimethylsiloxane (PDMS) device. The generated particles are ultimately polymerized by a mask-defined UV light beam emerging from the objective, and then flow within the unpolymerized monomer stream. The same group has further advanced their approach and combined particle synthesis and encoding with probe incorporation into a single process in order to generate multifunctional particles based on poly(ethylene glycol) (PEG) and bearing over a million unique codes (**Figure T12**).⁵³

2.2.2. Hard Inorganic Janus Particles

Janus particles via Desymmetrization at Planar Surfaces

Probably the most reliable strategy for the preparation of JPs, especially inorganic and hybrid ones, is based on using interfaces as a desymmetrization tool. One of the first strategies to fabricate JPs was the modification of the exposed surfaces of particle monolayers immobilized on planar substrates. The most popular synthetic modification of the unprotected particle surface is metal shading.⁵⁵ However, a variety of other approaches have also been developed, such as metal deposition in glancing angle mode,⁵⁶ microcontact printing,⁵⁷ UV photopolymerization,⁵⁸ plasma treatments,⁵⁹ reactive ion etching,⁶⁰ or binding of metal NPs.⁶¹ The particles may be physically or covalently attached to the layer, or entrapped in polymer films. In the case of metal shading, various metals can be deposited onto the exposed surfaces of silica (or latex) particle monolayers, yielding well-defined JPs with metal half shells. For example, gold and platinum are of great interest due to the possibility of conjugation with thiols and the catalytic properties, respectively, whereas iron, cobalt, or nickel can be used to create magnetic JPs.⁹

For instance, Ye and Carroll developed an approach to yield bimetallic JPs comprising silica beads of sizes ranging from 800 nm to 4 μm coated with different metals on their opposite hemispheres.⁶² The process involved coating a single layer of silica beads with one metal using e-beam evaporation, then lifting the layer and inverting it with the help of an adhesive tape and subsequent coating of the particles with the second metal. In this way, Au/Pt, Au/Ag, and Au/Ni Janus particles were prepared.

A simple approach to create optically tunable silica-gold patchy and multi-region JPs of different sizes was proposed by Yang and Composto et al.⁶³ In a typical procedure, amine-modified silica particles (106, 230, and 460 nm) were covalently attached through amide bond formation to a styrene-acrylic acid random copolymer film, into which they partially sank. The immersion depth, that is, the resulting Janus ratio of the particles, could be controlled by varying the reaction time. Afterward, negatively charged 15 nm gold NPs were assembled onto the positively charged modified silica surfaces, resulting in the formation of partly covered Janus particles (**Figure T13**). Treatment with Au:Pd, followed by annealing, led to the formation of a continuous cap of gold on the top surface of the silica particles.

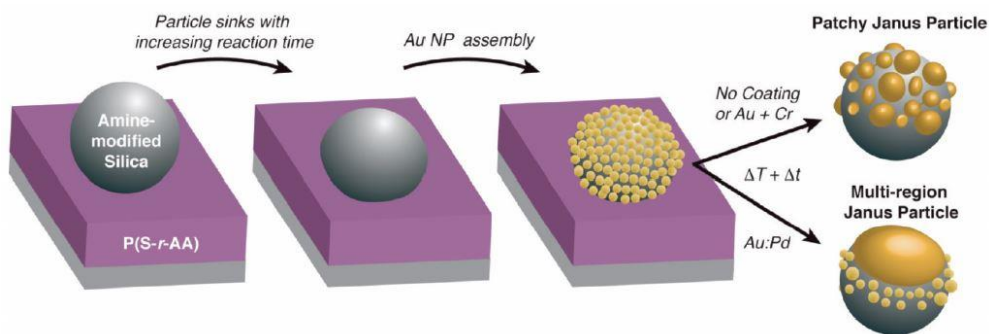


Figure T13. Schematic representation of the self-assembled formation of patchy and multi-region Janus particles.⁶³

Granick et al. introduced a strategy for the preparation of Janus and trivalent particles based on the microcontact printing technique.⁵⁷ For this purpose, a PDMS stamp was prepared by mixing Sylgard 184 agents and treated by oxygen plasma to provide it with the needed adhesion and wettability. A silane solution was spread onto the PDMS stamp by spin coating. Afterward, the stamp was brought in contact with the 1 μm sized silica particle monolayer. After applying mechanical pressure, the stamp was separated from the substrate, lifting the adhered particles. This resulted in silica particles chemically modified with amino silane at one pole. The opposite pole can be subsequently stamped in the second step. Furthermore, the size of the patches can be adjusted by adjusting the stiffness of the PDMS stamp.

Although desymmetrization at planar surfaces is a very straightforward technique for the production of JPs, it typically results in very low yields of the particles due to the limited interface as well as limitations in the particle size, excluding nanoscale JPs.

Janus Particles via Desymmetrization in High Internal Interface Systems

To overcome the problem of low particle yields during desymmetrization at planar surfaces, new concepts have evolved to replace these surfaces with high internal interface systems, such as particle-stabilized foams and emulsions. This strategy has proven to be particularly useful for the production of hard inorganic as well as hybrid JPs discussed later.

Among the systems providing high internal interfaces, Pickering emulsions are of greatest interest for particle immobilization, leading to considerable advances in the preparation of JPs. This method offers easy scalability and precise control as well as unsophisticated instrumentation. A Pickering emulsion, first described by S. U. Pickering in 1907, is a two-phase system consisting of oil and water, where the oil/water interface is stabilized by solid particles (for example, colloidal silica) binding to the interface via purely physical interactions.⁶⁴ The formation of Pickering emulsions is strongly favored with increasing particle size and becomes challenging for smaller particles, such as NPs smaller than 100 nm. Tight anchorage of particles is particularly important here to overcome rotational diffusion and desorption/resorption processes.⁹

Taking this consideration into account, Granick et al. has proposed to use molten paraffin wax as an oil phase.⁶⁵ In the first step, a Pickering emulsion is made at high temperature

(where the wax is molten), and then it is cooled down to “lock” the silica particles at the solidified wax-water interface, preventing particle rotation (**Figure T14**). The emulsions are sufficiently stable to be washed to remove non-adsorbed silica particles as well as to modify them chemically in solution. This allows a selective chemical modification of the particle outer surface. After the modification, wax can be dissolved in organic solvents, and the resulting particles can be further modified chemically. Ultimately, two kinds of Janus particles were prepared in this way (800 nm and 1.5 μm large): bipolar JPs with an anionic silica side and a cationic side modified by 3-aminopropyltriethoxysilane (APS), and charged/hydrophobic JPs with a cationic APS-modified side and a hydrophobic *n*-octadecanetriclorosilane (OTS)-modified side. In another report, the same group has demonstrated how to tune the Janus balance of the resulting JPs by controlling the immersion depth of the silica particles into the wax phase with the help of oppositely charged surfactants.⁶⁶ As a result, silica particles modified using different amounts of didodecyldimethylammonium bromide exhibited contact angles that could be varied controllably between 37° and 75° . A solvent-free synthesis of JPs was also shown by Granick et al., who modified the exposed surfaces of the immobilized silica particles in the dried Pickering emulsion droplets by exposure to silane vapor, thus overcoming the problem of particle desorption during the wet-chemical approach.⁶⁷

Ravaine et al. reported on the preparation of Janus particles as small as 100 nm through the utilization of the Pickering emulsion approach.⁶⁸ The method is based on a limited coalescence process, which implies that all the introduced silica particles are adsorbed at the wax-water interface. The selective modification of the silica particles was confirmed by adsorption of gold nanoparticles onto the silane-modified patches.

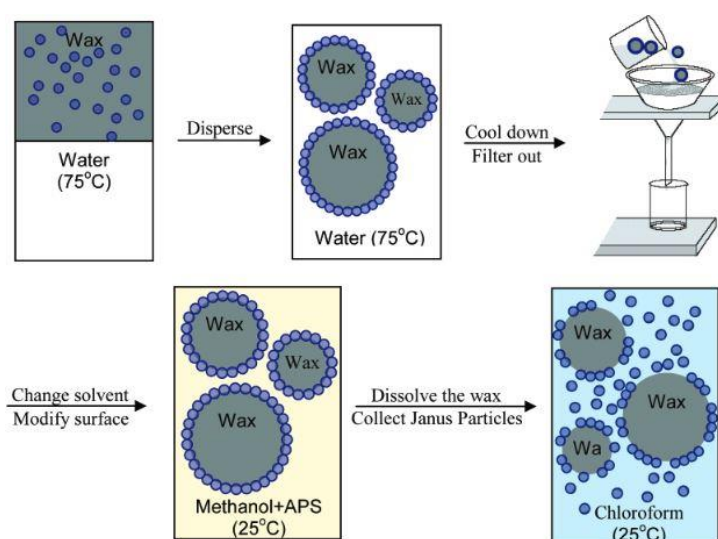


Figure T14. Schematic procedure to create Janus particles by functionalizing particles adsorbed onto an emulsion of water and oil and then cooling the sample so that the oil crystallizes to form a wax.⁶⁵

Inorganic nanoparticles (NPs) can provide rich functionality to the materials and a variety of appealing properties such as magnetic properties, conductivity, or photoactivity. The generation of inorganic Janus nanoparticles is a challenging task because of the difficulties of their selective modification. Most efforts to prepare Janus NPs typically concentrate on Au and Fe₃O₄ NPs.

For instance, Chen et al. demonstrated an approach to prepare Janus NPs based on ligand exchange reactions of a Langmuir monolayer of hydrophobic alkanethiolate-passivated Au NPs at relatively high surface pressures with hydrophilic thiol derivatives injected into the water subphase.⁶⁹ This resulted in NPs consisting of ca. 50% hydrophobic and 50% hydrophilic ligands on the particle surface distributed on two separate sides of the particles.

In another approach, Shumaker-Parry and co-workers reported on the solid phase synthesis of gold nanoparticle dimers through an asymmetric functionalization pathway.⁷⁰ First, the citrate-stabilized 41 nm large Au NPs were immobilized on a silanized glass surface (**Figure T15**). Second, they were modified with 11-mercapto-1-undecanol (MUOH), which resulted in the formation of a self-assembled monolayer (SAM) of thiol molecules on the outer surface of the Au NPs. Then the MUOH functionalized NPs were treated with either amine- or acid-terminated thiols through sonication and simultaneous liberation of the particles, which resulted in the formation of two kinds of JPs with hydroxyl/amine and hydroxyl/acid functionalized hemispheres, respectively.

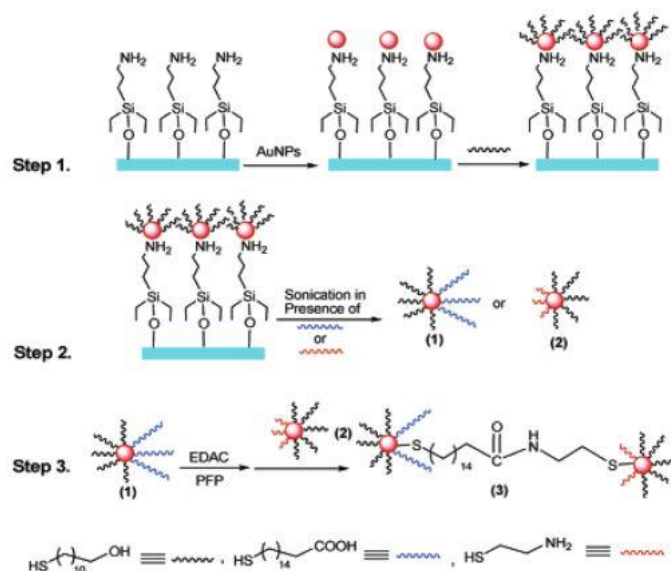


Figure T15. Synthesis of gold nanoparticle dimers.⁷⁰

The second major strategy toward the preparation of Janus inorganic NPs is based on the attachment or controlled growth of a second NP onto the primary one, creating dumbbell-shaped NPs. For instance, bifunctional dumbbell-like Au-Fe₃O₄ NPs were prepared by Sun et al. using decomposition of Fe(CO)₅ on the surface of the Au nanoparticles followed by oxidation in 1-octadecene solvent.⁷¹ The size of the particles was tuned from 2 to 8 nm for Au and from 4 to 20 nm for Fe₃O₄ NPs. The resulting multifunctional dumbbell-like JPs allow a

selective functionalization of the Au part with thiol-terminated molecules and biomolecules, whereas the Fe₃O₄ part provides the particles with magnetic properties.

2.2.3. Hybrid Organic / Inorganic Janus Particles

The variety of synthetic strategies discussed above can be used with particular modifications for the production of hybrid Janus particles, that is, Janus particles simultaneously having organic and inorganic parts. The most widely used JP architecture in this regard is an inorganic core particle toposselectively covered with either one or two distinct polymer shells. Such hybrid structure of the particles provides them with multi-functionality required to address diverse applications.

Janus particles via Desymmetrization at Planar Surfaces

Using a strategy based on planar plasma enhanced chemical vapor deposition polymerization, Tsukruk and co-workers fabricated organic-inorganic 3 μm large Janus particles.⁷² For this purpose, silica or titania microspheres were partially embedded into a sacrificial PS layer, followed by plasma enhanced polymerization to deposit different monomers onto the exposed surfaces, such as organic functionalized, reactive, responsive, and biomolecular materials ranging from acrylic compounds to organometallic molecules and amino acids (**Figure T16**). After the sacrificial layer was dissolved, robust half-fluorescent, half-metal-decorated, and half-shelled Janus particles were released.

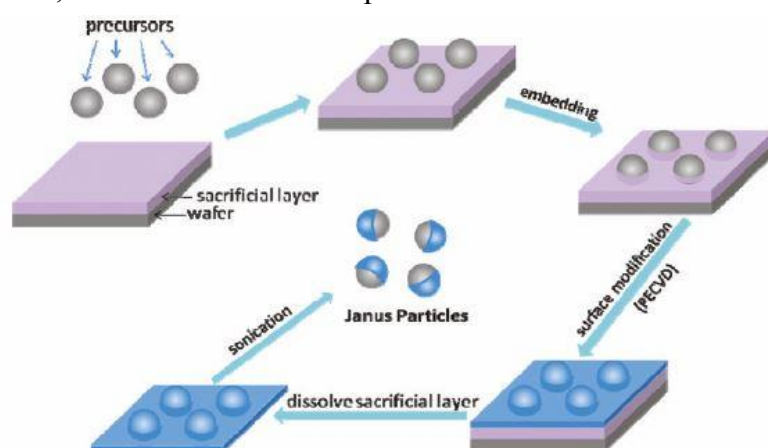


Figure T16. Janus particle fabrication using a sacrificial layer to embed the particles prior to plasma polymerization: upon dissolution of the PS layer, the particles are released with a characteristic half coating.⁷²

Janus Particles via Desymmetrization in High Internal Interface Systems

The Pickering emulsion-based strategy has been widely used for the preparation of hybrid JPs. For instance, Qu and Yang et al. prepared non-spherical silica Janus colloids through asymmetric wet-etching at the Pickering emulsion interface.⁷³ The exposed sides of the 320 nm large silica colloids were progressively etched with NH₄F resulting in a roughening of the exposed side and the removal of surface modifications. The non-etched surface still carried vinyl groups, thus, allowing polystyrene caps to be grown from that side through one-stage

emulsion polymerization after the release of the etched silica particles from the wax substrate. As a result, hybrid PS/silica JPs were produced and the PS side's shape could be altered from a cap or a single sphere to nano-flowers (Figure T17).

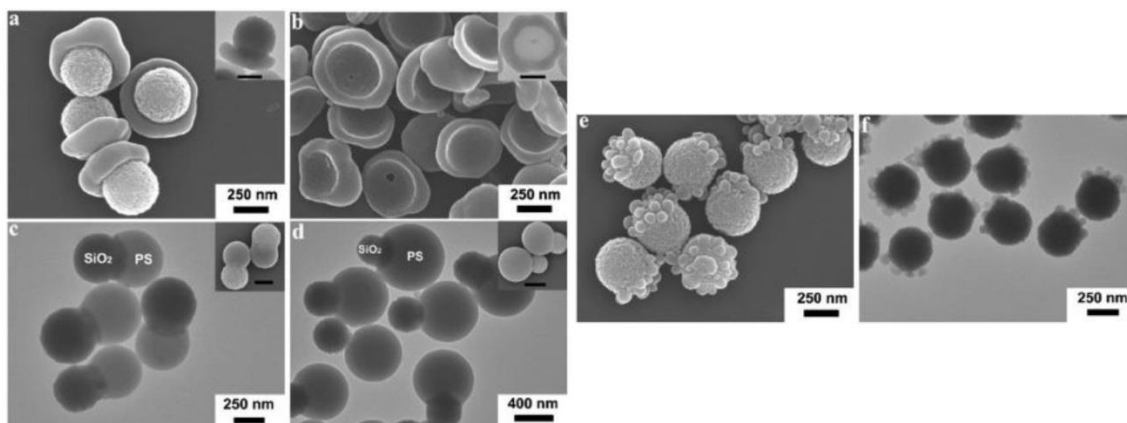


Figure T17. (a) SEM and inset TEM images of the Janus SiO_2/PS composite colloids with a PS cap grown on the corona side; (b) SEM and inset TEM images of the PS nano-caps after removing SiO_2 from (a); (c), (d) TEM and inset SEM images of the Janus SiO_2/PS dimers with increased PS volume fraction (the dark area corresponding to silica and the grey area corresponding to PS); (e), (f) SEM and TEM images of the Janus SiO_2/PS composite colloids with PS nano-flowers grown on the corona side.⁷³

In addition to wet-etching, many efforts have been focused on providing the particles with functionality through polymer chemistry by using controlled/living radical polymerization techniques. For instance, Yang and co-workers presented the fabrication of amphiphilic Janus colloids via simultaneous biphasic grafting of different polymer brushes onto the opposite sides of the silica spheres (450 nm) at a liquid/liquid Pickering emulsion interface via ATRP.⁷⁴ The silica spheres were modified with an ATRP-initiator prior to immobilization at the interface. The oil-in-water Pickering emulsion was formed with the water phase containing AAm and the toluene phase containing styrene, as well as appropriate water-soluble or oil-soluble ligands. The polymerization was initiated by adding CuCl and increasing the temperature. As a result, JPs having a silica core and biphasically grafted with PS and PAAm shells were produced. Colloid rotation was not initially frozen in this system; however, it was argued that additional hydrophilic/lipophilic interactions with the original Pickering colloid restrict the rotation.

A modified strategy for the preparation of biphasically grafted JPs was presented by Synytska et al., who proposed a combination of “grafting from” and “grafting to” approaches to fabricate stimuli-responsive and dipolar hybrid JPs.⁷⁵ The procedure is based on the formation of a wax/water Pickering emulsion stabilized by amine-modified silica particles and the following modification of their exposed surface with an ATRP initiator. In this way, side-selective polymerization of NIPAAm or tBA could be performed using the “grafting from” approach after the dissolution of the wax. After particle purification, the “grafting to” approach was used to couple carboxy-terminated P2VP chains with the amino groups on the particle surface in melt. The PtBA side of the JPs was further hydrolyzed to yield dipolar PAA/P2VP JPs, demonstrating pH-dependent assembly in solution.

Janus particles via Phase Separation in (Mini)emulsions

Inducing phase separation in a miniemulsion may be used not only for the preparation of soft, but also hybrid Janus particles. For instance, Hatton and co-workers proposed a sonochemical synthesis route to generate hybrid JPs with sizes below 100 nm based on the miniemulsion polymerization of nanodroplets formed from styrene, inorganic tetraethoxysilane, and a silane coupling agent (3-aminopropyl)trimethoxysilane.⁷⁶ Prolonged ultrasonication resulted in the phase separation of TEOS nodules from the formed latex particles, which remained linked together due to the added silane compatibilizer. If magnetite particles were dispersed in the organic phase before polymerization, magnetic JPs could be formed.

Janus Particles via Seeded Emulsion Polymerization

The seeded emulsion polymerization approach is typically used to prepare soft polymer-based JPs, but it can also be used to prepare hybrid organic/inorganic composite particles. For instance, Zhang and Yang et al. produced submicrometer sized Janus PAN/PS polymer colloids by seeded emulsion polymerization of styrene onto a cross-linked polyacrylonitrile (PAN) hollow colloid seed.⁷⁷ Both high crosslinking degree of PAN and the slow feeding of the monomer are crucial to fabricate well-defined JPs. Carboxylic acid groups can then be derived by selective hydrolysis of PAN, which facilitates a further favorable growth of other materials, for example, silica by a sol-gel process, or selective adsorption of Fe₃O₄ magnetic NPs, thereby forming Janus composite colloids. The same group has further synthesized anisotropic silica/polymer composite colloids by surface heterogeneous radical polymerization-induced dewetting.⁷⁸ Here, it is crucial to control the monomer concentration at a very low level.

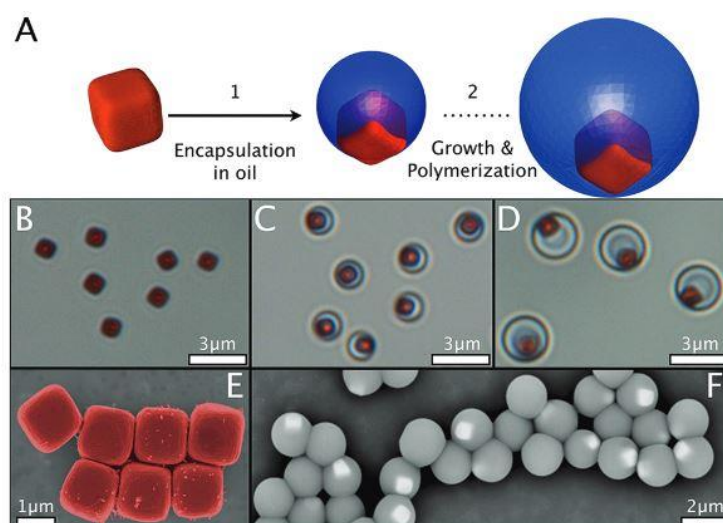


Figure T18. Particle fabrication. (A) Schematic diagram showing the synthetic steps involved in the preparation of particles with a single magnetic patch. (B–D) Encapsulation and growth followed by optical microscopy. (E) False-color SEM image showing the bare micromagnets. (F) SEM image of the final spherical particles carrying a single magnetic patch.⁷⁹

Sacanna et al. demonstrated an approach to prepare magnetic/polymeric hybrid JPs based on an organosilica polymer sphere with an embedded single hematite micromagnet.⁷⁹ For this purpose, the prepared uniform magnetic hematite microcubes were encapsulated into polymerizable silicon oil droplets in an oil-in-water emulsion, which was formed in situ via a polycondensation reaction between metastable water-soluble silanols that ultimately phase separate and form monodisperse droplets (**Figure T18**). Each cube acts as a nucleation site for the formation of an oil droplet, as a result, producing droplets with a single magnetic inclusion. The main feature of this mechanism is that, during the phase transfer from water to oil, the cubes are trapped at the interface, leaving one side of the cube exposed to the water phase. In the final step, radical polymerization was used to harden the oil phase, yielding patchy hybrid colloids.

Janus Particles via Microfluidics

Given the large size of the resulting structures, one way to create hybrid JPs using microfluidics is to incorporate inorganic NPs or colloids into the hydrogels. For instance, Lewis and co-workers demonstrated a microfluidic assembly route to create monodisperse colloid-filled hydrogel granules of tunable size, geometry, and composition.⁸⁰ For this approach, they have used silica microspheres of ca. 500 nm in diameter labeled with two different fluorescent dyes and side-by-side emulsified them in an aqueous acrylamide solution within a continuous oil phase. Next, the drops were photopolymerized to create an acrylamide hydrogel that freezes in the desired morphology. Both spherical and discoid hybrid Janus granules of controlled composition and sizes of ca. 100 μm were produced using this route.

Hybrid Janus Nanoparticles

Concerning Janus NPs with an inorganic core, one of the first ways to use desymmetrization in solution to prepare asymmetrically decorated hybrid JPs was realized by Li et al., who functionalized Au NPs with two different types of polymer chains on the opposite sides by combining “grafting to” and “grafting from” approaches (**Figure T19**).⁸¹

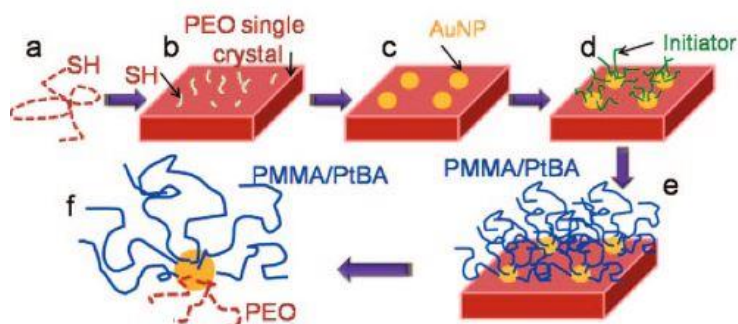


Figure T19. Schematic illustration of polymer-functionalized Janus Au NPs by combining “grafting to” and “grafting from” methods.⁸¹

In their synthetic route, thiol-terminated poly(ethylene oxide) (HS-PEO) was solution crystallized into lamellar single crystals, and Au NPs were then immobilized on the crystal

surface by mixing an ammonium-ligand-protected Au NP solution and the HS-PEO single crystal suspension. In this way, PEO was attached to the selected area of the Au NP surface through the “solid-state grafting to” method. A thiol-terminated initiator was then used to replace ammonium ligands on the “free” surface of Au NPs, yielding asymmetric PEO/AuNP/initiator structures. Finally, ATRP was performed on the initiator-coated side of the Au NPs through the “grafting from” approach, resulting in PMMA/PEO and PtBA/PEO Janus Au NPs after dissolving the substrates.

2.3. INTERFACIAL ACTIVITY & (SELF-) ASSEMBLY OF JANUS PARTICLES

2.3.1. Interfacial Activity of Homogeneously Decorated Particles

The phenomenon of solid particle adsorption at interfaces such as gas-liquid or liquid-liquid is of great interest due to its diverse potential applications in the stabilization of foams and emulsions, respectively. One of the crucial parameters is the hydrophobicity of the particles, which can be varied by coating them with different materials or to different extents, and dictates the type of the emulsion (oil-in-water or water-in-oil) and its coalescence stability. As a result, particles possessing intermediate hydrophobicity are the most effective for stabilizing submicrometer-sized oil or water droplets. Such particles typically have different ratios of hydrophobic and hydrophilic groups on the surface and exhibit different wettabilities, but in each case the overall wettability is uniform over the particle surface. Thus, uniform homogeneous particles with intermediate wettability possess high interfacial activity at oil-water interfaces, resulting in their ability to stabilize emulsions.⁸²

The desorption energy from an interface of a homogeneous particle (HP) derived by Pieranski⁸³ is expressed as:

$$E_{des.} = \pi R^2 \gamma_{OW} (1 - |\cos \beta|)^2 \text{ with}$$

$$\cos \beta = \frac{|\gamma_{HPO} - \gamma_{HPW}|}{\gamma_{OW}} \quad (1)$$

Herein, γ_{HPO} , γ_{HPW} , and γ_{OW} are the interfacial tensions of the homogeneous particle (HP) with oil (O) and water (W), and between the two phases (oil and water), respectively, R is the particle radius. The maximum of the desorption energy, $E_{des.}$, can be reached if $\gamma_{HPO} - \gamma_{HPW} \ll \gamma_{OW}$ and reads as $\pi R^2 \gamma_{OW}$. The relation also demonstrates that the desorption energy increases with increasing particle size.⁹

2.3.2. Interfacial Activity of Janus Particles

While having a particle character, Janus particles combine the amphiphilicity characteristic for low molecular weight surfactants or block copolymers. Therefore, one of the most appealing applications of JPs is the stabilization of different interfaces, for example, in

emulsions or foams. It arises from the ability of JPs to adsorb to the interfaces more efficiently than their homogeneous analogues.^{14, 82} In the case of Pickering emulsions, JPs with anisotropic wettability can stabilize them during longer periods of time and under more stressing experimental conditions (such as temperature changes or shear effects) than the homogeneous particles (HPs). Contradictory to HPs, JPs possess high interfacial activity regardless of their amphiphilicity degree, simply due to the spatial isolation of the regions with different wettability.⁸⁴ Accordingly, it is crucial to properly evaluate the colloidal stability in bulk and the interfacial activity of JPs to develop the aforementioned applications.

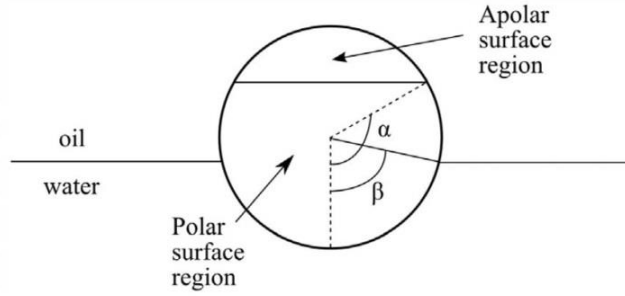


Figure T20. Geometry of a Janus particle within an oil–water interface. The relative areas of the polar and apolar particle surface regions are parameterized by the angle α . The immersion depth of the particle in the oil–water interface is parameterized by the angle β .⁸²

Binks and Fletcher accomplished a theoretical comparison between the desorption energies of particles with uniform wettability (HPs) and JPs adsorbed at an oil-water interface.⁸² The amphiphilicity degree was varied from zero to the maximum value. The amphiphilicity of JPs can be tuned by the variation of both the angle α (parameterizing the relative areas of the polar and apolar domains, **Figure T20**) and the magnitude of the difference between the θ_A and θ_P , which correspond to the equilibrium contact angles of the two distinct domains of the particle adsorbed at the oil-water interface. Zero amphiphilicity correlated to HPs corresponds to either $\alpha = 0^\circ / 180^\circ$, or $(\theta_A - \theta_P) = 0^\circ$. On the other hand, the highest degree of amphiphilicity is expected when $\alpha = 90^\circ$ and $|\theta_A - \theta_P| = 180^\circ$. The total surface free energy E of a JP at an oil-water interface as a function of the angle β (characterizing the immersion depth of the particles, **Figure T20**) can be expressed as:

$$\text{for } \beta \leq \alpha$$

$$E(\beta) = 2\pi R^2 \left[\gamma_{AO}(1 + \cos \alpha) + \gamma_{PO}(\cos \beta - \cos \alpha) + \gamma_{PW}(1 - \cos \beta) - \frac{1}{2}\gamma_{OW}(\sin^2 \beta) \right] \quad (2)$$

$$\text{for } \beta \geq \alpha$$

$$E(\beta) = 2\pi R^2 \left[\gamma_{AO}(1 + \cos \beta) + \gamma_{AW}(\cos \alpha - \cos \beta) + \gamma_{PW}(1 - \cos \alpha) - \frac{1}{2}\gamma_{OW}(\sin^2 \beta) \right] \quad (3)$$

Herein, R is the particle radius, and γ_{AO} , γ_{PO} , γ_{AW} , γ_{PW} and γ_{OW} are the interfacial tensions of the apolar domain-oil, polar-oil, apolar-water, polar-water, and oil-water interfaces, respectively.

Furthermore, the contact angles θ_A and θ_P correspond to the equilibrium angles given by the Young's equation as follows:

$$\cos \theta_A = \frac{\gamma_{AW} - \gamma_{AO}}{\gamma_{OW}} \quad (4)$$

$$\cos \theta_P = \frac{\gamma_{PW} - \gamma_{PO}}{\gamma_{OW}} \quad (5)$$

The average contact angle of the JP is weighted by the relative areas of the polar and apolar domains as follows:

$$\theta_{average} = \frac{\theta_A(1 + \cos \alpha) + \theta_P(1 - \cos \alpha)}{2} \quad (6)$$

The immersion angle β corresponding to the minimum surface energy configuration of the JPs depends on the relative magnitudes of α , θ_A and θ_P . There are three possibilities in this case:

$$\begin{aligned} \text{For } \alpha < \theta_A < \theta_P; \text{ then } \beta &= \theta_A \\ \text{For } \theta_A < \alpha < \theta_P; \text{ then } \beta &= \alpha \\ \text{For } \theta_A < \theta_P < \alpha; \text{ then } \beta &= \theta_P \end{aligned} \quad (7)$$

Eqs. (2) and (3) together with the inequalities in Eq. (7) allow the calculation of the minimum surface energy of the adsorbed particle, E_{ads} . The surface energy of the particle located entirely in either the oil (E_{oil}) or the water (E_{water}) phase is given by Eqs. (2) and (3) with β set to either 0° (for the particle in oil) or 180° (for the particle in water). The surface activity of the (Janus) particle was calculated by Binks and Fletcher⁸² as the desorption energy, which is defined as the free energy required to desorb the particle from the interface into either the oil or the water phase, ($E_{oil} - E_{ads}$) or ($E_{water} - E_{ads}$), whichever is the lowest.

The two most important conclusions drawn from the study performed by Binks and Fletcher⁸² are: (1) the desorption energies may be increased threefold by maximizing the amphiphilicity of JPs; (2) contrary to HPs, JPs retain their strong adsorption even for average contact angles of 0° and 180° .

Apart from theoretical calculations, there are various experimental studies concerning the surface activity and interfacial behavior of JPs adsorbed at fluid-fluid interfaces. Different experimental methods can be used to characterize the interfacial activity of interfaces loaded with JPs, such as the Langmuir film balance technique. However, the synthetic strategies often produce low amounts of JPs, which are insufficient to perform an experiment of the Langmuir balance. Other experimental methods include pendant drop tensiometry, which allows exploring the interfacial activity of JPs at different fluid-fluid interfaces with a much lower amount of JPs. It also enables performing dilatational surface rheology to characterize the collective behavior of the JPs at the interface of the pendant drop. Generally, in all the theoretical and experimental studies there are several main parameters that govern the interfacial activity of the JPs: particle shape, morphology, spatial distribution of the hydrophobic/hydrophilic domains, spreading solvent, colloidal stability, charge, and

composition of the JPs. Eventually, regardless of the synthetic and characterization strategies, JPs possess an enhanced interfacial activity compared to the corresponding HPs.⁸⁵

2.3.3. (Self-) Assembly of Janus Particles in Continuous Media

Self-assembly is the basic way of building complex structures in nature. It occurs on every level, from singular atoms and molecules to molecular aggregates, colloidal particles, and larger systems such as groups of animals, solar systems, and galaxies. The understanding of the self-assembly processes is of serious fundamental interest for the fabrication of complex materials, in which new functionalities can emerge that are not present in the individual building blocks. Therefore, it is necessary to better understand and control the self-assembly of particles, such as colloidal or nanoparticles, into defined superstructures in order to exploit their rich functionality (for example, their optical, electric, magnetic, or conductive properties) toward novel multifunctional materials.

Janus particles represent a unique class of multifunctional building blocks. On both colloidal and nanoparticle scale, they combine broken symmetry and chemical anisotropy in one particle. Therefore, the assembly of JPs can lead to a variety of sophisticated structures inaccessible to their homogeneous counterparts. Up to date, there are miscellaneous studies devoted to the (self-) assembly of JPs, which include amphiphilic, dipolar JPs, and JPs with special binding motifs, or magnetic/metallic caps for their assembly in external fields. Apart from the experimental works, there is also a variety of theoretical investigations based on computer simulation approaches toward the construction of phase diagrams for JPs with different architectures and compositions. The following section will give an overview and state-of-the-art concerning the (self-) assembly of Janus particles toward fascinating complex structures.

Self-Assembly of Soft, Nanoscale Janus Particles

In terms of the smallest unimolecular JPs, an example of amphiphilic Janus dendrimer self-assembly into uniform onion-like dendrimersomes was demonstrated by the group of Percec.²⁶ First, a library of Janus dendrimers was synthesized by a modular approach with dodecyl groups and triethylene glycol fragments used for hydrophobicity and hydrophilicity, respectively. Eventually, six primary structures of single-single amphiphilic Janus minidendrimers were shown to self-assemble into uniform onion-like dendrimersomes via simple injection of their solution in a water-miscible solvent into water or buffer (**Figure T21**). The size and the number of bilayers in the onion-like vesicles could be predicted by the final Janus dendrimer concentration.

In the context of soft polymer-based nanoscale JPs, different studies have been performed by the group of Müller in order to investigate how different architectures, such as spherical, cylindrical, and disc-shaped, would influence the self-assembly behavior. All of the used JPs were prepared through selective crosslinking of the SBM triblock terpolymer bulk phases. In the case of spherical particles, hierarchical self-assembly behavior of two kinds of JPs was

reported: fully hydrophobic JPs with PMMA and PS at the opposite sides,³⁷ and strongly amphiphilic JPs with PS and PMAA at the opposite sides.³⁶ In the first case, a combination of different experimental techniques have pinpointed the presence of an equilibrium between individual dissolved Janus micelles (unimers) and their aggregates (multimers), or the so-called supermicelles, which further formed hexagonal arrays on the surface.³⁷ In the second case, alkaline hydrolysis of PMMA into PMAA yielded strongly amphiphilic and water-soluble PMAA/PS JPs with a PB core.³⁶ In an aqueous solution the majority of the Janus micelles formed spherical supermicelles above a critical aggregation concentration of around 0.03 mg/l. On a second self-assembly level, the so-called giant micelle formation was observed with sizes between 100 nm and a few micrometers.

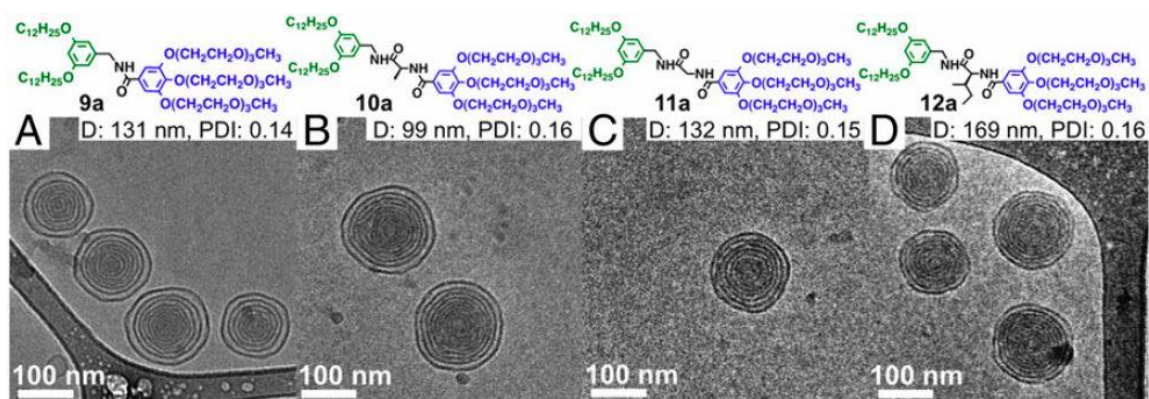


Figure T21. Representative cryo-TEM images of onion-like vesicles self-assembled by the injection of a THF solution of various Janus dendrimers in water (1 mg/ml). Diameter (D , in nm) and PDI of the onion-like vesicles were measured by DLS.²⁶

In the case of cylindrical JPs prepared from the same SBM terpolymer and composed of PS and PMMA hemicylinders, unimolecularly dissolved JPs could be observed in good solvents for both hemicylinders.⁸⁶ Self-assembly could be induced in acetone, which is a non-solvent for polystyrene, leading to the observation of fiber-like aggregates. The fibers consisted of 2-4 Janus cylinders, in which the inner insoluble PS hemicylinders were protected against the solvent by the extended PMMA chains. If the Janus cylinders were deposited from a more concentrated solution, a second type of superstructure was formed - fibrillar networks, in which the pore size depends on the concentration and deposition time of the sample (**Figure T22**).

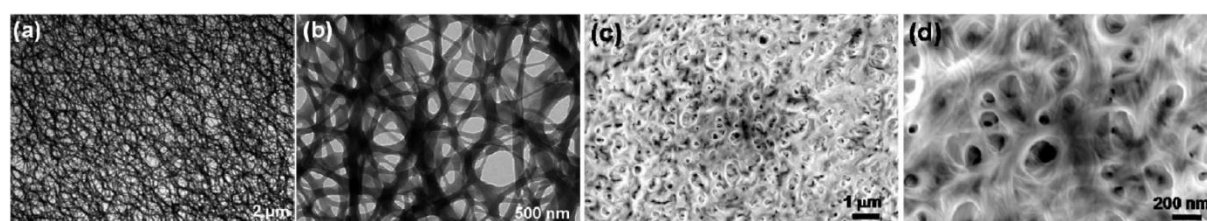


Figure T22. TEM images (a, b) of network-like aggregation patterns formed by deposition of Janus cylinders onto a TEM grid from a THF solution. (c, d) SEM images obtained by drying a solution of Janus cylinders in THF on a mica substrate.⁸⁶

As for soft, nanoscale disc-like JPs, their supramolecular aggregation behavior was observed in concentrated solutions.⁸⁷ The Janus discs were composed of a crosslinked PB core surrounded by PS and PtBMA polymer shells. Cryo-TEM investigations of the Janus disc solutions in THF (typically higher than 1 mg/ml) revealed the formation of superstructures composed of two back-to-back stacked Janus discs.

Self-Assembly of Amphiphilic Janus Colloids

Colloidal particles are a special type of programmed building blocks, because they can be synthesized with unprecedented control over their geometry and interactions. Therefore, colloidal self-assembly is not only an important model system to study the atomic world, but also a powerful tool for the development of materials with tunable and multifunctional properties. In this context, the self-assembly behavior of colloidal Janus particles is particularly interesting due to the potential novel types of structures that can be formed based on the asymmetry of JPs.

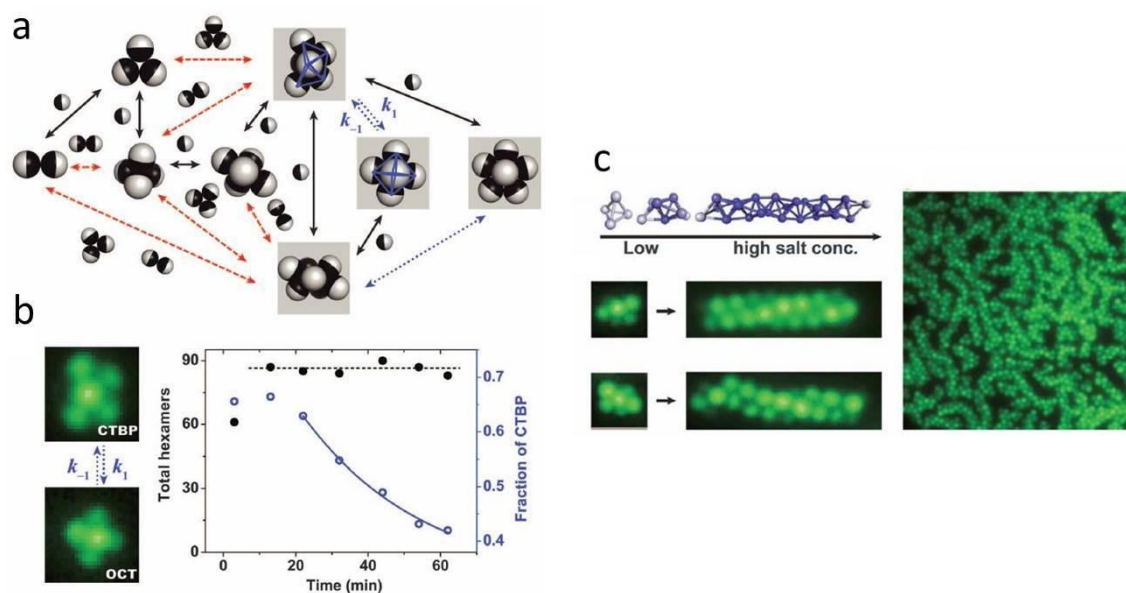


Figure T23. Clusters formed from amphiphilic Janus spheres. (a) Network of reaction pathways, all of which were observed in experiments at 3.8 mM NaCl. Reaction mechanisms of monomer addition, cluster fusion, and isomerization are denoted by black, red, and blue arrows, respectively. (b) A study of isomerization between two types of $N = 6$ clusters, the capped trigonal bipyramid (CTBP) and the octahedron (OCT). Once the total number of hexamers (black filled circles) has stabilized, isomerization (fraction of CTBP, blue open circles) is consistent with first-order reaction kinetics in time. (c) Triple helices formed at higher salt concentration and higher particle concentration.⁸⁸

In-depth investigations of the self-assembly behavior of 1 μm large amphiphilic Janus colloids comprising a hard SiO_2 core and hemispheres rendered strongly charged and hydrophobic respectively, were presented by Granick, Luijten, and co-workers.^{88, 89} By combining epifluorescence microscopy and Monte Carlo simulations, they have shown that amphiphilic JPs assemble in water into extended structures not formed by homogeneous particles.⁸³ First, in deionized water, the amphiphilic spheres repel each other so strongly that no clusters are formed. However, when the electrostatic screening length was tuned to 10 nm

through the addition of salt (1 mM KNO₃), the formation of small compact clusters containing less than 10 JPs occurred. Further increasing of the salt concentration enhances electrostatic screening, and the clusters link up into wormlike strings.

In another study reaction kinetics of the amphiphilic JP cluster formation was investigated, revealing that several types of clusters can occur in two different variants that rearrange in time through isomerization (**Figure T23 a**).⁸⁸ For instance, the capped trigonal bipyramid shape with cluster size $N = 6$ formed first, then gradually isomerized to the more symmetric octahedral shape (**Figure T23 b**). An increase in the salt concentration to 5 mM reduced the electrostatic repulsion and resulted in the formation of fascinating helical structures, called Boerdijk-Coxeter helices (**Figure T23 c**). Conclusively, the self-assembly of amphiphilic Janus spheres presents transient isomeric structures with long lifetime enabling their further fusion into stable, highly ordered non-equilibrium helices, which is a unique feature of JPs.

Dipolar Janus Colloids

A variety of groups reported on the self-assembly behavior of oppositely charged Janus colloids, typically based on PS or SiO₂ microspheres of 1 μm size or larger, provided that the size exceeds the electrostatic screening length.^{67, 90, 91} For instance, dipolar JPs prepared by Paunov et al. via microcontact printing of a water-insoluble ionic surfactant film onto colloid monolayers of opposite surface charge were shown to form linear chain aggregates in water at high salt concentrations.⁹⁰ Similarly, dipolar JP self-assembly into chains in aqueous solutions in the presence of salt was observed by Granick and co-workers, who prepared the corresponding JPs by modifying the exposed area of silica particles on wax colloidosomes via positively charged silane vapor deposition.⁶⁷ In terms of soft Janus microgels, micrometer-sized PNIPAAm microgels prepared by Kawaguchi et al. and having carboxylic and amino groups at their opposite sides self-assembled into chain structures at pH 4, where most of the carboxylic groups are protonated.⁹² In addition to chain structures formed during self-assembly of dipolar JPs, also cluster formation with definite shape and anisotropic distribution of electric charge was observed in the experiments and corresponding Monte Carlo simulations by Granick and co-workers (**Figure T24**).⁹¹ Hence, the occurrence of chain-like assembly or clusters may depend on the Janus ratio and the quality of the JPs.

On the other hand, computer simulations suggest a rich phase diagram for the self-assembly of dipolar colloidal JPs, ranging from co-crystals of unusual symmetry to open networks (gels) of crosslinked chains of particles. For instance, molecular dynamic computer simulations were used by Velev and co-workers to investigate the self-assembly of colloidal particles with permanent dipole moments immersed in a high-dielectric solvent.⁹³ Different types of phases were identified in the simulations, including face-centered-cubic, hexagonal-close-packed, and body-centered-tetragonal at high packing fractions as well as fluid, string-fluid, and gel phases at low packing fractions. Further simulations of binary mixtures of dipolar colloids revealed the existence of unique bicontinuous gel phases.⁹⁴ The large differences between the structures proposed by simulations and the ones experimentally

observed indicate on an unexplored area of dipolar JP self-assembly and the need for further experiments.

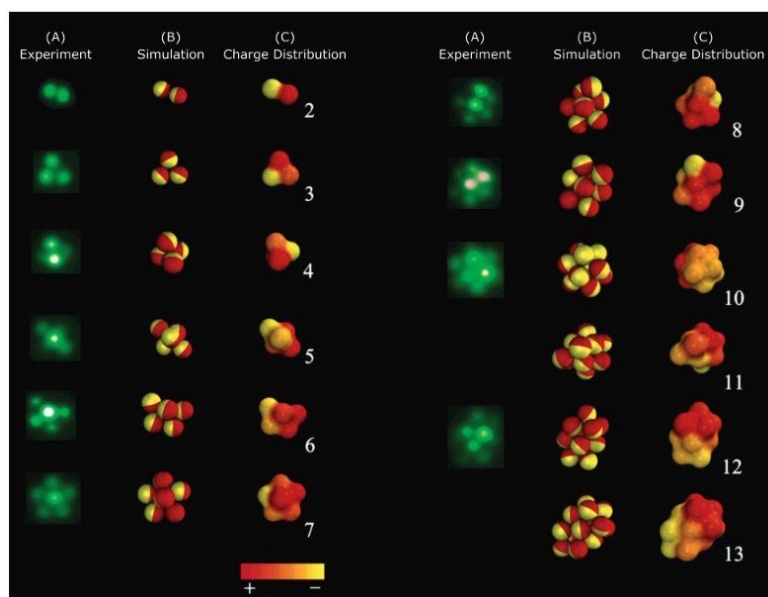


Figure T24. Comparison of experimental epifluorescence images and Monte Carlo computer simulations of the self-assembled structures of particles with near-equal positive and negative charges on the two hemispheres (denoted by red and yellow colors).⁹¹

Self-Assembly in Electrical Fields

Janus particles that exhibit different electric properties on their opposite hemispheres are typically fabricated through metal evaporation on monolayers of particles or selective immobilization of NPs onto one side of the JPs. As a result, such particles display a response to electric fields, which allows a programmable assembly depending on the strength of the applied field. One of the advantages of the JP assembly in external fields is that switchable self-assembled structures can be prepared, which is useful for the design of materials with directional electric, magnetic, and heat transfer properties.⁹

For instance, Velev and co-workers reported on the assembly of metallodielectric JPs composed of 4 μm large PS particles with a conductive layer of gold on one hemisphere driven by alternating current (AC) electric fields at frequencies above 10 kHz.⁹⁵ At low frequency AC electric fields (<10 kHz) the metallodielectric JPs move perpendicular to the electric field with their polystyrene hemisphere forward as a result of induced-charge electrophoretic force.⁹⁶ At high frequency electric fields, the particles assemble into new types of chain structures. A phase diagram was developed as a function of the AC electric field intensity versus field frequency revealing five different regions: disordered particles, regular and staggered chains, 2D crystallization, induced charge electrophoresis, and 3D bundles (**Figure T25**).⁹⁵ In the chain structures, the gold-coated halves of the neighboring particles align into lanes along the direction of the electric field, while the dielectric halves face in the other direction. The particles in the 2D metallodielectric crystals pack more tightly in the higher field strength. 3D bundles are formed when the particle chains stack on top of each other and merge. Particle configuration simulations were also performed and agreed well with

the experimentally observed results. Ultimately, such reversible field-directed assembly of JPs at high frequency could lead to the fabrication of photonic crystals of new symmetry types as well as other types of materials.

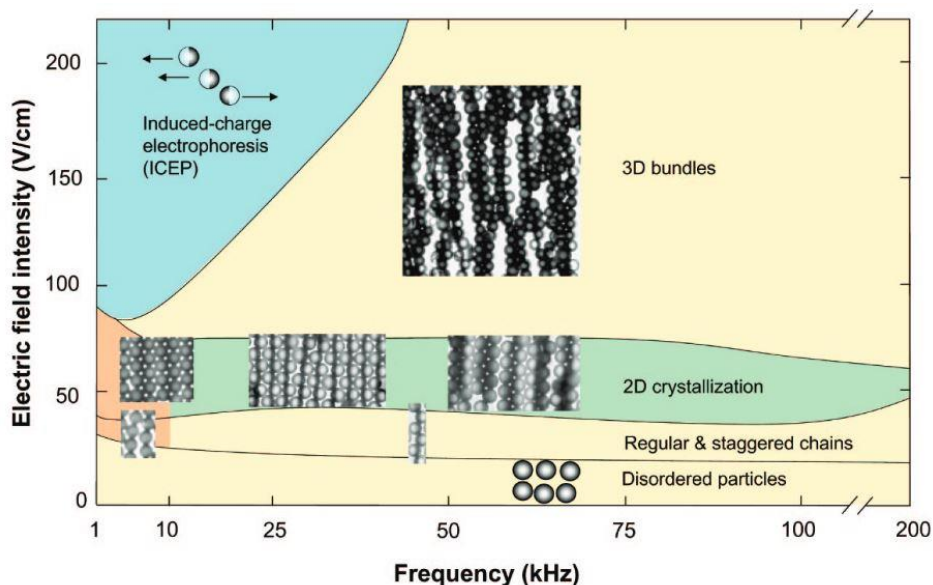


Figure T25. Dynamic and structural response of Janus particles to AC electric field intensity versus field frequency in a thin experimental cell. In the optical images, the gold-coated, conductive hemispheres appear dark and the bare, dielectric hemispheres appear light.⁹⁵

Manipulation and assembly of PS-based JPs with varied surface chemistry on one hemisphere under high frequency non-uniform AC electric fields was investigated by Zhu et al.⁹⁷ For this purpose, they used gold-coated carboxylated 3.8 μm large PS spheres either unmodified on the gold hemisphere, or modified by a SAM layer of a methyl-terminated or an amino-terminated alkanethiol. Pearl chains of JPs with an unmodified gold hemisphere were observed over the field frequency range from 25 kHz to 20 MHz, indicating on the dielectrophoresis (DEP)-directed assembly. Similar DEP-induced assembly was confirmed for JPs with the gold hemisphere modified by a methyl-terminated thiol. In contrast, zwitterionic JPs with an amine-terminated thiol coating on the gold-modified hemisphere assembled into random close-packed crystals due to strong electrostatic attraction enhanced by the alignment of the induced dipoles on the JPs.

Self-Assembly in Magnetic Fields

One of the advantages of using magnetic field-induced assembly of colloidal particles is that the magnetic interactions are reversible and rather independent of environmental parameters. The magnetic domain of the JPs can be situated as a thin spherical shell over the whole hemisphere, or as an individual particle in dumbbell-like particles.

Similar structures as the ones formed by metallodielectric JPs in AC electric fields were also observed for magnetic JPs in external fields. For instance, staggered chain structures of polystyrene JPs (4 μm) with iron-coated hemispheres could be observed under the action of a magnetic field.⁹⁸ The staggered chains not only oriented themselves in the direction of the applied field, but were also strong enough to withstand drag forces. However, when magnetic

chains approach each other they do not come together laterally to crystallize, as observed in the case of the electric field assembly. Assembly of magnetic JPs into regular chains upon the application of a magnetic field was also observed by Hatton et al.⁹⁹ The JPs were composed of submicrometer PS spheres coated with a closely packed magnetic Fe₃O₄ NP layer on one hemisphere.

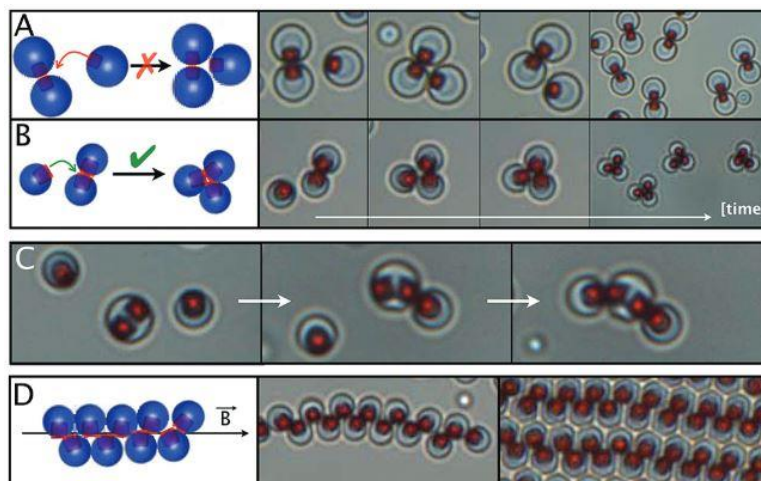


Figure T26. Magnetic-click colloidal assembly of monodisperse clusters, colloidal molecules and linear chains. (A and B) By varying their size, particles with a single magnetic patch (monovalent) can selectively form dimers or trimers depending on their steric hindrance parameter. (C) Time sequence showing the self-assembly of a colloidal molecule by means of directional magnetic bonds between a divalent and two monovalent particles. (D) When an external magnetic field is imposed, the clusters can be forced to rearrange into long linear structures or, at high particle volume fractions, into layered packings.⁷⁹

Reversible assembly of spherical JPs based on magnetostatic interactions was demonstrated by Sacanna et al.⁷⁹ The Janus particles were composed of monodisperse iron oxide micromagnets embedded at the surface of organosilica polymer particles. In the absence of external fields, the particles can self-organize into dimers or trimers if the magnetic patches are activated through the addition of salt (**Figure T26**). If a magnetic field is applied, the particles reorganize themselves into linear chains.

Granick and co-workers performed in-depth investigations of the magnetic JP assembly, demonstrating different types of structures ranging from chains and nanoribbons to superstructures with novel crystalline symmetry.¹⁰⁰⁻¹⁰² For instance, JPs composed of 3 μm spherical silica particles with thin nickel films directionally deposited onto one hemisphere were shown to self-organize through synchronization of their motion into micrometer-scale tubes in which the constituent particles rotate and oscillate continuously.¹⁰⁰ Janus particles with a different geometry, Janus rods, prepared by directionally depositing a thin nickel layer onto micrometer-sized silica rods, were shown to assemble in a different way than predicted for spherical particles.¹⁰¹ When subjected to a magnetic field, individual rods align with their long axis perpendicular to the field and subsequently stack into ribbons parallel to the field, regardless of their initial magnetization direction. The ribbons then form non-circular rings with bend, splay, and twist deformations. Furthermore, a rotating magnetic field instead of a static one was used to assemble spherical magnetic JPs into a variety of programmable structures.¹⁰² When driving the magnetic field into a regime of nonlinear response, the spheres

paired into dicolloids, which subsequently formed diverse new structures due to the peculiar properties of the dicolloids.

2.4. APPLICATIONS OF JANUS PARTICLES

2.4.1. Modification of Interfaces

As already mentioned in Section 2.3.2., one of the most fascinating applications of JPs is the stabilization of multiphase fluid mixtures such as emulsions, foams, or polymer blends. One of the main advantages of the Janus particles is their enhanced surface activity, which drives them to adsorb to the interfaces more efficiently than their homogeneous analogues. Therefore, this property was realized in many theoretical predictions and experimental studies resulting in the application of JPs as stabilizers.

Emulsions

The first successful emulsion polymerization using JPs as stabilizers was reported by Müller and co-workers.¹ The amphiphilic PS/PMAA Janus nanoscale micelles were employed as emulsifiers in the conventional emulsion polymerization of styrene and nBA. The two kinds of resulting latex particles had different T_g as well as different interactions between the latex particle and the hydrophobic PS sides of the JPs. The latex particle sizes exhibited extremely low polydispersities, and could be controlled by varying the content of the stabilizer. Notably, it was shown that the surface area stabilized by one JP exceeds its cross section several times. This study demonstrated for the first time the application possibilities of JPs in technologically relevant liquid/liquid interface systems.

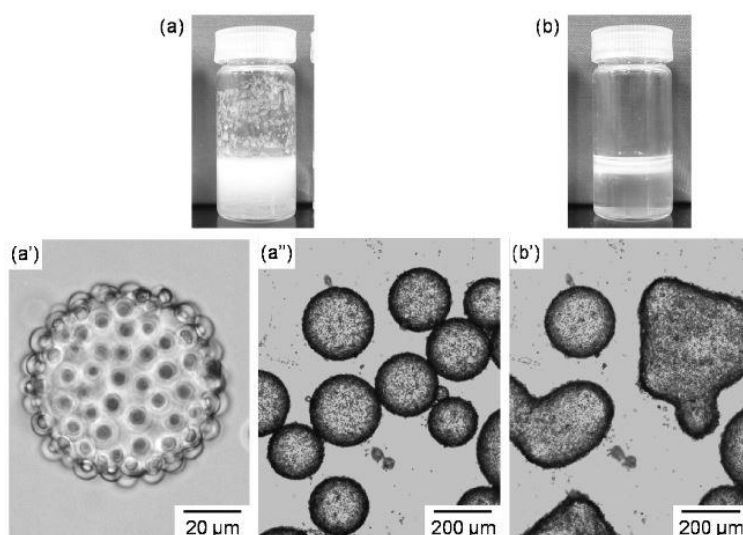


Figure T27. (a, b) Photographs of 1-octanol/water mixture after vigorous stirring in the presence of PMMA/P(S-BIEM)-g-PDMAEMA Janus particles, and (a', a'', b') optical micrographs of 1-octanol-in-water emulsion droplets stabilized by the Janus particles at pH 7.2 at (a, a', a'') 25°C and (b, b') after rising to 60 °C.⁴³

Significantly larger particles were also shown to stabilize oil/water interfaces. For instance, Okubo and co-workers applied stimuli-responsive mushroom-like PMMA/P(S-BIEM)-*graft*-PDMAEMA Janus particles as solid surfactants in a 1-octanol/water emulsion.⁴³ The stability of the formed Pickering emulsion can be controlled by external stimuli such as pH and temperature (**Figure T27**). To test the stabilizing efficiency of the JPs, P(S-BIEM)-*graft*-PDMAEMA core-shell particles were prepared and tested for their emulsion stabilization properties. It could be concluded that the pH region in which stable emulsions are obtained is much wider in the case of JPs compared to the core-shell particles.

As reported by Doyle and co-workers, the assembly of amphiphilic wedge-shaped JPs produced using continuous flow lithography resulted in oil-in-water and water-in-oil emulsion droplets of different shapes depending on their hydrophilic-to-hydrophobic balance.¹⁰³ Spherical emulsion droplets were formed when the particles had a large hydrophilic head and a small hydrophobic tail, whereas deformed emulsion droplets could be observed when the particles had a small hydrophilic head and a large hydrophobic tail.

Polymer Blends

Apart from liquid/liquid emulsion interfaces, another promising area for the application of JPs is based on their behavior in homopolymer mixtures or within block copolymers and their subsequent compatibilization.

In the first experimental study to employ JPs on a multigram scale, Müller and co-workers successfully used nanoscale PS/PMMA JPs to efficiently compatibilize polymer blends of PS and PMMA under high-shear conditions in a twin-screw miniature mixer (**Figure T28**).² It was shown that the JPs locate themselves exclusively at the interface between the two polymer phases due to their interfacial activity, and the domain sizes of the dispersed phase decrease with an increasing content of JPs. Moreover, the compatibilization efficiency of JPs was found to be superior compared to the other state-of-the-art block copolymer-based compatibilizers.

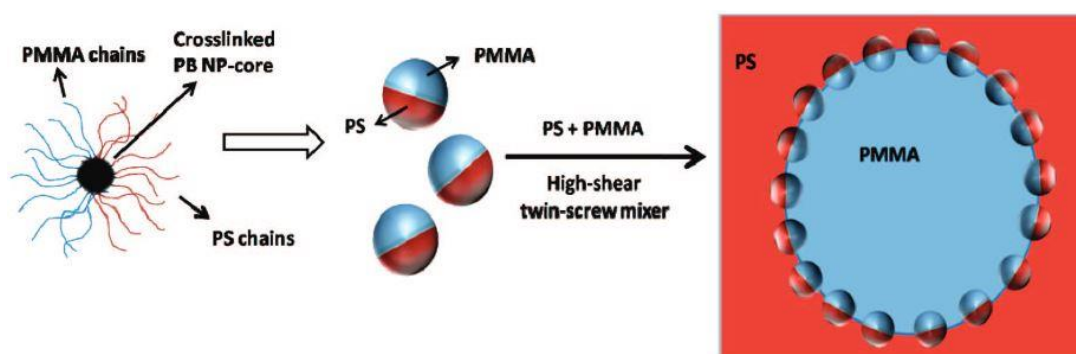


Figure T28. Schematic representation of Janus particles and their adsorption at the blend interface of a PS/PMMA blend.²

In terms of block copolymers, Yan and Böker et al. performed mesoscale simulations to investigate the self-assembly of JPs with different architectures and geometries such as

spheres, rods, and discs in diblock copolymers.¹⁰⁴ Due to the affinity of each side of the JPs to one on the blocks in the diblock copolymer, all of the particles strongly adsorbed at the interface. Depending on the architecture of the JPs, their orientation with respect to the interface can be controlled. Conclusively, the simulations suggested that this type of self-assembly can have beneficial effects on the processing properties of the resulting nanocomposites.

Functional, Structured, and Responsive Interfaces

Besides the simple stabilization effects of JPs in emulsions and polymer blends, another promising feature of JPs is the possibility to use them for nano- and micro-structuring of interfaces. Based on the favorable orientation and low diffusion of JPs at the interface, the inner and outer sides of the emulsion droplets can be selectively modified.

For instance, Sailor and Link demonstrated a selective orientation of bifunctional porous Si smart-dust particles containing a hydrophobic green mirror and a hydrophilic red mirror at the interface between an organic liquid and water according to their polarity resulting in a homogeneously colored emulsion droplet.¹⁰⁵ Sensing can be accomplished when the liquid at the interface penetrates into the porous mirrors, inducing predictable shifts in the optical spectra of both mirrors. In another approach, Krupenkin and co-workers employed the self-assembly of selectively gold-functionalized hexagonal Si/SiO₂ micromirrors (Janus tiles), produced using photolithographic techniques, on the surface of an oil droplet to create a concave liquid mirror (**Figure T29**).¹⁰⁶ The best results with regard to reflectivity and alignment of the micromirrors were observed using pentyl benzoate as the oil phase. More than 80% of the micromirrors demonstrated proper orientation (gold face toward oil). The utilized approach can enable a wide range of new optofluidic devices.

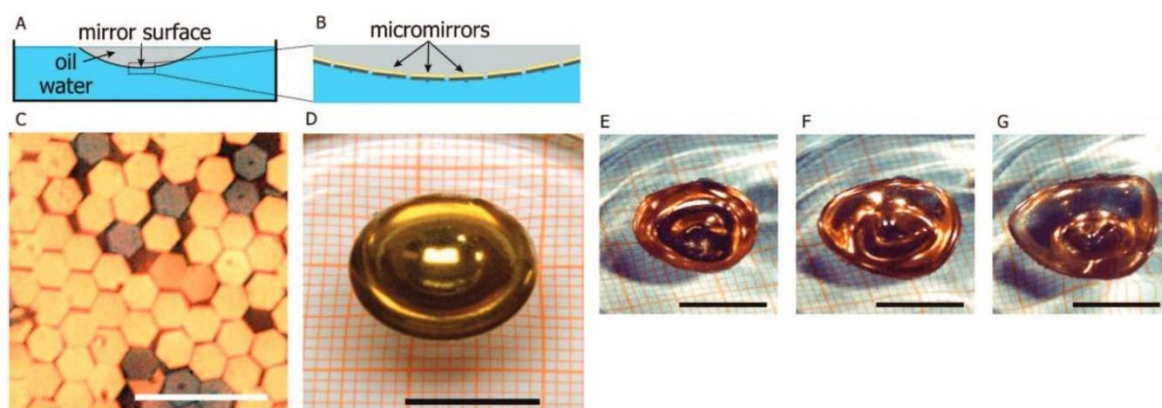


Figure T29. Self-assembled liquid mirror and micromirror organization: (A) A droplet of oil containing micromirrors in suspension is floated on a water surface. (B) The micromirrors assemble at the oil-water interface with the gold face oriented toward the oil phase. (C) This orientation is preferred due to the relative surface energies of the gold and silicon faces. (D) The micromirror assembly creates a mirror with the curvature of the oil-water interface. (E, F, G) Frame captures (450 ms between frames) of an acoustically excited liquid mirror. Scale bars: (C) 25 μm , (D, E, F, G) 1 cm.¹⁰⁶

Another example concerning the utilization of JPs for the structuring of liquid/liquid interfaces was proposed by Kim and Yang et al., who used porous and rough Janus

microspheres with superhydrophobic and hydrophilic faces to create a highly flexible and impregnable water-repelling interface through the self-assembly of the JPs.⁶⁰ The resulting membrane of Janus microspheres remained stable when a water droplet was placed on it and even retained its shape under a dynamic disturbance. Furthermore, the Janus microspheres could be used to prepare liquid marbles, which could be manipulated with magnets or tweezers.

In terms of technological applications, Synytska et al. demonstrated control over the wettability of substrates through the immobilization of amphiphilic JPs.^{107, 108} For instance, JPs were chemically bound with one side to the surface of textiles, while their hydrophobic side was facing the environment, thus, making the textile surface more hydrophobic.¹⁰⁸ The character of JP immobilization depended on the size of the employed JPs. As a result, submicrometer large JPs, which were bound on the fiber surface, were shown to be very efficient for the design of water-repellent fabrics. In another contribution, the assembly of JPs into aggregates in solution and their subsequent deposition onto a pre-modified substrate were used to prepare hierarchical rough layers which possess a certain level of fractality.¹⁰⁷ The layers prepared with JPs were ultra-hydrophobic, which is very promising for the engineering of materials with self-cleaning properties.

2.4.2. Applications of Individual Janus Particles

Aside from the enhanced interfacial activity of the Janus particles, their asymmetric nature is another promising advantage worth exploring in the context of their applications. They possess considerable anisotropy with respect to the rotational orientation, which results in view-dependent physical properties favorable for diverse applications. Additionally, their asymmetric character can be used to perform spatially confined catalysis.⁹

Rotationally Anisotropic Optical Properties - Modulated Optical Nanoprobes

Anisotropic optical properties, which depend on the rotation of the particle, can be translated to JPs through their selective functionalization with fluorescent molecules or reflective coatings. The rotational orientation of JPs can be manipulated via external fields, for instance, if the JP is functionalized with a magnetic compartment. Different rotational properties can further be used for detection purposes in specially designed optical measurement setups.

The concept of modulated optical nanoprobes (MOONs) was first developed by Anker and Kopelman.^{5, 109, 110} They have prepared MOONs by coating one hemisphere of a fluorescent particle (typically silica or PS) with a thin layer of metal, such as aluminum or gold, so that the fluorescence is emitted only from the other hemisphere.¹¹⁰ Such half-coated particles reflect light in a manner that depends strongly on their orientation, allowing the orientation to be tracked using either reflection and/or fluorescence. Additionally, MOONs blink when they rotate, therefore, their optical signal can be distinguished from the background, improving the optochemical sensing measurements. In the absence of external magnetic fields, or if the

particle does not possess magnetic material, the rotational motion of the MOONs in solution is due to the Brownian motion, which is why they are called Brownian MOONs (**Figure T30**). The time series of Brownian MOON intensity fluctuations contains information about the local rheology as well as information about the particle shape, size, and its interaction with the environment, which allows the use of Brownian MOONs for microrheological measurements.

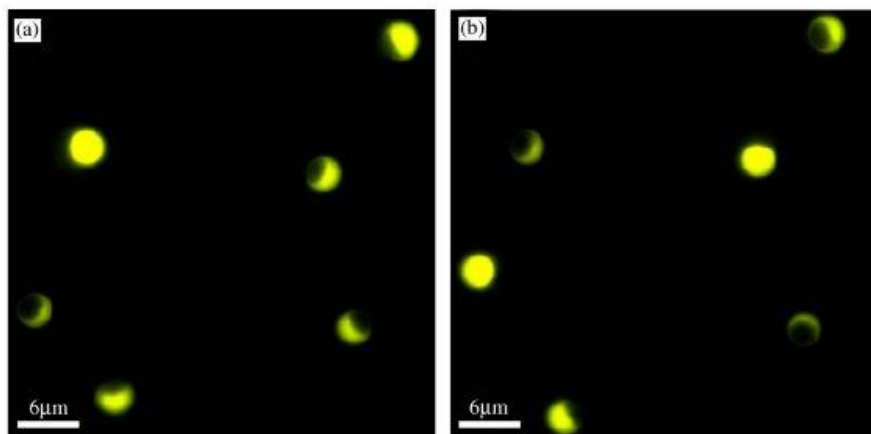


Figure T30. (a, b) Fluorescence from six different $3.4 \mu\text{m}$ aluminum-capped Brownian MOONs individually rotating through the phases of the moon at two different times.¹¹⁰

The concept was further modified to create magnetically modulated optical nanoprobes (MagMOONs) in order to magnetically modulate the signal from fluorescent probes, thus, separating it from other interferences, such as autofluorescence, electronic offsets, and other background signals.⁵ The resulting MagMOONs blink in response to rotating magnetic fields. The separation of the blinking probe signal from the background allows a detection of very low analyte concentrations, even in the presence of autofluorescence. To demonstrate the principle of MagMOON immunoassays, streptavidin coated gold-capped superparamagnetic MagMOONs were immersed in solutions with a mixture of Oregon Green labeled biocytin (OG) and Phycoerythrin-labeled biotin (PE).¹⁰⁹ The OG peak served as a reference and illustrated the principle of a competitive assay: the OG is in competition with the PE for the binding sites on the particle. As a result, MagMOON fluorescence could be separated from the background signal of the excess unbound biotin-labeled dyes.

E-Paper Display Technology

Nowadays, E-paper displays based on electronic ink are a rapidly growing technology. Typically, Janus microcapsules containing black and white particles with different charges are placed between the electrodes and, depending on the applied bias, either black or white particles migrate to the top electrode to absorb (black) or reflect (white) the light.^{111, 112} In this way, pixels are created. However, JPs possessing both electrical and color anisotropy inside a single particle would allow to improve the technology and resolution, creating individual single particle pixels.⁹

One of the first contributions on the utilization of JPs for E-paper display applications was published by Nisisako et al.⁴ Polymeric bicolored JPs having asymmetric charge distribution and pigments of carbon black and titanium oxide at the opposite sides were produced using a microfluidic co-flow system. Electrical actuation of the JPs was demonstrated by fabricating a display panel and placing electrodes on top and below a monolayer of particles (**Figure T31**). In the presence of an external electric field, the particles turned to orient their black hemispheres to the negatively charged panel and vice versa. The particles could be flipped by reversing the electric field gradient.

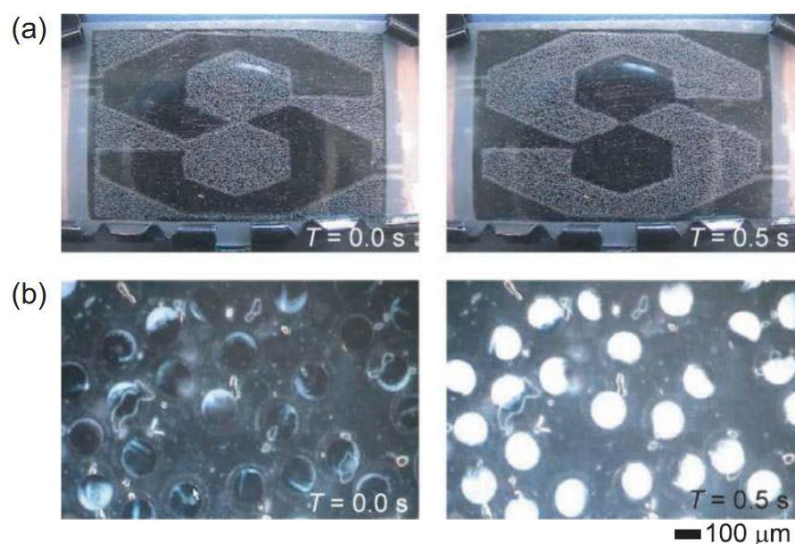


Figure T31. Electrical actuation of the synthesized Janus spheres: a) color switching test using the prepared particles. A voltage of 100 V was applied between the 0.4 mm gap of two electrode panels (40 mm × 40 mm) at a switching frequency of 1 Hz; b) magnified top view of the display panel in (a).⁴

Sheridon et al. reported on the preparation of a Gyricon reflective light display based on hemispherical black and white (bichromal) balls. The resulting display had a diffuse reflectance of more than 18% and a contrast ratio of more than 6:1. The viewing angle approached that of paper.¹¹³ In another contribution, Yang and co-workers synthesized electroresponsive photonic Janus balls with black and structural color regions based on an optofluidic approach.¹¹⁴ The particles were prepared through emulsification of two suspensions, one of them containing pure silica particles in an ethoxylated trimethylolpropane triacrylate resin (ETPTA) and the other one containing silica particles in ETPTA along with carbon black particles. As a result, the silica particles self-organized in ETPTA into an fcc lattice on one hemisphere, whereas the other hemisphere was black due to the carbon black pigments. The structural colors (in this case red and green) arising from the nonplanar fcc lattice showed favorable optical properties such as a viewing-angle-independent reflection color. Such photonic Janus balls can be used as color pigments in reflection-mode displays (including E-paper), by creating the pixels with RGB-colored Janus balls.

Self-Propulsion

In the recent years, chemically powered self-propelled micro-/nanomotors have gained significant interest due to the possibility of both autonomous motion mimicking biological functions and cargo delivery at small scales. Such nanomotors may lead to a new class of active nanocarriers with potential biomedical relevance. Asymmetric particles, such as JPs, are excellent platforms for the design of self-propelling beads based on spatially confined catalysis.

For instance, Howse et al. achieved autonomous propulsion of micrometer-sized polystyrene beads half-coated with platinum based on the autodegradation of H_2O_2 into oxygen and water catalyzed by the platinum.⁶ The particle is propelled forward due to the non-equilibrium distribution and local gradients of partly gaseous products after the decomposition of H_2O_2 . The concept of self-propulsion was extended by Sen and co-workers, who reported on polymerization-powered microparticle motion.¹¹⁵ The micromotor was powered by the ring-opening metathesis polymerization of norbornene using a Grubbs' catalyst attached to the silica face of 1 μm gold-capped silica JPs (**Figure T32**). Additionally, the motor exhibited the phenomenon of chem taxis by moving up the monomer gradient.

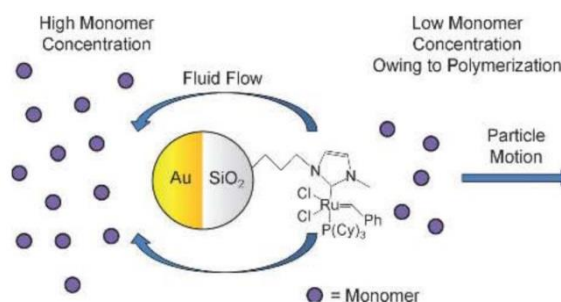


Figure T32. The motor consumes monomers at the silica face, creating an area of low monomer concentration. Fluid in the low concentration region flows towards the higher concentration region at the gold face. Consequently, the motor moves in the opposite direction.¹¹⁵

In another contribution, Sanchez et al. produced self-propelled Janus nanomotors based on hollow mesoporous silica nanoparticles, which are powered by three different enzyme biocatalytic reactions: catalase, urease, and glucose oxidase.¹¹⁶ The effective external force generated by a single nanomotor was measured using optical tweezers. The resulting fully biocompatible Janus nanomotors driven by nontoxic fuels are very promising for biomedical applications. Another concept of Janus micromotors was presented by Wang and co-workers, who fabricated self-propelled activated carbon-based Janus micromotors, which display efficient locomotion in environmental matrices and offer effective “on-the-fly” removal of a wide range of organic and inorganic pollutants from water.¹¹⁷ The micromotors were prepared by a selective Pt patch deposition onto the surface of activated carbon microspheres and driven by H_2O_2 decomposition. The decontamination efficiency of the Janus motors was shown to be significantly higher compared to static activated carbon particles.

2.4.3. Janus Particles for Biological Applications

Functional nanoparticles are of great interest for biological applications and already demonstrated success in the sensitive detection of pathogens, specific cell labeling, imaging, and targeted delivery. The possibility to combine several functionalities in one single Janus particle makes them very promising from the point of view of biological applications.⁹

For instance, Lahann's group developed a microstructured bio-hybrid material based on anisotropic polymer particles with spatially-controlled affinity towards human endothelial cells (**Figure T33**).³ The bi-compartmental JPs were synthesized via electrohydrodynamic co-jetting, with one side modified with biotin (subsequently modified with streptavidin) and each side additionally labeled with green and red fluorescent dyes, respectively. To demonstrate compartment-specific binding between the JPs and human cells, streptavidin-modified JPs were incubated with human endothelial cells that were labeled with either biotinylated antibody against platelet endothelial cell-adhesion molecule (PECAM), or with a biotinylated isotype antibody, which exhibits only low-level, non-specific binding to the cells. Additional modification of the particle surface with PEG significantly decreased the non-specific binding. As one compartment of the JPs exhibited no binding affinity towards human endothelial cells, the particles not only bound to the top of the cells, but also associated all around the perimeter of the cells forming a single particle layer.

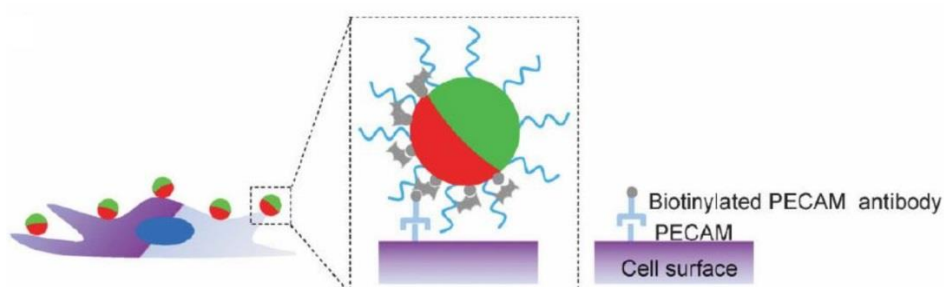


Figure T33. Scheme for the binding of bi-compartmental particles to cells via streptavidin present on the particle surface of one compartment and biotin from cell-specific antibody (in this case PECAM).³

In terms of imaging applications, Sun and co-workers reported on dumbbell-like Au-Fe₃O₄ NPs, which possess both a magnetic (Fe₃O₄) and an optically active plasmonic (Au) unit, and are therefore suitable for simultaneous magnetic and optical detection.¹¹⁸ The Fe₃O₄ part was modified with the epidermal growth factor receptor antibody (EGFRA), which was linked to the surface through polyethylene glycol (PEG) and dopamine, while the Au part was protected by the SH-PEG-NH₂ polymer. Further, the dumbbell NPs were shown to be suitable as a probe for A431 (human epithelial carcinoma cell line) cell imaging, which are known to overexpress EGFR. The preferred binding between EGFR in the cells and EGFRA on the NPs enabled the dumbbell NPs to adsorb on the A431 cells. Magnetic resonance imaging analysis showed that cells labeled with NPs shorten the T₂ relaxation of the surrounding water molecules, whereas the Au part allowed obtaining reflection images with a scanning confocal microscope.

A combined imaging and magnetolytic therapy approach was proposed by Hu and Gao.¹¹⁹ They prepared JPs (180 nm) based on a fluorescent dye-loaded amphiphilic block copolymer, poly(styrene-*block*-allyl alcohol), in one hemisphere and magnetic NPs assembled in the other one. It was further demonstrated that the orientation of such JPs can be magnetically modulated toward optical imaging applications. The possibility of magnetolytic therapy was realized through magnetic field modulated cell membrane damage. The nanocomposites attached quickly to the cell surface and the subsequent application of a spinning magnetic field resulted in the majority of the tumor cells being killed due to the mechanical force acting on the cell membranes.

The interactions between Janus particles and lipid bilayer membranes were probed by Balazs and co-workers using dissipative particle dynamics simulations.¹²⁰ It was demonstrated that when the membrane rips and forms a hole due to an external stress, the nanoscopic JPs diffuse to the edge of the hole and form a stable pore, which remains stable after the stress is released. When such particle-lined pore is formed, a small increase in the membrane tension readily reopens the pore, allowing transport through the membrane. Thus, the JPs introduce a controllably “re-sealable” pore in the membrane, which can be opened or closed through a change in the surrounding conditions, such as pH, temperature, or salt concentration. The amphiphilic nature of JPs is a crucial component of such behavior, since parts of the particles must interact with the hydrophobic regions and the other parts must interact with the aqueous solution in the hole.

2.4.4. (Multi-) Functional Surfaces

Functional, responsive surfaces are of great interest nowadays due to a variety of their potential industrial applications in, for example, the anti-icing or anti-fouling coating technologies. Typically, mono-functional, solely hydrophilic or hydrophobic, surfaces are being exploited for these applications. However, a combination of several properties in a single surface may produce a synergistic effect and lead to the enhanced desired features of the material. Therefore, an increasing number of studies are being dedicated to heterogeneous surfaces, which combine the advantageous properties of several components in one surface.

Janus particles are a unique class of multifunctional particles, which possess two different functions in one single building block. Therefore, they are perfect candidates to construct truly multifunctional materials through their specific assembly. One fascinating way to create such materials would be to prepare structured surfaces consisting of Janus particles. The resulting surfaces would exhibit heterogeneity on different scales and multi-functionality required for specific applications.

Up to date, there are no known contributions concerning the preparation or applications of functional surfaces based on Janus particles. We have pursued this approach in the present thesis and developed structured layers formed by hybrid hairy Janus particles with controlled heterogeneity. The layers were further tested for their application in the area of anti-icing as

well as anti-fouling surfaces. Ultimately, this may lead to an additional appealing field of technological applications for the multifunctional asymmetric JPs.

2.5. SUMMARY

Janus particles are truly unique among other functional and patchy particles, since they combine two distinct functionalities at their opposite sides, resembling block copolymers and molecular amphiphiles. As demonstrated in **Figure T1**, the number of contributions regarding the topic of JPs is rapidly growing each year, which indicates on the significance of this field of research. The recent development of a variety of synthetic strategies to produce JPs has led to a palette of resulting JP structures with tunable chemical and physical properties as well as geometries. Based on the physical properties of JPs, they may be classified into three groups: soft or polymer-based, hard or inorganic, and hybrid organic/inorganic JPs that combine both soft and hard portions in a single particle. The advances in the synthetic approaches originate from different disciplines – classical organic synthesis, polymer chemistry, nanoparticle synthesis, colloidal chemistry, etc. The challenge faced in the JP preparation process is the breaking of the homogeneous particle symmetry, whereas the developed technique must be efficient in terms of scalability and price. Progress made in the aforementioned disciplines makes the design of JPs with tailored functionalities and architectures possible on a reasonable time and price scale at high yields. Nevertheless, to allow real technological applications of JPs, all of these parameters still need to be improved. Another important parameter to consider in the design of JPs is their functionality. In this context, it is beneficial to combine the functionality of inorganic materials with the tunable interactions possessed by organic or polymer motifs. Smart polymers are key features to produce truly multifunctional responsive and adaptive JPs.

In terms of JP properties, their main advantage is the enhanced interfacial activity originating from their chemical asymmetry. JPs were shown to adsorb to the interfaces more efficiently than their homogeneous analogues, which makes them perfect candidates for the stabilization of different interfaces in, for instance, emulsions or foams. Another advantage is their bi-functionality – the possibility to selectively modify different regions of one single particle providing them with desired functions. Furthermore, a large number of research contributions have been devoted to the (self-) assembly of JPs, revealing a wide range of fascinating superstructures, which could not be assessed with homogeneous particles. The assembly of JPs is typically studied in continuous media with or without the application of external fields. Different types of interactions can be addressed, such as van der Waals, electrostatic, hydrogen bonding, covalent, coordination, capillary, convective, shear, optical, and electromagnetic forces. The asymmetry of JPs results in their assembly into asymmetric hierarchical structures with unique anisotropic properties not provided by the assembly of isotropic particles. Programmed assembly of JPs is therefore gaining more and more interest due to the possibility to construct special functional materials with appealing properties.

As for the applications of JPs, several concepts were shown to be promising and close to real technological applications. For instance, the aforementioned enhanced interfacial activity of JPs can be used to address the stabilization of emulsions or polymer blends on a significant scale. Functional surfaces and interfaces based on JPs can exhibit self-cleaning effects, whereas immobilization of JPs onto textiles can lead to water-repellent fabrics with controlled porosity. Individual JPs were shown to be used as modulated optical nanoprobe and as building blocks for electronic displays. Furthermore, JPs are also very promising for biological applications concerning cell labeling, imaging, and targeted delivery. The main challenge for future success remains the scalability and efficiency of the JP synthesis, which is linked to the cost and time amounts as crucial parameters in technological applications. Moreover, the competition of JPs with homogeneous or less defined colloids, nanoparticles, and polymer-based assemblies is huge.

Nevertheless, the true potential of JPs lies in their unique broken symmetry distinguishing them from other structures. If the necessary improvements will be made in all three areas - synthesis of the JPs, their assembly, and applications – this can lead to truly novel classes of multifunctional materials.

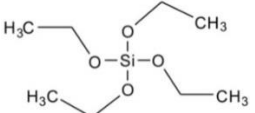
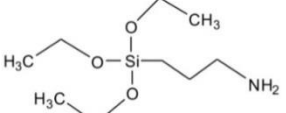
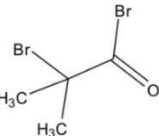
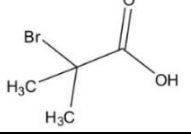
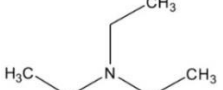
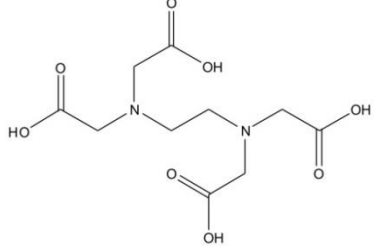
CHAPTER III

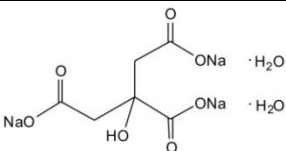
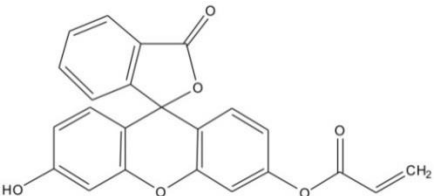
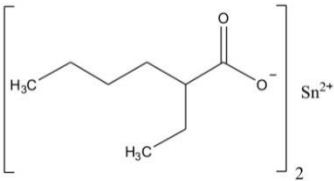
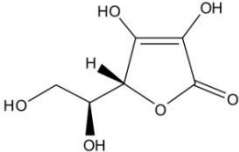
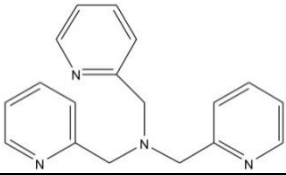
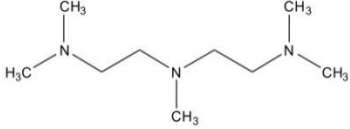
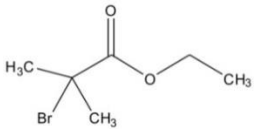
Materials & Methods

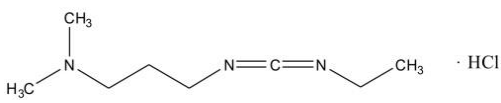
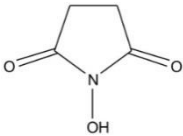
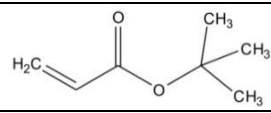
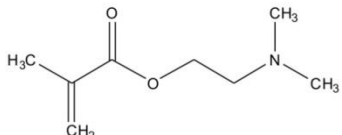
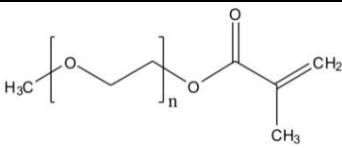
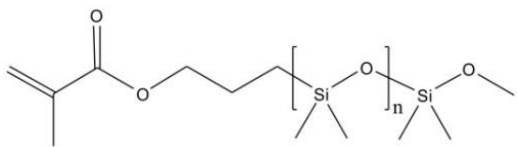
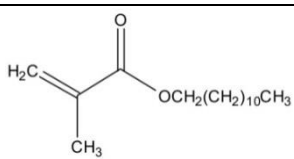
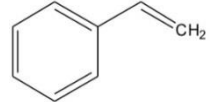
3.1. MATERIALS

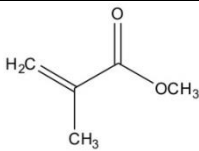
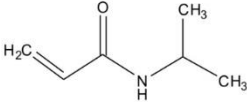
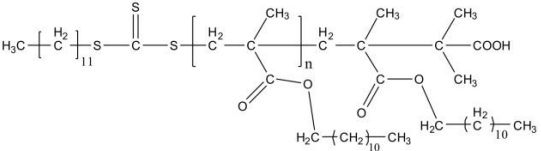
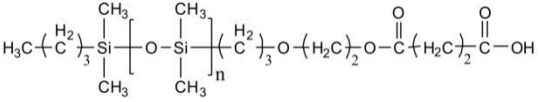
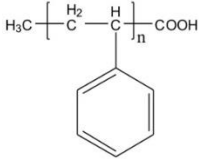
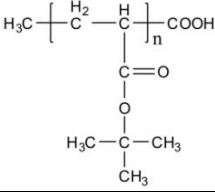
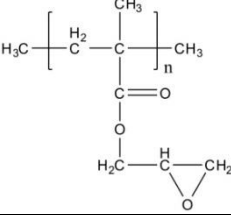
All the materials used in this work are summarized in **Table M1.**, including the structural formula of the chemical substance, its name, purity of the product, and the supplier. Materials which required purification prior to the use are marked with an *. Further information about the purification procedures is given after the table.

Table M1. List of materials used in the experiments in the present thesis.

Structure	Name	Purity	Supplier
	Tetraethyl orthosilicate (TEOS)	99 %	Fluka
$\text{Al}_2\text{O}_3 \cdot 2\text{SiO}_2 \cdot 2\text{H}_2\text{O}$	Kaolinite	natural	Sigma-Aldrich
$\text{NH}_3 \cdot \text{H}_2\text{O}$	Ammonium hydroxide	28-30%	Acros Organics
H_2O_2	Hydrogen peroxide	30%	VWR
EtOH	Ethanol	absolute	VWR
	3-Aminopropyltriethoxysilane (APS)	97 %	ABCR
	α -Bromoisobutyryl bromide (BrIn)	98 %	Aldrich
	α -Bromoisobutyric acid	98 %	Aldrich
CH_2Cl_2	Dichloromethane, anhydrous (DCM)	99.8 %	Acros Organics
	Triethylamine	99 %	Sigma-Aldrich
	Ethylenediaminetetraacetic acid (EDTA)	99.4-100.6 %	Sigma-Aldrich

	Sodium citrate dihydrate	99 %	Aldrich
NaHCO ₃	Sodium bicarbonate	99.7 %	Sigma-Aldrich
Na ₂ S ₂ O ₄	Sodium dithionite	85 %	Sigma-Aldrich
	Fluorescein <i>o</i> -acrylate	97 %	Aldrich
CuBr ₂	Copper(II) bromide	99.999 %	Aldrich
	Tin(II) 2-ethylhexanoate (Sn(II))	95 %	Aldrich
	L-Ascorbic acid (AA)	99 %	Sigma
	Tris(2-pyridyl-methyl)amine (TPMA)	98 %	Aldrich
	<i>N,N,N',N'',N'''</i> -pentamethyldiethylenetriamine (PMDTA)	99 %	Aldrich
C ₃ H ₇ NO	<i>N,N</i> -dimethylformamide, anhydrous (DMF)	99.8 %	Sigma-Aldrich
	Ethyl α -bromoisobutyrate (EBiB)	98 %	Aldrich
C ₆ H ₅ CH ₃	Toluene	99.8 %	Sigma-Aldrich
CH ₃ COCH ₃	Acetone	99.8 %	Sigma-Aldrich
CHCl ₃	Chloroform	99.5 %	Sigma-Aldrich
HCl	Hydrochloric acid, 36.5-38 %	BioReagent	Sigma
CH ₃ SO ₃ H	Methanesulfonic acid	99.5 %	Sigma-Aldrich
NaOH	Sodium hydroxide, pellets	97 %	Sigma-Aldrich

KCl	Potassium chloride	99 %	Sigma-Aldrich
$(\text{CH}_3\text{CH}_2)_2\text{O}$	Diethyl ether, anhydrous	99.7 %	Aldrich
-	Paraffin wax, mp 53-57 °C	-	Aldrich
	<i>N</i> -(3-Dimethyl-aminopropyl)- <i>N'</i> -ethylcarbodiimide hydrochloride (EDC)	BioXtra	Sigma-Aldrich
	<i>N</i> -Hydroxysuccinimide (NHS)	98 %	Aldrich
CH_2Cl_2	Dichloromethane	99.99 %	Acros Organics
C_6H_{14}	Hexane	95 %	Sigma-Aldrich
$\text{C}_4\text{H}_8\text{O}$	Tetrahydrofuran (THF)	99.99 %	Acros Organics
$\text{CH}_3\text{OC}_6\text{H}_5$	Anisole	99.9 %	Sigma-Aldrich
CH_3I	Iodomethane	99 %	Sigma-Aldrich
$\text{CH}_3(\text{CH}_2)_{14}\text{CH}_3$	Hexadecane, anhydrous	99 %	Sigma-Aldrich
Al_2O_3	Aluminum oxide (basic, neutral, or acidic)	98 %	Sigma-Aldrich
	<i>Tert</i> -butyl acrylate (<i>t</i> BA)	98 %*	Aldrich
	2-Dimethylaminoethyl methacrylate (DMAEMA)	98 %*	Aldrich
	Poly(ethylene glycol) methyl ether methacrylate (PEGMA)	*	Aldrich
	Monomethacryloxypropyl terminated polydimethylsiloxane (asymmetric, 6-9 cSt., PDMSMA)	*	ABCR
	Lauryl methacrylate (LMA)	96 %*	Aldrich
	Styrene	99 %*	Sigma-Aldrich

	Methyl methacrylate (MMA)	99 %*	Aldrich
	N-Isopropylacrylamide (NIPAAm)	99 %*	Aldrich
	Carboxy terminated poly(lauryl methacrylate), M _n : 11 000 g/mol (PLMA)	-	Polymer Source
	Carboxy terminated polydimethylsiloxane, M _n : 10 000 g/mol (PDMS)	-	Polymer Source
	Carboxy terminated polystyrene, M _n : 48 000 g/mol (PS)	-	Polymer Source
	Carboxy terminated poly(<i>tert</i> -butyl acrylate), M _n : 42 000 g/mol (PtBA)	90 %	Polymer Source
	Poly(glycidyl methacrylate), M _n : 42 000 g/mol (PGMA)	-	Polymer Source
Si	Single-crystal silicon wafers, <100> orientation	*	Silicon Materials

Millipore water was obtained from Milli-Q (Millipore). Conductivity: 0.055 $\mu\text{S}/\text{cm}$.

Purification of the Monomers: *Tert*-butyl acrylate (*t*BA), 2-dimethylaminoethyl methacrylate (DMAEMA), poly(ethylene glycol) methyl ether methacrylate (PEGMA), monomethacryloxypropyl terminated polydimethylsiloxane (PDMSMA), lauryl methacrylate (LMA), styrene, and methyl methacrylate (MMA) were purified by passing each of them two times through a column with basic, neutral and acidic aluminum oxides (Al_2O_3). *N*-isopropylacrylamide (NIPAAm) was recrystallized from hexane. For this purpose, a saturated solution of NIPAAm in boiling hexane was prepared. Afterward, the solution was cooled down to room temperature and the NIPAAm crystals were filtered out and dried under vacuum.

Purification of Silicon Wafers: First, highly polished single-crystal silicon wafers of <100> orientation were cut into 10 x 20 mm pieces. Afterward, they were immersed into a mixture of

equal amounts of hydrogen peroxide, ammonium hydroxide and water, and stirred for 1 hour in a water bath at 70 °C in order to get a uniform SiO₂ layer with silanol groups. Then the wafers were rinsed two times with water and dried with compressed nitrogen. The thickness of the SiO₂ layer measured by null-ellipsometry was (1.5 ± 0.2) nm.

3.2. SYNTHETIC & MODIFICATION APPROACHES

3.2.1. Preparation of Reference “Flat” Surfaces Using Silicon Wafers

Pre-modification of Silicon Wafers: Silicon wafers were used as substrates for the grafting of polymer brushes. First, the wafers were cleaned as described above. Second, the cleaned wafers were immersed into a 2 wt% solution of 3-aminopropyltriethoxysilane (APS) in ethanol and mixed for two hours at room temperature at 120 rpm to introduce amino groups onto the surface. The wafers were then rinsed with ethanol and dried. Third, an initiator for surface-initiated atom transfer radical polymerization (SI-ATRP) was immobilized onto the wafer surface as follows: the APS-modified wafers were stirred for two hours at room temperature and 120 rpm speed in a solution consisting of 100 ml anhydrous dichloromethane (DCM), 0.5 ml α -bromoisobutyryl bromide (BrIn) and 1.0 ml triethylamine. Afterward, the wafers were rinsed with DCM, ethanol and water, and used for polymerization. The thicknesses of the APS and BrIn layers measured by null-ellipsometry were (0.8 ± 0.2) nm and (0.4 ± 0.1) nm, respectively.

Surface-Initiated Atom Transfer Radical Polymerisation (SI-ATRP): Activators regenerated by electron transfer (ARGET) ATRP¹²¹ was used in this work in order to graft polymers from the surface of silicon wafers or particles (“grafting from” approach). In a typical procedure, the initiator-modified wafer was immersed into a solution (in a test tube) consisting of appropriate amounts (**Table M2**) of the monomer, solvent, copper (II) bromide (CuBr₂, 0.1 M solution in DMF), *N,N,N',N'',N''*-pentamethyldiethylenetriamine (PMDTA, 0.5 M solution in DMF), and ethyl α -bromoisobutyrate (EBiB). The test tube was sealed with a septum, and the mixture was purged with argon for 10 minutes, followed by the addition of the reducing agent (RA), tin(II) 2-ethylhexanoate (Sn(II)) or ascorbic acid (AA, 1 M solution in DMF), through the septum via syringe. The polymerization was then performed at an appropriate temperature in a water (oil) bath during a defined time interval at 140 rpm (**Table M2**). Afterward, the wafers were rinsed with appropriate solvents and dried. In the case of the *tert*-butyl acrylate polymerization, it was then hydrolyzed in methanesulfonic acid (by simply immersing the wafer) to yield poly(acrylic acid). The thicknesses of the polymer layers were measured by null-ellipsometry and maintained in a (20 ± 10) nm interval for all of the used polymers.

Table M2. Amounts of the substances and the respective conditions used for the SI-ATRP on silicon wafers.

Target Polymer	Monomer	Solvent	CuBr ₂ , μ l	PMDTA, μ l	EBiB, μ l	RA, μ l	T, °C	Time, min
PAA	4 ml tBA	-	60	60	0.15	120, Sn(II)	115	90
PDMAEMA	2 ml DMAEMA	2 ml DMF	32	32	0.15	100, Sn(II)	70	30
P(PEGMA)	3 ml PEGMA	3 ml ethanol	60	60	0.15	200, AA	60	90
P(PDMSMA)	1.5 ml PDMSMA	1.5 ml anisole	32	32	0.15	100, Sn(II)	110	150
PLMA	2 ml LMA	2 ml anisole	200	200	0.15	200, Sn(II)	70	30
PS	4 ml styrene	-	100	100	0.15	300, Sn(II)	90	30

3.2.2. Synthesis of Homogeneously Decorated Silica Particles

Synthesis of Monodisperse SiO₂ particles: Silica particles with the diameters of 100, 200, 400, 600, and 1000 nm were prepared using a multi-step hydrolysis-condensation procedure of tetraethylorthosilicate (TEOS) in an ammonium hydroxide-ethanol solution based on the Stöber approach.¹²²

In the first step, 100 nm large silica particles were synthesized by adding 1.5 ml of TEOS into a mixture of 50 ml of ethanol and 3 ml of ammonium hydroxide in a 250 ml polypropylene bottle. The solution was then stirred at room temperature at 500 rpm overnight.

In the second step, 200 nm large silica particles were synthesized by using the seed solution of 100 nm large silica particles without further purification. 25 ml of the seed solution were mixed with 175 ml of ethanol and 12 ml of ammonium hydroxide in a 250 ml polypropylene bottle, then 6.0 mL of TEOS were added via syringe, and the mixture was stirred at room temperature at 500 rpm overnight.

In the third step, 400 nm large silica particles were synthesized by a sequenced addition of TEOS (6 x 1 ml TEOS each 45 min) into a mixture of 12 ml of ammonium hydroxide in 175 ml of ethanol and 25 ml of unpurified 200 nm particle seed solution. Again, the mixture was stirred at room temperature at 500 rpm overnight.

In the fourth step, 600 nm large silica particles were synthesized by using the 200 nm large particle seed solution. 25 ml of the seed solution were mixed with 175 ml of ethanol and 12 ml of ammonium hydroxide. 9 ml of TEOS were then added to the mixture (1 ml each 45 min) via syringe. The mixture was stirred at room temperature at 500 rpm overnight.

In the fifth step, 1000 nm large silica particles were synthesized. For this purpose, 50 ml of the seed 400 nm large particle solution were mixed with 350 ml of ethanol and 24 ml of ammonium hydroxide. 12 ml of TEOS were then added (1 ml each 45 min) via syringe. The mixture was stirred at room temperature at 500 rpm overnight.

Silica particles of each diameter were then acquired from the seed mixtures by centrifugation (15 min at 10k rpm for smaller particles, 5 min at 5k rpm for bigger particles). Each synthesis step yielded 2 to 4 grams of silica particles. The particles were cleaned 5 times by re-suspension in ethanol and subsequent centrifugation. The obtained silica particles were then dried in a vacuum oven under reduced pressure and 60°C temperature.

Pre-Modification of Silica Particles: Purified and dried silica particles were then modified with 3-aminopropyltriethoxysilane (APS) to introduce amino groups onto the surface. This was achieved by mixing the particles for 12 hours in a 5% APS solution in ethanol. The particles were then purified by centrifugation in ethanol 6 times, and dried under vacuum at 60 °C. Next, the ATRP-initiator (α -bromoisobutyryl bromide) was immobilized onto the amino-modified particle surface from its solution in dry dichloromethane (0.7 ml BrIn in 35 ml DCM) in the presence of triethylamine (1.4 ml). The reaction was carried out at room temperature under constant stirring (700 rpm) for 2 hours. The modified particles were then purified by centrifugation/redispersion in dichloromethane, water, and ethanol, and dried under vacuum at 60°C.

Surface-Initiated Atom Transfer Radical Polymerisation (SI-ATRP): As in the case of planar substrates (silicon wafers), ARGET-ATRP (“grafting from” approach) was used in order to graft polymers from the surface of the initiator-modified silica particles. In a typical procedure, the initiator-modified particles (500 mg) were placed in a test tube with a magnetic stirrer and a septum, appropriate amounts of the monomer and solvent were added to the particles, and the particles were dispersed in an ultrasonic bath, followed by the addition of CuBr₂ (0.1 M solution in DMF), PMDTA (0.5 M solution in DMF) and EBiB. The mixture was then sonicated and purged with argon for 10 minutes, and the reducing agent (RA), Sn(II) or AA (1 M solution in DMF), was added through a septum via syringe. The polymerization was then performed at an appropriate temperature in a water (oil) bath during a defined time interval at 700 rpm (**Table M3**). Afterward, the particles were collected by centrifugation and washed by at least 8 cycles of centrifugation/redispersion in appropriate solvents. Then the polymer-modified particles were dried under reduced pressure at 25°C.

In the case of the *tert*-butyl acrylate polymerization, it was then hydrolyzed with methanesulfonic acid to yield poly(acrylic acid). For this purpose, the PtBA-covered particles were dispersed in 5 ml of chloroform in a Teflon centrifuge vial, 2 ml of methanesulfonic acid were added and the mixture was stirred for 5 minutes with a magnetic stirrer. Afterward, diethyl ether was added to dilute the mixture, and the particles were collected by centrifugation. The resulting PAA-covered particles were additionally washed 3 times in diethyl ether and 2 times in ethanol, and dried under reduced pressure at 25°C.

Table M3. Amounts of the substances and the respective conditions used for the SI-ATRP on silica particles.

Target Polymer	Monomer	Solvent	CuBr ₂ , μ l	PMDTA, μ l	EBiB, μ l	RA, μ l	T, °C	Time, min
PAA	5 ml tBA	-	70	70	0.15	130, Sn(II)	115	120
PDMAEMA	3 ml DMAEMA	3 ml DMF	48	48	0.15	150, Sn(II)	70	120
P(PEGMA)	3 ml PEGMA	3 ml ethanol	60	60	0.15	200, AA	60	180
P(PDMSMA)	3 ml PDMSMA	3 ml anisole	64	64	0.15	200, Sn(II)	110	180
PLMA	3 ml LMA	2 ml anisole	135	135	0.15	150, Sn(II)	70	60
PS	4 ml styrene	-	100	100	0.15	300, Sn(II)	90	90
PMMA	4 ml MMA	3 ml dioxane	55	55	0.15	100, Sn(II)	80	90

3.2.3. Synthesis of Spherical Silica-Based Janus Particles

Preparation of Colloidosomes: 1 μ m and 200 nm large silica particles were synthesized using the Stöber approach as described above (Section 3.2.2.) and used for the preparation of big and small Janus particles respectively. First, silica particles were modified with APS as described above in order to introduce amino groups onto the surface. Next, colloidosomes were prepared with the APS-modified particles of the desired size (1 μ m or 200 nm) using a wax-water Pickering emulsion approach.^{75, 107} In the case of 1 μ m large silica particles, 1 g of particles was first suspended in 100 ml of chloroform in a 250 ml round-bottom flask for 60 min using an ultrasonic bath. Then, 10 g of paraffin wax were added to the dispersion at 50°C and it was further sonicated for 60 min. Afterward, chloroform was removed using a rotating evaporator (50 °C, 350 mbar). The wax-particle mixture was placed under a mechanical stirrer in a water bath heated to 85°C and 150 ml of boiling water were added to the flask. The mixture was stirred with a half-moon stirrer at 1200-1300 rpm for 60 min at 85°C. Then the formed emulsion was poured into liquid nitrogen and the ice was collected. After thawing of ice at room temperature, the colloidosomes were separated from the water by filtration and washed with Millipore water. Then the colloidosomes were dried on the filter paper under vacuum at 25°C. The same procedure was employed for the 200 nm APS-modified silica particles, the only difference being in the particle-to-wax ratio, which was 1:20 (instead of 1:10 as in the case of 1 μ m large particles). The emulsion with smaller particles was stirred at a higher speed of 1400-1600 rpm.

Immobilization of the ATRP-Initiator: α -bromoisobutyric acid was immobilized onto the exposed particle surface. The procedure used was the same for both particle sizes. First, 9.5 g of dried colloidosomes were placed in a 250 ml round-bottom flask with a magnetic stirrer

and a septum. 60 ml of DI water were added and the colloidosome suspension was cooled down to 1°C in a cooling water bath. Next, 4.23 g of *N*-(3-dimethylaminopropyl)-*N'*-ethylcarbodiimide hydrochloride (EDC) were dissolved in 29 ml of DI water in a 100 ml round-bottom flask and the solution was cooled down to 1°C with dry ice. 2.42 g of α -bromoisobutyric acid and 0.21 g of *N*-hydroxysuccinimide (NHS) were dissolved in 29 ml of DI water and cooled down to 3°C. Both solutions were combined (a white precipitate was formed) and added to the flask with colloidosomes. pH of the mixture was adjusted to 5. The reaction was conducted at 1°C at 400 rpm in a cooling water bath for 22 hours. After modification, the reaction mixture was filtered and the colloidosomes were washed with Millipore water and dried on the filter paper under vacuum at 25°C. Afterward, the wax was dissolved by dispersing the colloidosomes in hot hexane (60°C), and the modified particles were collected via centrifugation. The particles were additionally washed by 6 centrifugation/redispersion cycles in hot hexane, 2 in DCM and 1 in ethanol. The washed particles were then dried under reduced pressure at 60 °C. As a result, silica particles partly covered with the ATRP-initiator and partly covered with APS were obtained ($\text{SiO}_2\text{-NH}_2/\text{Br}$).

Grafting of the First Polymer Using SI-ATRP (“Grafting from” Approach): The first polymer was grafted from the initiator-covered side of the Janus particles using the “grafting from” approach as described above for the homogeneously decorated particles (Section 3.2.2.). The same amounts of substances and reaction conditions were used (**Table M3**). After polymerization, particles partly covered with the desired polymer and partly covered with APS were obtained (for example, $\text{SiO}_2\text{-PDMAEMA/NH}_2$).

Grafting of the Second Polymer Using the “Grafting to” Approach: Carboxy terminated polymers were grafted onto the APS-covered side (containing amino groups) of the Janus particles modified by the first polymer. For this purpose, 300 mg of silica particles with the grafted first polymer (for example, $\text{SiO}_2\text{-PDMAEMA/NH}_2$) were dispersed in 20 mL of a 1 wt% solution of the desired carboxy terminated polymer (all listed in **Table M1**) in an appropriate solvent in a 50 ml round-bottom flask. The mixture was stirred with a magnetic stirrer for 2 hours at room temperature at 700 rpm. Next, the solvent was evaporated and the particles were annealed at 150°C overnight (12 h). The ungrafted polymer was removed by multiple redispersion of particles in an appropriate solvent and subsequent centrifugation. The particles were then dried at 25°C under vacuum. As a result, Janus particles covered with two polymers at their opposite sides were obtained (for example, $\text{SiO}_2\text{-PDMAEMA/PLMA}$).

3.2.4. Synthesis of Homogeneously Decorated Kaolinite Particles

Separation of Kaolinite Particles: Kaolinite particles (natural, Sigma-Aldrich) were used as received without further purification and separated based on their size by sedimentation in DI water using grain size separation (Atterberg method). The conventional Atterberg method is used for separating grain size fractions according to their settling velocity. After the

kaolinite particles were put into a sedimentation cylinder, DI water was added up to the desired settling height. The closed cylinder was shaken until the suspension was homogeneous. When the necessary settling time for a given equivalent diameter (e.g., 2 μm) was reached (calculated according to Stokes law), the supernatant suspension (e.g., only material $<2 \mu\text{m}$) was decanted and dried. In this way, 100 nm – 2 μm large kaolinite particles were separated after the settling time of 2 days.

Purification of Kaolinite Particles: The acquired kaolinite particles were purified by the EDTA method to remove calcium and magnesium carbonates. 1-3 g of kaolinite particles were stirred in a 250 ml round-bottom flask with a magnetic stirrer and a septum in 200 ml of 0.1 M ethylenediaminetetraacetic acid (EDTA) solution for 1 hour at room temperature and 700 rpm, then collected by centrifugation (10k / 15min), washed in water 5 times via centrifugation/redispersion and dried under vacuum at 60°C. Deferration was then conducted via the dithionite-citrate-bicarbonate (DCB) method. For this purpose, 2 g of dry kaolinite particles purified by the EDTA method were dispersed in an ultrasonic bath in 90 ml of a citrate-bicarbonate solution (15.88 g of sodium citrate and 1.85 g of sodium bicarbonate in 200 ml of DI water) for 30 min and the dispersion was heated in a water bath to 75°C, after which sodium dithionite was added in two portions (2 g + 2 g after 10 min). The mixture was allowed to stir for 10 more minutes at 700 rpm and the particles were then collected by centrifugation. Further, the collected particles were washed 3 times in the citrate-bicarbonate solution and 3 times in water, and then dried under vacuum at 60°C.

Modification of Kaolinite Particles: Purified kaolinite particles were then modified with APS and BrIn following the procedures used for the homogeneously decorated silica particles. In brief, kaolinite particles were modified with APS by mixing the particles for 12 hours in a 5 wt. % solution of APS in ethanol. The particles (K-APS) were then purified by centrifugation/redispersion in ethanol for 6 times and dried under vacuum at 60 °C. Next, the ATRP-initiator (α -bromoisobutyryl bromide) was immobilized onto the particle surface from its solution in dry dichloromethane (0.7 ml BrIn in 35 ml DCM) in the presence of triethylamine (1.4 ml). The reaction is carried out at room temperature under constant stirring at 700 rpm for 2 hours. Kaolinite particles (K-Br) were then purified by centrifugation/redispersion in DCM, water and ethanol and dried under vacuum at 60°C.

Surface-Initiated Atom Transfer Radical Polymerisation (SI-ATRP): As in the case of homogeneously decorated silica particles, the “grafting from” approach was used to graft polymers from the initiator-modified particle surface (Section 3.2.2). The same amounts of substances and reaction conditions were used (**Table M3**). After polymerization, particles fully covered with the desired polymer were obtained (for example, K-PDMAEMA).

3.2.5. Synthesis of Platelet-like Kaolinite-Based Janus Particles

Simultaneous Grafting of Two Polymers Using SI-ATRP: Kaolinite particles fully covered with BrIn (K-Br, Section 3.2.4.) were used for the polymerization. The polymerization of two different polymers was conducted simultaneously in an emulsion formed by oil in the water phase. For the water phase, 5 g of water-soluble PEGMA, DMAEMA, or NIPAAm, 1 ml of PMDTA (0.5 M solution in DMF), 1 ml of CuBr₂ (0.1 M solution in DMF), 15 mg of α -bromoisobutyric acid, and 1 ml of AA (1 M solution in DMF) were dissolved in 15 ml of DI water. A 2-neck 100 ml round-bottom flask with initiator-modified kaolinite particles (500 mg) and the water phase ATRP mixture was put in a water bath heated to 70°C, and continuously purged with Ar during the whole polymerization process. The oil phase ATRP mixture consisted of 3 g of either PDMSMA or LMA as a water-insoluble monomer, 2 ml of anisole as a solvent, 200 μ l of CuBr₂ (0.1 M solution in DMF), 28 mg of tris(2-pyridylmethyl)amine (TPMA), 0.15 μ l of EBiB, and 200 μ l of Sn(II). This mixture was introduced to the water phase and mixing by a mechanical half-moon stirrer was started. The simultaneous ATRPs were conducted for 2 hours at 1200-1400 rpm mixing speed. After polymerization, the resulting kaolinite Janus particles (for example, K-PDMAEMA/PLMA) were collected by centrifugation, washed 8 times by centrifugation/redispersion in appropriate solvents and dried under vacuum at 25°C.

Preparation of Mono-Component Janus Particles: Mono-component kaolinite Janus particles with PDMAEMA and PLMA were prepared as described above, the only difference being the absence of one of the monomers. For the synthesis of PDMAEMA/Br JPs, pure anisole was taken as an oil phase, and for the synthesis of PLMA/Br JPs, pure water was used as a water phase.

3.2.6. Preparation of Structured Functional Surfaces

Washed silicon wafers (the purification procedure is described in Section 3.1.) were used as substrates for the particle-based coatings. Poly(glycidyl methacrylate) (PGMA) was spin coated onto the wafer from its 1 wt. % solution in chloroform in two steps: (1) rpm = 100, time = 11 s, $R/s^2 = 1900$; (2) rpm = 2000, time = 31 s, $R/s^2 = 1900$. Afterward, the wafer was annealed for 20 minutes at 150°C in a vacuum oven in order to chemically graft PGMA. The obtained PGMA layer thickness measured by null-ellipsometry was (80 ± 3) nm. Polymer-modified particles (homogeneously decorated or Janus) were immobilized onto a PGMA-coated silicon wafer by a solvent casting method.¹²³ For this purpose, a 10 wt% dispersion of the particles was prepared in an appropriate solvent (typically, ethanol was used for hydrophilic polymers, chloroform or toluene – for hydrophobic ones); the dispersion was deposited dropwise onto a PGMA-coated wafer and dried. The wafer was annealed at 150°C for two hours in a vacuum oven. Multilayers were then removed by ultrasonication. The quality of the prepared coatings was checked by an optical microscope, SEM and AFM.

3.3. CHARACTERIZATION TECHNIQUES

3.3.1. Scanning Electron Microscopy (SEM) & Cryo-SEM

The scanning electron microscope (SEM) is one of the most versatile instruments for the examination and analysis of the microstructure morphology, which provides high resolution down to the nanometer scale. A focused electron beam is used to systematically scan across the surface of the sample, producing a large number of signals, which are then converted into a visual signal displayed on a cathode ray tube. Thus, image formation in SEM is based on the signal acquisition from the interactions of the electron beam with the specimen. These interactions can be divided into two major categories: elastic and inelastic interactions.

The principle of an SEM is shown schematically in **Figure M1**.¹²⁴ The microscope column and the electronics console are the two main parts of each SEM. The microscope column consists of the electron gun (with the components cathode, Wehnelt cylinder, anode), one or two condenser lenses, two pairs of beam deflection coils (scan coils for X, Y deflection), the objective lens, and several additional apertures. The specimen chamber is located at the lower end of the microscope column and it contains the specimen stage as well as detectors for the different signals generated by the electron beam-specimen interactions (for example, BSE and SE detectors). The pressure in the specimen chamber is typically about 10^{-4} Pa. The electronics console includes electric power supplies for the acceleration voltage (the usual range is about 0.5–30 kV) as well as the condenser and objective lenses, the scan generator, and electronic amplifiers for the different signals acquired. In the modern SEMs a PC is typically used to control the electron beam, to select signals and to record and store the acquired digital images.

To form an image, the beam electrons are first emitted from the cathode and accelerated by a voltage of 0.5–30 kV between the cathode and the anode. As a result, the smallest beam cross-section, the crossover, with a diameter of about 10–50 μm is formed near the anode. This spot size is too large to produce a sharp image, and the crossover is therefore demagnified by the lens system consisting of one or two condenser lenses and one objective lens and focused on the specimen surface. Pairs of beam deflection coils scan the electron probe line by line across a small area of the specimen. Simultaneously, the scan generator controls the deflection coil system of a monitor. Topography is one of the most important factors contributing to the image contrast.¹²⁴

In the present work, SEM was used very frequently to control each step of the homogeneously decorated or Janus particle synthesis. With the help of SEM it was possible to evaluate the silica or kaolinite particle size distribution, their morphology, the existence of the polymer shell around the particles after polymerization, etc. The quality of the prepared structured functional surfaces before and after different kinds of measurements was also checked with SEM. All SEM images were acquired on a NEON 40 EsB CrossBeam SEM from Carl Zeiss NTS GmbH, operating at 3 keV in the secondary electron (SE) and InLens

modes. In order to enhance the electron density contrast, the samples were coated with platinum (3.5 nm) using a Leica EM SCD500 sputter coater.

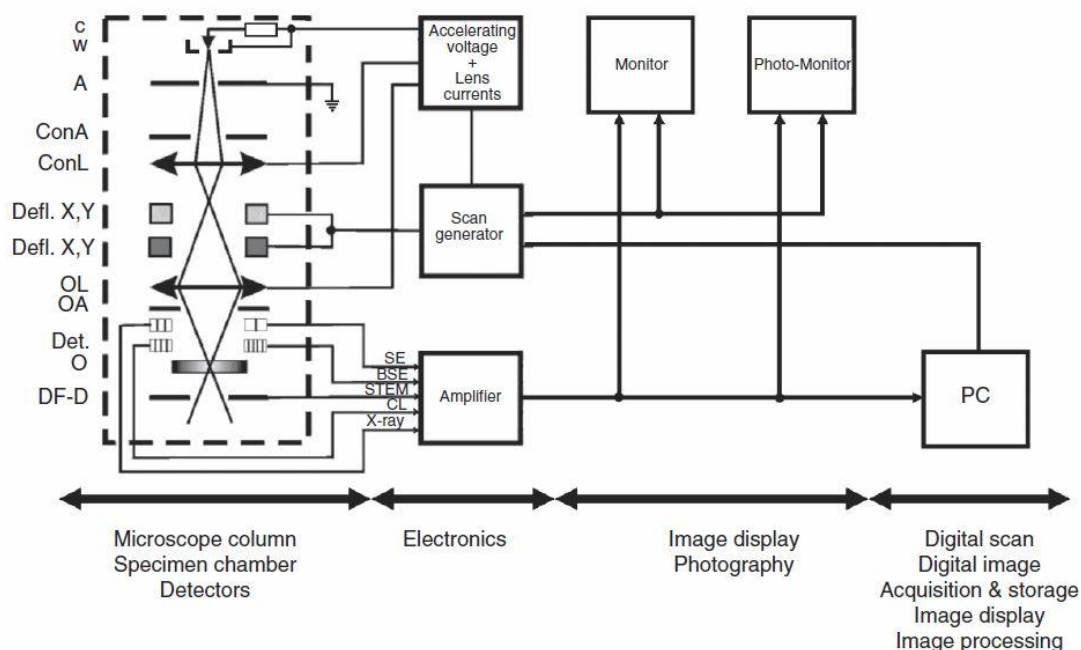


Figure M1. Scheme of a conventional SEM: C – cathode, W – Wehnelt cylinder, A – anode, ConA – condenser aperture, ConL – condenser lens, Defl. X, Y – pair of beam deflection coils in the X or Y direction, OL – objective lens, OA – objective aperture, Det. – detectors, O – specimen, DF-D – dark-field detector, SE – secondary electrons, BSE – backscattered electrons, STEM – scanning transmission electron microscope signal, CL – cathodoluminescence, X-ray – X-ray signal.¹²⁴

Cryo-SEM: Low temperature scanning electron microscopy (cryo-SEM) is of great interest for the investigation of samples in the frozen-hydrated state. In a typical procedure, the sample is first fixated by flash-freezing in liquid nitrogen or high-pressure freezing. Second, the sample is transferred under vacuum to a sputter coater, where it is coated with a conductive layer of metals or carbon at a low temperature. Finally, the sample is inserted into a SEM chamber equipped with a cryo-stage and investigated under high vacuum.¹²⁵

In the present work, cryo-SEM was used to investigate the behavior of water droplets on the layers of particles modified by one polymer, and the layers of Janus particles. For this purpose, micrometer-sized frozen droplets were formed on particle layers through condensation and subsequent instantaneous freezing. The following procedure was implemented for the preparation of samples for cryo-SEM imaging. First, the wafer with a particle coating was cooled down in liquid nitrogen and was then brought to ambient conditions. As a result, a layer of ice, and subsequently water droplets, was formed on the surface of the wafer. The wafer was then quickly frozen in liquid nitrogen and transferred to the Leica EM SCD500 sputter coater, where it was coated with platinum for 30 seconds at -130°C (estimated thickness of the platinum layer – 3.5-4.0 nm). The Leica EM VCT100 vacuum cryo-transfer system was used to load the sample in the SEM. Imaging was performed at -135°C at 0° and 45° tilt angles.

3.3.2. Transmission Electron Microscopy (TEM) & Cryo-TEM

Transmission electron microscopy (TEM) is a microscopy technique in which an ultra-thin specimen is illuminated by a highly collimated kilovolt electron beam. Electrons are transmitted through the specimen, interacting with it as they pass through.¹²⁴ A typical TEM consists of four major parts: an electron optical column, a vacuum system, the necessary electronics (lens supplies for focusing and deflecting the beam and the high voltage generator for the electron source), and control software. The electron column includes the electron gun, electromagnetic lenses, apertures as well as a fluorescent screen and/or a digital camera (**Figure M2**). The electron beam comes from the electron gun, and is condensed into a nearly parallel beam at the specimen by the condenser lenses. The specimen must be thin enough to transmit electrons (typically 0.5 μm or less). The transmitted electrons are collected and focused by the objective lens after passing through the specimen. Afterward, a magnified real image of the specimen is projected by the projection lens onto the viewing device at the bottom of the column. The entire electron path from gun to camera must be under vacuum.¹²⁶

The electron gun: The electron source in the TEM has to fulfill a number of certain requirements such as high brightness and coherence, high current efficiency, long life under available vacuum conditions, stable emission characteristics, and low energy spread.¹²⁴ Currently, there are three main types of electron sources: tungsten, lanthanum hexaboride (LaB_6), and field emission gun (FEG). LaB_6 guns depend on thermionic emission of electrons from a heated source; in this case it is a lanthanum hexaboride crystal. LaB_6 sources can provide up to 10x more brightness than tungsten and have significantly longer lifetimes, but require higher vacuum levels.¹²⁴

Optics: The optical column of a TEM typically comprises two or three condenser lenses, an objective lens, and up to six imaging lenses below the sample. The condenser lens system is used to focus the electron beam onto the sample, while the objective lens is used to produce an image of the specimen which is then magnified by the remaining imaging lenses and projected onto the viewing device.¹²⁶ The optical properties of the objective lens mostly dominate the final quality of the image formed. The two most important lens aberrations in the TEM are spherical and chromatic aberrations.¹²⁴ They present limitations to the resolution of the TEM and therefore have to be corrected. Apertures, which are located in the optical column of the TEM, stop the beam electrons which are not required for image formation, for example, scattered electrons.

Specimen stage: The specimen holder and the goniometer into which it is fitted are the most important mechanical components of the TEM. The most common design is the side-entry design in which the specimen is attached to a rod that is inserted into the goniometer.¹²⁴ The specimen is placed on a TEM grid, which is a metal ring with a standard 3.05 mm diameter, the thickness and mesh size ranging from a few to 100 μm .

Energy filter: Energy filtering is very important for many applications of the TEM, it employs the removal of inelastically scattered electrons. Energy filters are required for

electron energy-loss spectrometry (EELS) as well as energy-filtering transmission electron microscopy (EFTEM). An energy filter, such as the Ω -filter developed by Zeiss, can be integrated into the TEM column. In the Ω -filter, electrons of different energies are separated via four sector magnets and directed along an Ω -shaped beam path onto the optical axis of the microscope.¹²⁷

In the present work, TEM was frequently used to directly visualize the synthesized silica particles, to control their size distribution, as well as to determine the polymer shell thickness around homogeneously decorated and Janus particles. All TEM images were taken with a Libra 120 cryo-TEM from Carl Zeiss NTS GmbH equipped with a LaB₆ source and an Ω -filter. The acceleration voltage was 120 kV and the energy filter with an energy window of 15 eV was used. Samples for TEM were prepared by immersing a TEM grid in a dispersion of the respective particles for 20 s and removing excess liquid afterwards with filter paper. Gold grids with a carbon film (300 mesh, CF300-Au-50) were used for the analysis (Electron Microscopy Sciences, USA).

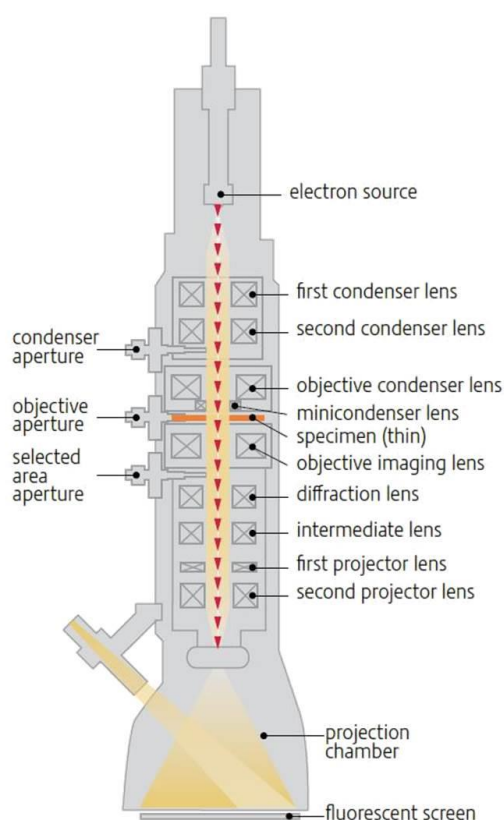


Figure M2. Schematic illustration of a conventional TEM electron column.¹²⁶

Cryo-TEM: Sample damage which is unavoidable during conventional sample preparation, such as drying, fixing, or sectioning, can be avoided using cryo (freezing) techniques. Vitrification is a rapid freezing process that occurs so quickly water molecules do not have time to crystallize, instead forming a vitreous (amorphous) solid that does little or no damage to the sample structure.¹²⁶ In cryo-TEM, the sample is directly visualized in its vitrified state, which requires some additional features to the conventional TEM. The most important part of the cryo equipment in the specialized holder for the TEM grid with the specimen. The time

period of sample viewing in cryo-TEM is often limited as most samples are sensitive to radiation damages.¹²⁸

In the present work, cryo-TEM was used to directly visualize the synthesized core-shell polymer-decorated silica particles – both homogeneously decorated and Janus. In this way, hydrophilic polymers could be visualized in their swollen state (in water). With the help of cryo-TEM, the polymer shell thickness in swollen state could be determined, and stimuli-responsive properties of the polymers could be investigated by varying the pH of the prepared suspensions. Janus particle assembly in water was also investigated. All cryo-TEM images were taken with a Libra 120 cryo-TEM from Carl Zeiss NTS GmbH equipped with a LaB₆ source and an Ω -filter. Samples for cryo-TEM were prepared as follows: the respective particles were dispersed in water (0.5 mg/ml) by ultrasonication for 20 min; pH was adjusted if needed. Prior to the analysis, 3.5 μ l of the sample were taken, blotted and vitrified in liquid ethane at -178 °C. Ultimately, an approximately 200 nm thick ice film was examined in the TEM.

3.3.3. Atomic Force Microscopy (AFM)

Atomic force microscopy (AFM) is a very high resolution type of scanning probe microscopy (SPM), in which the topology of the sample is traced by a sharp probe that is scanned line by line over the sample.¹²⁴ The probe in the AFM is a sharp tip, typically less than 5 μ m tall and less than 10 nm in diameter at the apex. The tip is located at the free end of a cantilever, which is usually 100-500 μ m long. Silicon or silicon nitride cantilevers are most frequently used. The cantilever bends and deflects according to the forces between the tip and the sample surface. The cantilever deflections as the tip is scanned over the sample by means of a piezoactuator are measured by the detector. Using the measured deflections, a computer is able to generate a map of surface topography. A controller regulates, collects and processes the data as well as drives the piezo scanner. Most AFMs use optical techniques to detect the position of the cantilever (**Figure M3**). In a typical setup, a light beam from a laser diode bounces off the back of the cantilever and onto a position-sensitive photo-detector. The position of the laser beam on the detector changes if the cantilever bends. Ultimately, the system can detect sub-Ångstrom vertical movement at the end of the cantilever where the tip is located.¹²⁹ The three primary AFM modes are contact, non-contact, and TappingMode.

Contact AFM: In contact AFM used in this work, the tip is in continuous contact with the sample. The tip employed for contact AFM typically has a low spring constant. As the scanner traces the tip across the sample, the contact force causes the cantilever to bend to accommodate changes in topography. A constant deflection (“setpoint” deflection) between the cantilever and the sample is maintained by the feedback loop. In this way, the force between the tip and the sample remains constant. Two other forces are generally present during contact AFM imaging in addition to the repulsive force: a capillary force, which is exerted by the thin liquid layer (water) often present on the sample surface under ambient conditions, and the force exerted by the cantilever itself.¹²⁹

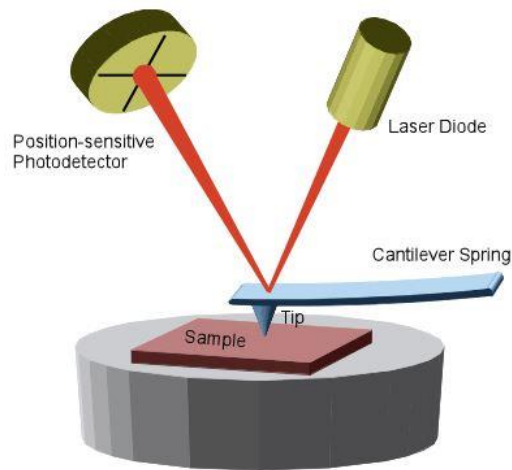


Figure M3. Typical optical detection scheme in AFM.¹³⁰

Force measurements: Apart from imaging the topography of solid surfaces, the AFM can also be used to measure force-versus-distance curves. These so-called force curves provide valuable information about the properties of the material, such as elasticity, hardness, adhesion, and surface charge densities. “Force measurements” are therefore based on the interactions of the tip with the sample. In a typical force measurement, the cantilever deflection is measured while the sample is moved up and down by applying a voltage to the piezoelectric translator, onto which the sample is mounted. Liquid cells may be used to acquire force curves in a liquid. As a result of a force measurement, the cantilever deflection (Z_c) versus position of the piezo scanner normal to the surface (Z_p) is measured (**Figure M4**). Z_c and Z_p must be converted into force and distance to get a force-versus-distance curve. The force F is calculated by multiplying the deflection of the cantilever with its spring constant k_c : $F = k_c Z_c$. The tip-sample separation D , which is also called “distance”, is evaluated by adding the deflection to the position: $D = Z_p + Z_c$.¹³¹ During step (1) the tip descends and approaches the surface, there is no contact with the surface yet (**Figure M4**). During step (2) the tip is pulled down by attractive forces near the surface. As the tip presses into the surface in step (3), the cantilever bends upward. Then the piezo retracts and the cantilever relaxes downward until the tip forces are in equilibrium with the surface forces. In step (4) piezo continues retraction, and the cantilever bends down due to the surface attraction holding onto the tip. The tip finally breaks free of surface attraction during step (5), and the cantilever rebounds sharply upward.¹³²

Colloidal probe technique: The colloidal probe technique typically employs gluing of silica or glass spheres onto the cantilever. There are several advantages of this technique, given that the used spherical particles are smooth and have a defined radius: (1) the force can be analyzed more quantitatively; (2) the total force is higher, thus, the measurement can be more sensitive; (3) probes can be varied by attaching particles of different chemical composition; (4) hydrodynamic force measurements become possible. Silica microspheres, made by a sol-gel process, are the most widely used colloidal probes; their root mean square (RMS) roughness is typically less than 1 nm over $1 \mu\text{m}^2$.¹³¹

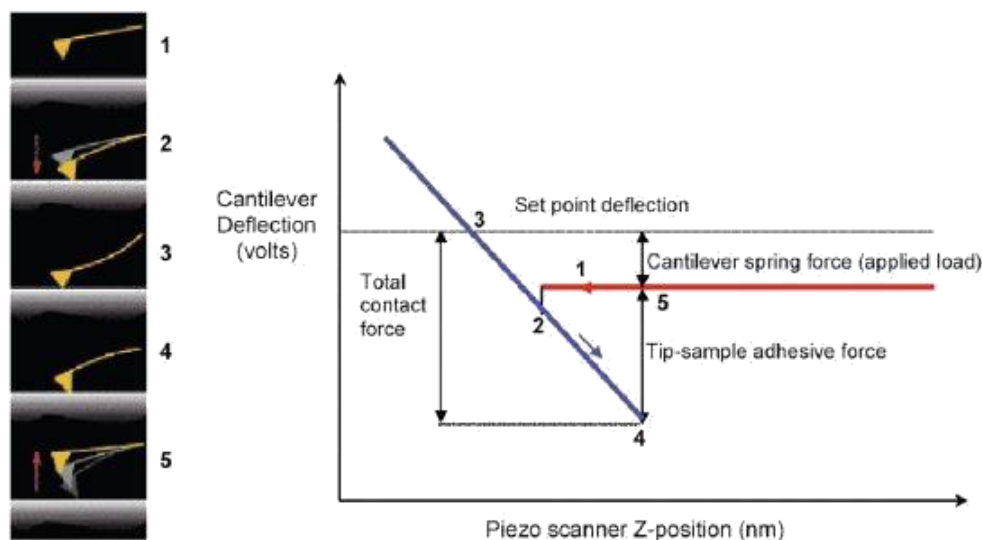


Figure M4. Schematic of a typical AFM force curve. The approaching (red) and retracting (blue) curves are shown on the right.¹³³

In the present work, AFM was frequently used to obtain topography images of the flat polymer brush-covered as well as structured particle-based surfaces, to check the quality of the prepared particle layers, and to make force measurements in order to investigate the adhesive/responsive properties of the polymers grafted to the particle surface as well as to map the distribution of different polymers in the Janus particle-based samples. All AFM images were taken with a Bruker Dimension® Icon™ AFM (Bruker, USA). Contact mode in air or in fluid was used to capture topographical images and force-distance curves in air or under water, respectively. Triangular sharp Si₃N₄ cantilevers (DNP-10, Bruker, USA) with a spring constant of 0.06 N/m were used for the measurements. The “Point & Shoot” option in the AFM software was utilized for all samples to accurately trigger force measurements at desired locations. Employing this mode, several (3-4) force curves were obtained from a single particle in particle-based surfaces to control their reproducibility. Several topographical images with the respective force curves were recorded for each analyzed sample both in air and under water. Interaction forces under water were measured in an open fluid cell in a sealed chamber for the AFM at room temperature. Fresh DI water was used for the measurements. The samples were left to equilibrate in water for 20 minutes before the measurements. Additionally, tipless Si₃N₄ cantilevers (NP-O10, Bruker, USA) with a spring constant of 0.35 N/m and modified with a colloidal probe (glued 5 μm large SiO₂ particle) were used for the force measurements using the Force Volume mode (16x16 μm force maps with a 1 μm step size were recorded). Average force-distance curves corresponding to each sample were calculated using 10 representative force curves.

3.3.4. Visible Light & Fluorescence Microscopy

Visible light microscopy: A light microscope is an optical instrument which uses visible light to produce a magnified image of an object (specimen) that is projected onto the retina of the eye or onto an imaging device. Two microscope components of fundamental importance

for image formation are: (1) the objective lens, which is used to collect light diffracted by the sample and to form a magnified real image at the real intermediate image plane near the eyepieces or oculars, and (2) the condenser lens, which is used to focus light from the illuminator onto a small area of the sample. Other components of an optical microscope include the tube and eyepieces, the lamp collector and lamp socket and its cord, filters, polarizers, retarders, and the microscope stage and stand with coarse and fine focus dials. First, the sample on the microscope stage is analyzed by the objective lens, which produces a magnified real image of the object in the ocular image plane. When looking in the microscope, the ocular acts together with the eye's cornea and lens projecting a second real image onto the retina.¹³⁴

In the present work, the optical microscope was used frequently to control the quality of the prepared particle-based functional surfaces before and after different kinds of measurements. All optical microscopy images were taken with an Olympus BX51 microscope equipped with an Olympus UC30 digital camera and the analySIS docu software (Olympus Soft Imaging Solutions GmbH).

Fluorescence microscopy: Light microscopy optics can be adjusted for fluorescence microscopy, which makes it possible to examine the distribution of single molecular species in a specimen or even detect individual fluorescent molecules. In contrast to other types of light microscopy, fluorescence microscopy allows visualization of specific molecules that fluoresce in the presence of excitatory light. Non-fluorescent molecules are commonly tagged with a fluorescent dye in order to make them visible. Fluorescence microscopes contain special filters and use a unique method of illumination to form images of fluorescent light emitted from excited molecules in a sample. The filters isolate and manipulate two different sets of excitation and fluorescent wavelengths. A band of shorter excitation wavelengths is directed from the illuminator to the sample, whereas a band of longer fluorescence wavelengths is emitted from the sample and forms an image of the sample in the image plane.¹³⁴

In the present work, fluorescence microscopy was used in order to prove the Janus character of the synthesized silica-based Janus particles and to investigate the self-assembly of Janus particles in bulk depending on different media conditions. For this purpose, a fluorescent dye, fluorescein *o*-acrylate, was incorporated into one polymer shell of the Janus particles during polymerization. All fluorescence images were obtained using an Axio Imager.A1m microscope with a 100× oil immersion objective (Carl Zeiss Microscopy GmbH, Germany) equipped with a mercury lamp. For data acquisition a standard FITC (exciter: D480/30x; dichroic: 505DCLP; emitter: D535/40m; Chroma Technology Corp., USA) filter set in conjunction with a Photometrics Cascade II: 512 camera (Visitron Systems GmbH, Germany) and a MetaMorph imaging system (Universal Imaging, USA) were used.

3.3.5. Electrokinetic Measurements

The electrokinetic potential on the surface of a solid in contact with a polar medium is dictated by the dissociation of surface groups, preferential adsorption of cations or anions, adsorption of polyelectrolytes, isomorphic substitution of cations and anions, and accumulation or depletion of electrons. An electric double layer is present on the surface of the solid and it includes two regions: a fixed or immobile layer and a diffuse or mobile layer, while a “slipping plane” or shear plane lies between these two. Relative movement between the fixed and the diffuse layers can be caused by externally applied electrical or mechanical forces. The potential at this surface is called the electrokinetic or zeta (ζ) potential. This potential can be experimentally determined by an externally applied electrical field, which causes a relative movement of the solid and liquid phases (electrophoresis, electro-osmosis), or, vice versa, a relative movement of the solid and liquid phases, which generates an electrical potential or produces an electrical current (streaming potential/streaming current, sedimentation potential).¹³⁵

Particle electrophoresis: During particle electrophoresis, the electrophoretic mobility of the particles (v) is determined over a wide range of their diameters, and the zeta potential is calculated using the Smoluchowski equation:

$$\zeta = \frac{v\eta}{E_{ext}.\epsilon_0\epsilon_r} \quad (8)$$

where η is the viscosity of the liquid, E_{ext} is the external electric field intensity, and ϵ_0 and ϵ_r are the permittivity of the free space and the liquid, respectively.¹³⁵

In the present work, electrokinetic measurements via electrophoresis were applied frequently to control each step of the silica or kaolinite particle surface modification – from the native particles to the polymer-modified homogeneously decorated and Janus particles. For this purpose, the pH-dependent measurements of the particles in dispersion were carried out with a Zetasizer Nano ZS (Malvern Instruments Ltd., UK) and an MPT-2 autotitrator. For all the measurements, the particles were suspended in a solution of 10^{-3} M KCl in water (10 mg/24 ml or 0.42 mg/ml). The pH of the prepared suspensions was controlled by adding 0.1 M KOH or HCl aqueous solutions. Three measurements were recorded for each sample at each pH value.

Streaming potential measurements: The zeta potential of coarse powders, fibres, plates, sheets, coatings, membranes, etc. is typically determined via streaming potential measurements. Since the determination of the zeta potential depends on the existence of single capillaries or capillary bundles, their length to cross-sectional area ratio L/Q has to be determined and the streaming potential has to be measured as a function of the pressure decay in the capillary (capillary bundle).¹³⁵

In the present work, streaming potential measurements were employed in order to control each step of the wafer modification and to perform pH-dependent measurements on the

particle-based structured surfaces. All streaming potential measurements were carried out with the Electrokinetic Analyzer (EKA; Anton Paar GmbH, Austria) in order to reveal the surface potential of the prepared coatings. Two silicon wafers with or without a particle coating were placed parallel face to face to build a streaming channel inside a specially designed cell for rectangular samples. An electrolyte solution (10^{-3} M KCl solution in water) was circulated through this channel. The streaming potential vs. pressure loss was measured by Ag/AgCl electrodes.

3.3.6. Dynamic Light Scattering (DLS)

Dynamic light scattering is a technique which is used to determine the size distribution of small particles in suspension or polymers in solution.¹³⁶ In a typical light scattering experiment, a laser beam is shot through a polarizer and into the sample. Light scattered by the particles is received by a photo multiplier tube and the resulting image, which is known as a speckle pattern, is projected onto a screen. This process is repeated at short time intervals and the resulting set of speckle patterns is analyzed by an autocorrelator, which compares the intensity of light at each spot over time. After the generation of the autocorrelation data, different mathematical approaches can be used to obtain the required information from it, such as the diffusion coefficient, which is then used to calculate the hydrodynamic radius of the particles.¹³⁷

In the present work, dynamic light scattering measurements were used in order to determine the hydrodynamic radius and the particle size distribution of silica particles, either native or polymer-modified, and to evaluate the stimuli-responsive properties of polymers grafted to the surface of the particles. All DLS measurements were performed using 0.5 mg/ml particle suspensions on a Zetasizer Nano ZS (Malvern Instruments Ltd., UK) equipped with a 633 nm He-Ne laser and with a non-invasive back scatter technology for increasing the particle size sensitivity.

3.3.7. Contact Angle Measurements

If one considers a liquid drop resting on a flat, horizontal solid surface, the contact angle can be defined as the angle formed by the intersection of the liquid-solid interface and the liquid-vapor interface. The interface where solid, liquid, and vapor co-exist is defined as the “three-phase contact line”. If the water contact angle is less than 90° , it indicates that the wetting of the surface is favorable, water spreading over a large area on the surface is observed, and the surface may be considered hydrophilic. Water contact angles greater than 90° indicate that the wetting is unfavorable, contact of the water droplet with the surface is minimized, and the surface may be considered hydrophobic. Superhydrophobic surfaces typically have water contact angles higher than 150° . Contact angles formed by expanding and contracting the liquid are defined as the advancing contact angle θ_a and the receding contact angle θ_r , respectively. The difference between the advancing angle and the receding

angle is called the hysteresis: $H = \theta_a - \theta_r$. The most frequently used technique for the contact angle measurements is a direct measurement of the tangent angle at the three-phase contact point on a sessile drop profile. The equipment typically consists of a horizontal stage to mount the sample, a motor-driven syringe to control the rate of liquid addition and removal, an illumination source, and a camera to make photographs of the drop profile.¹³⁸

In the present work, contact angle measurements were performed frequently to measure the wettability of various surfaces – from “flat” to particle-based structured surfaces. The advancing and receding water contact angles were measured by the sessile drop method using a conventional drop shape analysis technique (OCA 35; DataPhysics Instruments GmbH, Germany). Fresh DI water was used for the measurements. For the advancing contact angle measurement, a 10 μl water droplet was placed gradually onto the sample surface at a 0.25 $\mu\text{l}/\text{sec}$ rate. For the receding contact angle measurement, the pump was reversed, and the droplet volume was contracted. Both advancing and receding contact angle values were recorded at five different locations of the sample. Average values were then calculated. Sliding water contact angles were measured with different droplet volumes: 5 μl , 10 μl , and 20 μl . All measurements were carried out at 24°C and a relative humidity of (40 \pm 3) %, which were kept constant.

3.3.8. Null-Ellipsometry

Ellipsometry is a very sensitive non-destructive optical technique to derive information about surfaces, for instance, to determine the thicknesses of thin polymer films on solid substrates. The ellipsometric technique is based on a suitable manipulation of the polarization state by auxiliary polarizing elements and the measured sample. The basic configuration of an ellipsometer is the polarizer-compensator-sample-analyzer (PCSA) configuration, which consists of a light source, linear polarizer (P), retarder (also called compensator, C), sample (S), linear polarizer (called analyzer, A), and detector. In null-ellipsometry, the typical procedure consists of finding component settings for extinguishing the light at the detector.¹³⁹ As a result, the phase and the amplitude parameters are determined, which depend on the sample characteristics, such as the thickness parameters.

In the present work, the thickness of polymer layers on wafers in dry state was measured at $\lambda = 632.8$ nm and a 70° angle of incidence with a null-ellipsometer (Multiscope, Optrel Berlin, Germany) in a standard PCSA configuration described elsewhere.¹⁴⁰

3.3.9. Thermogravimetric Analysis (TGA) and Gel Permeation Chromatography (GPC)

In the present work, TGA and GPC were used as complementary techniques to determine the grafting density of polymer brushes on the silica or kaolinite particle surface. TGA measurements were performed in order to measure the thickness of the polymer layer on the particle surface. All measurements were conducted in air atmosphere on a TGA Q 5000_{IR}

analyzer (TA Instruments, USA). The molecular weight of bulk polymers (M_n and M_w) obtained after precipitation has been evaluated using GPC (Gradient HPLC Series 1100, Agilent Technologies Inc., USA).

3.3.10. Attenuated Total Reflectance Fourier Transform Infrared Spectroscopy (ATR-FTIR)

In the present work, ATR-FTIR measurements were performed in order to qualitatively trace each step of kaolinite particle surface modification as well as to quantitatively determine the amounts of grafted polymers.

Qualitative analysis: FTIR spectra were recorded using Vertex 70 and Vertex 80v FTIR spectrometers (Bruker, Germany) equipped with DLaTGS- and MCT-detectors. To characterize the substances qualitatively, the DRIFT unit (diffuse reflectance; “Praying Mantis” (HARRICK), used to characterize thin grafted polymer layers on Janus particles) or KBr-pellet preparation technique (drop casting films of initial compounds on KBr-pellets; used to analyze initial substances and to find their spectral distinctions) was used. In the case of the KBr-preparation technique, the spectral range was $4000\text{-}400\text{ cm}^{-1}$ (only for DLaTGS detector), and 32 scans were co-added for every spectrum. To perform the DRIFT measurements successfully the unit requires an MCT-detector to increase both sensitivity and signal-to-noise ratio. The spectral range in this case was $4000\text{-}600\text{ cm}^{-1}$, because of MCT-detector’s limitations, and 200 scans were co-added to every spectrum to obtain a reliable spectroscopic averaging. Spectral resolution was 2 cm^{-1} in all cases. A base line correction and KBr-subtraction were carried out for every spectrum.

Quantitative analysis: Details of the calibration procedure are given elsewhere.⁷⁵ Briefly, the grafted amount of the respective polymer was estimated using calibration curves plotted using the absorbance spectra of the samples made from mixtures of the polymer and particles (50 mg; mixed and pressed with KBr-powder as a pellet). The spectra were recorded using similar spectroscopic settings as for qualitative measurements. The characteristic bands at 2850 cm^{-1} (symmetric stretching vibrations of the methylene group in PLMA), and 2770 cm^{-1} (symmetric stretching vibrations of the methyl group coupled to the amine in PDMAEMA) were used for the estimation of the grafted amount of polymers in the case of K-PDMAEMA/PLMA particles.

CHAPTER IV

Results & Discussion

4.1. SPHERICAL HYBRID HAIRY JANUS PARTICLES

4.1.1. Motivation

Janus particles are a unique class among colloidal particles, comprising two different functionalities at their opposite sides. In particular, Janus particles with a contrast in wettability (hydrophobicity-hydrophilicity) over their surface are able to mimic the functionality and the behavior of molecular surfactants. Their amphiphilic nature yields higher trapping energies to fluid interfaces¹⁴¹ and can lead to the formation of thermodynamically stable emulsions,¹⁴² as opposed to emulsions stabilized by homogeneous particles, which are typically only kinetically stable.¹⁴³ For these applications, it is fundamental to design Janus particles in a controlled way and monitor, characterize and understand their behavior at fluid interfaces (e.g., oil-water or air-water).

There are numerous strategies that have been proposed for the fabrication of Janus particles with variable and controlled size/functionality, however, the large-scale production of such particles with a well-defined and tunable Janus ratio, which is the relative patch size, still remains a challenge. Several strategies have been proposed for the tuning of the Janus ratio, such as changing the ratio of monomer contents in an individual droplet in a microfluidics-based approach,¹⁴⁴ controlling the immersion depth of particles into polymer fibers,¹⁴⁵ or tuning various conditions in the template-assisted glancing angle deposition method.¹⁴⁶ Herein, we have developed an alternative and very simple approach to vary and control the Janus ratio, which could be applied to micrometer- and submicrometer-sized particles on a large scale.

Owing to the lack of suitable techniques to measure directly the adsorption and orientation of (sub)micron JPs in situ at a fluid interface, previous studies have been limited to objects in the tens of microns range.¹⁴⁷⁻¹⁴⁹ In these cases, visualization is straightforward, but the investigated objects do not possess the technological relevance of colloidal JPs. Recently, a new method was developed that overcomes these limitations and allows the investigation of the wetting behavior of colloidal particles as small as 10 nm in diameter at oil-water interfaces.¹⁵⁰ The approach is based on freeze-fracture, shadow-casting (FreSCa) cryo-scanning electron microscopy and makes use of unidirectional metal coating of particles protruding from a flash-frozen water-oil interface, after removal of the oil phase. Similarly to a sundial, the portion of the particle sticking out from the frozen interface casts a shadow upon the metal coating, which encodes the height of the object relative to the interface. For spherical particles, like the ones investigated in this study, the latter can be directly converted

into a contact angle with the fluid interface. Therefore, we have applied this technique to a range of micron-sized JPs with varying ratios of different surface functionalizations, and measured directly their contact angles at a water-toluene interface.

4.1.2. Experimental Part

Variation of the Janus ratio: 1 μm large mono-component Janus particles, which are Janus particles with one grafted polymer shell, were prepared as described in Section 3.2.3. Variations of the particle Janus ratio were performed by controlling the depth of penetration of APS-modified silica particles into the wax phase during the preparation of the wax-water Pickering emulsion (preparation of colloidosomes). For this purpose, variations of the pH value of the boiling water added to the mixture were carried out. In a set of experiments, water with pH 2, 6, and 10 was added to the mixture, and the acquired colloidosomes were ultimately examined by SEM. The ATRP-initiator was then immobilized onto the exposed particle surface, and the polymer (PDMAEMA or PS) was grafted from the initiator-modified particle surface using the SI-ATRP “grafting from” approach as described in Section 3.2.3.

FreSCa imaging: Full details on the sample preparation for FreSCa cryo-SEM measurements can be found in ¹⁵⁰. In brief, millimeter squared, flat particle-laden oil-water interfaces are prepared in a customized copper holder by initially injecting 0.5 μl of the particle suspension and then covering it with the other fluid phase. The holder is then clamped and the samples are flash-frozen in a liquid propane jet freezer (Bal-Tec/Leica JFD 030, Balzers/Vienna). After freezing, the samples are mounted onto a double fracture cryo-stage under liquid nitrogen and transferred under inert gas in a cryo-high vacuum airlock ($< 5 \times 10^{-7}$ mbar, Bal-Tec/Leica VCT010) to a pre-cooled freeze-fracture device at -140°C (Bal-Tec/Leica BAF060 device). The samples are then fractured at -120°C to expose the interface and coated by unidirectional tungsten deposition at an elevation angle (α) of 30° to a thickness of 3 nm and by additional 2 nm with a continuously varying angle between 90° and 30° . The first metal deposition creates a shadow behind each of the particles protruding from the frozen, fractured interface. The second deposition is needed to avoid charging of the shadow during imaging, which may compromise image quality at high magnifications. Metal-coated samples are finally transferred under high vacuum ($< 5 \times 10^{-7}$ mbar) at -120°C to a pre-cooled cryo-SEM (Zeiss Gemini 1530, Oberkochen) for imaging with a secondary electron detector.

Contact angle measurements: Details of the contact-angle measurements can also be found in the literature.¹⁵⁰ Briefly, if the particles have a contact angle at the interface that is significantly larger than the tungsten deposition angle of 30° , clear shadows can be measured. From the shadow length and the particle diameter at the interface, the particle height relative to the interface, and thus the contact angle, can be accurately calculated. In the case of contact angles close to or lower than the tungsten-deposition angle, no shadow is cast by the particles at the interface. In this case, the contact angle can still be measured by comparing the particle cross-section at the interface to πR^2 , in which R is the particle radius.

4.1.3. Results and Discussion

We synthesized hybrid hairy Janus particles (JPs) starting from the synthesis of spherical micron-sized SiO₂ particles, which are subsequently decorated with polymer chains grafted selectively onto one side of the SiO₂ core. The JP functionalization was carried out by using the recently developed wax-water Pickering emulsion approach,⁷⁵ described in Section 3.2.3. Briefly, SiO₂ particles modified with an amino silane (APS) were mixed with paraffin wax and water at a temperature of 85 °C, at which the wax is molten. Vigorous stirring of this mixture results in the formation of a particle-stabilized oil-water emulsion and, as a result, solid wax colloidosomes - wax droplets with immersed modified SiO₂ particles (see **Figure R1**). The side of the SiO₂ particles that stays exposed to the water phase is further modified with an ATRP-initiator and, after the dissolution of the wax, grafted with a polymer, either poly(2-dimethylaminoethyl methacrylate) (PDMAEMA), or polystyrene (PS) via SI-ATRP (“grafting from” approach).

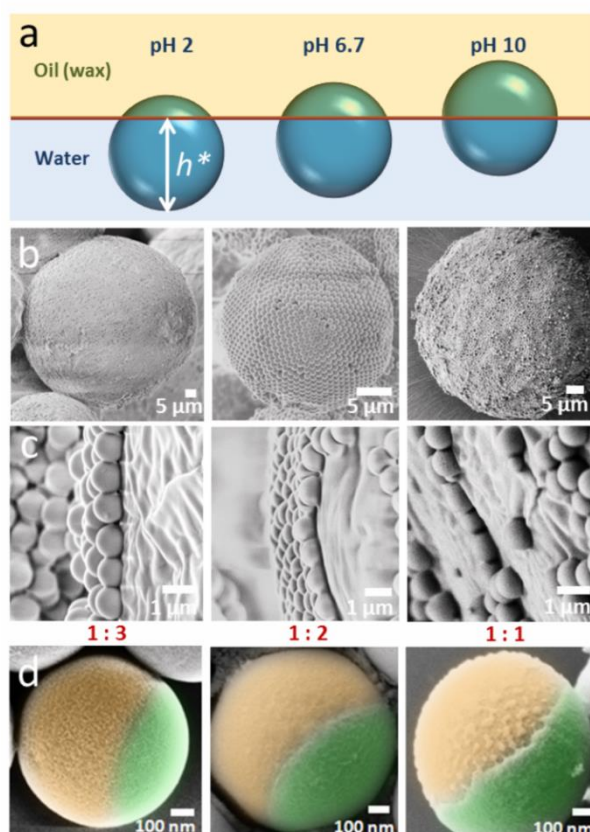


Figure R1. Illustration of the JP preparation with controlled chemical compositions and Janus ratios: a) Schematics of the position of APS-modified SiO₂ particles at the water-wax interface at different pHs; b) colloidosomes obtained at different pHs; c) close-up of the particles on the wax surface, highlighting the different protrusion corresponding to different Janus ratios; d) JPs with different Janus ratios obtained at different pHs. The orange side corresponds to the polymer-coated part and the green side corresponds to the APS-modified part.¹⁵¹

The Janus ratio of the synthesized JPs is determined by the degree of immersion of the APS-modified SiO₂ particles in the wax, which can be controlled by adjusting the pH value of the water (see **Figure R1**). The Janus ratio is defined as the ratio between the portion of the

surface covered with APS and that covered with the polymer (**Figure R1**; the APS-modified part is green, the polymer-coated part is orange). The polymer- and the APS-modified sides can be distinguished in the SEM images owing to their different morphologies: APS areas are smooth, whereas areas covered by the polymer appear rougher.

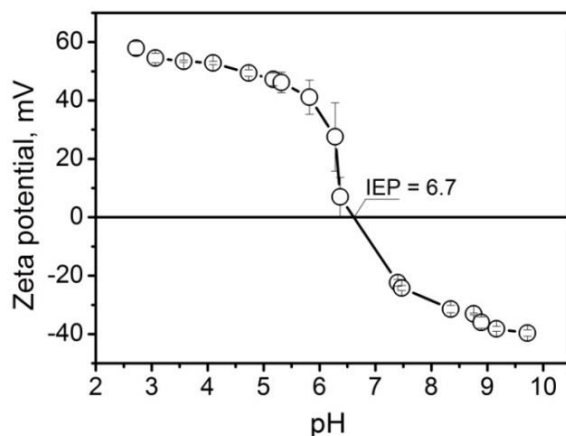


Figure R2. pH dependence of the zeta potential of APS-modified SiO_2 particles.

As it can be seen from a typical zeta potential vs. pH curve for the APS-modified silica particles reported in **Figure R2**, the APS layer can be positively or negatively charged, depending on the pH value. Since the amino group has a basic character, the isoelectric point (IEP) is located at pH 6.7. At low pH values, such as pH 2, the amino groups on the particle surface are protonated and positively charged, thus the particle surface is more hydrophilic, whereas at pH 6.7 (the IEP) the amino groups are uncharged, which leads to a more hydrophobic surface. At higher pH values (e.g., pH 10), negative values of the zeta potential are observed, owing to the saturation of the solution with negative counterions (OH^- , Cl^-), which are eliminated in the colloidosome preparation process. Thus, at high pH values the particles remain hydrophobic, and an increasing protrusion into the wax is observed. The grafted APS layer is considered to be a dense monolayer of APS molecules with a thickness of 0.8 nm, as measured on reference silicon wafers using null-ellipsometry. The grafting density of APS is about 4 molecules/ nm^2 .¹⁵² The grafting density of the grafted polymers was estimated to be 0.2 chains/ nm^2 (evaluated from the results of thermogravimetric analysis (TGA) and gel permeation chromatography (GPC)). To further verify that the pH affects the wettability of the APS-modified SiO_2 particles at the surface of the wax droplets, we measured the contact angle of water with different pH values on APS-modified silicon wafers immersed in *n*-hexadecane. *n*-Hexadecane was used as a liquid analogue of wax. We found that, accordingly to the zeta potential measurements, the water contact angle increases with increasing pH, in response to the change of the charge of amino groups. Assuming that these angles correspond to those of the APS-modified SiO_2 particles at the wax-water interface, we can calculate the immersion degree of the particles into the wax droplets normalized to the particle radius (h^* , see **Figure R1**) as described earlier¹⁵³ using the Equation 9:

$$h^* = (1 - \cos \theta_a)/2 \quad (9)$$

Herein, θ_a is the advancing contact angle of *n*-hexadecane (as a model for wax) on the particle surface (see **Table R1**).

Table R1. Advancing (θ_a) and receding (θ_r) water contact angles of an APS-modified wafer immersed in *n*-hexadecane.

pH	θ_a [°]	θ_r [°]	Expected degree of immersion of the particle in wax, h^* ([%])
2	63 ± 1	23 ± 1	0.25 (25%)
6.7	74 ± 1	40 ± 1	0.36 (36%)
10	73 ± 1	51 ± 2	0.35 (35%)

The experimentally observed degrees of immersion of the particles in the wax (**Figure R1**) are in good quantitative accordance with the estimated ones (**Table R1**). The particles are immersed only to about 25% in wax at pH 2, which correlates reasonably with the experimentally observed degree of particle immersion from the SEM images. The immersion degree increases with the pH value and is about 35% and 50% in the cases of pH 6.7 and 10, respectively. Very interestingly, the expected degree of immersion at pH 6.7 and 10 is similar, as opposed to the experimentally observed values (**Table R1**). The origin of this discrepancy is most probably due to the differences in the receding contact angles and, correspondingly, to the presence of the contact angle hysteresis on the particle surface (see θ_r values for pH 6.7 and 10). In general, controlling the pH allowed us to create Janus particles with different Janus ratios: 1:3 (pH 2); 1:2 (pH 6.7); 1:1 (pH 10). The JPs used for the contact angle measurements are summarized in **Table R2**.

Table R2. Summary of the JPs used in this study for the contact angle measurements.

Particle name	Functionalization	Janus ratio	Solvent	Contact angle [°]	θ_J [°]
JP1	PS/NH ₂	1 : 2	toluene	118 ± 29	109
JP2	PS/NH ₂	1 : 3	toluene	133 ± 20	120
JP3	PDMAEMA _q /NH ₂	1 : 3	water	25 ± 6	60
JP4	PDMAEMA/NH ₂	1 : 3	water	43 ± 4	60
JP5	PDMAEMA/NH ₂	1 : 1	water	28 ± 8	90
HP1	NH ₂	-	water	24 ± 7	-
HP2	PS	-	toluene	129 ± 17	-

Importantly, PDMAEMA/NH₂ Janus particles with different Janus ratios (JR 1:3, and 1:1) showed reasonable changes of the hydrodynamic diameter (D_h) as a function of pH, measured using dynamic light scattering (DLS). It was found that PDMAEMA/NH₂ JPs with JR 1:3 (higher amount of grafted PDMAEMA) showed stronger swelling behavior and higher values of D_h at all pH values compared to the PDMAEMA/NH₂ JPs with JR 1:1. For instance, for the PDMAEMA/NH₂ JPs with JR 1:3 at pH 2, 6, and 10, the value of D_h was found to be 2900,

1970, and 1700 nm, respectively (the standard deviation for all systems is approximately 140 nm). Conversely, the PDMAEMA/NH₂ JPs with a JR of 1:1 showed lower values of D_h: 2600, 1800, and 900 nm, respectively. No large differences in D_h values (measured in toluene) for the PS/NH₂ Janus particles with Janus ratios of 1:2, and 1:3 were observed.

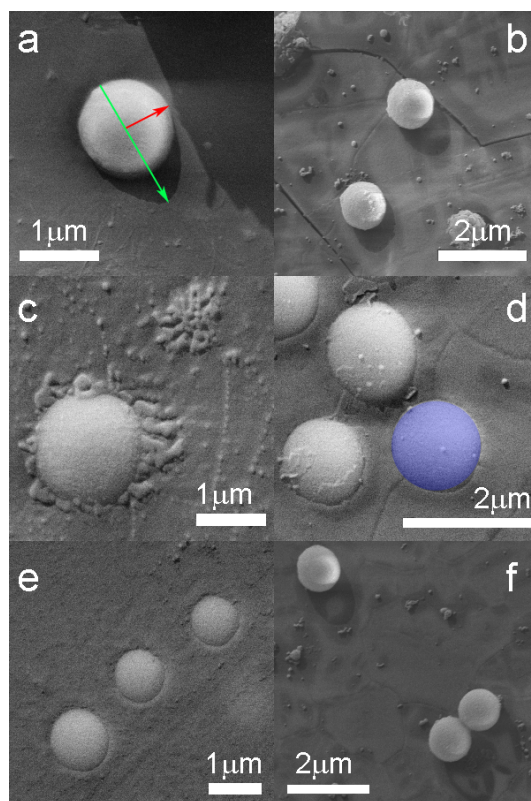


Figure R3. FreSCa cryo-SEM images of the particles: a) JP1; b) JP2; c) JP3, some frozen toluene residues are stuck around the particle contour at the interface; d) JP5; e) HP1; f) HP2. On the JP1 particle the shadow length and the particle radius are highlighted. On the JP4 particle the cross-section at the interface is highlighted. In both cases, these quantities are used to calculate the contact angles.

As previously mentioned, the contact angle measurements of the JPs were carried out by FreSCa cryo-SEM. In these measurements, a small volume of a water (or toluene) suspension of the JPs was loaded into a copper cell to fill a 200 mm deep cavity and then carefully covered by toluene (or water) to form a macroscopically flat, particle-laden oil-water interface. MilliQ water was used in all the measurements. The holder was closed with a flat copper plate, and the sample was flash-frozen by two liquid propane jets. The cooling is sufficiently fast that the water phase vitrifies and “grabs” the particles at the interface. Afterwards, the sample was fractured to remove the frozen oil and expose the interface for imaging. A unidirectional thin tungsten coating at 30° makes the surface of the sample conductive for SEM imaging at cryo temperatures and simultaneously causes a shadow to form behind each feature (particle) protruding from the interface. The shadow length encodes the height of the particle center relative to the interface, and thus the particle contact angle through the relation $\theta = \cos^{-1}(|h - R|/R)$, in which h is precisely the protrusion height of the particle from the frozen interface and R is its radius. For highly hydrophilic particles, that is, with contact angles close to or lower than the tungsten deposition angle, no shadow is cast. In

this case, the particle contact angle is measured by comparing the particle cross-section visible at the interface with the particle equatorial cross-section, πR^2 .¹⁵⁴ Examples of FreSCa cryo-SEM micrographs for the JPs in this study are reported in **Figure R3**.

In particular, **Figure R3 a-b** show that the particles JP1 and JP2 have an overall hydrophobic character due to the PS coating, as also confirmed by the control particles HP2, fully coated with PS and reported in **Figure R3 f**. In all these cases, a clear long shadow is found behind each particle, which indicates a strong protrusion into the toluene. Conversely, JP3 and JP5 (similar images were taken for JP4), see **Figure R3 c-d**, are mostly immersed in the water phase, without the presence of a clear shadow, which indicates an overall hydrophilic character. In this case, the behavior is also confirmed by the homogeneous particle control HP1, shown in **Figure R3 e**. From the shadow length and the particle radius (**Figure R3 a**), or from the particle cross-section at the interface (**Figure R3 d**), we calculated the particle contact angles at the water/toluene interface, as reported in **Table R2**.

Previous theoretical study has established that JPs can exhibit two adsorption regimes at the interface.¹⁴⁸ The first one is called the Janus regime, in which the particle actually behaves like a colloidal surfactant, and where the contact line at the interface is pinned in correspondence to the Janus boundary, that is, the boundary between the different surface functionalizations. In this case, the more and less polar spherical caps are exposed to the water and the oil, respectively. The particle contact angle at the interface corresponds to the angle of the Janus boundary relative to the particle center, θ_J (see **Figure R4**). There is also a second regime, where, in spite of the differences in the surface functionality, the particle behaves effectively like a homogeneous object, and it adsorbs at the interface with a contact angle corresponding to the contact angle of one of the two lobes. Ondarçuhu and co-workers established that the occurrence of one regime or the other depends on the Janus ratio as well as on the wettability contrast between the two portions of the JP, defined as $\Delta\theta = (\theta_A - \theta_P)/2$, in which θ_A and θ_P are the contact angles of the apolar and polar domains of the particle surface, respectively.¹⁴⁸

In the case of our JPs, by measuring the control homogeneous particles uniformly coated by PS or NH₂, we obtain a wettability contrast of 52° for the PS/NH₂ JPs, whereas the PDMAEMAq/NH₂ and PDMAEMA/NH₂ JPs have a much smaller wettability contrast of 16°, as a result of the hydrophilic character of PDMAEMA, which drops to approximately 5° if the PDMAEMA is quaternized. In the absence of uniformly coated PDMAEMA particles, the contact angles used to estimate the wettability contrast are the advancing contact angles of water in *n*-hexadecane on PDMAEMA and PDMAEMAq-coated silicon wafers, which are (55 ± 2)° and (20 ± 2)°, respectively. As a consequence, we observe that the contact angles measured for the PS/NH₂ JPs are consistent with contact-line pinning at the Janus boundary, and thus with a fully functional amphiphilic behavior. Indeed, since most of the particle surface is coated with PS, these particles exhibit contact angles of approximately 120° (Janus ratio 1:2), or higher (ca. 133° for the Janus ratio 1:3; **Table R2**). These results are reasonable, since the higher contact angle on the PS/NH₂ particle with the Janus ratio 1:3 corresponds to

the higher surface coverage with PS and higher surface roughness (rough morphologies of the PS part were confirmed by SEM analysis). Conversely, the PDMAEMA/NH₂ (quaternized or not) JPs exhibit a contact angle significantly different from θ_J , and in most cases corresponding to the contact angle of the NH₂-functionalized portion of the particle (**Table R2**). Therefore, we can conclude that those particles behave as homogeneous colloids.

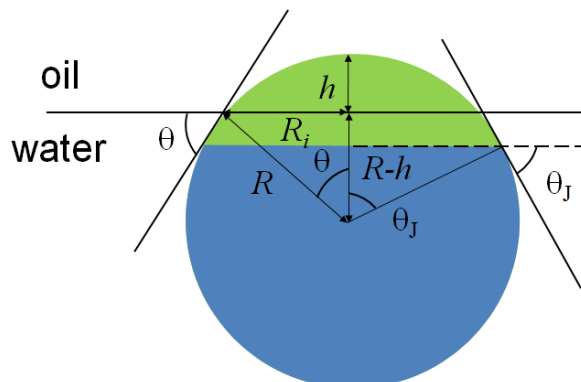


Figure R4. Schematic of a JP adsorbed at a water/oil interface. θ is the contact angle, while θ_J is the angle corresponding to the Janus boundary. If the two angles coincide, the contact line is pinned at the Janus boundary, and the particle behaves as a true amphiphilic object. Otherwise, the measured contact angle corresponds to the contact angle of the material that intersects the interface.

4.1.4. Summary

We have developed a flexible route for the fabrication of diverse types of hybrid hairy Janus particles with the possibility of easily tuning both the Janus ratio and the chemical functionality of the different portions of the particle surface. Additionally, we have employed a new methodology to measure directly and in situ the position/contact angle of such Janus microparticles at a water-oil interface. In particular, our results extend to the colloidal domain, whereas previous results were obtained with much larger JPs. It was indicated that the amphiphilic behavior of JPs at an interface is related to the Janus ratio and the wettability contrast between the two portions of the surface. We found that only in the case of large wettability contrasts our microparticles are in a true Janus regime. In the case of smaller wettability contrasts, the particles behave like homogeneous objects, with a contact angle coinciding with the contact angle of one of the surface parts. Our results indicate that having simply two different functionalities on a particle surface does not necessarily imply amphiphilic behavior. The kind of nanoscale characterization that we have performed then becomes a fundamental step to test, characterize, and optimize the design of functional Janus microparticles for a large range of technological applications.

4.2. PLATELET-LIKE HYBRID HAIRY JANUS PARTICLES

4.2.1. Motivation

As summarized in Section 2.2., there are plenty of synthetic methods for the design of Janus particles, according to which particles with different shapes, such as spheres, rods, and discs can be synthesized. The main challenge in the synthesis of Janus particles remains the scalability, which is the point that often prevents the Janus particles from being employed in real industrial applications.

Disc-like or platelet-like Janus particles are particularly interesting. For example, the energy of detachment of disc-like particles from an interface is much larger than that of rods or spheres.¹⁵⁵ Therefore, discs (platelets) are expected to be the most efficient for the stabilization of foams, emulsions, and polymer blends. Practically, disc-like Janus particles can be synthesized by microfluidic jetting, or interfacial polymerization.¹⁵⁶ For instance, Yang et al. reported on the fabrication of inorganic silica Janus nanosheets and their Janus performance as a solid surfactant.¹⁵⁶ Kaolinite, which is a clay mineral formed from aluminosilicate particles with a flattened disc-like shape, is extremely abundant in nature. The diameter of kaolinite particles is ca. 1-20 μm , and the height is ca. 1 μm . Recently, Müller et al. suggested a novel way for the synthesis of hybrid disc-like Janus particles using site-selective modification of layered-silicate kaolinites at their two opposing basal planes, the tetrahedral and the octahedral surface, which were capped by distinct functional groups, allowing their further modification with two distinct polymers.¹⁵⁷

We further advanced the kaolinite-based approach for the large-scale synthesis of platelet-like Janus particles by employing a simultaneous “grafting from” immobilization of hydrophilic and hydrophobic polymers using surface-initiated ATRP.¹⁵⁸ The chemical composition and functionality as well as the density of the polymer shells can be accurately controlled during the synthesis. Because of its simplicity, the developed method can readily be up-scaled for the synthesis of large amounts of Janus particles, up to several grams in one batch, making them a potential industrially-relevant Janus system.

4.2.2. Experimental Part

Synthesis of platelet-like kaolinite-based Janus particles: The synthesis of mono- or bi-component kaolinite-based Janus particles is described in detail in Sections 3.2.4. and 3.2.5. Colloidosomes were prepared with kaolinite modified with the ATRP-initiator (K-Br) to confirm the location of the particles at the wax-water interface using the approach described in Section 3.2.3.

Preparation of emulsions stabilized with kaolinite-based particles: Emulsions with non-modified, homogeneously decorated, and Janus-type kaolinite particles were prepared, and their stability was studied over a period of 1 week. They were prepared by homogenizing

water and *n*-hexadecane at room temperature for 5 min. with an Ultrasonic Disintegrator UDS 751 (TOPAS GmbH) in the presence of 1 wt % of kaolinite particles. The volume fraction of *n*-hexadecane was 0.2. Samples for optical microscopy investigations were taken at once from the prepared emulsions. Camera images were then taken after certain amounts of time to investigate the stability of the emulsions.

Side-selective adsorption of nanoparticles on kaolinite JPs: Gold nanoparticles (Au NPs) about 20 nm in diameter were used to selectively label the PNIPAAm- and PDMAEMA-modified regions of the kaolinite JPs by coordination and electrostatic interactions, respectively. For this purpose, Au NPs were synthesized by a reduction of gold chloride, according to a procedure described elsewhere.¹⁵⁹ Further, samples with kaolinite JPs were prepared by dispersing 1 mg of JPs in 1 ml of the Au NP solution (as synthesized) and diluting the dispersion with 2 additional ml of DI water. The samples were then examined with SEM. Homogeneously decorated 100 nm large poly(acrylic acid) (PAA)-covered particles were used to selectively label the PDMAEMA-modified region of the kaolinite JPs through electrostatic interactions. The PAA-covered particles were synthesized as described in Section 3.2.2.; their 1 mg/ml dispersion was prepared in DI water. Further, 1 mg of JPs was dispersed in 1 ml of DI water, and 200 μ l of the PAA-covered particle dispersion were added slowly, while stirring. The sample was then examined with SEM.

4.2.3. Results and Discussion

The used strategy for the synthesis of platelet-like Janus particles is illustrated in **Figure R5**. The kaolinite particles (**Figure R5 a**) are first chemically modified to provide them with functionality suitable for the initiation of the atom transfer radical polymerization (ATRP); that is, alkyl bromide groups are immobilized by sequential treatment of kaolinite particles with 3-aminopropyltriethoxysilane (APS; **Figure R5 b**), and α -bromoisobutryl bromide (BrIn, **Figure R5 c**). Next, an emulsion was prepared, consisting of a water solution of a hydrophilic monomer and a solution of a hydrophobic monomer in a water-immiscible organic solvent. Initiator-modified kaolinite particles were added to the emulsion (**Figure R5 d**). Because of their surface energy (40 mJ/m^2), which is between the surface energies of water (72 mJ/m^2) and oil (28 mJ/m^2), flattened kaolinite particles efficiently stabilize water-solvent emulsions because they adsorb strongly at the liquid-liquid interface. The particle can readily turn around the axis that goes through their flattened sides, while flipping of the particle is hardly possible because considerable energy excess is required. Hydrophilic and hydrophobic polymers were thus immobilized on the opposite sides of the resulting Janus particles, when polymerization was started in both the oil and the water phases. Finally, hybrid hairy Janus platelets with dense polymer shells were obtained (**Figure R5 e**).

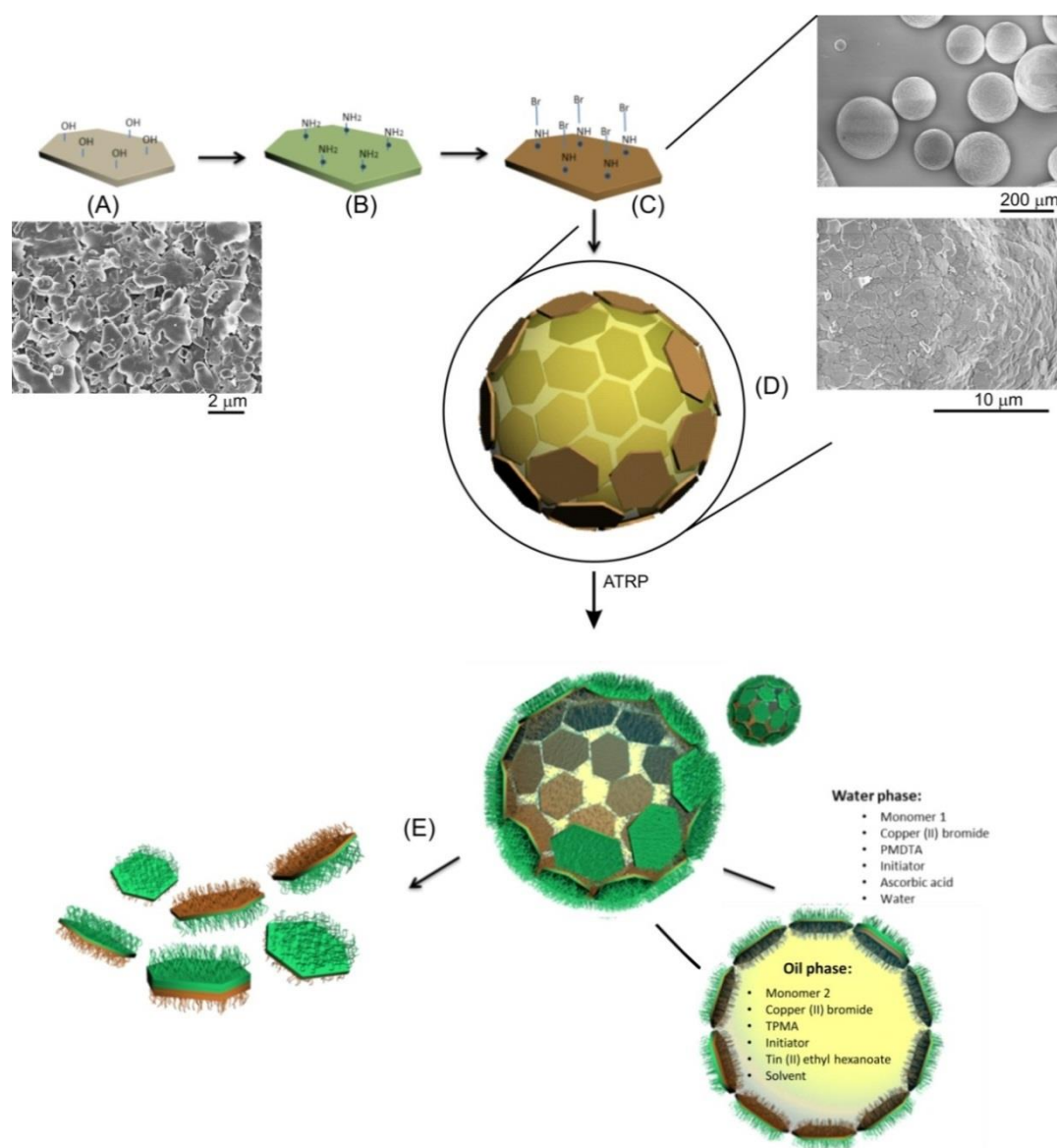


Figure R5. Scheme of a large-scale synthesis of kaolinite-based Janus particles with dense polymer shells: (A) native kaolinite particles after separation (Atterberg method) and washing; (B) kaolinite particles modified with APS; (C) kaolinite particles modified with ATRP BrIn; (D) emulsion droplets stabilized with premodified K-Br and representative SEM images of wax colloidosomes prepared thereof; (E) hairy Janus particles with dense polymer shells.¹⁶⁰

We started from the investigation of the chemical treatment effect of the kaolinite particles on the efficiency of further modification. For this purpose, we compared the electrokinetic properties of kaolinite particles which were treated with an ammonium-peroxide mixture (AMM, NH₄OH:H₂O₂:H₂O) with the ones purified by EDTA and the dithionite-citrate-bicarbonate (DCB) method. Native kaolinite particles, independently from the purification procedure, are negatively charged over the whole range of pH values, their isoelectric point (IEP) is below pH 2.5, and they are more acidic than silica (**Figure R6**, black curves). However, the trend of the whole zeta potential vs. pH curve is more negative in the case of the particles purified with EDTA/DCB (**Figure R6**, black curve, solid circles) as compared to those washed with AMM (**Figure R6**, black curve, empty circles). Treatment with an amino silane dramatically shifts the IEP into the basic region (IEP = 6.5) (**Figure R6**, red curve,

solid circles), if the particles were previously treated with EDTA/DCB. On the other hand, the shift in the IEP after modification of the particles washed with AMM with an amino silane is moderate (IEP = 3.6) and does not approach the IEP of a silicon wafer modified with the same silane (IEP = 8.0). Moreover, the IEP of the Janus particles synthesized using the initial AMM purification procedure is smaller than that of the Janus particles prepared using the EDTA/DCB procedure (**Figure R6**, blue curves). Therefore, EDTA/DCB-treated particles were used for the subsequent immobilization of α -bromoisobutyryl bromide (BrIn).

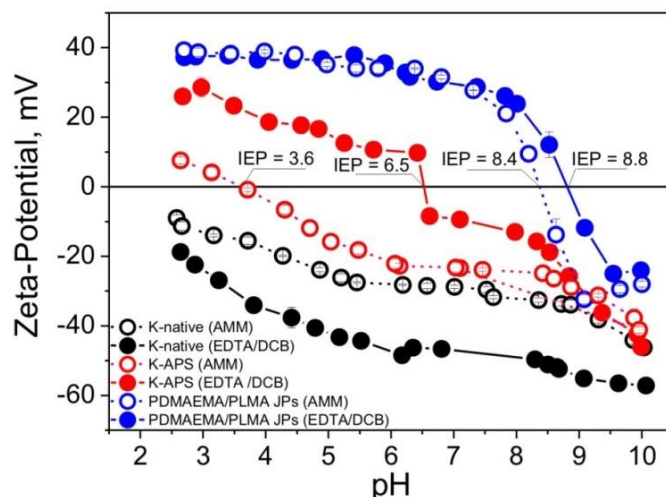


Figure R6. Zeta potential vs. pH of kaolinite particles at different steps of modification: empty black circles – native kaolinite particles treated with an ammonium-peroxide mixture (AMM); solid black circles – native kaolinite particles treated with EDTA and the dithionite-citrate-bicarbonate (DCB) method; empty red circles – APS-modified kaolinite particles treated with AMM; solid red circles – APS-modified kaolinite particles treated with EDTA/DCB; empty blue circles – polymer-modified kaolinite Janus particles treated with AMM; solid blue circles – polymer-modified kaolinite Janus particles treated with EDTA/DCB.

Polymerization of methyl methacrylate on initiator-modified kaolinite particles using ARGET-ATRP¹²¹ was performed in order to determine the number of available initiator sites, and the grafting density. We added a small amount of a free initiator to the monomer solution and assumed that the molecular weight of the polymer obtained in solution is comparable to that of the grafted polymer chains. The molecular weight of the polymer in solution obtained by GPC was $M_n = 76\ 800$; $M_w = 250\ 000$ g/mol. The amount of the grafted polymer determined by TGA was 20 wt. %. The grafting density (Equation 10) was determined by considering the surface area of the kaolinite particles, which was evaluated by BET measurements: $S_{BET} = 22.276$ m²/g (N_A is the Avogadro's number; f_{pol} is the polymer mass fraction according to TGA analysis). The estimated value of the grafting density was ca. 0.11 chains/nm², which is comparable to the previously reported value of the grafting density, obtained using ARGET-ATRP on a SiO₂ substrate.

$$\Gamma(\text{chains} / \text{nm}^2) = \frac{f_{pol}}{1 - f_{pol}} \frac{N_A}{M_n S_{BET}} \quad (10)$$

Next, we investigated the behavior of Br-modified kaolinites at the water-oil interface. This experiment was done using paraffin wax as the oil phase. The initiator-modified kaolinites were mixed with molten paraffin and water, forming a particle-stabilized emulsion, and

finally cooled down. The use of wax allowed a SEM investigation of the formed colloidosomes at room temperature. It was found that paraffin droplets have spherical shapes with the sizes between 50 and 200 μm after cooling down to room temperature, and crystallization of the wax (**Figure R7**). The surface of the obtained paraffin wax droplets is fully covered with flattened kaolinite particles, which form a monolayer (**Figure R7 c**). This behavior can be fully explained by considering the surface tensions of water, oil, and initiator-modified particles, which are 72, 28, and 40 mJ/m^2 , respectively. The surface tension of initiator-modified particles is in between those of the two liquids; therefore, their segregation between the liquids is energetically favorable.

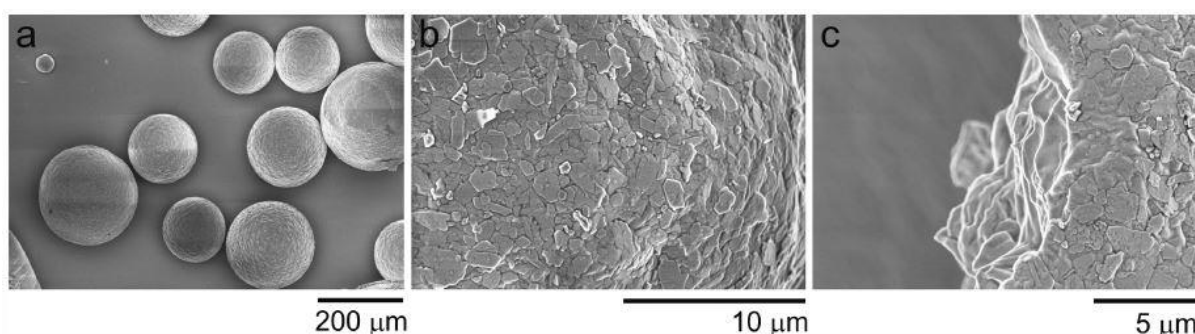


Figure R7. Representative SEM images of paraffin colloidosomes prepared from initiator-modified kaolinite particles (K-Br) and wax.

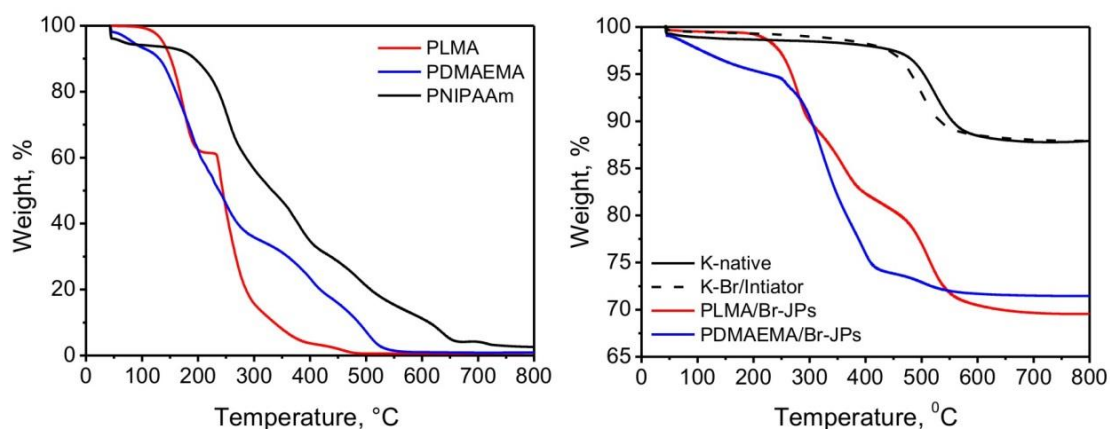


Figure R8. TGA curves of pure polymers (left), and mono-component Janus particles: PDMAEMA/Br-JPs and PLMA/Br-JPs (right).

Next, we performed a separate site-selective grafting of hydrophilic and hydrophobic monomers. For this purpose, the initiator-modified particles were added to an emulsion of anisole in a water solution of 2-(dimethylamino)ethyl methacrylate (DMAEMA, hydrophilic monomer), and in another experiment to an emulsion of lauryl methacrylate (LMA, hydrophobic monomer) in water. The mass loss, measured by TGA, is ca. 30% in both cases (**Figure R8**). Considering that only half of each kaolinite disc is modified by the grafted polymer chains, the thicknesses of the grafted layers (H) are found to be ca. 40 nm (Equation 11):

$$H(nm) = \frac{2f_{pol}}{\rho_{pol}S_{BET}(1-f_{pol})} \quad (11)$$

Therefore, based on the values of the distance between the grafting sites and the shell thickness, the polymer layer can be considered to be in brush regime.

In the next step, we performed simultaneous polymerizations of hydrophilic DMAEMA and hydrophobic LMA monomers in an emulsion. The obtained particles were thoroughly characterized using electrophoresis, TGA, and FTIR spectroscopy. The IEP of PDMAEMA/PLMA Janus particles was found to be at pH 8.4, which is in between the values of the IEPs of homogeneously decorated particles with the same polymers (IEP_{PDMAEMA} = 9.9; IEP_{PLMA} = 4.4) (**Figure R9 a**). This is an indication of a successful grafting of two polymers. The value of the IEP of Janus particles, however, does not allow an estimation of their composition (ratio between both polymers on one Janus particle), because the polymers have different swelling properties (PDMAEMA is a polyelectrolyte and is highly swollen in water; PLMA is hydrophobic and does not swell in water), and their contribution to the total charge of the particles can hardly be estimated. We also synthesized PNIPAAm/PLMA Janus particles using a similar approach.

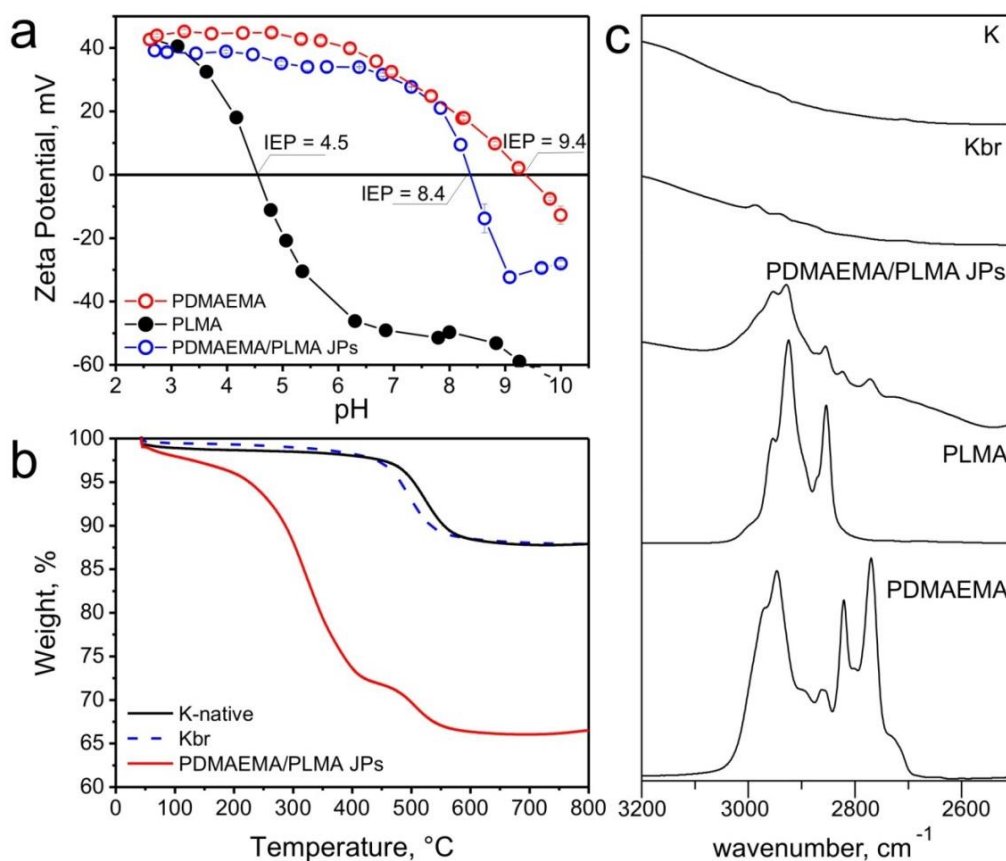


Figure R9. Properties of the homogeneously decorated and Janus particles: (a) - zeta potential (red line – PDMAEMA-modified particles; black line – PLMA-modified particles; blue line – PDMAEMA/PLMA JPs); (b) - TGA (black line – native kaolinite particles; blue line – initiator-modified particles, Kbr; red line – PDMAEMA/PLMA JPs); (c) - FTIR spectra (K – native kaolinites, Kbr – initiator-modified kaolinites, PDMAEMA/PLMA JPs, PLMA and PDMAEMA as pure polymers).

Further, the grafted amount of PDMAEMA and PLMA was estimated using TGA and FTIR spectroscopy (**Figure R9 b, c**). The mass loss measured by TGA in the case of bi-component Janus particles was comparable to the mass loss of mono-component Janus particles (**Figure R8**), meaning that the thickness of polymer layers is 2 times smaller, that is, 20 nm. It was found that the FTIR spectra of the Janus particles contain characteristic bands for both polymers: PLMA (at 2850 cm^{-1}) and PDMAEMA (at 2770 cm^{-1}); therefore, it is the direct evidence for the successful grafting of both polymers. We estimated the ratio between the two polymers using a calibration curve obtained from FTIR spectra of polymer mixtures with different compositions. It was found that the ratio between PDMAEMA and PLMA in the Janus particles is PDMAEMA:PLMA = 4.3:5.7; that is, Janus particles are symmetric. Therefore, based on the TGA and FTIR results, one can conclude that the thickness of each polymer layer is ca. 20 nm, and the layers are in brush regime.

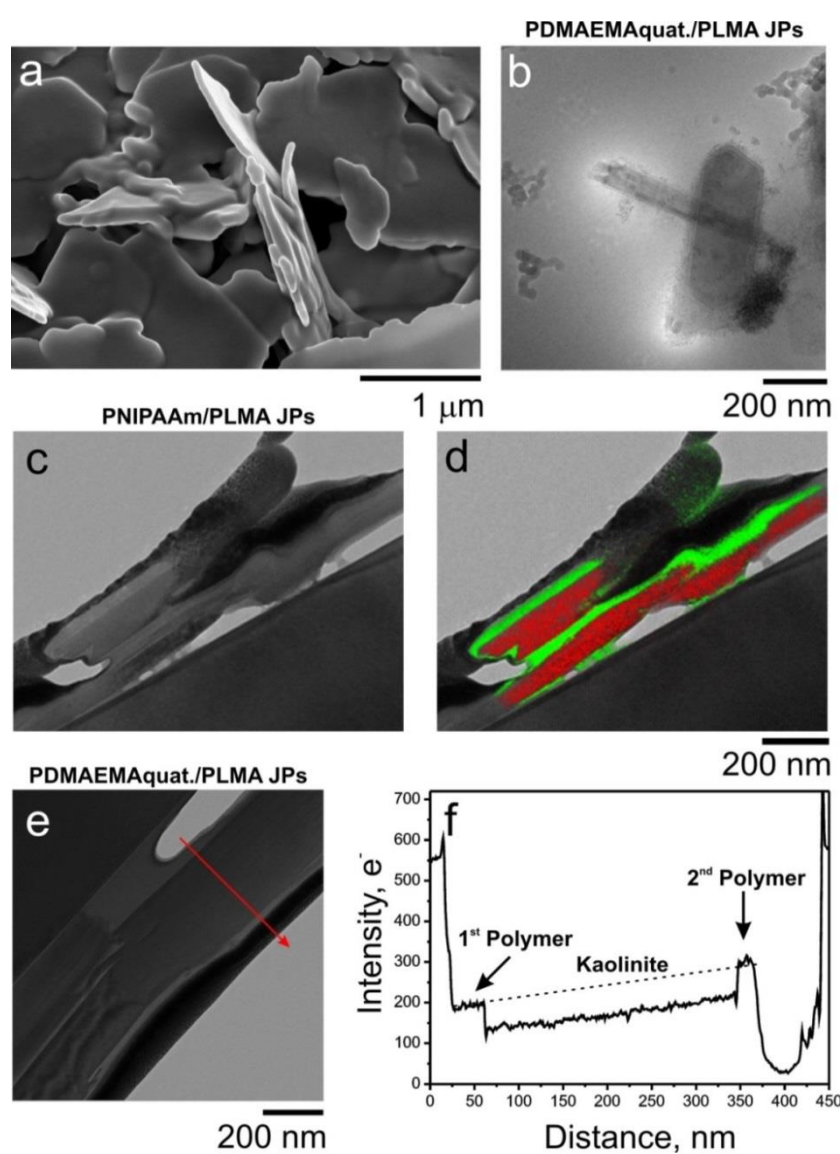


Figure R10. Electron microscopy investigation of the kaolinite Janus particles: (a) SEM, and (b) cryo-TEM images of PDMAEMA/PLMA-JPs, PDMAEMA was quaternized with CH_3I for better contrast; (c) TEM, and (d) EFTEM images of a PNIPAAm/PLMA Janus particle FIB lamella, red and green (d) are the signals for oxygen and carbon, respectively; (e) TEM image of a PDMAEMA_{quat.}/PLMA Janus particle FIB lamella; (f) intensity profile along the red arrow in (e).

The microscopic investigation of the synthesized Janus particles was performed in order to further prove the successful grafting of polymers. Polymer-modified particles have a smoother surface (**Figure R10 a**) than the native ones because of the polymer shell. One can also see, using cryo-TEM, the shell of the swollen in water quaternized-PDMAEMA (the polymer was quaternized with CH₃I for better contrast) around the PDMAEMA/PLMA Janus particles (**Figure R10 b**). The contrast between the different phases of PNIPAAm/PLMA Janus particles was investigated using TEM and EFTEM methods. One can distinguish between the inorganic core with its strong oxygen signal, and the polymer shell with its strong carbon signal (**Figure R10 c, d**). We could also observe contrast between the quaternized-PDMAEMA and PLMA sides (**Figure R10 e, f**): the polymer shell on one side of the particle is darker (PDMAEMA) than on the other (PLMA). The thickness of each layer evaluated using TEM images was found to be in the range of ca. 30 nm, which is comparable to the results of TGA and FTIR. Thus, based on scanning and transmission electron microscopy observations, we can conclude that the grafting of polymers from both sides of kaolinite particles was successful.

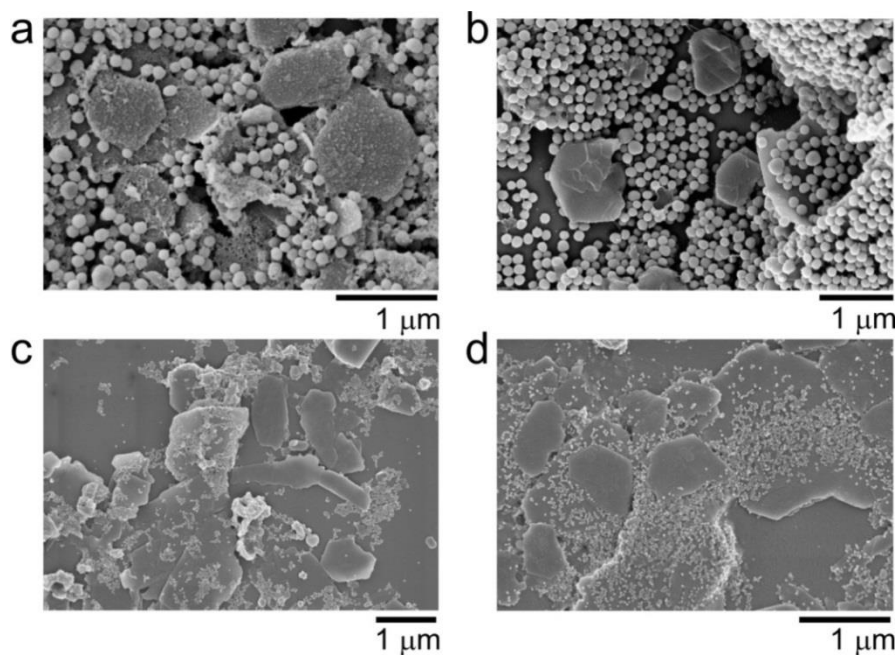


Figure R11. Side-selective adsorption of PAA NPs on (a, b) PDMAEMA/PLMA-JPs, and Au NPs on (c) PDMAEMA/PLMA-JPs, and (d) PNIPAAm/PLMA-JPs.

Moreover, we further proved the Janus character of the synthesized particles by side-selective adsorption of negatively charged PAA-coated SiO₂ particles onto the PDMAEMA/PLMA Janus particles as well as adhesion measurements. In particular, we observed that PAA-coated SiO₂ particles do not adsorb on all kaolinite particles. Some of the particles remain absolutely uncoated. The observed effect can readily be explained by considering the properties of each polymer: PLMA is hydrophobic and uncharged; PDMAEMA is hydrophilic and positively charged; PAA is hydrophilic and negatively charged. PAA particles are strongly electrostatically stabilized and do not adsorb on any hydrophobic as well as hydrophilic uncharged or negatively charged surface. On the other

hand, PAA particles are strongly adsorbed on the positively charged PDMAEMA surface due to electrostatic attractions. Therefore, the character of adsorption of PAA particles can be considered as an indication of the grafted polymer: PDMAEMA sides of the Janus particles are covered by PAA particles, while the PLMA ones are bald (**Figure R11 a, b**). Similar experiments with side-selective adsorption were performed with Au nanoparticles (negatively charged, ZP = -35 mV) on quaternized PDMAEMA/PLMA-JPs (**Figure R11 c**) as well as PNIPAAm/PLMA-JPs (**Figure R11 d**). In both cases, Au NPs are selectively adsorbed either onto PDMAEMA, or PNIPAAm sides.

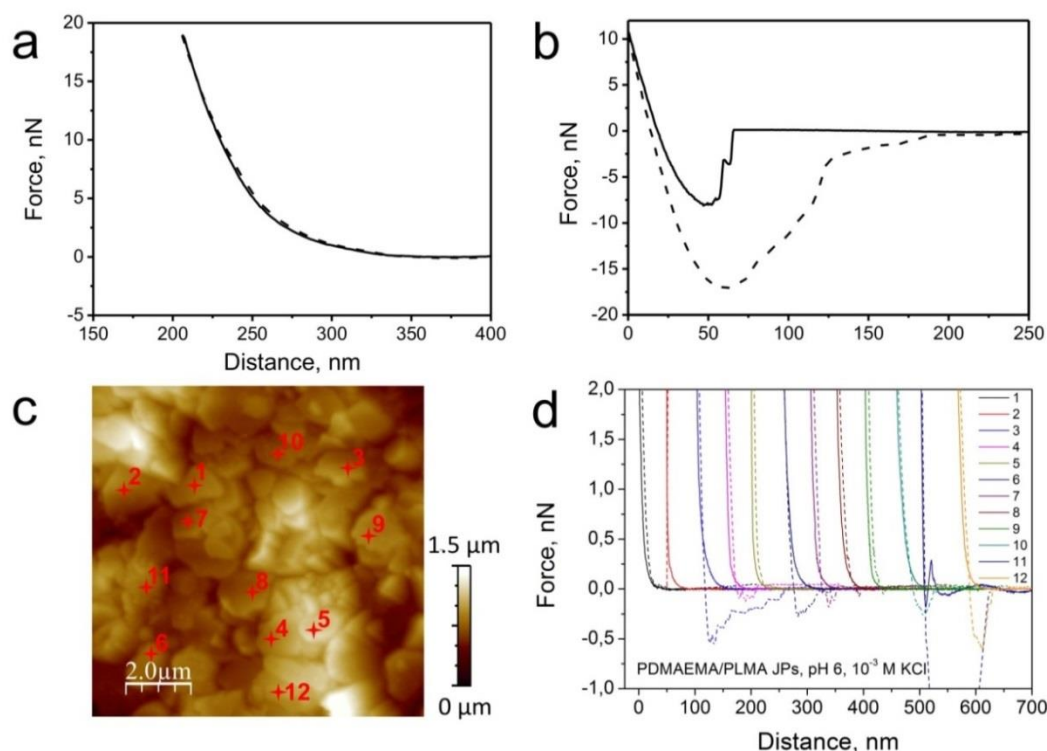


Figure R12. AFM direct force measurements underwater on PDMAEMA/PLMA Janus particles: (a, b) force-distance curves obtained on pure PDMAEMA and PLMA surfaces, respectively; (c) topography image of the Janus particles; (d) force-distance curves corresponding to the selected Janus particles in (c).

AFM force measurements in aqueous conditions at controlled pH and ionic strength confirm different properties of the opposite sides of the bi-component Janus particles (**Figure R12**). The grafted polymers PDMAEMA and PLMA have different adhesive properties. In particular, PDMAEMA is non-adhesive (**Figure R12 a**) underwater, while PLMA is strongly adhesive (**Figure R12 b**). We performed test force measurements of the Janus particles adsorbed on a silica wafer (totally, more than 20 Janus particles were tested in each image, a representative experiment is shown in **Figure R12 c**). It was found that half of them are absolutely non-adhesive, and the other half are adhesive (adhesion force is ca 0.3-0.5 nN), which is an indication of the different properties of the opposite sides of the Janus particles (**Figure R12 d**).

Finally, we have demonstrated an application of amphiphilic PDMAEMA/PLMA Janus particles for the stabilization of water-oil emulsions. It was found that the oil droplets stabilized by PDMAEMA/PLMA Janus particles are much smaller than the droplets stabilized

by unmodified kaolinite. Moreover, the amphiphilic PDMAEMA/PLMA Janus particles are more efficient for the stabilization of an emulsion than native kaolinite: the emulsion with Janus particles remains stable for 7 days, while the emulsion with native particles starts to separate after 1 min (**Figure R13**).

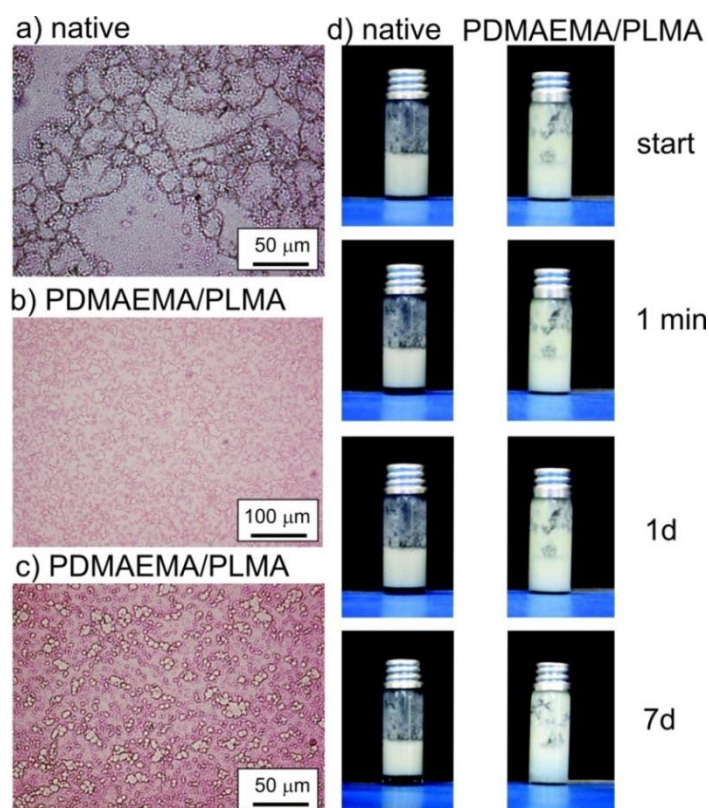


Figure R13. Stabilization of a water-oil emulsion by native kaolinites and PDMAEMA/PLMA Janus particles: (a) – microscopy image of the emulsion stabilized by native kaolinite particles after 15 min; (b, c) - microscopy images of the emulsion stabilized by Janus kaolinite particles after 15 min; (d) photo snapshots of the emulsions stabilized by native kaolinite particles and Janus particles after different time intervals (as prepared, after 1 minute, 1 day, and 7 days).

4.2.4. Summary

In summary, we have developed a novel approach for the large-scale synthesis of hybrid platelet-like Janus particles with hairy polymer shells. The method is based on the fabrication of an emulsion consisting of water and oil solutions of hydrophilic and hydrophobic monomers, respectively, which is stabilized by initiator-modified kaolinite particles. The advantage of this approach is its simplicity and the possibility of the synthesis of large amounts of Janus particles at once – up to several grams in a single batch. Scalability is unfortunately the main limitation of photolithography, which was also used for the fabrication of platelet-like Janus particles,^{161, 162} as well as one of the main challenges in the synthesis of Janus particles in general. The proposed approach can be applied to various surfaces with disc-like or platelet-like geometry, and hence can aid in the design of advanced functional materials for different technological applications such as stabilization of emulsions, and ultimately the design of anti-icing or anti-fouling coatings.

4.3. (SELF-) ASSEMBLY OF SPHERICAL HYBRID HAIRY JANUS PARTICLES

4.3.1. Motivation

As summarized in Section 2.3., colloidal self-assembly is a very powerful tool for the development of materials with tunable and multifunctional properties. The self-assembly process of colloidal particles can be governed by different forces, including van der Waals, electrostatic, hydrogen bonding, covalent, coordination, capillary, convective, shear, optical, and electromagnetic forces.^{10, 11, 163}

Furthermore, shape change at the building block level through the implication of patchy particles leads to their assembly into special asymmetric structures with unique anisotropic properties, which starkly contrast with the isotropic ones.^{12, 13, 164-167} Progress has been made in the field of the Janus particle assembly, as summarized in Section 2.3. However, difficulties still arise when trying to achieve both spatial and chemical control over the assembly process, which can result in a limited yield, and thus limited applications of the prepared nanomaterials.

Moreover, almost all of the works concerning the Janus particle assembly employ the so-called “bare” particles, and only few studies investigate “hairy” Janus particles – particles with grafted polymer shells.^{168, 169} The advantages of such hairy Janus particles are the advanced functionality provided by the grafted polymers, and the mechanical stability of the hybrid system, which would lead to the additional stability of the assembled structures. The final functionality of the particles can be tuned endlessly by selecting various combinations of stimuli-responsive polymers.

Therefore, we have investigated the self-assembly of hairy Janus particles decorated with a variety of different functional polymers, such as hydrophobic and hydrophilic, charged and uncharged, positively and negatively charged ones, thus extending the choice of interaction forces governing the assembly process.

4.3.2. Experimental Part

1 μm large SiO_2 particles homogeneously decorated with PDMAEMA, PAA, P(PEGMA) (hereinafter referred as PEG), PLMA, and PS, as well as 1 μm large SiO_2 PDMAEMA/PAA, PDMAEMA/PLMA, PDMAEMA/PS, and P(PEGMA)/PLMA (hereinafter referred as PEG/PLMA) Janus particles were synthesized according to the procedures described in Sections 3.2.2.-3.2.3.

In order to observe the self-assembly behavior of bi-component Janus particles, different sets of dispersions were prepared. All of the dispersions had a concentration of 1 mg/ml. Oppositely charged polyelectrolyte-modified JPs (PDMAEMA/PAA-JP) were dispersed either in water or in a salt solution (5 mM KCl). The pH value was adjusted to 2, 6, and 9 with

the help of HCl or NaOH. Reference particles, fully covered with either PDMAEMA, or PAA (PDMAEMA-FC and PAA-FC, respectively), were dispersed in analogous media. Amphiphilic JPs (PEG/PLMA-JP) were dispersed either in water, or in toluene. Charged/hydrophobic JPs (PDMAEMA/PLMA-JP and PDMAEMA/PS-JP) were dispersed in water, salt solution (5 mM KCl), and toluene. Reference particles, fully covered with PEG, PLMA, PS, or PDMAEMA (PEG-FC, PLMA-FC, PS-FC, and PDMAEMA-FC, respectively), were dispersed in water and toluene. The prepared dispersions were sonicated for 10 min prior to microscopy investigations. The self-assembly behavior of Janus and fully covered particles was explored in dispersions by means of fluorescence microscopy. The number of clusters used to obtain the graphs depends strongly on the investigated system. In the case of large aggregates (for example, PDMAEMA/PAA-JP at pH 6), a total of 80 clusters could be found in 10 fluorescence microscopy images. In the case of intermediate aggregation (PEG/PLMA-JP, PDMAEMA/PLMA-JP, PDMAEMA/PS-JP), typically 200-500 clusters were counted. In the case of single particle prevalence (for example, PEG-FC in H₂O), up to 1200 particles and particle clusters were counted. Overall, an area of more than 68890 μm^2 was examined for each sample. The thickness of the dispersion layer under the cover slip was 62 μm . Since the size of the particles was 1 μm , they were not limited in their movement, and only very big aggregates could be pinned to the surface of the glass.

4.3.3. Results and Discussion

Synthesis and Characterization of Janus particles

Four hybrid hairy Janus particle systems with different kinds of polymer chains grafted to the opposite sides of the SiO₂ core particles were synthesized through the combination of the “grafting from”/“grafting to” approaches⁷⁵ for the investigation of their self-assembly in bulk (**Table R3**). The synthetic procedures of the Janus as well as homogeneously decorated particle preparation are described in Sections 3.2.2.-3.2.3. The prepared Janus particles were characterized by means of SEM, TEM, and electrokinetic measurements. SEM images have revealed a Janus ratio of 1:2, i.e. 1/3 of the surface is covered with the polymer grafted by the “grafting to” approach, and 2/3 of the surface are covered with the polymer grafted by the “grafting from” approach (**Figure R14**). The thickness of the polymer layers was evaluated using TEM by examining mono-component Janus particles obtained after the grafting of the first polymer (**Table R3**). The thickness of the second polymer layer, which was grafted via the “grafting to” approach, was always 5-7 nm, as obtained from TGA results. Homogeneously decorated particles were also characterized by means of electrokinetic measurements, and TGA (**Table R3**). The grafting density of the polymers on the silica particle surface is typically 0.2 chains/nm².

Cryo-TEM investigations were performed on an example of oppositely charged PDMAEMA/PAA-JP with a core diameter of ca. 200 nm (**Figure R15**). First, mono-component Janus particles with only the PDMAEMA polymer were examined. It was found

that the polymer chains can be observed selectively on one side of the particles, which confirmed the side-selective grafting of this polymer. We found that the PDMAEMA polymer is swollen (**Figure R15**, upper pictures) and positively charged (see **Figure R16**) at pH 2. Next, bi-component PDMAEMA/PAA-JP were examined. We found that the thickness of the PAA layer (5-10 nm) is smaller than that of PDMAEMA (30-40 nm). This difference allows a clear distinguishing between the different sides of the JPs. In particular, it was found that the PDMAEMA layer shrinks when pH changes from 2 to 6, which can be explained by the deprotonation of PDMAEMA chains and their collapse. Similar behavior was observed in a salty water solution at pH = 6.

Table R3. Janus and homogeneously decorated particle samples and their properties.

System	Component	Properties	Layer thickness	IEP
PDMAEMA/PAA-JP	PDMAEMA	positively charged, hydrophilic	7 nm	4.4
	PAA	negatively charged, hydrophilic		
PEG/PLMA-JP	PEG	uncharged hydrophilic	12 nm	4.7
	PLMA	hydrophobic soft		
PDMAEMA/PLMA-JP	PDMAEMA	positively charged, hydrophilic	8 nm	8.2
	PLMA	hydrophobic soft		
PDMAEMA/PS-JP	PDMAEMA	positively charged, hydrophilic	8 nm	8.0
	PS	hydrophobic hard		
PDMAEMA-FC	PDMAEMA	positively charged, hydrophilic	12 nm	9.9
PAA-FC	PAA	negatively charged, hydrophilic	15 nm	< 2
PEG-FC	PEG	uncharged hydrophilic	10 nm	- strongly swollen
PLMA-FC	PLMA	hydrophobic soft	15 nm	4.5
PS-FC	PS	hydrophobic hard	14 nm	4.0

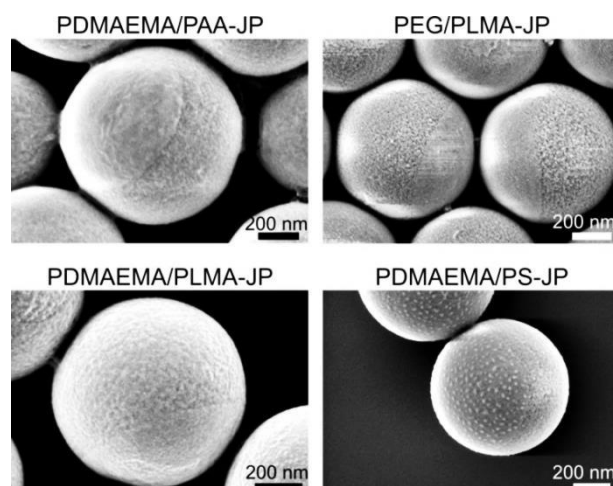


Figure R14. Representative SEM images of different Janus particles.

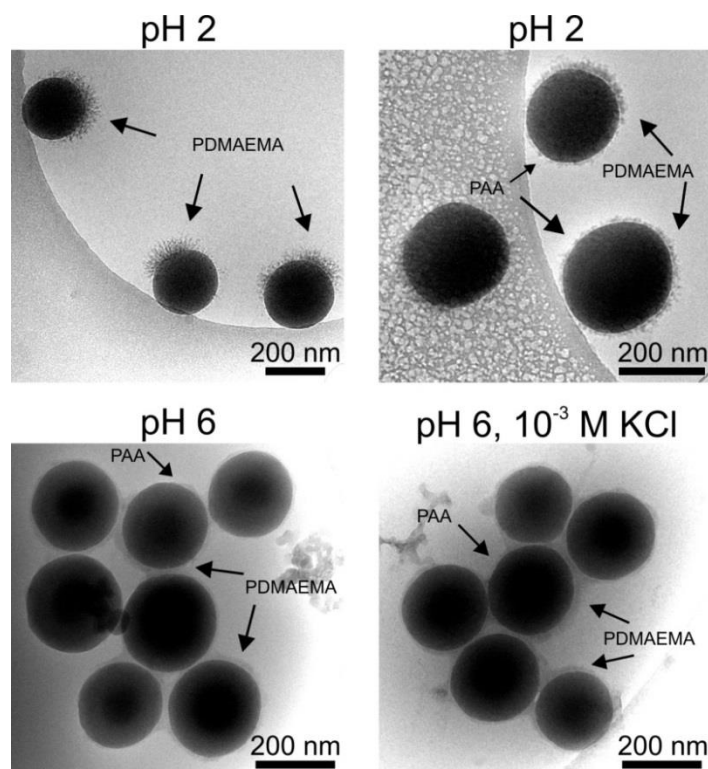


Figure R15. Representative cryo-TEM images of 200 nm mono-component PDMAEMA/NH₂-JP, and bi-component PDMAEMA/PAA-JP at different pH values and salt concentrations.

Electrokinetic measurements confirm the successful grafting of polymers onto the silica particles (**Figure R16**). For example, the IEP of the mono-component PDMAEMA/NH₂-JP is close to that of fully covered PDMAEMA particles. The grafting of the second polymer (PAA) shifts the IEP in between the IEP of PAA-FC and the IEP of PDMAEMA-FC. Moreover, the IEP of PDMAEMA/PLMA-JP and PDMAEMA/PS-JP is similar but a little shifted from the IEP of the mono-component PDMAEMA/NH₂-JP, which also confirms the successful grafting of the second polymer. The slight shift of the IEP can be explained by the hydrophobic character of the second component of the JPs (PLMA or PS), which does not swell in water (or KCl solution). The zeta potential vs. pH curve for the PEG/PLMA-JP is typical for an uncharged polymer curve.

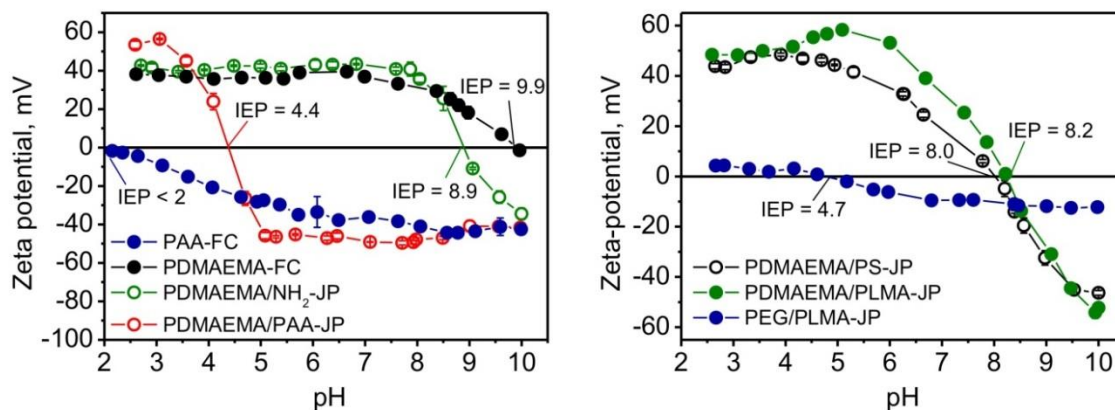


Figure R16. Electrokinetic (electrophoresis) measurements of the synthesized Janus particles: dependence of the zeta potential on the pH value.

Self-Assembly of Janus Particles

Next, we investigated the self-assembly of the obtained Janus particles at different conditions, such as pH and media (water or toluene). We found that the Janus particles form clusters consisting of a different number of particles (**Figure R17**). In order to quantify the self-assembly, we counted the number of clusters formed by different numbers of particles. In particular, we made plots showing the dependence of the number of clusters vs. the number of particles in each cluster (how many clusters are formed by, for example, 4 particles), and the number of particles in clusters vs. the number of particles in each cluster (how many particles are there in all clusters formed by, for example, 4 particles). The first plot is more sensitive to the smaller aggregates, while the second plot is more sensitive to the larger aggregates.

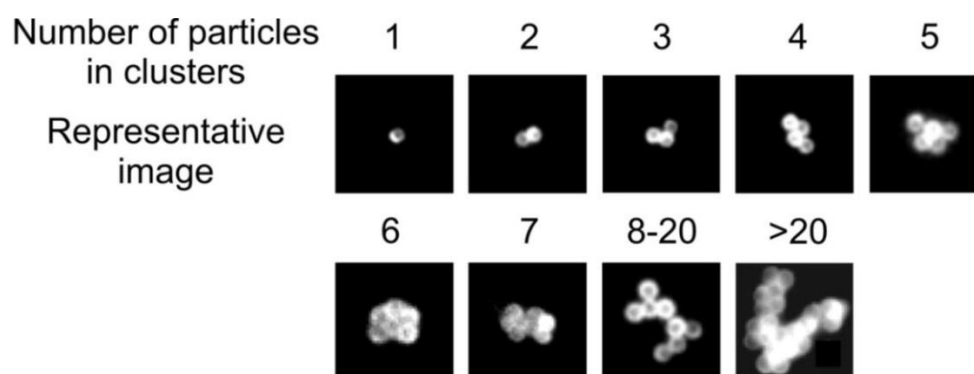


Figure R17. Examples of the Janus particle clusters consisting of a different number of individual particles.

Self-assembly of the first system (oppositely charged PDMAEMA-PAA-JP) as well as the reference systems (PAA-FC, PDMAEMA-FC, and their mixture) was investigated depending on the pH value (**Figure R18**, **Figure R19**). At pH 2 only the polycation PDMAEMA is swollen and positively charged (see ZP curve for PDMAEMA, **Figure R16**), whereas the polyanion PAA is in a collapsed state and is uncharged (see ZP curve for PAA, **Figure R16**). At pH 6 both polymers are charged. At pH 9 we observed a situation opposite to that of pH 2 – the polycation PDMAEMA is collapsed and uncharged (see ZP curve for PDMAEMA, **Figure R16**), whereas the polyanion PAA is in a swollen state and negatively charged (see ZP curve for PAA, **Figure R16**). The self-assembly of JPs was compared with the aggregation of particles covered by individual polymers (PAA-FC and PDMAEMA-FC) as well as their mixture. Fully covered PAA particles (**Figure R18 a**, **Figure R19 a**) demonstrate very high aggregation stability and do not form aggregates at pH = 6 and pH = 9, when PAA is strongly negatively charged ($\text{IEP} < 2$; $\text{pK}_a = 4.2-4.5$) and forms a shell that prevents flocculation. At low pH values (pH = 2) the PAA chains are uncharged and collapsed, as a result, PAA-coated particles tend to form aggregates (doublets, triplets, and large aggregates), while a considerable amount of particles (>50%) remains non-aggregated. Fully covered PDMAEMA particles demonstrate an opposite scenario (**Figure R18 b**, **Figure R19 b**). They almost do not form aggregates at pH 2 and 6, when the polymer is strongly charged ($\text{IEP} = 10$, $\text{pK}_a = 7.3-7.5$) and swollen. Similarly to PAA-FC, PDMAEMA-FC form very large aggregates (>60%) when the polymer chains are uncharged and collapsed, which happens at high pH

values (pH = 9). At pH = 9 some amount of the particles (< 10 %) remains non-aggregated. Mixing of PAA and PDMAEMA fully covered particles leads to a more complex aggregation behavior (**Figure R18 c**, **Figure R19 c**). There is a coexistence of individual particles (ca. 60%) and aggregates at extreme pH values (pH = 2 and pH = 9). The agglomerates at low pH values are most probably formed by the PAA-covered particles, while the agglomerates at high pH values are formed by the PDMAEMA-covered ones. The individual particles at high pH values are therefore the PDMAEMA-covered ones, while the individual particles at low pH values are the PAA-covered ones. The mixed particles form large aggregates (> 80%) at pH 6, and the fraction of individual particles remains negligible (< 10%). Both polymers are charged at these conditions and interact electrostatically with each other, which leads to aggregation.

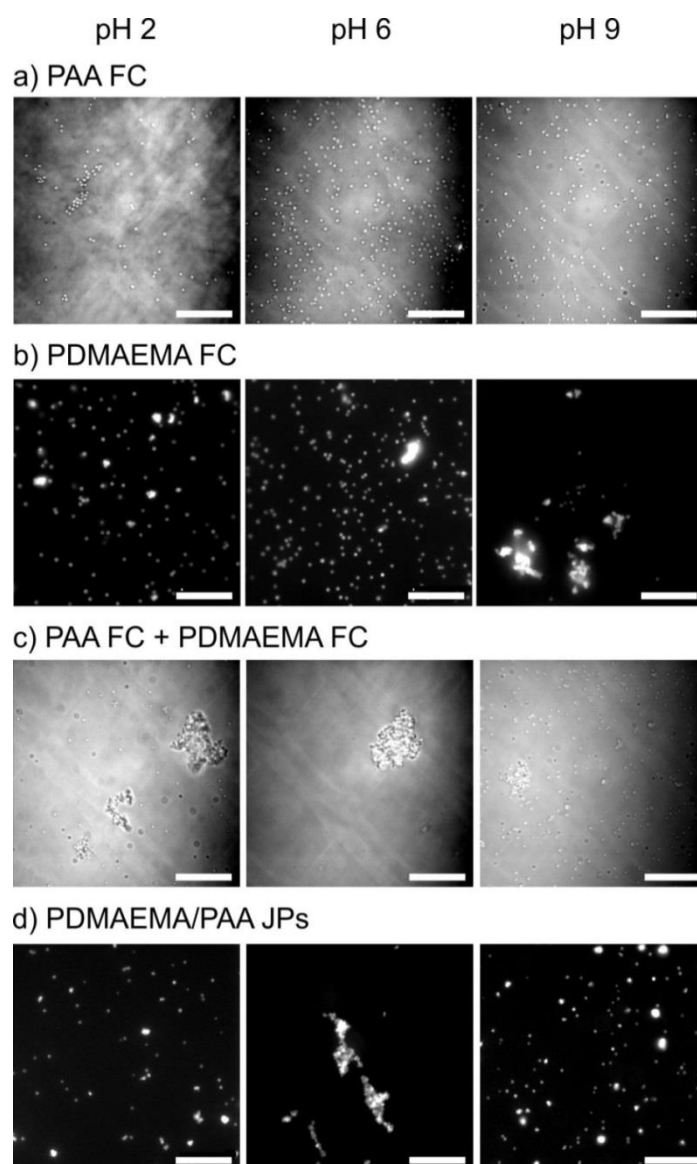


Figure R18. Representative fluorescence microscopy images of fully covered PAA (a), PDMAEMA (b), their mixture (c), and PDMAEMA/PAA-JPs (d) at different pH values. Scale bars: 20 μ m.

The assembly behavior of Janus particles is similar to that of the particle mixture (**Figure R18 d**, **Figure R19 d**). Many large aggregates are formed at pH 6 when both polymers are

charged and electrostatic interactions occur. At a low pH value we observed individual particles (ca. 20%), agglomerates formed by 2-5 particles (ca. 60%), as well as large agglomerates (8-20 particles, ca. 20%). We believe that small agglomerates are formed by Janus particles, which are oriented by their non-swollen part, which is PAA, towards each other.

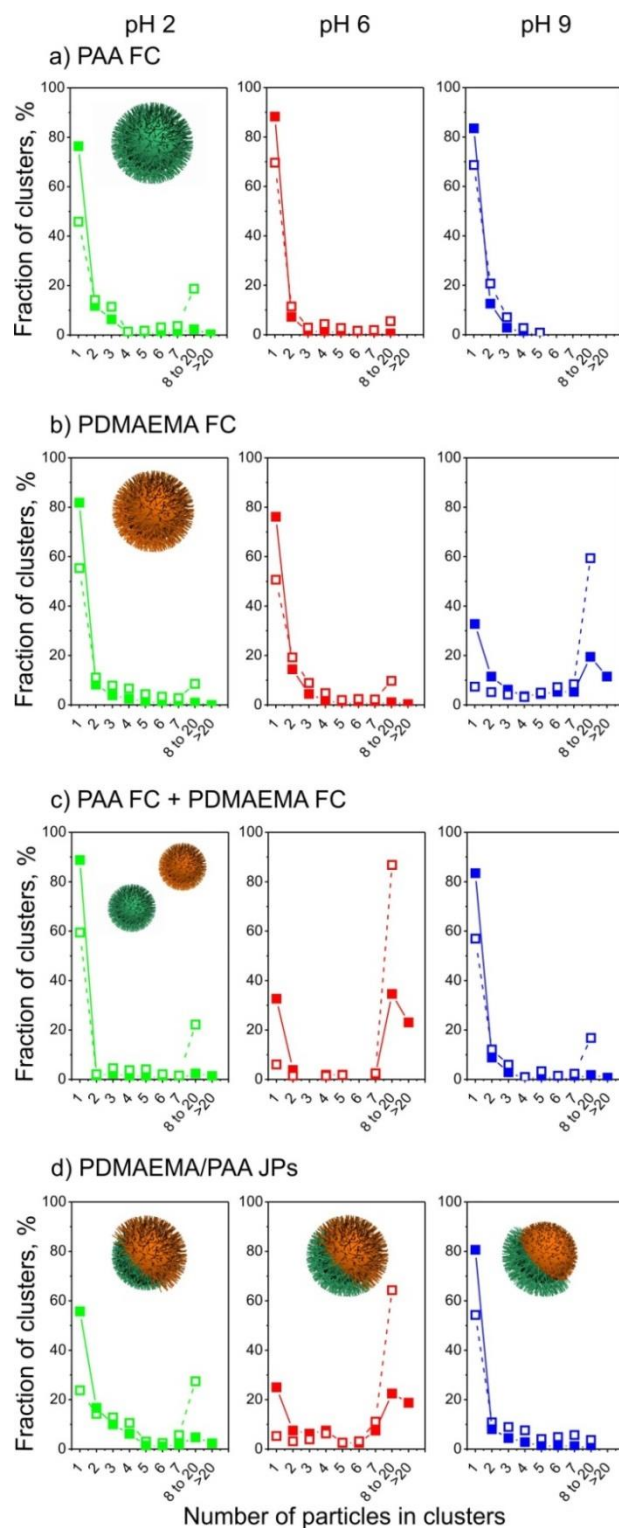


Figure R19. Aggregation behavior of charged colloidal particles (fully covered PAA (a), PDMAEMA (b), their mixture (c), and PDMAEMA/PAA-JP (d)) depending on the pH value. Solid points represent the number distribution of clusters, empty points – the mass distribution. Orange polymer in the cartoons – PDMAEMA, green – PAA.

We also found that PDMAEMA/PAA-JP tend to form chain-like aggregates in pure water dispersions due to the Janus character of the particles (**Figure R20**). Other kinds of particles (fully covered particles and their mixture) do not form such chains. We believe that the particle chains are formed when the PDMAEMA-covered side of one particle sticks to the PAA-covered side of the other particle. Further, we observed that unordered aggregates are formed in a salty solution. In fact, ions screen charged groups and reduce the coulombic interaction strength leading to a lower contrast between the two polymers, which most probably reduces the specificity of the particle binding to each other.

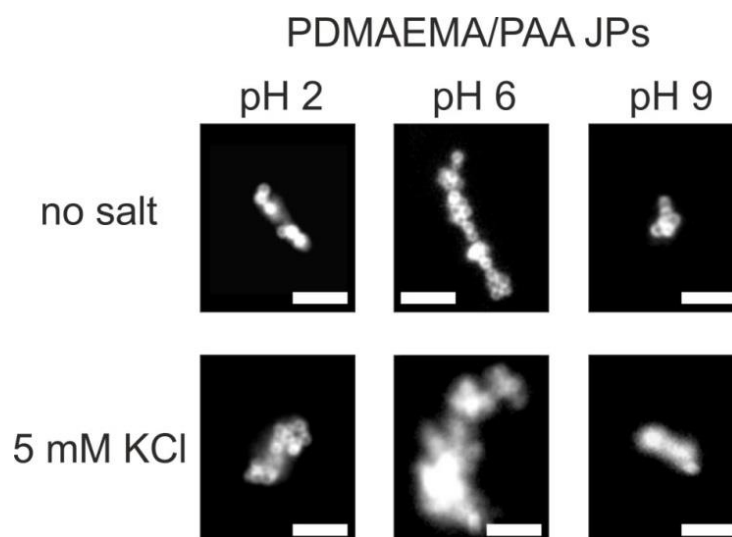


Figure R20. Representative fluorescence microscopy images of the structures formed by PDMAEMA/PAA-JP depending on the pH value and the ionic strength. Chain-like structures are observed in pure water. Scale bars: 5 μ m.

Next, we investigated the self-assembly behavior of amphiphilic JPs (PEG/PLMA-JP, PDMAEMA/PLMA-JP, and PDMAEMA/PS-JP) in water and toluene (**Figure R21**, **Figure R22**). We varied the hydrophilic polymers: in PEG/PLMA-JP the hydrophilic polymer is uncharged (PEG), while in PDMAEMA/PLMA-JP the hydrophilic polymer is charged (PDMAEMA). We also varied the hydrophobic polymer: in PDMAEMA/PLMA-JP the hydrophobic polymer is soft (PLMA, $T_g = -35^\circ\text{C}$), while in PDMAEMA/PS-JP the hydrophobic polymer is hard (PS, $T_g = 105^\circ\text{C}$). We first tested the aggregation behavior of colloidal particles fully covered by each of the polymers – PEG-FC, PDMAEMA-FC, PS-FC, and PLMA-FC – in water and toluene (**Figure R21/Figure R22 a-d**). We observed that the PEG-modified fully covered particles are dispersible in both water and toluene. The PDMAEMA-modified ones are dispersible in water and form aggregates in toluene. The PLMA- and PS-modified particles are dispersible in toluene and form large aggregates (non-dispersible) in water.

Furthermore, we found that the PEG/PLMA-JP are highly dispersible in both water and toluene, while a small amount of chain-like aggregates is formed (**Figure R21/Figure R22 e**). Dispersibility of PEG/PLMA-JP in toluene can easily be explained by the fact that both polymers are soluble in toluene. Dispersibility of PEG/PLMA-JP in water, where PLMA is non-soluble, can be explained by the fact that the area of the particles' surfaces covered with

PEG is considerably larger than that covered with PLMA (2:1 Janus ratio). As a result, PEG forms a shell around the particle core, which prevents the particles from aggregation. Small amount of particles form chain-like aggregates due to the sticking of PEG/PLMA-JP with their PLMA sides (**Figure R23**).

PDMAEMA/PS-JP and PDMAEMA/PLMA-JP demonstrate very similar aggregation behavior: aggregates with similar size distribution are observed in both solvents (**Figure R21/Figure R22 f-g**). In fact, PDMAEMA is a hydrophilic polymer, which swells in water, but, contrary to PEG, does not swell in toluene. This limits the dispersability of these particles in toluene, and JPs most probably form aggregates where they touch each other with their PDMAEMA sides. A similar situation is observed in water. In this case, hydrophobic polymers PLMA and PS prevent the dispersing of JPs, and they form aggregates where individual JPs touch each other with their hydrophobic sides (PS or PLMA).

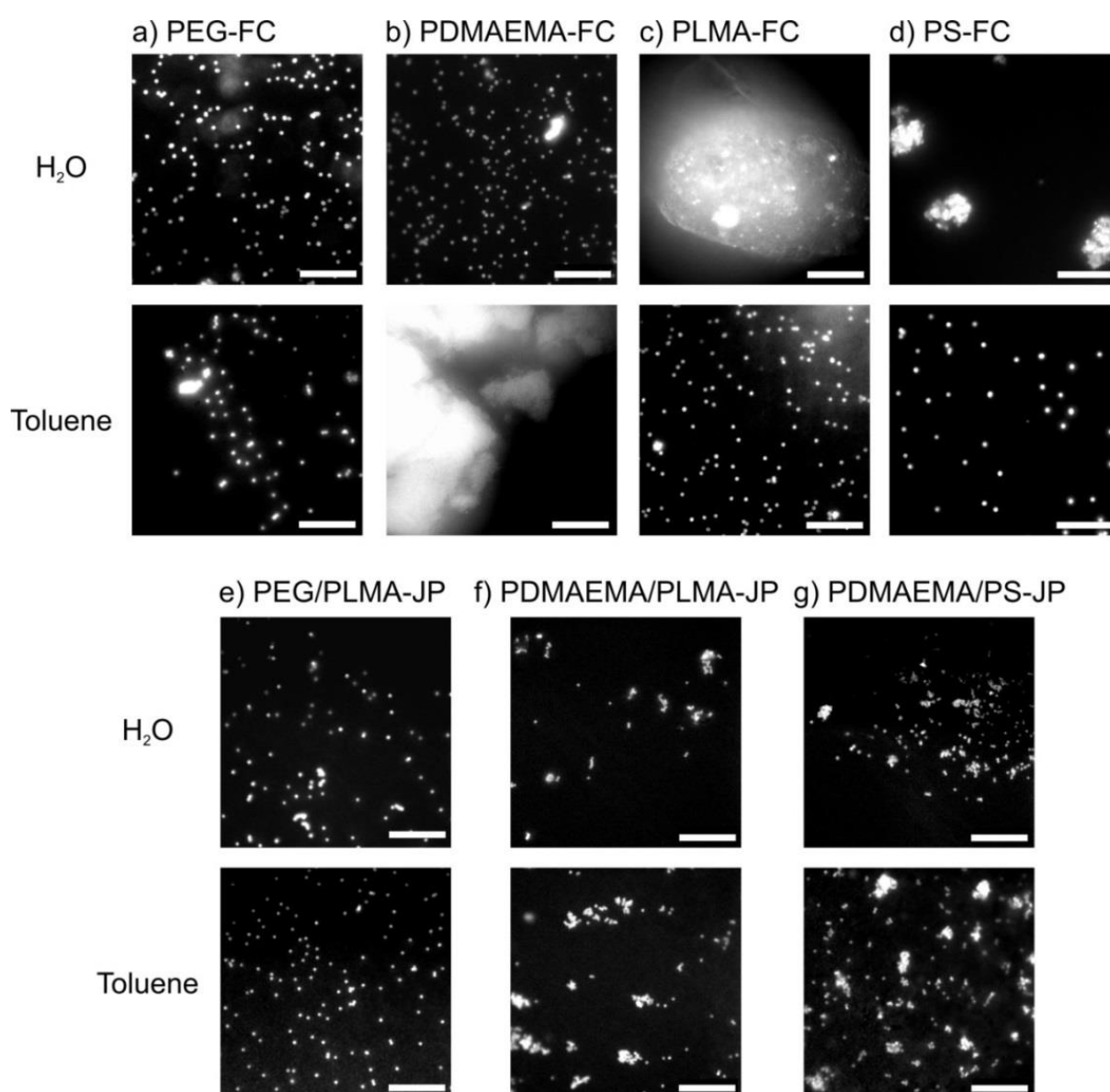


Figure R21. Representative fluorescence microscopy images of the reference PEG-FC (a), PDMAEMA-FC (b), PLMA-FC (c), PS-FC (d), and amphiphilic Janus particles: PEG/PLMA-JP (e), PDMAEMA/PLMA-JP (f), and PDMAEMA/PS-JP (g) in different media. Scale bars: 20 μm .

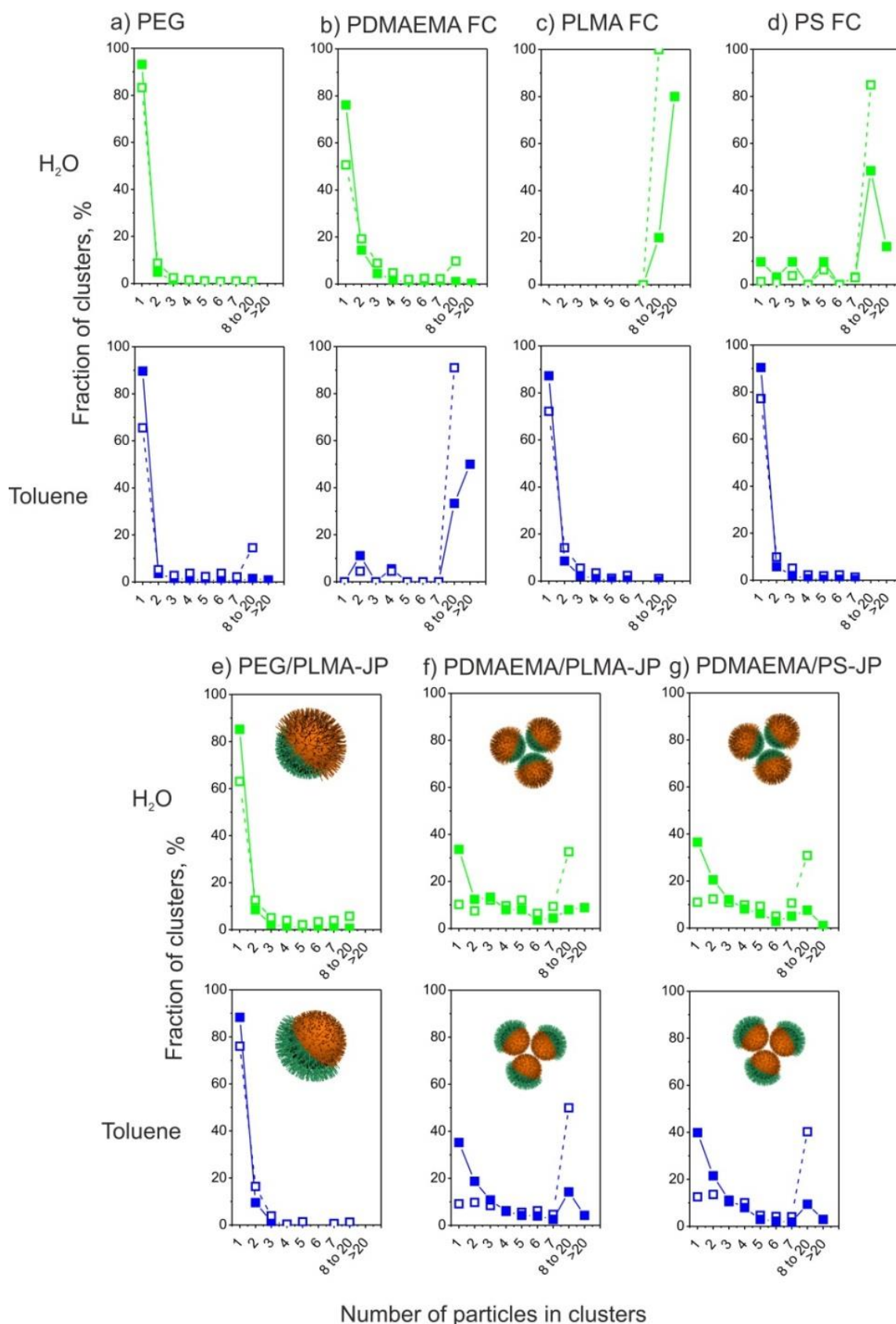


Figure R22. Aggregation behavior of the reference PEG-FC (a), PDMAEMA-FC (b), PLMA-FC (c), PS-FC (d), and amphiphilic Janus particles: PEG/PLMA-JP (e), PDMAEMA/PLMA-JP (f), and PDMAEMA/PS-JP (g) in DI water, or toluene (solid symbols – number distribution / open symbols – mass distribution). Orange polymer in the cartoons – PDMAEMA, green – PLMA or PS.

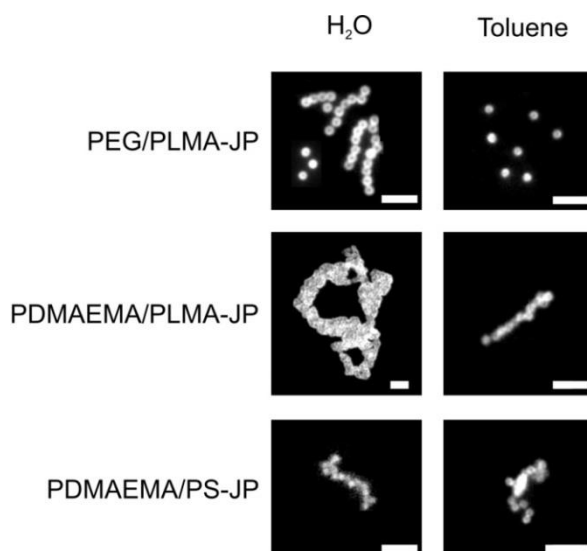


Figure R23. Representative fluorescence microscopy images of the structures formed by amphiphilic JPs depending on the media. Chain-like structures observed under all conditions. Scale bars: 5 μ m.

Notably, similar to PDMAEMA/PAA-JP, PDMAEMA/PLMA-JP and PDMAEMA/PS-JP form chain-like aggregates both in pure water dispersions and in toluene due to the Janus character of the particles (**Figure R23**). A proposed scenario for such aggregation behavior in water is illustrated in **Figure R24**. PEG/PLMA-JP and PDMAEMA/PLMA-JP Janus particles have one hydrophilic side, which is swollen in water, and one hydrophobic side. As a result, these particles tend to stick to each other with their hydrophobic sides in water (hydrophobic attraction) in order to minimize the unfavorable contacts between PLMA and water. This leads to the formation of linear chain-like agglomerates. The character of these agglomerates depends, however, on the kind of Janus particles. PEG/PLMA-JP form one-particle-thick chains, whereas PDMAEMA/PLMA-JP and PDMAEMA/PS-JP form thicker chains. We believe that due to the highly swollen state of PEG in water, it doesn't allow the particles to come too close to each other with their PLMA sides. As a result, the area of possible contact between the hydrophobic sides is reduced, which leads to the formation of linear chains (**Figure R24 a**).

In the case of PDMAEMA/PLMA-JP and PDMAEMA/PS-JP, a more complex aggregation behavior is observed due to the fact that PDMAEMA is swollen in water and positively charged. We believe that the particles still tend to touch each other with their hydrophobic sides; however, there are possibilities for them to have more neighboring particles due to the large size of the polymer patches. In the case of 'stickier' PLMA, larger structures are formed (**Figure R24 b**). When the electrostatic repulsion of the PDMAEMA sides is hindered by increasing the ionic strength, even larger linear structures are formed. A similar mechanism was observed in the work of Granick et al., where they used the same effects to construct linear 3D helical structures from amphiphilic particles, however, without hairy morphologies.⁸⁸

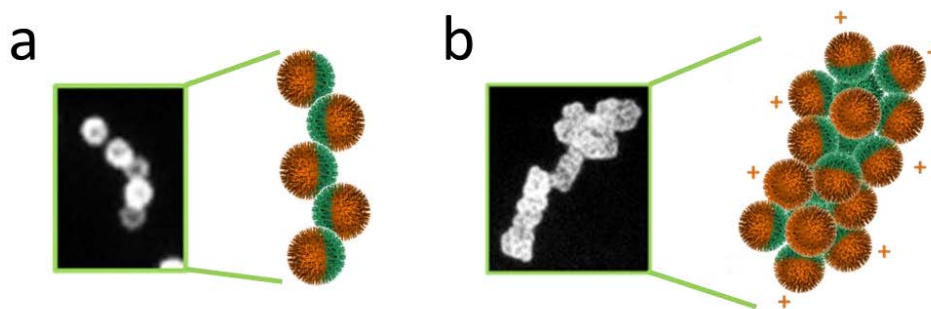


Figure R24. Proposed structures of the chain-like aggregates formed by PEG/PLMA-JP (a), and PDMAEMA/PLMA-JP (b) Janus particles in DI water: fluorescence microscopy images (analogous to **Figure R23**) and representative cartoons.¹⁷⁰

4.3.4. Summary

In summary, we have thoroughly investigated the assembly behavior of different kinds of functional hairy Janus particles. We systematically varied the nature of the polymers forming the Janus particle shell. For this purpose, we used hydrophilic positively (PDMAEMA) or negatively (PAA) charged, and uncharged (PEG), as well as different hydrophobic (PLMA, PS) polymers. Homogeneously decorated particles served as a reference in the experiments. We investigated and compared the aggregation behavior of different homogeneously decorated particles, their mixtures, and Janus particles. Ultimately, we found that homogeneously decorated particles form aggregates in the solvents or at pH values where the polymer chains forming the shell are not soluble, or collapsed. The mixture of oppositely charged particles (PAA-FC and PDMAEMA-FC), and PDMAEMA/PAA Janus particles demonstrated very similar aggregation behavior in an aqueous environment at different pH values, however, the difference between the aggregation behavior of mixed particles and the Janus ones is in the shape of the aggregates: a mixture of particles formed unordered large aggregates, while the Janus particles formed chain-like structures. Amphiphilic hairy Janus particles covered with hydrophilic and hydrophobic polymers (PEG/PLMA-JP, PDMAEMA/PLMA-JP, and PDMAEMA/PS-JP) also formed chain-like structures with different thicknesses in water and organic solvents (toluene). Such ordered structure formation indicates on the unique features of the Janus particle assembly compared to the homogeneous particles, which typically form unordered aggregates, and opens new paths into the programmed development of specially designed materials.

Conclusively, the results of the self-assembly experiments indicate that the understanding of the Janus particle assembly is crucial for the programmed formation of desired structures. The main advantage of the hairy polymer shells used in the design of the Janus particles is their stimuli-responsive properties, which allow for a reversible assembly of the building blocks. Moreover, the Janus particles we used can be easily prepared on a large scale, thus, opening even more perspectives for the applications of the assembled nanoclusters.

4.4. MATERIALS BASED ON HYBRID HAIRY JANUS PARTICLES

There are numerous works concerning the synthesis of Janus particles with various architectures. Many studies are devoted to the investigation of the (self-) assembly behavior of the Janus particles. Notably, much less works are published regarding the applications of the synthesized Janus particles, especially their application for the design of new multifunctional materials. Therefore, our goal was to go deeper into the design of materials based on our developed hybrid hairy Janus particles. Three examples will be shown in this context: Janus particles with immobilized metallic nanoparticles for catalytic applications, and (multi) functional surfaces prepared with Janus particles for anti-icing and anti-fouling applications.

4.4.1. Janus Particles for Catalytic Applications

4.4.1.1. Motivation

Recently, nanocatalysts with advanced tunable architectures of different sizes and compositions have attracted significant attention.¹⁷¹⁻¹⁷³ Consequently, the Janus geometry could be applied to the catalysts to provide them with a higher and thus sufficient level of heterogeneity required to address the problems of stability, recovery, reuse, etc. The spatial isolation of catalytic species on a Janus particle could provide direct access to reactants, and hence opens new paths in the field of interfacial and simultaneous catalysis.

Janus geometries have already been previously used for the design of novel solid catalysts.¹⁷⁴⁻¹⁸² The concept of Janus-type solid catalysts is particularly advantageous in the field of interfacial catalysis due to the high interfacial energy, and thus excellent emulsion-stabilizing properties of the Janus particles.^{82, 183} Another advantage is an easy recovery of such catalysts from the reaction mixtures, which makes them recyclable. Additionally, high interfacial area provided by the Janus particles can facilitate better conversion and mass transfer between phases.

Despite the diversity of JPs used for catalytic applications, it must be noted that all of the above mentioned examples consider the so-called “bare” JPs, that is, particles that do not have “hairy” polymer shells (or polymers, for that matter) involved in their final design. Nevertheless, the role of the polymer could be very important in the creation of novel hybrid Janus catalysts. Firstly, polymer shells with a high contrast in hydrophobicity on the opposite sides of the JPs would increase their affinity towards different phases (e.g. oil and water) in an emulsion (interfacial catalysis), thus stabilizing it to a higher extent than the corresponding bare particles.¹⁶⁰ Secondly, the “hairy” polymeric architectures and their ability to swell and de-swell could provide a better distribution of the catalytic NP species throughout the catalyst surface, and hence allow better substance transport to the catalyst, and higher reaction rates. Thirdly, stimuli-responsive polymers can be used as shells, which would allow a great extent of control over the reaction, for example, inducing or, on the contrary, blocking the catalytic

activity would be possible upon external stimuli. Finally, if grafted to an inorganic core, polymer shells would increase the complexity of the Janus catalyst, making its architecture well-defined, hybrid, and robust, thus, providing the catalyst with a high level of heterogeneity required for successful heterogeneous catalysis.

Therefore, we have designed an advanced hybrid hairy Janus-type catalyst, which comprises an inorganic silica core covered with two distinct polymeric shells (hydrophilic and hydrophobic) on its opposite sides, while the catalytic species (in our case silver or gold NPs) are immobilized directly into the hydrophilic stimuli-responsive polymer shell. The role of the hydrophilic polymer is to ensure a homogeneous distribution of the NPs throughout its hairy chains upon swelling in water, thus providing better substance transport possibilities. On the other hand, the role of the hydrophobic polymer is to provide the catalyst with amphiphilicity, and to alleviate its use for interfacial catalysis. The prepared hairy hybrid JP-NP complex is directly visualized through TEM and cryo-TEM. Furthermore, its catalytic performance is tested by applying it in several benchmark reactions, such as the reduction of Methylene Blue, Eosin Y and 4-nitrophenol.

4.4.1.2. Experimental Part

Energy-dispersive X-ray spectroscopy (EDX) / SEM: The elemental maps of the particles suspended on a TEM grid were acquired with a scanning electron microscope (SEM) Ultra 55 (Carl Zeiss Microscopy GmbH, Oberkochen, Germany) equipped with a Quantax XFlash 5060 energy dispersive X-ray spectrometer (Bruker Corporation, Billerica (MA), USA). The SEM was operated at an acceleration voltage of 6 kV, and a transmitted electron (TE) detector was used for imaging.

Ultraviolet-visible (UV-Vis) spectroscopy: UV-Vis spectroscopy was performed with Thermo Genesis 6 equipment using standard quartz glass vials with an optical path of 1 cm.

General procedure for the incorporation of metal nanoparticles: The 200 nm large SiO₂-PAA/PS-JP Janus particles were synthesized as described in Section 3.2.3. In a typical procedure of metal nanoparticle incorporation, 40 mg of the prepared PAA/PS-JP were dispersed in 40 ml of deionized water and sonicated for 10 min. The suspension was left to swell for additional 48 h. Afterward, the mixture was placed in an ultrasonic bath for 5 min, 5 ml of a 10 mM AgNO₃ aqueous solution (5 mM solution was used in the case of H[AuCl₄]) were added in a single portion, and stirring was continued for 5 min. Next, 1 ml of triethylamine was added to the mixture in a single portion, which caused the suspension to change its color from colorless to brown (Ag), or deep violet (Au). Upon the addition of triethylamine, metal ions were reduced, and the respective nanoparticles (Ag or Au NPs) were formed and stabilized within the PAA part of the PAA/PS-JP. The reaction mixture was stirred for 12 h and was then centrifuged (5000 rpm, 20 min). The supernatant colored solution was discarded and the remaining solid was washed with deionized water (10 ml) and

centrifuged again. Then the remaining solid was dispersed in 40 ml of water. This suspension was further used for the catalytic experiments.

General procedure for the catalytic reduction of dyes: 0.25 ml of the Ag-functionalized PAA/PS-JP suspension were added to a mixture of 40 ml of the specific dye (Methylene blue or Eosin Y) 10^{-5} M aqueous solution, and 2 ml of freshly prepared aqueous sodium borohydride (0.1 M) solution. Immediately after the addition, samples were taken each minute and analyzed by UV-Vis spectroscopy, until the measured absorbance reached a constant value.

General procedure for the catalytic reduction of 4-nitrophenol: The appropriate reactions were performed in the same manner as for the dye reduction experiments stated above using the Au-functionalized PAA/PS-JP suspension at a temperature of 40 °C.

4.4.1.3. Results and Discussion

Synthesis of hybrid hairy PAA/PS-JP: Janus particles with a silica core diameter of 200 nm and a shell consisting of two polymers – hydrophilic PAA and hydrophobic PS – on the opposite sides of the particles were synthesized through a combination of “grafting from” and “grafting to” approaches, as described in Section 3.2.3. After grafting the first polymer (PAA) onto the modified silica particles, the mono-component JPs were characterized by cryo-TEM. It can be clearly seen from the images (**Figure R25**) that the particles have a Janus character, that is, PAA was selectively grafted onto one side of the silica particles. PAA/NH₂-JP were investigated at a high pH value (pH 10) to ensure the swelling and better visualization of the PAA polymer chains. The thickness of the swollen PAA layer at pH 10 was found to be 50 ± 10 nm. It was also concluded that the particles mostly have a 1:1 Janus ratio (area covered with PAA : area covered with PS). The grafting density of the polymer chains on the silica particle surface obtained from thermogravimetric analysis (TGA) and gel permeation chromatography (GPC) results is 0.2-0.3 chains/nm².

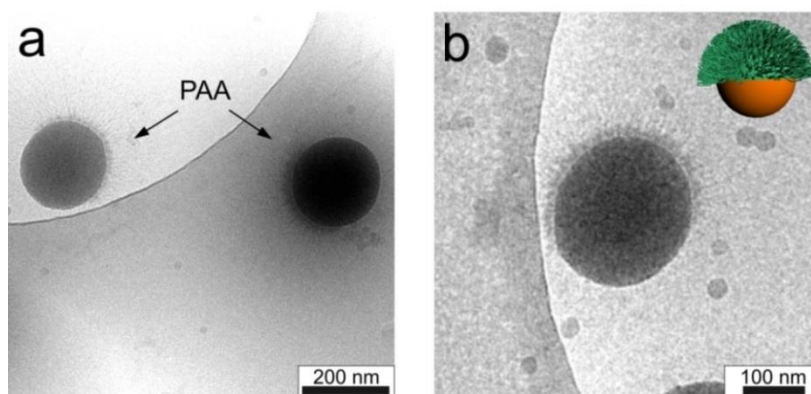


Figure R25. Representative cryo-TEM images at different magnifications of the synthesized 200 nm hybrid hairy PAA/NH₂-JP: (a) two representative polymer-decorated Janus particles; (b) close-up image of one polymer-decorated Janus particle.

Modification of JPs with metal nanoparticles: Metal nanoparticles (Ag or Au NPs) were selectively immobilized into the PAA shell of the PAA/PS-JP, and the resulting hybrid JP-NP systems were subsequently used to catalyze different reactions (**Figure R26**).

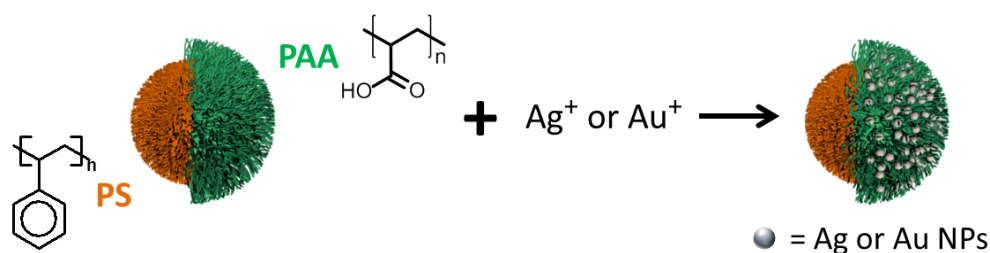


Figure R26. Scheme of the selective NP immobilization onto PAA/PS-JP for catalytic applications.¹⁸⁴

The prepared 200 nm PAA/PS-JP were immersed in deionized water and left to swell for 48 h. After that the particles were again re-dispersed by sonication and treated with 10 or 5 mM solutions of the respective metal source (AgNO₃ or H[AuCl₄]). Triethylamine was added to this mixture, which initiated the reduction process, as indicated by a color change from colorless to brown (silver) or dark violet (gold). The suspensions were stirred for 12 h and then the metal NP-functionalized JPs were separated by centrifugation, washed and re-dispersed in water (see Section 4.4.1.2. for a more detailed procedure).

Broad absorption bands at 432 nm and 533 nm were observed, which are characteristic for the plasmon resonance of silver and gold NP (**Figure R27**),¹⁸⁵⁻¹⁸⁸ respectively, and therefore, indicate on the successful formation of these nanostructures.

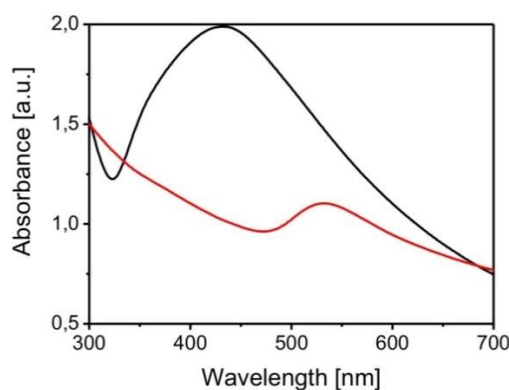


Figure R27. Plasmon resonance bands measured in a diluted sample of the respective NP-functionalized PAA/PS-JP (solvent water; Ag: black curve; Au: red curve).

Characterization of the modified JPs: The formation of metal NPs on the PAA/PS-JP was confirmed by transmission electron microscopy (TEM) measurements (**Figure R28 a, b**). Considering the obtained images, the formation of NPs with mean diameters of 12 ± 4 nm for Ag, and 15 ± 6 nm for Au was observed. A broad particle size distribution was characteristic for both metals, which can be attributed to the diffusion of further metal ions from the surrounding solution through the swollen polymer, and has been observed for similar polymeric stabilizers as well.^{189, 190}

Additionally, TEM images revealed selective localization of the corresponding NPs in the PAA shell of the JPs (**Figure R28 a, b; Figure R29 a, b**). The PS-coated side of the PAA/PS-JP is hydrophobic, and PS does not swell upon immersing the particles in water. On the other hand, the PAA-coated side is hydrophilic, and PAA swells in water. The swelling range of PAA is between pH 4 and pH 10. However, a complete swelling is expected in the pH range from 7 to 10. The modification of JPs was conducted in deionized water at a pH value of 7-8, because of the triethylamine addition. The swelling/deswelling of polymers has led to an intercalation of metal ions within the hydrophilic polymer (PAA), which is also influenced by the incorporated carboxylic acid groups acting as a linking moiety.¹⁹¹

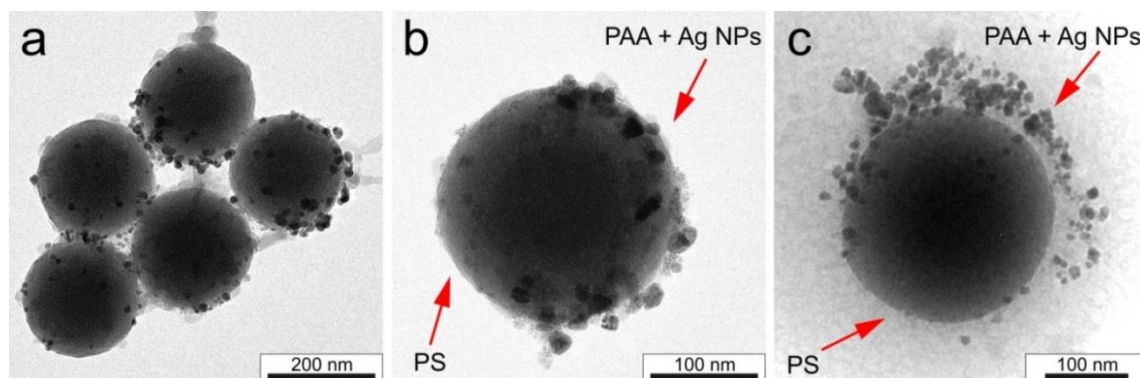


Figure R28. Characterization of hybrid hairy Janus catalysts: representative TEM (a, b) and cryo-TEM (c) images of PAA/PS-JP with selectively immobilized Ag NPs in the PAA shell.

Cryo-TEM images of the corresponding samples revealed the distribution of NPs in the PAA polymer shell (**Figure R28 c, Figure R29 c, and Figure R30**). At pH 7-8 the PAA chains are stretched out, and therefore the NPs are adsorbed throughout the length of the polymer chains. Due to their amphiphilicity, the JPs sometimes assemble in clusters in water, and it could be clearly seen that they face each other with their PS sides (hydrophobic attractions), leaving the metal NPs in the PAA shell on the outer contour of the clusters (**Figure R30 a-c**). When visualizing single particles, selective functionalization of the JPs with the metal NPs could again be observed (**Figure R28 c and Figure R30 d**).

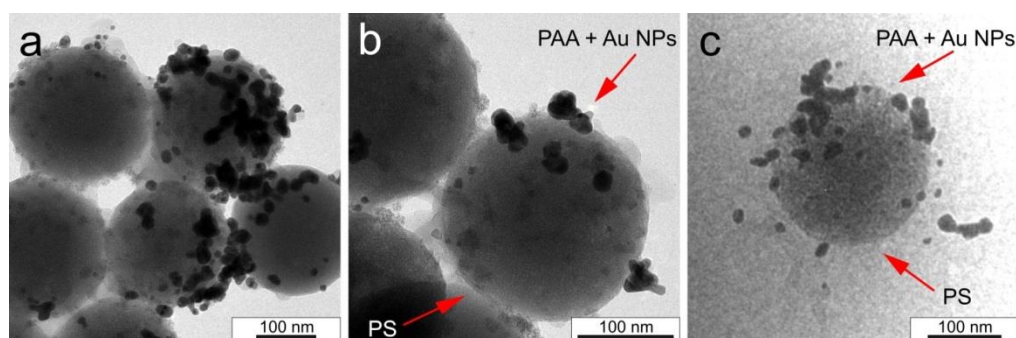


Figure R29. Representative TEM (a, b) and cryo-TEM (c) images of Au NPs immobilized selectively into the PAA shell of the PAA/PS-JP.

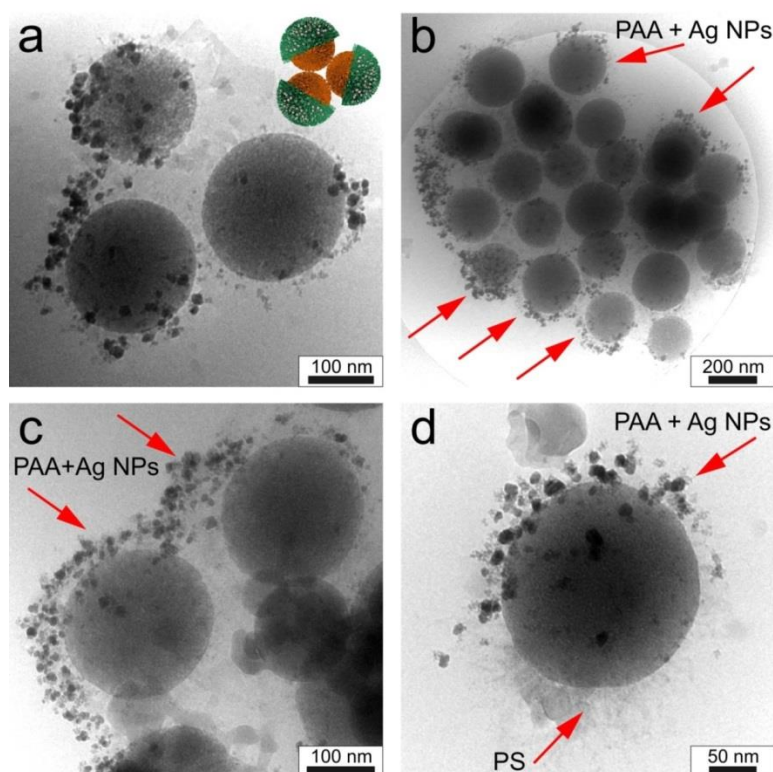


Figure R30. Representative cryo-TEM (a-d) images of Ag NPs immobilized selectively into the PAA shell of PAA/PS-JP. Formation of clusters was observed (a-c), where the swollen PAA shell with incorporated Ag NPs is facing outwards (see inset in a).

DLS measurements of the PAA/PS-Ag-JP catalyst system at different pH values revealed the stimuli-responsive behavior of the PAA brush (**Figure R 31**). At pH 2 aggregation of the particles is observed due to the collapsed state of the PAA chains. The situation completely changes starting from pH 7, at which the PAA polymer is fully swollen, therefore preventing the aggregation of the JPs due to electrostatic and steric effects. At pH 10 the same tendency to form single particles instead of aggregates is observed. The results correlate perfectly with the stimuli-responsive behavior of JPs without the adsorbed NPs.⁷⁵ Thus, the immobilized Ag nanoparticles do not hinder the stimuli-responsive behavior of the PAA brush, and the polymer provides a good distribution of the metallic NPs throughout its chains when in a swollen state (as confirmed by the cryo-TEM measurements, **Figure R28 c** and **Figure R30**).

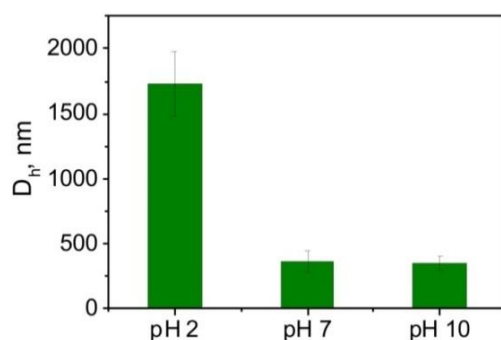


Figure R 31. Dependence of the hydrodynamic diameter D_h on the pH values of the PAA/PS-Ag-JP dispersion measured by DLS (original size of PAA/PS-Ag-JP in the dry state was 200 nm).

The role of the polymers is crucial in our hybrid Janus catalysts. The catalytic species (Ag or Au NPs) are specifically located in the hydrophilic hemisphere of the JPs. The hydrophilic PAA thus provides a very good distribution of the nanoparticles in its chains, which swell upon immersion in water. Such distribution prevents the metal NPs from aggregation, and provides better substance transport to the catalyst. In addition, PAA is a stimuli-responsive polymer, and its stimuli-responsive behavior could be further used for a precise control of the catalytic activity of our catalyst. Hydrophobic PS, on the other hand, provides the JPs with a high contrast in hydrophobicity at their opposite sides (advancing water contact angle on PAA-modified substrates is $58 \pm 2^\circ$, receding contact angle: $14 \pm 2^\circ$; on PS: $100 \pm 2^\circ$, and $77 \pm 2^\circ$, respectively), which makes them perfect candidates for emulsion stabilization in interfacial catalysis.

EDX analysis of the PAA/PS-Ag-JP sample was performed in order to confirm the chemical composition of the metal NPs (**Figure R32**). EDX mapping of silver revealed a contrast in the places, where the NPs were adsorbed (**Figure R32**). The spectrum of area 1 shows a clear Ag signal. The gold signal comes from the TEM grid, as gold TEM grids with a carbon film were used for the experiments.

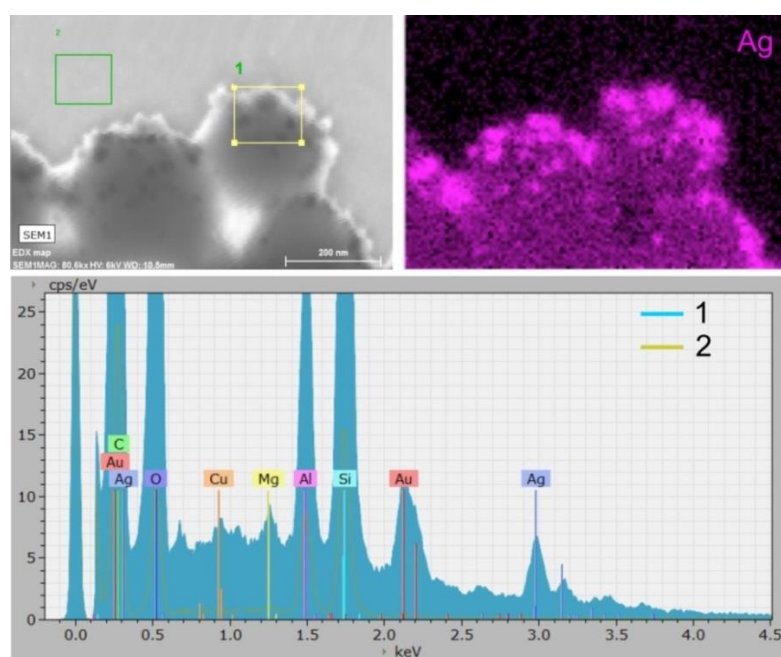


Figure R32. EDX analysis of PAA/PS-Ag-JP. Upper left panel: STEM image of the particles; upper right: Ag mapping; lower panel: EDX spectrum of areas 1 and 2.

Further, we have prepared emulsions stabilized either by the PAA/PS-Ag-JP catalyst system, or by the reference PAA-modified fully covered (PAA FC) particles (**Figure R33**) at pH = 7. Photographs directly after emulsion preparation show that the emulsion stabilized by the homogeneously decorated PAA FC particles already started to disintegrate, revealing a phase separation between the oil and water (**Figure R33 a**). On the other hand, the emulsion stabilized by the Janus PAA/PS-Ag-JP catalyst remained stable. Light microscopy images of the emulsion show that the emulsion droplets in the case of PAA FC are much bigger if compared to the homogeneously distributed small droplets in the case of PAA/PS-Ag-JP

Janus-based system (**Figure R33 b**). These results indicate that the developed Janus JP-NP catalyst is perfectly suitable for emulsion stabilization, and therefore for the future use in interfacial catalytic reactions. The addition of an acidic solution (pH=2) leads to a rapid destabilization of the emulsion with JPs, which results in the formation of a layered structure and an increase in the droplet size (**Figure R33 c**). The emulsion is destabilized at pH=2, because PAA is in its less hydrophilic non-dissociated form.

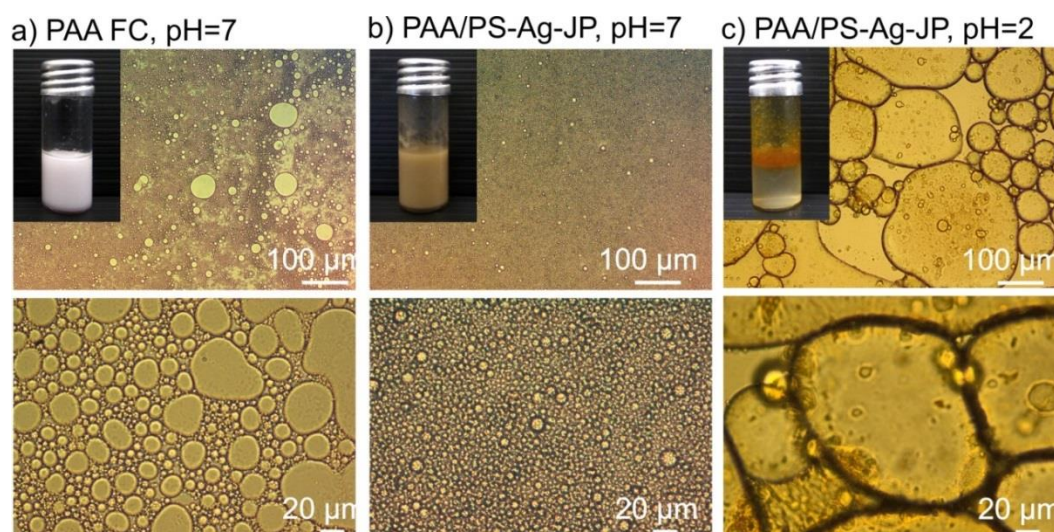


Figure R33. Representative photographs and light microscopy images at different magnifications of the emulsions prepared with fully covered PAA-modified 200 nm large particles (a), as well as the Janus PAA/PS-Ag-JP catalyst system at pH 7 (b), and pH 2 (c).

Catalytic reduction of dyes: To investigate the accessibility of the immobilized metal nanoparticles, the reduction of two different dyes (Methylene Blue = MB, eosin Y = EOY) as convenient benchmark systems was applied. For instance, a schematic illustration of the Methylene Blue catalytic reduction is shown in **Figure R34 a**. In a typical procedure, a 10^{-5} M aqueous solution of the respective dye was mixed with a freshly prepared 0.1 M sodium borohydride solution and stirred for 1 min. Afterwards, 0.25 ml of the respective Janus particle suspension (0.33 mg of particles) were added, and then samples were taken at 30 s (60 s for EOY) intervals and analyzed by UV-Vis spectroscopy. The natural logarithm of the observed absorbance was plotted over the elapsed time. After linear fitting, the specific k values were accessible from the slope of the obtained regression curve. Regarding the obtained results, a complete reduction was observed for both dyes (**Figure R34 b-d** and **Figure R35 a**). The difference between the obtained k values for MB (0.017 s^{-1}) and EOY (0.42 s^{-1}) can be explained by the interactions of the acidic PAA matrix with the deprotonated dye functionalities. Regarding the logarithmic plot for the Eosin Y experiment, an initiation phase was observed (**Figure R34 d**). We suppose that the diffusion of EOY through the PAA matrix takes longer than for MB, since the interactions between the acidic PAA and the deprotonated groups of EOY are possible. Therefore, the rate constants were only determined in the linear region. In comparison, MB does not show a similar behavior, which means the reduction process of MB starts from the very beginning of the reaction. Furthermore, the

decomposition of the herein reported systems is tremendously increased compared to silver nanoparticles deposited on, for example, plain silica spheres.¹⁹²

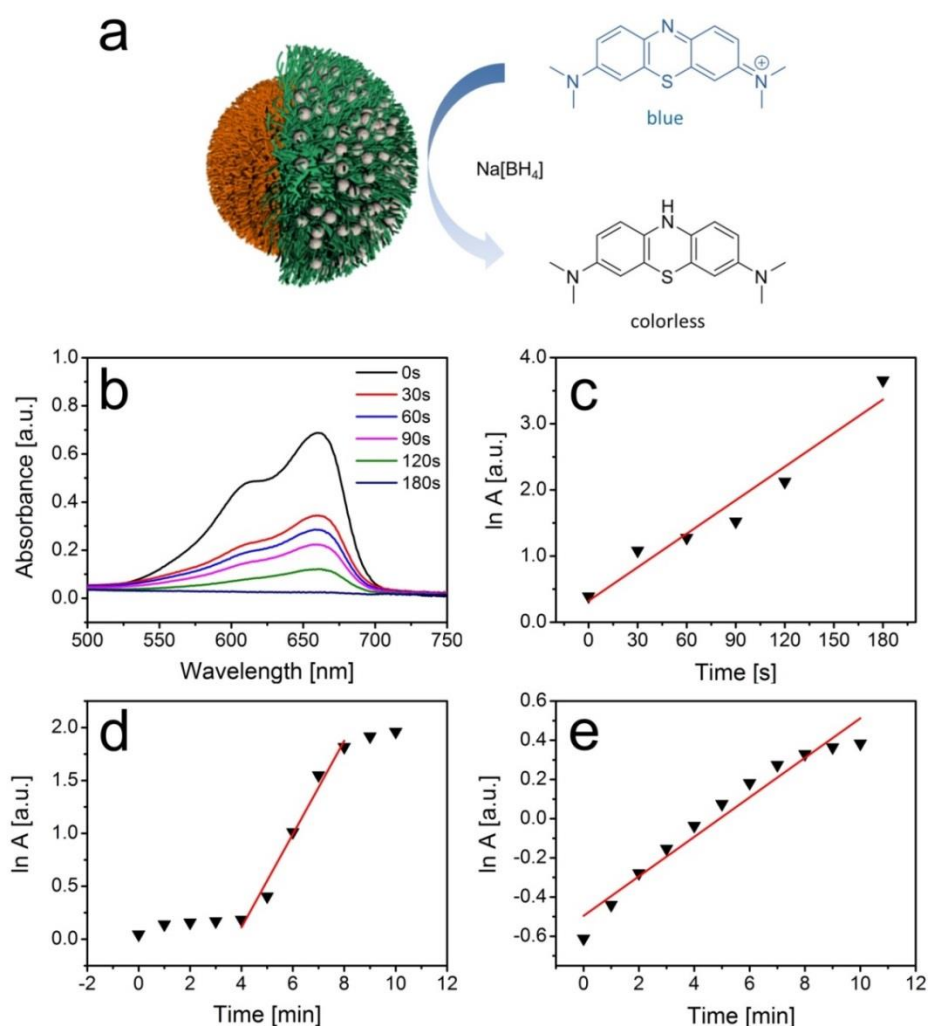


Figure R34. (a) Schematic illustration of the catalytic Methylene Blue reduction with sodium borohydride in the presence of Ag NP-modified PAA/PS-JP; (b) UV-Vis spectra of the catalytic Methylene Blue reduction; logarithmic plots of the decreasing absorbance over elapsed time for the catalytic reduction of Methylene Blue (c), and Eosin Y (d) in the presence of Ag NP-modified PAA/PS-JP; (e) logarithmic plot of the decreasing absorbance over elapsed time for 4-nitrophenol reduction catalyzed by Au NP-functionalized PAA/PS-JP.

The catalytic reduction of 4-nitrophenol was conducted in a similar manner as described above (reduction experiments with dyes), with the only difference being that these experiments were carried out at a higher temperature (40 °C). A successful reduction of 4-nitrophenol was observed for the Au-functionalized JPs (**Figure R34 e**, **Figure R35 b**). The observed k value of this reaction ($k_{app} = 0.101 \text{ s}^{-1}$) must be considered as apparent, since the concentration of sodium borohydride has an influence on k (as described in the reference)¹⁹³. Therefore, the comparison with other systems, such as, for example, bimetallic nanoparticles,¹⁹⁴ or Au particles deposited on ceria,¹⁹⁵ is difficult. Nevertheless, the observed k_{app} value is somewhat smaller than for the reported systems, but the reduction takes place with smaller amounts of the catalyst.

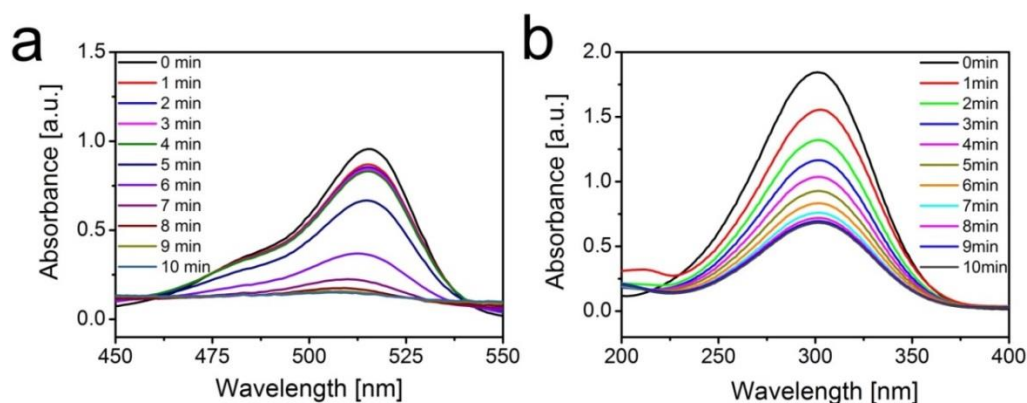


Figure R35. UV-Vis spectra of the catalytic (a) Eosin Y, and (b) 4-nitrophenol reduction in the presence of Ag NP-functionalized (a) or Au NP-functionalized (b) PAA/PS-JP, respectively.

Finally, we demonstrated a combination of the abilities of PAA/PS-Ag-JP to stabilize emulsions and catalyze the reduction of dyes (**Figure R36**). For this purpose, we prepared a water-oil emulsion stabilized by PAA/PS-Ag-JP, which also contained the Eosin Y dye. The emulsion is stable and red because of the dye (**Figure R36 a**). The addition of NaBH_4 leads to a rapid disappearance of the red color due to the reduction of the dye. Moreover, the emulsion was destabilized (**Figure R36 b**), and the pH of the emulsion became around 10. We neutralized the excess of NaBH_4 in the emulsion with an acid to get pH=6 and re-emulsified it again by ultrasonication. The formed emulsion was stable (**Figure R36 c**). Ultimately, we centrifuged the emulsion (**Figure R36 d**) and got separate layers of water and oil (**Figure R36 e**). The PAA/PS-Ag-JP precipitated at the bottom of the tube and at the interface between the liquid phases, which demonstrated the possibility of the successful JP recovery.

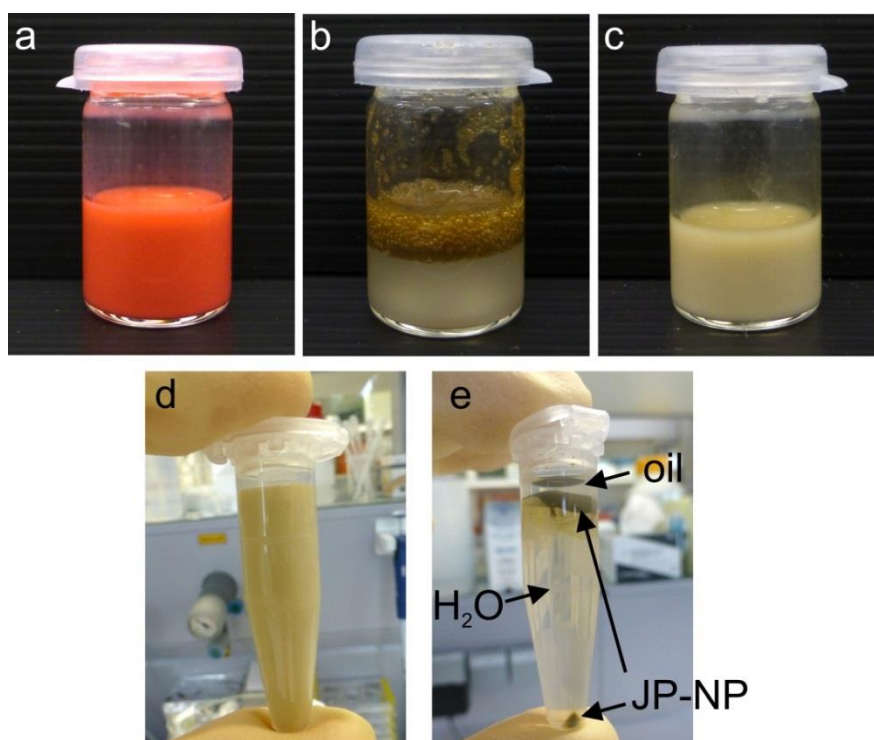


Figure R36. Reduction of Eosin Y in an emulsion stabilized by PAA/PS-Ag-JP: photographs of (a) water-oil emulsion stabilized by PAA/PS-Ag-JP and containing Eosin Y; (b) the same emulsion after the addition of NaBH_4 and 10 minutes of incubation; (c) and (d) – redispersed emulsion at pH = 6 after the reduction of Eosin Y; (e) emulsion from (d) after centrifugation.

4.4.1.4. Summary

Within this part of the work, a novel type of hybrid hairy Janus catalyst comprising a silica core along with two types of polymer shells on its opposite sides (hydrophilic PAA and hydrophobic PS) has been designed. We have demonstrated successful selective functionalization of such amphiphilic Janus particles with either Ag or Au nanoparticles, which could be achieved in a straightforward manner. As a result, the catalytic species were localized selectively in the hydrophilic PAA-covered hemisphere of the hairy Janus particles, which was confirmed by EDX, TEM, and cryo-TEM analysis. The synthesized JPs with incorporated metallic nanoparticles demonstrated high interfacial activity and efficient stability of water-oil emulsions that can be tuned by pH. Furthermore, the accessibility of Ag and Au NPs was demonstrated by applying convenient benchmark reactions like the reduction of Methylene Blue, Eosin Y, and 4-nitrophenol. A successful and effective reduction of two dyes, and a nitro compound with extremely low amounts of catalyst was conducted. Finally, we demonstrated that such Janus catalysts are particularly promising for interfacial catalysis. Thus, the significant advantages of the use of JPs with immobilized metallic nanoparticles are: (1) JPs effectively stabilize emulsions, (2) the emulsion can be destabilized by utilizing the responsive properties of the JPs, and (3) JPs can easily be recovered after the reaction and reused again.

4.4.2. Janus Particles as Building Blocks for (Multi-) Functional Coatings

4.4.2.1. Anti-Icing / Deicing Coatings

4.4.2.1.1. Motivation

The development of surfaces with reduced icing or easy deicing is of paramount importance for the wind turbine technology, automotive and aircraft industry. In fact, inhibition of the ice layer formation allows not only a consequent reduction of costs, but also decreases the number of emergency situations. The commonly used methods for the prevention of icing and promotion of deicing are based either on electrical heating of the surfaces, which results in simple ice melting, or on the use of antifreeze substances, which reduce the water freezing temperature. Nonetheless, the most favorable solution of this problem, which is now broadly explored, is the design of passive anti-icing coatings, i.e. coatings, which prevent icing and do not require power consumption.¹⁹⁶⁻¹⁹⁸

There are few main strategies for the design of such passive anti-icing coatings. One of them is based on the lowering of the ice adhesion. Reduced ice adhesion can be achieved by the fabrication of hydrophobic¹⁹⁹ or superhydrophobic surfaces,²⁰⁰⁻²⁰⁷ or the use of hydrophobic lubricants.²⁰⁸ In the first case (hydrophobic and superhydrophobic surfaces) the contact area between the surface and ice is simply reduced.²⁰⁹⁻²¹¹ In fact, superhydrophobic materials demonstrate good anti-icing properties, but once an ice layer is formed, it can hardly

be removed. Removal of the ice layer can also lead to a loss of the superhydrophobic properties. In the second case (hydrophobic lubricants), ice can easily be removed because of the hydrophobic lubricant softness.^{203, 208, 212, 213} Moreover, superhydrophobic surfaces are not always ice-repellent, especially when the size of the features is large and water droplets can penetrate between them.²¹⁴ The use of oily liquids as anti-icing materials is also not favorable due to their insufficient mechanical stability. Another anti-icing strategy is based on the inhibition of the ice growth. Reduced ice growth can be achieved in two ways. The first way is to utilize the colligative properties of solutions.^{215, 216} For example, hydrophilic polymers reduce the freezing point of water, and ice crystals can simply slide off due to the presence of an unfrozen water layer.²¹⁷ The second approach is to employ antifreeze proteins, which kinetically decrease the point of ice crystal formation.²¹⁸ Nevertheless, the disadvantage of such hydrophilic materials is a very fast growth of ice crystals on their surface.

In other reports, condensation and freezing phenomena of microscopic droplets were analyzed on the micro-patterned topographical surfaces.^{211, 219, 220} Hatton et al. demonstrated that topographical control over water condensation and freezing was achieved at the micrometer scale via the deposition of hydrophilic polymers and particles on the tips of selected patterned, superhydrophobic surfaces.²¹¹ Indeed, the hydrophilic/hydrophobic heterogeneity and roughness allow a controlled nucleation and growth of ice crystals.^{219, 220} Commonly, the photolithographic approach was used for the fabrication of such patterned surfaces.

In this work, we want to demonstrate that our amphiphilic hybrid hairy Janus particles can be successfully employed for the design of structured surfaces with controlled ice nucleation and growth, as well as with extremely low ice adhesion strength. Eventually, Janus particles can easily be prepared on a large scale, and can be used to cover large surface areas by simple spraying or solvent casting. Therefore, the presented approach could open new perspectives for the creation of a unique kind of industrially relevant anti-icing coatings.

4.4.2.1.2. Experimental Part

Samples for the anti-icing testing: A list of all samples prepared for the anti-icing testing is summarized in **Table R4**. Reference flat surfaces were prepared as described in Section 3.2.1. The corresponding homogeneously decorated and Janus particles were synthesized as described in Sections 3.2.2.-3.2.3. Structured surfaces based on the particles were prepared as described in Section 3.2.6. Their quality was checked with SEM (**Figure R46**).

Kinetics of ice growth experiments: The experiments were carried out by taking seven identical samples (2cm×1cm) from each set and mounting them horizontally onto the cooling plate within the humidity controlled chamber. Kinetics of ice formation on different surfaces was measured at -2°C under high humidity conditions (80%) by measuring the weight of the surfaces after certain time intervals. Weight difference of the samples before and after frost

formation corresponds to the amount of ice formed with time. After removal of each sample 5 min stabilization time was required to maintain the proper conditions for testing.

Table R4. List of the prepared samples for the icing experiments

Sample ID	Description
P(PEGMA) flat	P(PEGMA) polymer brush on a Si wafer
P(PDMSMA) flat	P(PDMSMA) polymer brush on a Si wafer
SiO ₂ -P(PEGMA)	Fully covered 1 μm SiO ₂ particles with a P(PEGMA) shell
SiO ₂ -P(PDMSMA)	Fully covered 1 μm SiO ₂ particles with a P(PDMSMA) shell
SiO ₂ -P(PEGMA)/P(PDMSMA)-JP	Spherical SiO ₂ -based core-shell Janus particles with two polymer shells

Ice Adhesion Strength Measurements: Ice adhesion measurements were performed in the temperature and humidity controlled chamber, where the temperature of the chamber was maintained at -10°C and the relative humidity at 80%. A cylindrical ice column was prepared on the sample surface using a hydrophobic syringe, which was filled by fresh Milli-Q water. The diameter of the ice cylinder on the substrate was 16 mm and its weight was approximately 1.4 g. Ice cylinders were kept inside the chamber for 16 h at -10°C, then they were mounted on a beam inside a home-made centrifuge apparatus. The centrifuge setup constructed is similar to the setup described elsewhere.^{221, 222} Counterweight with a reference sample was always used at the opposite end of the beam to balance the weight during spinning. The samples were spun inside the centrifuge situated in the chamber at -10°C to determine the rotational speed at which the detachment of the ice cylinder occurred. The time at which the ice cylinder was detached from the surface was detected by a sound from the microphone sensor which was ingrained into the centrifuge walls. The ice adhesion force on the sample surfaces was presumed to be equivalent with the centrifugal force, $F_c = m\omega^2r$, where m is the mass of the ice cylinder, ω is the rotational speed, and r is the radius of the centrifuge beam. Subsequently, the ice adhesion strength, which is a shear stress, was calculated by the equation $\tau = F_c/A$, where A is the contact area of the ice cylinder on the substrate, and d is the diameter of the ice cylinder: $A = \pi d^2/4$.

4.4.2.1.3. Results and Discussion

To test the anti-icing behavior, we have fabricated robust surfaces with hydrophilic/hydrophobic heterogeneity using 1 μm large hybrid hairy Janus particles with a silica core along with hydrophilic poly(poly(ethylene glycol) methyl ether methacrylate) and hydrophobic poly(monomethacryloxypropyl terminated polydimethylsiloxane) polymer shells (P(PEGMA)/P(PDMSMA)-JP, **Figure R38 a**). The Janus ratio of the fabricated particles, that is, the ratio between the hydrophilic P(PEGMA) and the hydrophobic P(PDMSMA) sides, was 2:1. The Janus particles were synthesized as described in Section 3.2.3. Functional

surfaces composed of the Janus particles were prepared on silicon wafers pre-modified with PGMA, which served as an adhesive promoter for the particles. The particles were physically attached to the PGMA layer (PGMA layer thickness: 80 ± 3 nm), which facilitated the robustness of the prepared surfaces.

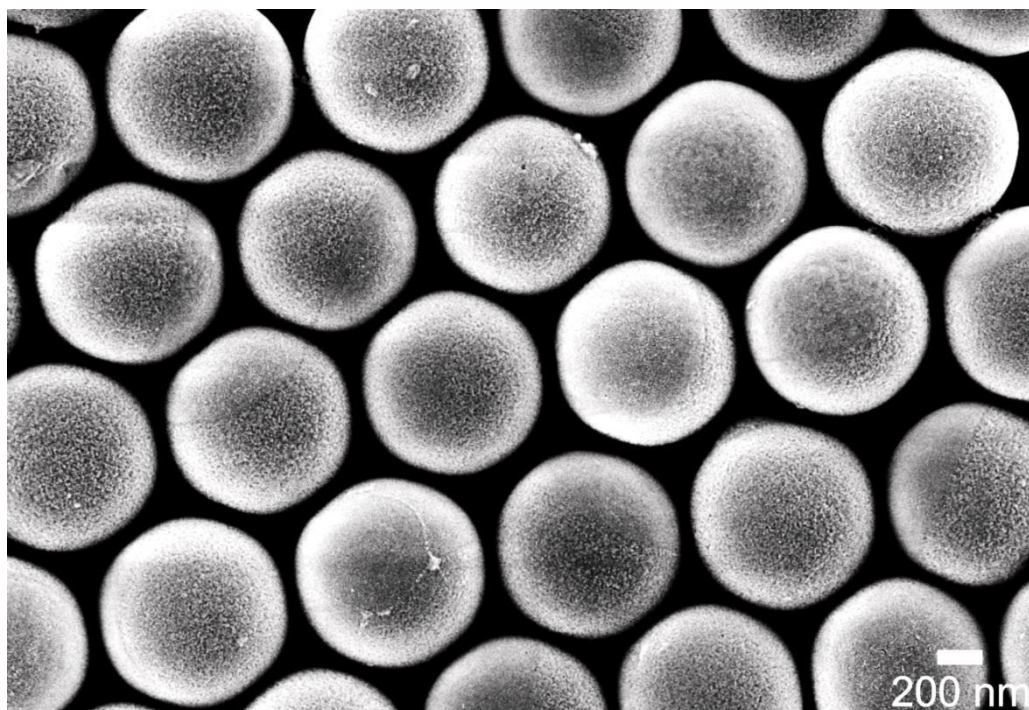


Figure R37. Representative SEM image at a 25k magnification of the coating prepared with P(PEGMA)/P(PDMSMA) Janus particles. The P(PEGMA)-covered sides of the particles appear rougher in the SEM. This observation is based on the fact that the silica particles are smooth before the first polymerization, and after it the P(PEGMA) morphology is revealed. The grafting of PDMS results in smoother sides of the particles.

In addition, we fabricated reference layers made from colloidal particles of the same size homogeneously decorated with each of the polymers: either hydrophilic P(PEGMA), or hydrophobic P(PDMSMA), as well as flat surfaces modified by the same polymers (**Table R4**). The particle layers were prepared by a simple solvent casting method, that is, by depositing and drying particle dispersions on pre-modified silicon wafers (Section 3.2.6.). We found that all particle layers are mechanically stable, and the particles are not removed during the ice test experiments (surfaces were checked before and after the ice adhesion measurements). The layers formed by bi-component Janus particles are typically disordered. In the SEM images, all kinds of orientation can be observed: JPs turned with their hydrophobic side up; JPs with their hydrophilic side facing up, and JPs partially exposing both sides to different extents (**Figure R37**, **Figure R38 b**).

In order to gain statistical insight into the orientation of Janus particles in the prepared layers, their distribution and orientation was investigated by probing the adhesion properties of the top layer of the JPs using AFM direct force measurements. The measurements were carried out under normal air pressure and increased humidity (80%). These are the conditions, which were used for the subsequent ice adhesion testing. Under these conditions the

P(PEGMA)-modified side of the particles is less adhesive than the P(PDMSMA)-modified one (**Figure R38 c**). For a given particle, only its overall contribution to the hydrophilicity/hydrophobicity of the layer was determined, an approximation justified by the particles' small size (**Figure R38 d**). After statistical analysis of the particles in five 20x20 μm topographical AFM images, we found that the distribution of the particles oriented with their hydrophobic or hydrophilic side to the top is ca. 55%:45%, respectively. Thus, we fabricated mechanically robust layers of Janus particles, and the orientation of the Janus particles in the layers was random.

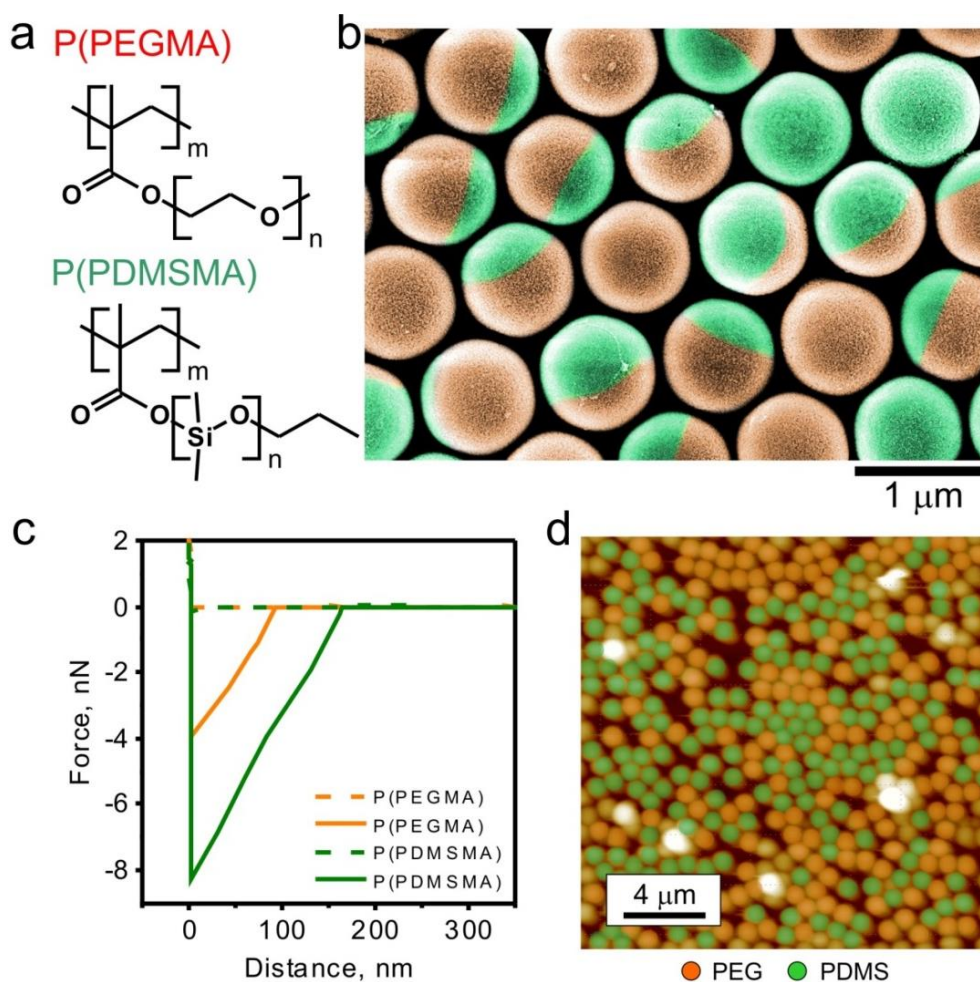


Figure R38. Representative layers prepared with P(PEGMA)/P(PDMSMA)-JP: (a) – chemical formulas of the polymers; (b) – false color SEM image (orange side - P(PEGMA); green side - P(PDMSMA)); based on the original image in **Figure R37**); (c) – direct force measurements performed with a sharp tip on the reference layers of P(PEGMA)- and P(PDMSMA)-covered particles at 80% relative humidity (dashed line – approaching curve, solid line – retracting curve; the respective force curves measured under water are displayed in **Figure R39**); (d) – false color mapping of the Janus particle orientation using direct force measurements (orange - P(PEGMA); green - P(PDMSMA)).

We found that flat P(PEGMA)- and P(PDMSMA)-modified surfaces are hydrophilic ($\theta_a = 30^\circ$, $\theta_r = 10^\circ$) and hydrophobic ($\theta_a = 120^\circ$, $\theta_r = 90^\circ$), respectively (**Figure R40 a-d**). Importantly, roughness enhances the intrinsic properties of the polymers, and makes hydrophobic surfaces even more hydrophobic, and the hydrophilic ones even more hydrophilic. In particular, the advancing and receding contact angles on the layers formed by

P(PDMSMA)-modified particles ($\theta_a = 150^\circ$, $\theta_r = 90^\circ$) are higher than those on a respective flat surface. The contact angles on the layers formed by P(PEGMA)-modified particles ($\theta_a = 20^\circ$, $\theta_r = 10^\circ$) are slightly lower than those on a respective flat surface (**Figure R40 a, b**). The values of advancing and receding water contact angles on the layers formed by Janus particles are in between the values measured for the layers of particles modified either by pure P(PEGMA), or pure P(PDMSMA). Additionally, the values of sliding angles were also used to assess the wetting properties of the particle layers (**Figure R40 c, d**). Particularly, we observed no sliding of water droplets on P(PEGMA)-modified surfaces, which is due to their high hydrophilicity and strong spreading effects. The values of sliding angles on pure P(PDMSMA)-modified surfaces are very high, and the water droplets are pinned. In addition, the values of sliding angles on the layers made of Janus particles are slightly higher than those on the P(PDMSMA)-modified surfaces (**Figure R40 d**). Thus, both types of measurements (advancing/receding contact angles as well as sliding angles) clearly show that the wetting properties of the bi-component Janus particle layers are intermediate between those of homogeneous particle-based surfaces modified by only one polymer.

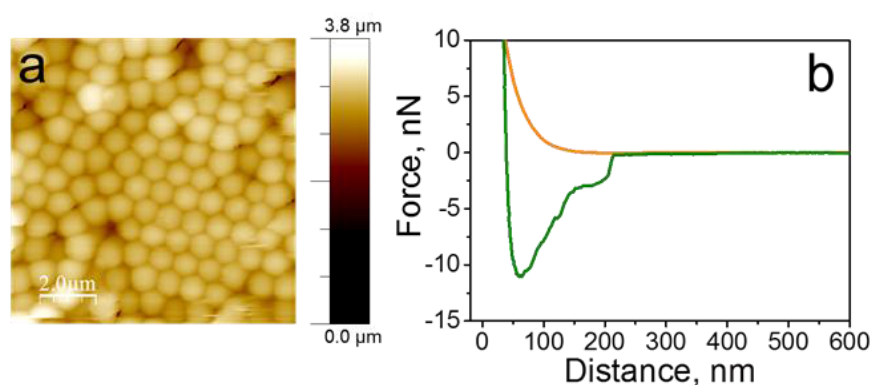


Figure R39. Topographical AFM image under water (a) and direct force measurements under water (b) on the prepared P(PEGMA)/P(PDMSMA) Janus particle layer: typical average P(PEGMA) force curve, (orange curve), typical average P(PDMSMA) force curve (green curve) measured with a sharp tip.

Further, we microscopically investigated the behavior of water droplets on the layers of particles modified by one polymer, and the layers of Janus particles (**Figure R40 e-g**) by means of cryo-SEM measurements. In a typical measurement, micrometer-sized frozen droplets were formed on particle layers through condensation and subsequent instantaneous freezing. It was observed that frozen water droplets are spread, and their contact angle is small on a hydrophilic surface with P(PEGMA)-modified particles (**Figure R40 f**). It could be concluded that water penetrates into the pits between the particles due to the hydrophilicity of the P(PEGMA). On the other hand, water droplets are compactly shaped and spherical on a hydrophobic surface with P(PDMSMA)-modified particles (**Figure R40 e**). Moreover, water does not penetrate between the particles due to the hydrophobicity of P(PDMSMA). Droplets formed on the surface made from Janus particles have different shapes (**Figure R40 g**). Some of them are spherical and look like droplets on the P(PDMSMA). Some droplets are flattened, and their shape is similar to the shape of the droplets on the P(PEGMA)-modified layers.

Other droplets are nearly spherical but have clear pinning points (“mixed” droplets) where they are “pinned” to the particles. Thus, microscopic investigations by means of cryo-SEM analysis again confirmed that the wetting of surfaces formed by Janus particles is intermediate between those formed by P(PEGMA)- and P(PDMSMA)-modified particles.

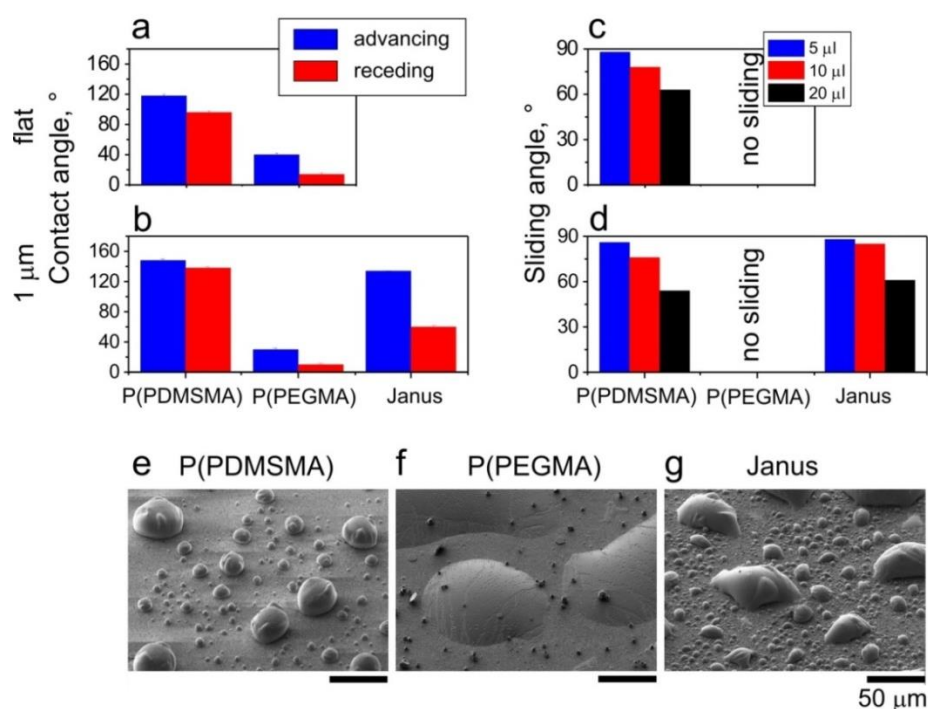


Figure R40. Summary of the wetting properties of the structured surfaces made from colloidal particles modified by P(PDMSMA), P(PEGMA), and bi-component P(PEGMA)/P(PDMSMA) Janus particles (a-d). Representative cryo-SEM images of the frozen water droplets on the surfaces formed by 1 μm P(PDMSMA) (e), P(PEGMA) (f), and P(PEGMA)/P(PDMSMA) Janus particles (g).

Next, we tested the icing properties of the Janus particle layers, and compared them to the icing of the layers formed by fully covered particles modified with either hydrophilic P(PEGMA), or hydrophobic P(PDMSMA), as well as with flat surfaces modified with the same polymers. It was found that the highest and lowest rates of ice formation (ice weight and ice layer thickness) are intrinsic to the hydrophilic P(PEGMA)- and the hydrophobic P(PDMSMA)-modified surfaces, respectively (**Figure R41 a, b**). This difference can readily be explained by the known fact that polar substances (water) “like” polar P(PEGMA) and “dislike” non-polar P(PDMSMA). Furthermore, the Janus particle-modified surfaces occupy an intermediate position between the hydrophobic and the hydrophilic ones, indeed, demonstrating an intermediate ice growth rate in accordance with our expectations.

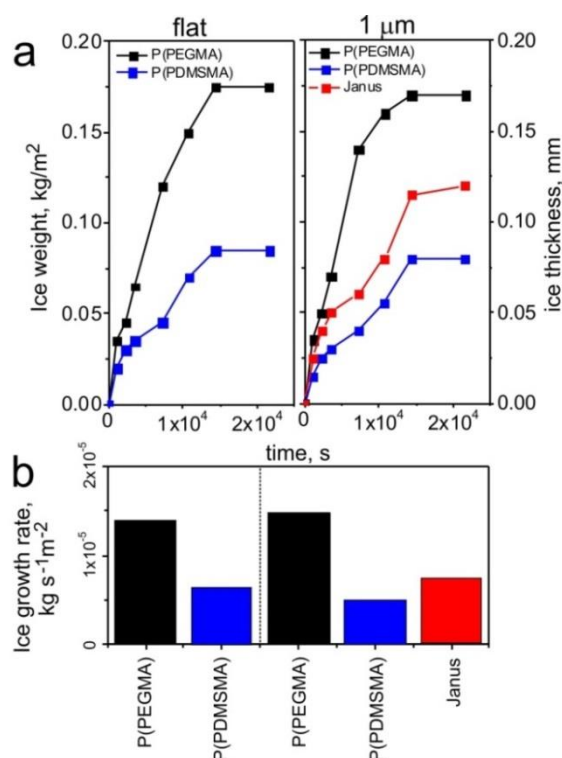


Figure R41. Ice weight (a), and ice growth rate (b) measurement results on the flat surfaces, on the surfaces prepared with particles modified by one polymer (either P(PEGMA) or P(PDMSMA)), as well as on the surfaces prepared with bi-component hybrid Janus particles.

We looked deeper into the frost layer formation on the coating made from bi-component Janus particles (**Figure R42**, **Figure R43**) using optical microscopy. For this purpose, we have mounted the sample on a Peltier element, and gradually lowered the temperature to -20°C for the freezing cycle, and increased it to 5°C for the thawing cycle, while observing the changes directly under the microscope. We found that the cooling first leads to the condensation of micrometer-sized water droplets from air (**Figure R42 a, b**). Then their size gradually increases, as more water condenses on the surface. Further cooling leads to the supercooling of the droplets, and they remain unfrozen until the temperature reaches ca. -20°C . At this temperature we observed nucleation and fast growth of crystal dendrites,²²³⁻²²⁶ the size of which approaches hundreds of microns (**Figure R42 c**). The growing of dendrites is not due to the condensation of water from vapor, but due to the consumption of the neighboring water droplets without contacting them. Apparently, the small unfrozen water droplets are metastable (supercooled at -20°C), and easily evaporate and re-condense on the surface of the growing ice crystals. Thus, we simultaneously observed ice in the form of dendrites and unfrozen water droplets. At some point, the remaining small water droplets freeze and form small ice crystals (**Figure R42 d**). In this moment, fast growth of dendrites is slowed down, and their further growth is solely provided by the condensation of water molecules from air. Thus, there are two kinds of ice crystals on the layer formed by bi-component Janus particles: dendrites, and small ice crystals, which are attached with their whole base area to the particles. Moreover, there is a considerable area without ice on the layer made of Janus particles. Additionally, we compared the growth of dendrites and small

ice crystals, and found that at the beginning the area occupied by the dendrites increases more than 200 times faster than the area occupied by the small crystals (**Figure R43**). Thawing results in the formation of water droplets, but because of the large contact angle hysteresis (difference between the advancing and receding contact angles), water droplets remain pinned to the surface.

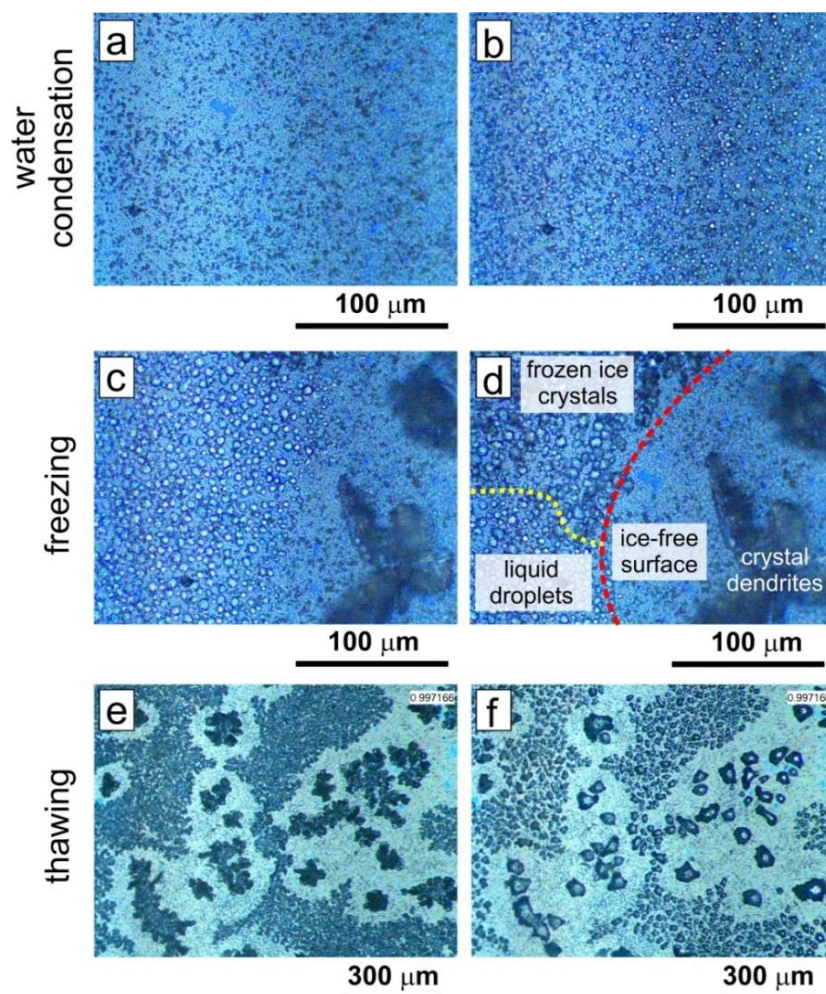


Figure R42. Representative optical microscopy images of a P(PEGMA)/P(PDMSMA) Janus particle-modified surface during icing on a Peltier element: (a) native surface; (b) surface after the water droplet condensation; (c) heterogeneous nucleation and growth of large ice crystals; (d, e) freezing of the condensed water droplets; (f) thawing of ice.

The observed scenario of ice growth on such surfaces made of Janus particles is completely different from the ice growth on pure hydrophobic and pure hydrophilic surfaces.²²⁷ On pure hydrophobic P(PDMSMA)-modified surfaces, we typically discovered a condensation of water droplets, which freeze and form slowly growing ice crystals due to the condensation of water molecules from vapor. The formation of large rapidly-growing crystals was very seldom. On the contrary, on pure hydrophilic P(PEGMA)-modified surfaces we noticed that water condenses and forms a continuous layer, which freezes and slowly grows due to the condensation. Thus, we can speculate that the formation of dendrites is due to the heterogeneous hydrophilic/hydrophobic Janus structure of the particles, which leads to the heterogeneous nucleation of ice.

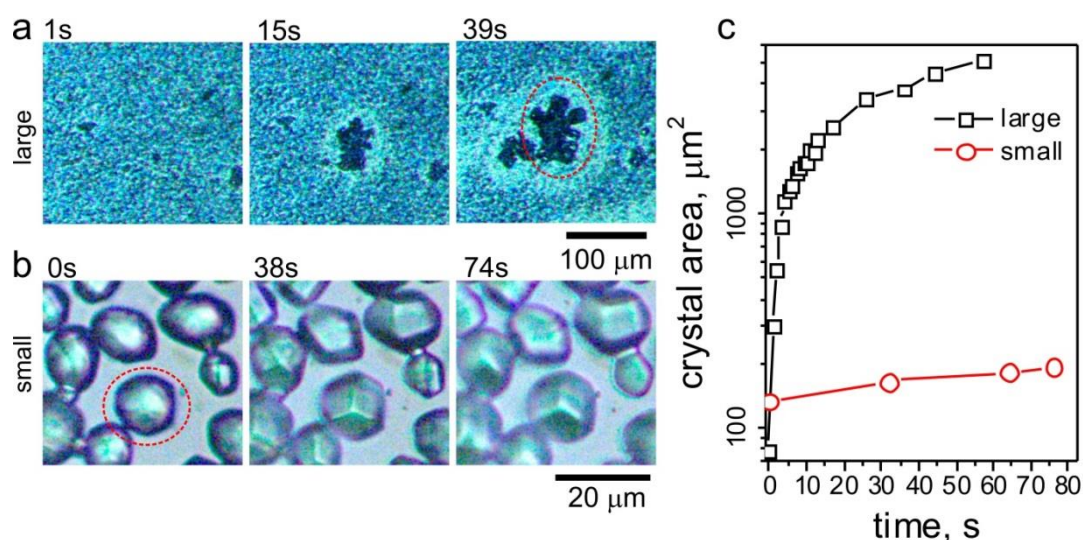


Figure R43. Growth of ice crystals on a P(PEGMA)/P(PDMSMA) Janus particle-modified surface: (a) – large crystals; (b) – small crystals; (c) – comparison of the surface area increase under ice crystals marked by dashed circles in (a) and (b).

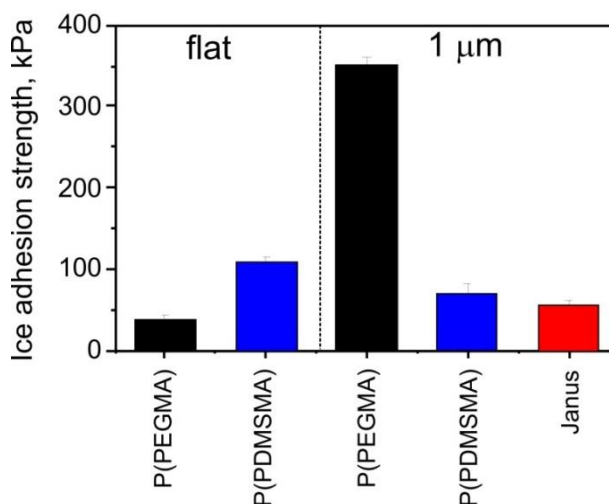


Figure R44. Ice adhesion measurement results on the flat surfaces, on the surfaces prepared with particles modified by one polymer (either by P(PEGMA) or P(PDMSMA)), as well as on the surfaces made from bi-component hybrid Janus particles.

Finally, we investigated the adhesion of ice on the layers of Janus particles as well as on the reference ones. It was found that ice adhesion depends not only on the properties of the polymers, but also on the roughness of the surface (flat surface or particle layer, **Figure R44**). In fact, the flat P(PEGMA)-modified surface demonstrated very low ice adhesion (< 50 kPa), whereas increasing roughness dramatically increased the ice adhesion values. Low adhesion of ice to the flat P(PEGMA) surface can be explained by the “antifreeze” properties of P(PEGMA) – the freezing point of poly(ethylene glycol)-water solutions is in the range of -10°C to -25°C. High ice adhesion on surfaces formed by 1 μm large P(PEGMA)-modified particles can be explained by the penetration of water through the pores between the particles due to surface tension. The water then freezes in the pores, which results in a strong mechanical contact between the surface and the ice layer on top. The ice adhesion strength on flat and rough P(PDMSMA) surfaces is similar, and is about 70 kPa and 110 kPa,

respectively. The most interesting and unexpected point is, however, that the ice adhesion on layers prepared with bi-component Janus particles is lower than that on the layers of particles modified by hydrophilic or hydrophobic polymers, and is about 40 kPa. The reproducibility of the results was confirmed by a number of repeated measurements. As a matter of fact, such low adhesion of ice to the layers formed by Janus particles is unusual, because the Janus particles are disordered in the layer, and hydrophobic and hydrophilic sides are distributed equally throughout the coating surface. If compared to the results reported in literature, such ice adhesion values are in the same range as the best (the lowest) ice adhesion values on other potential anti-icing coatings. For instance, it is much lower than that on flat highly hydrophobic surfaces (ca. 100 kPa), and comparable to the values, which are expected and experimentally measured for the superhydrophobic surfaces.¹⁹⁹ The ice adhesion strength on self-lubricating liquid water layer surfaces reported by Chen et al. was slightly higher - around 55 kPa.²¹³ Similar ice adhesion values were demonstrated by Kulinich et al. – from around 40 to 80 kPa, when tested on various superhydrophobic surfaces.²⁰⁷ A coating with an aqueous lubricating layer was prepared by Dou et al., and it exhibited ice adhesion values of around 30 kPa.²¹⁶

Conclusively, our experiments show the formation of ice dendrites, and low ice adhesion on the surfaces formed by hydrophilic/hydrophobic hybrid Janus particles. On the other hand, it is clear that the conditions of the ice formation in the adhesion tests, and microscopy investigations are different. In the first case, ice is formed on a solid surface, which is in contact with liquid water. In the second case, ice is formed on a solid surface, which is in contact with the water vapor (gas phase). Our experiments show that the wetting properties do not define the strength of adhesion: values of water contact angles as well as shapes of frozen water droplets (cryo-SEM analysis) on the layers of Janus particles are intermediate between the ones on the hydrophobic and hydrophilic layers. The only considerable difference between the properties of the layers made of Janus and not Janus particles (homogeneously decorated hydrophilic and hydrophobic ones) is the different mechanism of ice formation: we observed a formation of many ice dendrites on the layers of Janus particles, which were not observed on the layers of either hydrophobic or hydrophilic particles. These dendrites are formed due to the heterogeneous nucleation at the particle-vapor interface. We believe that the heterogeneous nucleation of ice occurs at the particle-water interface during the preparation of the samples for the ice adhesion tests. As a result of a different nucleation mechanism, ice must also have a different morphology when it grows on the layers of either hydrophilic, or hydrophobic particles, or when it grows on the heterogeneous layer of hydrophilic-hydrophobic Janus particles. A direct microscopic observation of the icing of a thick water layer on the layers of particles was impossible, because freezing occurred extremely fast (less than 1s), and the formed ice crystals hindered the observation of the process on the surface.

4.4.2.1.4. Summary

In summary, we have demonstrated for the first time the applicability of hydrophilic/hydrophobic hybrid hairy Janus particles for the design of advanced and effective anti-icing surfaces with synergistic properties. We observed that, in contrast to the icing of common homogeneous hydrophilic and hydrophobic surfaces, where first water droplets condense, then freeze, and finally the formed small ice crystals slowly grow, there are large crystals on the heterogeneous surfaces of the hydrophilic/hydrophobic Janus particle layers formed due to the heterogeneous nucleation. These ice crystals grow extremely quickly due to the consumption of not-yet-frozen water droplets from the surface. As a result, large ice dendrites are formed, and a considerable part of the surface becomes ice-free. We also observed that the ice adhesion strength on the layers of Janus particles is extremely low - ca. 40 kPa, which is much lower than the ice adhesion on the homogeneous layers of hydrophobic and hydrophilic particles. We believe that the reduced ice adhesion to the layers of Janus particles originates from the heterogeneous ice nucleation. Conclusively, we foresee great potential in the functional surfaces based on hybrid hairy Janus particles with controlled nucleation and growth of ice, as well as extremely low ice adhesion strength, for the development of advanced and effective ice-free coatings.

4.4.2.2. Anti-Fouling / Fouling-Release Coatings

4.4.2.2.1. Motivation

Marine biofouling, the accumulation of microorganisms, plants, algae, or animals on seawater contacting equipment (e.g., pipelines, cooling and filtration systems, fishing nets, ship hulls, and bridge pillars) can have severe consequences leading to increased fuel consumption.²²⁸ The annual worldwide costs of marine biofouling may run into billions of dollars explaining the outstanding interest in the development of effective and economical control measures. In contrast to the strongly adhering mature biofilms, the initial stages of the biofilm formation are generally reversible. Hence, many proposed anti-fouling strategies rely on the prevention/intervention of the initial bacterial adhesion rather than on the removal of mature biofilms.²²⁹ Initial bacterial adhesion can be greatly influenced by the surface chemistry (functional groups, electrostatic charge), surface energy, mechanical properties (elastic modulus, shear forces), environmental conditions (pH, temperature, nutrient levels, competing organisms), and surface topography. Therefore, a plethora of different anti-fouling approaches based on surfaces with diverse properties has been proposed to prevent the initial adhesion of bacteria, most of which rely either on the use of homogeneous (such as hydrophobic or hydrophilic),²³⁰⁻²⁴¹ heterogeneous (such as amphiphilic, patterned, or mixed),²⁴²⁻²⁵⁶ or 3D surfaces (such as microtopographic patterned surfaces).²⁵⁷⁻²⁶⁶

Hydrophobic fouling-release coatings do not inhibit settlement of biofoulers *per se*, but allow for their easy removal by minimizing the adhesion strength between the organisms and the surface.^{228, 231} Presently, PDMS and fluoropolymers are the commonly used fouling-

release materials.²³⁵ In particular, PDMS is attractive due to its low surface energy, low glass transition temperature, and low elastic modulus.²³⁰ However, the efficiency of the current PDMS coatings is limited by their insufficient mechanical stability, necessitating improving and reinforcing their properties by adding other moieties or fillers, such as carbon nanotubes, nanoclay, etc.²⁶⁷

Hydrophilic anti-fouling coatings resist protein adsorption and cell adhesion due to the low polymer-water interfacial energy levels.^{232, 268} In particular, PEG is a widely used, non-toxic, biocompatible antifouling polymer coating.^{233, 234, 236-239} The efficacy of PEG is determined by its chain length, grafting density, and type of branching architecture.^{269, 270} However, the majority of currently applied PEG-based systems employ either covalent grafting or adsorption of PEG onto a surface, model SAMs, or PEG-containing block copolymers, all of which typically result in coatings with limited robustness – a problem to be overcome for industrial applications.

Surface topography, namely, structural features of the substrates with varying size, spacing, aspect ratio, and/or roughness can also affect the adhesion of fouling organisms. Substrate topography can either enhance or reduce the recruitment of fouling organisms. It was indicated that the size and spacing of topographic features with regards to the dimension of fouling organisms are fundamental to the surface defense against fouling.^{257-259, 271} Thereby, control of surface topography in the nano- to micrometer size range can play a pivotal role in the anti-fouling approaches.

A recent trend in the design of experimental surfaces for anti-fouling purposes is to create surfaces with compositional (chemical) heterogeneity in order to combine the advantageous properties of hydrophilic anti-fouling and hydrophobic fouling-release surfaces. Several methods to create heterogeneous surfaces have been reported, such as surface-initiated polymerization, adsorption of SAMs, or layer-by-layer deposition of alternating hydrophilic and hydrophobic polymers.^{242-244, 272, 273} For instance, amphiphilic hyperbranched fluoropolymer (HBFP)-PEG as well as HBFP-PDMS-PEG networks with anti-adhesive and fouling-release properties were reported as examples of heterogeneous surfaces with lateral scales in the nanometer range.^{245, 274} Other promising examples are based on amphiphilic triblock surface-active block copolymers with different side chains, such as PEG, PDMS, or fluorinated side chains.^{232, 247, 248, 275, 276} Furthermore, the domain size of the heterogeneities is an important parameter to consider when designing anti-fouling and fouling-release surfaces.²⁷⁷

In the present work, we propose for the first time a new approach for the design of amphiphilic anti-fouling surfaces based on immobilized hybrid hairy Janus particles as solid amphiphilic block copolymer prototypes. The employed Janus particles are either based on spherical silica particles, or platelet-like kaolinite particles, and are grafted with hydrophilic P(PEGMA) and hydrophobic P(PDMSMA) polymers at the opposite sides of the core. We have pursued a systematic approach to test the anti-fouling performance of the developed multi-functional surfaces and compared it to the performance of mono-functional particle-

based and flat surfaces as well as unmodified particle-based surfaces and silicon wafers. The advantages of the developed Janus particle-based surfaces are: (1) they combine both chemical and topographical heterogeneity; (2) they can easily be prepared on a large scale via simple spraying or solvent casting; (3) they are robust against mechanical perturbations; (4) it is possible to cover large areas of the surface using particles as building blocks; (5) kaolinite Janus particles are a low-cost alternative material than can be prepared on a large scale toward industrial applications.

4.4.2.2.2. Experimental Part

Samples for anti-fouling measurements: A list of all samples prepared for the anti-fouling measurements is summarized in **Table R5**. Reference flat surfaces were prepared as described in Section 3.2.1. The corresponding homogeneously decorated and Janus spherical and platelet-like particles were synthesized as described in Sections 3.2.2.-3.2.5. Structured surfaces based on the particles were prepared as described in Section 3.2.6.

Bacteria culture: *Cobetia marina* (DSM 4741), an aerobic, gram-negative bacterium, was obtained from DSMZ (Braunschweig, Germany) and stored frozen in stock aliquots in a nutrient medium (40 g/l sea salts + 10 g/l tryptone [both Sigma-Aldrich, Munich, Germany]; pH 7.8) containing 20 % glycerol at -80 °C. Experimental stock preparations were maintained on agar slants (nutrient medium + 5 g/l peptone + 1 g/l yeast extract + 15 g/l agar [all Sigma Aldrich]) and were stored at 4 °C for up to 4 weeks.

Biofilm formation assay: For the experiments, a single colony from an agar slant was inoculated in 50 ml nutrient medium and grown overnight with shaking at 28 °C. On the next day, the overnight culture was diluted 1:200 in fresh nutrient medium and grown until an OD₆₀₀ of 0.2 was reached. Flat or particle-containing substrates were glued to sterile segmented glass petri dishes using double-sided tape to prevent movement of the samples and adhesion of bacteria to the unmodified backside of the samples during the experiment. Subsequently, the diluted bacteria suspension was added to each segment of the petri dish and the samples were incubated at 28 °C at 90 rpm (dynamic culture) or 35 rpm (static culture) on a shaker for 24 hours. Then, the bacterial solution was discarded, unbound cells were removed by two washes with nutrient medium, and the samples were transferred to 15 ml centrifuge tubes containing 5 ml sterile 0.9% NaCl. Bacteria were removed from the sample surfaces by vortexing for 15 s followed by sonication for 5 min at 4 °C to prevent heating of the sample (an initial test had verified that close to 100% of the attached bacteria were removed from the samples using this procedure). Samples were removed from the centrifuge tubes; bacteria were pelleted by centrifugation at 3000g for 5 min and resuspended in 1 ml of fresh 0.9% NaCl. Subsequently, the amount of viable microbial cells in culture was determined using the BacTiter-Glo™ Assay (Promega, Madison, USA), which is based on the quantification of ATP present following the manufacturer's instructions. Briefly, 100 µl of

each bacterial suspension was pipetted in triplicate into a 96 well plate followed by 100 μl of an ATP reagent. Samples were briefly mixed in a plate shaker, incubated for 5 min at room temperature, and finally chemiluminescence was measured in a plate reader (Tecan GENios, Maennedorf, Switzerland). Within a single experiment, four individual samples were analyzed for each substrate type. After incubation in a bacterial solution, one of the samples was taken for SEM imaging, and the other three were used for the quantification of viable microbial cells. Five independent experiments were conducted.

Table R5. List of the prepared samples for the anti-fouling experiments.

Sample ID	Description
Native wafer	Unmodified Si wafer
Native SiO ₂	Unmodified 1 μm large silica particles
Native kaolinite	Purified unmodified kaolinite particles
P(PEGMA) flat	P(PEGMA) polymer brush on a Si wafer
P(PDMSMA) flat	P(PDMSMA) polymer brush on a Si wafer
K-P(PEGMA)	Fully covered kaolinite particles with a P(PEGMA) shell
K-P(PDMSMA)	Fully covered kaolinite particles with a P(PDMSMA) shell
SiO ₂ -P(PEGMA)	Fully covered 1 μm SiO ₂ particles with a P(PEGMA) shell
SiO ₂ -P(PDMSMA)	Fully covered 1 μm SiO ₂ particles with a P(PDMSMA) shell
K-P(PEGMA)/P(PDMSMA)-JP	Platelet-like kaolinite-based Janus particles with two polymer shells
SiO ₂ -P(PEGMA)/PDMS-JP	Spherical SiO ₂ -based Janus particles with two polymer shells

4.4.2.2.3. Results and Discussion

Synthesis of Hybrid Hairy Janus Particles and Preparation of Coatings

Both spherical and platelet-like hybrid hairy Janus particles (based on silica or kaolinite particles, respectively) as well as homogeneously decorated particles were synthesized in order to prepare structured functional surfaces for the anti-fouling experiments. The particles were grafted with hydrophilic P(PEGMA) and hydrophobic P(PDMSMA) (or PDMS) polymers. The synthetic procedures for their preparation are summarized in Sections 3.2.2.-3.2.5. The Janus ratio of the SiO₂-P(PEGMA)/PDMS-JP is 1:2 (PDMS:P(PEGMA)); **Figure R45**, and the Janus ratio of K-P(PEGMA)/P(PDMSMA)-JP is ca. 1:1 (as described in Section 4.2.). The grafting density of the polymer chains on the spherical and platelet-like particle surface obtained from TGA and GPC results is 0.2-0.4 chains/nm².

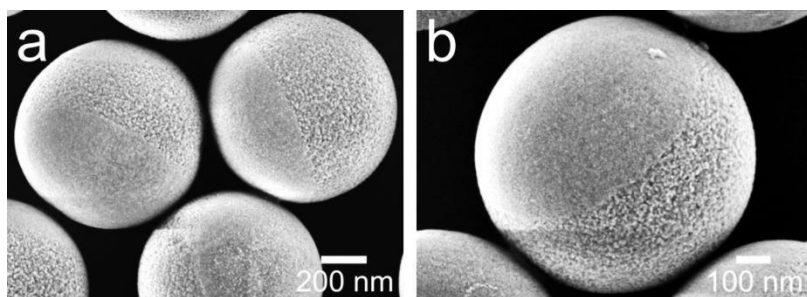


Figure R45. Representative SEM images of the $\text{SiO}_2\text{-P(PEGMA)/PDMS-JP}$ Janus particles revealing their Janus architecture and the Janus ratio 1:2 (PDMS:P(PEGMA)). Rough side – P(PEGMA), smooth side – PDMS.

The rationale for the use of the two geometries for the Janus particles was to test if the bacterial attachment would depend on the topographical features of the surface. The advantage of the platelet-like Janus particles is that they are easily prepared on a large scale due to the reduced number of steps during their synthesis, thus, revealing a promising potential toward the industrial applications of the developed surfaces. Subsequently, the Janus particles were immobilized on silicon wafers pre-modified with PEGMA, which serves as a non-covalent adhesive promoter. The selected coating preparation technique was intentionally chosen over covalent immobilization, as it allows the particle-based surfaces to be prepared on a large scale via simple spraying or solvent casting, an advantage prerequisite for the future technological applications. On the other hand, covalent immobilization would involve time- and resource-consuming operations that would prevent the widespread applications of the developed surfaces. Ultimately, surfaces with different morphologies were formed (**Figure R46**). Likewise, reference layers made from non- and mono-functionalized spherical and platelet-like particles, as well as flat surfaces modified either with P(PEGMA), or P(PDMSMA), were prepared. The negative control was an unmodified silicon wafer. A full list of the prepared samples is summarized in **Table R5**.

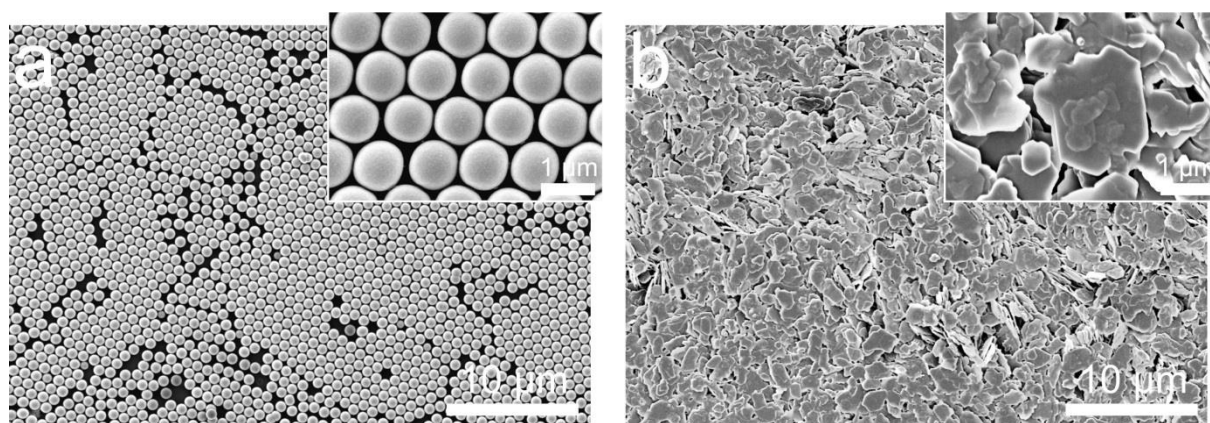


Figure R46. SEM images at different magnifications of the coatings based on spherical $\text{SiO}_2\text{-P(PDMSMA)}$ (a) and platelet-like K-P(PDMSMA) (b) particles.

The RMS roughness of the polymer-modified particle-based coatings was determined by AFM topography imaging under water. Compared to kaolinite particle-based coatings, spherical particle-based surfaces were found to be slightly less rough: 130 ± 14 nm vs. 180 ± 20 nm. Despite the fact that kaolinite particles are flat compared to spherical SiO_2 particles,

latter ones are organized in a regular monolayer on the surface, whereas kaolinite particles form multilayers, thus increasing the RMS roughness values. Modification of both particle types with polymers did not significantly affect RMS roughness of the resulting coatings.

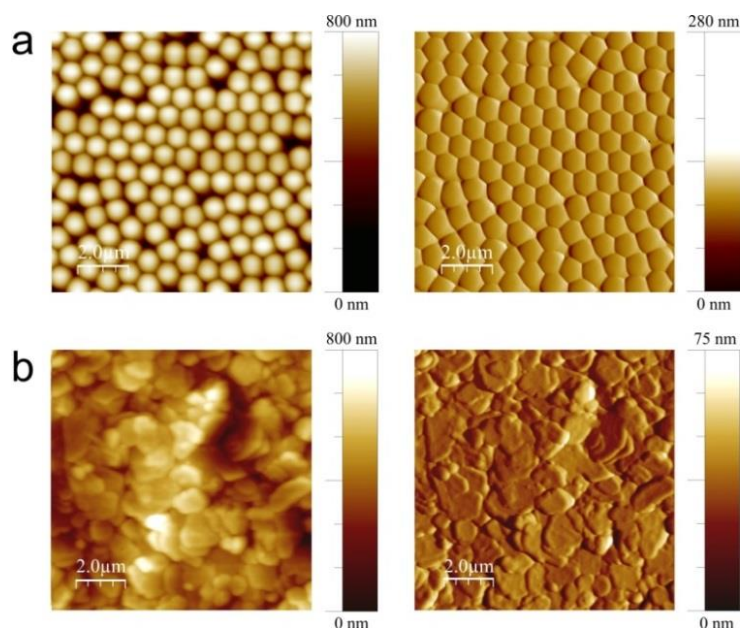


Figure R47. Representative AFM topography images recorded under water and used for the evaluation of the RMS roughness: (a) spherical SiO_2 -based particle surface (SiO_2 -P(PDMSMA)); (b) platelet-like kaolinite-based particle surface (K-P(PEGMA)).

Distribution of the Particles in the Coating Films: As discussed earlier in Section 4.4.2.1., the orientation of spherical Janus particles in the coatings is random, with some particles exposing either their P(PEGMA) or PDMS side, or lying on their side, thus exposing both polymers to the surrounding (**Figure R38**). Based on the SEM image analysis, it was concluded that the Janus particles tend to assemble into heterogeneous structures, where the size of the hydrophilic and hydrophobic domains is between several hundreds of nanometers to several micrometers.

To estimate the amount of hydrophobic or hydrophilic moieties exposed to the surrounding (and thereby accessible to the fouling organisms) under water, AFM force maps were acquired using the colloidal probe technique on the coatings made from spherical Janus particles under water, while the homogeneously decorated particle coatings served as a reference (**Figure R48**). Under these conditions, the hydrophilic P(PEGMA) polymer grafted on the surface of the SiO_2 particles is highly hydrated and thus completely non-adhesive to the 5 μm large SiO_2 colloidal probe, demonstrating an elastic repulsion (**Figure R48 a**). In contrast, the collapsed hydrophobic P(PDMSMA) polymer is significantly more adhesive to the colloidal probe (**Figure R48 b**). In the case of the Janus particle coatings, both types of force-distance curves were measured on the surface, indicating on the presence of both polymers (**Figure R48 c**). Therefore, due to the significantly different adhesion properties of the polymers, the individual force-distance curves within the acquired force maps for the Janus particles can be classified as either typical for P(PEGMA), or for P(PDMSMA). The distance between the individual measurement points in the force maps was chosen to be 1 μm .

This step size corresponds to the average size of most spherical bacteria and should therefore provide a realistic picture of the interactions of bacteria when approaching the examined coatings under water. Statistical analysis of the force-distance curves resulted in a 52%:48% distribution of the hydrophobic to hydrophilic particle orientation ratio.

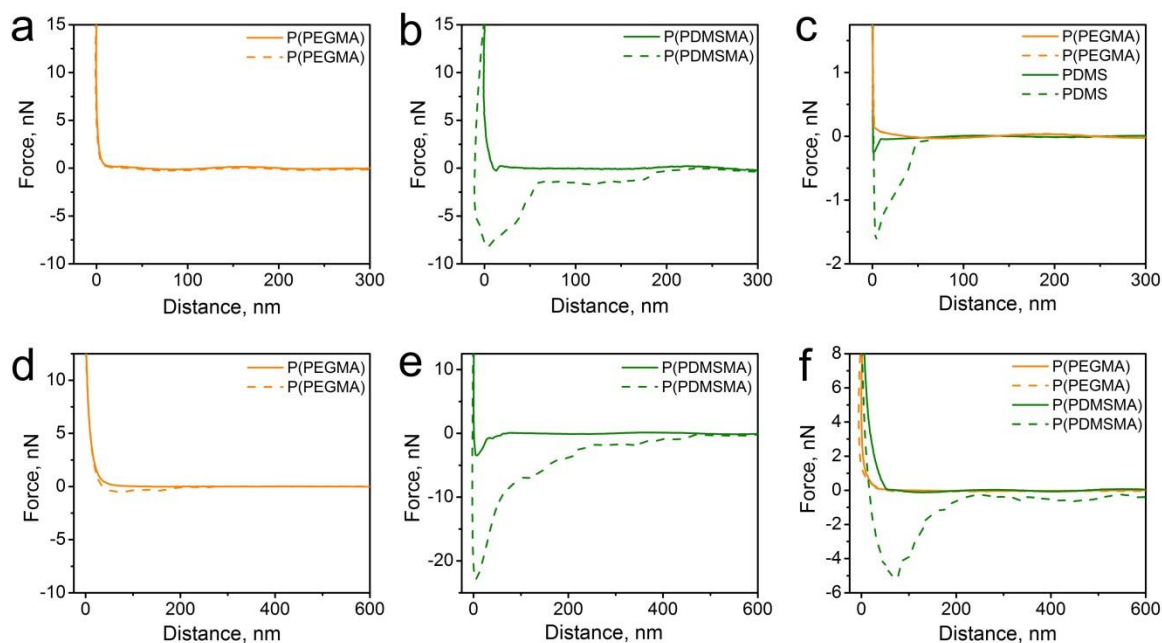


Figure R48. Representative average AFM force-distance curves acquired from the force maps measured under water in the case of spherical (a-c) and platelet-like (d-f) particle layers with a colloidal probe showing the different adhesive properties of the polymers on the surface of the particles: (a) SiO_2 -P(PEGMA); (b) SiO_2 -P(PDMSMA); (c) SiO_2 -P(PEGMA)/PDMS-JP; (d) K-P(PEGMA); (e) K-P(PDMSMA); (f) K-P(PEGMA)/P(PDMSMA)-JP.

The orientation of the platelet-like Janus particles was examined in a similar way (**Figure R48 d-f**). Due to their geometry the particles randomly lie either with their P(PEGMA) side, or their P(PDMSMA) side facing the surrounding (**Figure R47 b**). Force-distance curves obtained under water in the case of fully covered particle layers demonstrate a similar adhesive behavior of the polymers as in the case of the SiO_2 particle layers (**Figure R48 d, e**). Likewise, two types of force-distance curves can be measured on the Janus particle layer, indicating on the presence of both P(PEGMA) and P(PDMSMA) polymers (**Figure R48 f**). The distribution of force-distance curves with features characteristic for hydrophobic vs. hydrophilic polymers was found to be 44%:56%, respectively. Thereby, it can be concluded that both spherical and platelet-like JP-based coatings expose the hydrophobic and hydrophilic moieties in similar amounts to the surrounding. Similarly to spherical Janus particles, platelet-like Janus particles also form heterogeneous domains with slightly bigger sizes between 1-10 μm , which was concluded from the force maps.

Coating Robustness: In order to be considered as potentially relevant for industrial applications, the presented coatings must be robust under application-relevant conditions. Therefore, we performed three different kinds of experiments on spherical SiO_2 -based particle surfaces (serving as an example) in order to test the mechanical robustness of the particle

layers: (i) AFM imaging in contact mode with sequentially increasing contact forces exerted by the AFM tip on the samples (**Figure R49**), (ii) immersion of the surfaces in an ultrasonic bath for different time intervals (**Figure R50**), and (iii) incubation of the surfaces for three days in DI water on a shaker (100 rpm, **Figure R51**).

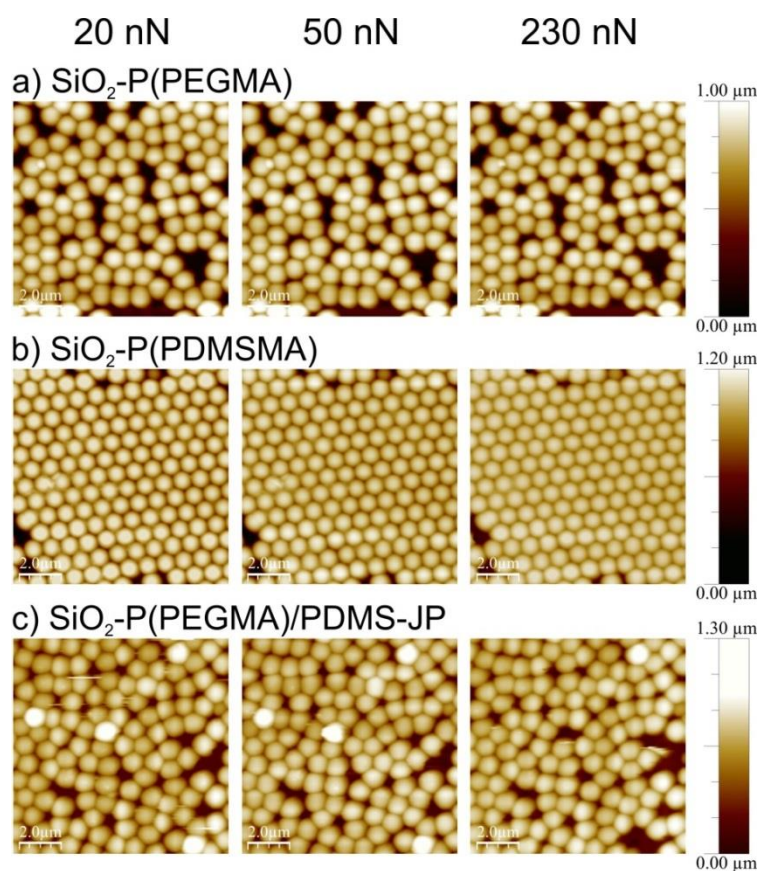


Figure R49. AFM topography images of the SiO_2 particle-based surfaces recorded in contact mode under water using different contact forces of the tip on the sample: (a) SiO_2 -P(PEGMA); (b) SiO_2 -P(PDMSMA); (c) SiO_2 -P(PEGMA)/PDMS-JP.

In the first set of experiments, AFM topography images were recorded on particle-based coatings immersed in water with increasing contact forces (20, 50, and 230 nN). It could be demonstrated that the surfaces are very robust. No particles were dislodged for contact forces up to 230 nN (**Figure R49**).

Ultrasonication is a rather harsh treatment. The forces exerted on the particle-based coatings are considered to be significantly higher compared to the AFM experiments (**Figure R50**). Despite this fact, all three kinds of coatings are stable after 1 min of ultrasonication treatment, revealing a monolayer of particles (**Figure R50, 1 min**). However, while the SiO_2 -P(PDMSMA) and SiO_2 -P(PEGMA)/PDMS-JP particle layers remain stable even after 2 minutes in an ultrasonic bath, the SiO_2 -P(PEGMA) layer starts to disintegrate, revealing particle-free areas (**Figure R50, 2 min**). Increasing the ultrasound exposure time to 5 min leads to a partial decomposition of all three tested particle layers (**Figure R50, 5 min**). However, much more particle-free areas are visible in the case of the SiO_2 -P(PEGMA) layer.

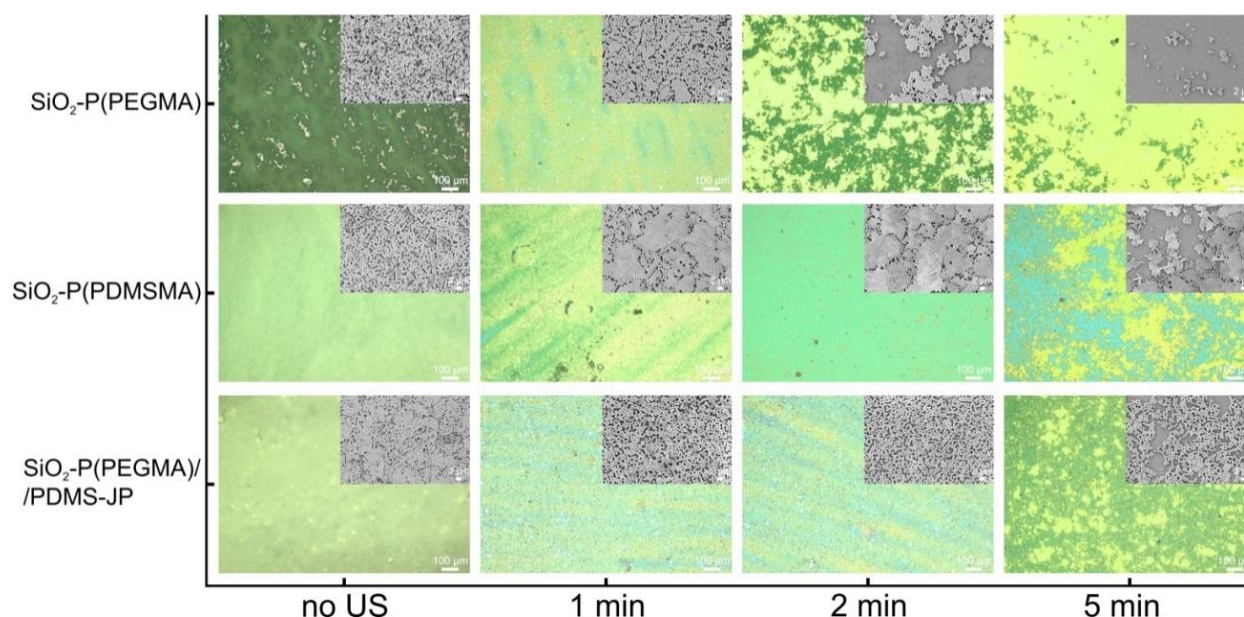


Figure R50. Representative light microscopy at low magnifications and SEM images (insets) at high magnifications of the SiO₂ particle-based coatings after different exposure times in an ultrasonic bath (US).

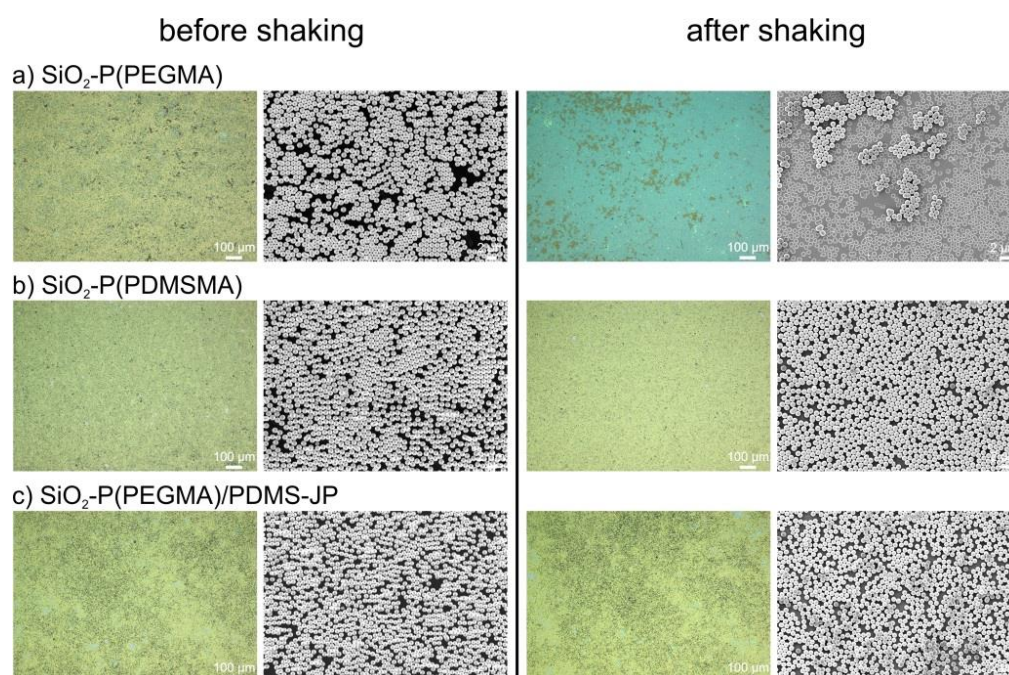


Figure R51. Representative light microscopy images at low magnifications and SEM images at high magnifications of the particle-based coatings before (left section) and after (right section) three days of continuous shaking in DI water at 100 rpm speed: (a) SiO₂-P(PEGMA), (b) SiO₂-P(PDMSMA), and (c) SiO₂-P(PEGMA)/PDMS-JP particle layers.

In the third approach, the particle-based coatings were incubated for three days in DI water with shaking. Representative light microscopy and SEM images of the particle-based layers before and after incubation are summarized in **Figure R51**. Notably, even under such mild conditions (in terms of shear forces), the P(PEGMA)-modified particle layer was almost completely decomposed after three days (**Figure R51 a**). This observation can probably be explained by the hydration of the P(PEGMA)-shell that decreases the particle adhesion to the

substrate. Layers with P(PDMSMA)-decorated hydrophobic particles and P(PEGMA)/PDMS amphiphilic Janus particles remained unaffected after the experiment (**Figure R51 b, c**). This indicates that the hydrophobic attraction forces between the particles were strong enough to prevent the decomposition of the coating (even in the case of Janus particles, which are partly hydrophilic).

These experiments, all of which were performed under water, demonstrate the robustness of the hydrophobic and Janus particle layers, and their suitability for the further anti-fouling experiments and future applications. Coatings prepared from homogeneously decorated and Janus kaolinite particles can also be considered as similarly robust, as can be concluded from the anti-fouling experiments, during which the coatings were perfectly stable and no layer disintegration was observed (SEM images of the coatings after the experiments are presented in **Figure R54**).

Since it emerged that the hydrophilic SiO₂-P(PEGMA) coatings are unstable under application-relevant conditions, we modified the protocols for their preparation to obtain stable coatings for the preceding antifouling experiments. Briefly, the P(PEGMA)-decorated particles were chemically grafted to the substrate using several steps. First, APS-covered particles (either SiO₂ or kaolinite) were chemically grafted to the PEGMA layer on the silicon wafer. Second, after modification of the particle layer with the ATRP-initiator, surface-initiated polymerization was performed directly on the particle layer. Such coating preparation technique is, however, much more tedious compared to the simple solvent evaporation we use for the P(PDMSMA) or the Janus particle layer preparation and is not compatible with the potential large-scale production/application of the described coatings. Hence, the P(PEGMA)-decorated particle layers serve only as reference layers due to their limited robustness, which disallows their further application.

Electrokinetic and Wetting Behavior: In the next step, the electrokinetic behavior of the developed coatings was evaluated. The representative zeta-potential vs. pH plots are typical for non-polar polymers that do not possess dissociable groups (**Figure R52 a**, spherical; **Figure R52 b**, platelet-like). An increase in the negative zeta-potential with increasing pH values is observed due to increased adsorption of hydroxyl ions. Representative SiO₂-P(PEGMA) and K-P(PEGMA) curves have a less pronounced slope due to the swelling of the hydrophilic P(PEGMA) polymer on the particle surface. The addition of hydrogen or hydroxyl ions to the system results in their adsorption deeper in the swollen polymer chains, thus leaving fewer ions on the surface. On the other hand, representative SiO₂-P(PDMSMA) and K-P(PDMSMA) curves have a more pronounced slope due to the collapsed hydrophobic P(PDMSMA). In this case, all the ions added are adsorbed on the surface of the collapsed polymer chains, thus, influencing the zeta-potential value to a higher extent than in the case of P(PEGMA). Representative curves for both spherical and platelet-like Janus particle layers occupy an intermediate position. Therefore, it can be concluded that both polymers –

hydrophilic swollen P(PEGMA) and hydrophobic non-swollen P(PDMSMA) – are exposed on the surface of the JP-based coatings.

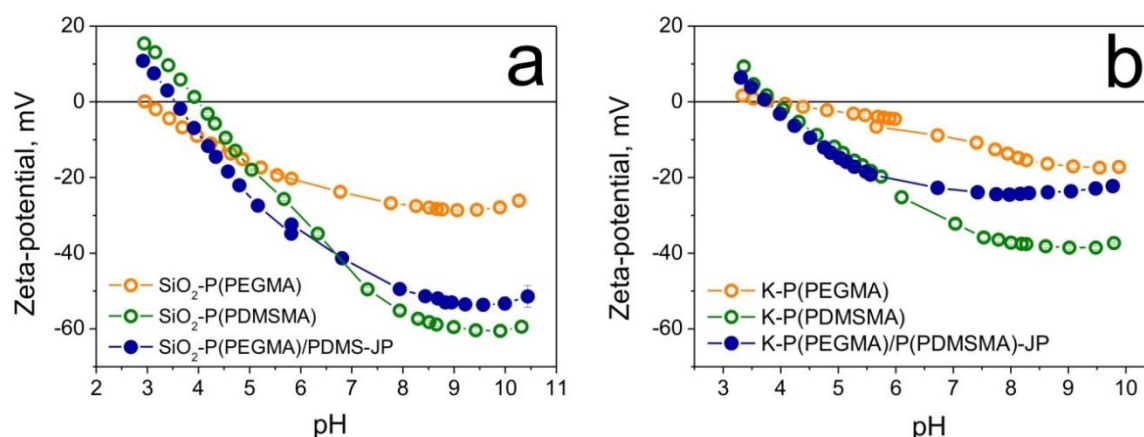


Figure R52. Streaming potential measurements on the coatings prepared with: (a) spherical SiO₂-based fully covered (orange and green lines) and Janus (blue line) particles; (b) platelet-like kaolinite-based fully covered (orange and green lines) and Janus (blue line) particles.

Furthermore, we have investigated the wetting behavior of the Janus particle layers using water contact angle measurements and compared it to the wetting properties of unmodified, modified flat surfaces, and surfaces made of fully covered P(PEGMA)- and P(PDMSMA)-modified particles (**Figure R53**). Freshly cleaned, unmodified silicon wafers are very hydrophilic, demonstrating a complete wetting behavior, whereas unmodified SiO₂ as well as kaolinite particle coatings demonstrate slightly higher advancing contact angles ($\theta_a = 52^\circ$ and 41° , respectively), while the receding contact angles are less than 10° (complete wetting). Flat P(PEGMA)- and P(PDMSMA)-modified surfaces are hydrophilic ($\theta_a = 40^\circ$, $\theta_r = 23^\circ$), and hydrophobic ($\theta_a = 105^\circ$, $\theta_r = 82^\circ$), respectively (**Figure R53**). The advancing and receding contact angles on the layers formed by P(PDMSMA)-modified particles (SiO₂-P(PDMSMA): $\theta_a = 148^\circ$, $\theta_r = 90^\circ$; K-P(PDMSMA): $\theta_a = 127^\circ$, $\theta_r = 65^\circ$) are higher than the values determined for the respective flat surfaces, while the contact angles on layers formed by P(PEGMA)-modified particles (SiO₂-P(PEGMA): $\theta_a = 38^\circ$, $\theta_r = 3^\circ$; K-P(PEGMA): $\theta_a = 40^\circ$, $\theta_r = 3^\circ$) are slightly lower than the values determined for the respective flat surfaces. On the other hand, the values of advancing and receding water contact angles on the layers formed by Janus particles (spherical: $\theta_a = 134^\circ$, $\theta_r = 60^\circ$; platelet-like: $\theta_a = 123^\circ$, $\theta_r = 44^\circ$) are in between the values measured for the layers of particles modified by pure P(PEGMA), or pure P(PDMSMA) (**Figure R53**). Hence, the advancing/receding contact angle measurements also confirm the presence and accessibility of both polymers on the bi-component Janus particle layer surface. Thus, electrokinetic and wetting measurements showed that the properties of the Janus particle layers are intermediate between the properties of the particle layers modified with hydrophobic P(PDMSMA), and with hydrophilic P(PEGMA).

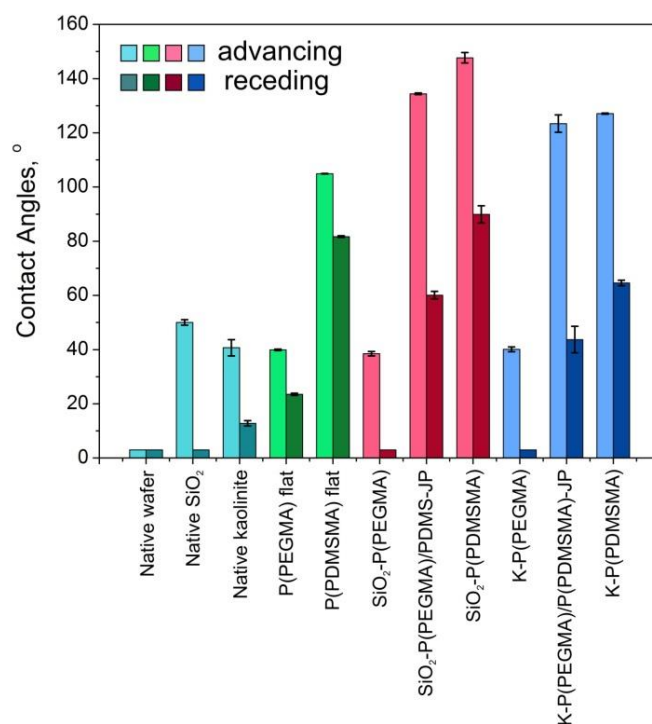


Figure R53. Advancing and receding contact angle values of the prepared reference unmodified (turquoise columns), modified flat surfaces (green columns), as well as coatings with SiO₂-based (pink columns), and kaolinite-based (blue columns) fully covered and Janus particles.

Settlement of the *Cobetia Marina* Bacteria

Layers formed from spherical and platelet-like Janus particles, as well as reference layers formed from uncoated and fully covered particles, as well as flat samples modified by the same polymers, were tested for their anti-fouling performance. Unmodified native silicon wafers were used as a negative control. The marine, biofilm-forming bacterial strain *Cobetia marina* was seeded in growth medium onto the different substrates and was incubated for 24 hours under either static conditions with low shear forces (representing e.g. standing water), or dynamic conditions with high shear forces (representing e.g. a moving ship hull). Subsequently, the number of attached bacteria was quantified by a chemoluminescence assay that quantifies adhering viable bacteria by determining the amount of ATP present (see Experimental Section for details). The results of the biofilm formation assay are displayed in **Figure R55**. Due to significant differences in the absolute values of the ATP-based assay between the independent experiments, the results were normalized against the negative control (unmodified native silicon wafer) under static conditions. Additionally, we investigated all sample types after their incubation in bacterial solution by means of SEM in order to visualize the adherent bacteria, and to gain insight into the distribution of the bacteria on the surfaces (**Figure R54**).

Static conditions: Under low shear stress, static conditions surfaces containing particles (spherical and kaolinite) fully covered with hydrophilic P(PEGMA) performed equally well compared to the benchmark flat control surfaces covered with the same polymer (**Figure R54**, **Figure R55**). Interestingly, the performance was independent of the particle geometry, and

almost similar amounts of cells were found on kaolinite- and SiO₂-based surfaces. In contrast, hydrophobic, fouling-release coatings do not prevent adhesion of microorganisms *per se*, but rather facilitate the detachment/removal of the attached foulers when sufficiently high shear forces are applied. Therefore, significantly more cells attached to flat as well as particle-based P(PDMSMA) surfaces (as compared to P(PEGMA)-based surfaces) under low shear stress, static conditions (**Figure R54, Figure R55**). However, these coatings still performed significantly better than the negative control (unmodified silicon wafer) and then the particle-based surfaces without polymer coatings. These results prove that the hydrophobic polymer coating has a significant effect on the bacterial retention even under these low shear stress conditions. Interestingly, the particle-based surfaces without polymer coatings performed significantly better than the negative control, demonstrating that the topography of the particle-based surfaces positively influences their antifouling properties. On SEM images, it was observed that the bacteria tend to organize themselves in large colonies on the P(PDMSMA)-based particle surfaces as compared to the rather uniform distribution of isolated cells on the P(PEGMA)-based surfaces (**Figure R54**). Interestingly, the fraction of hydrophilic P(PEGMA) on the Janus particle-based coatings significantly reduced the attachment of bacteria compared to the particle-based surfaces fully covered with P(PDMSMA) only. The distribution of bacteria observed in SEM was found to be intermediate between that observed on P(PEGMA)- and P(PDMSMA)-based surfaces – some of the bacteria were found to be organized in moderately large colonies, while isolated cells were also present on the surface (**Figure R54**). Additionally, it was found that the bacteria mainly attached to the surface of the particle layer, and typically did not adsorb in the voids between the particles (**Figure R54**). Even in the case of irregular, rough kaolinite-based coatings, bacteria were mostly located on top of the topographical irregularities. On these exposed positions, presumably less force has to be applied to remove the undesirable accumulation of bacteria on the surface during cleaning cycles in potential future applications.

Dynamic conditions: Compared to the static culture conditions, significantly less cells attached to the samples under high shear stress, dynamic conditions (compare the unmodified silicon wafer negative control in **Figure R55 a & b**). Nevertheless, the negative control as well as the particle-based surfaces without polymer coatings still performed significantly worse compared to the polymer-modified flat and particle-based surfaces (**Figure R55 b**). Interestingly, flat and particle-based surfaces fully covered with P(PEGMA) performed at similar levels as compared to the static conditions indicating that the hydrophilic coatings already reached their optimal performance at the low shear stress conditions. In contrast, flat and particle-based surfaces fully covered with P(PDMSMA) as well as the Janus particle-based surfaces performed significantly better (as compared to the static conditions), at levels comparable to the P(PEGMA)-based surfaces. The observed tendencies were additionally supported by the SEM measurements (**Figure R54**). Again, it must be stressed that the P(PEGMA)-based surfaces were proven to have limited robustness (**Figure R49, Figure R50,**

Figure R51), and the technique by which they were prepared disallows their real application as anti-fouling surfaces.

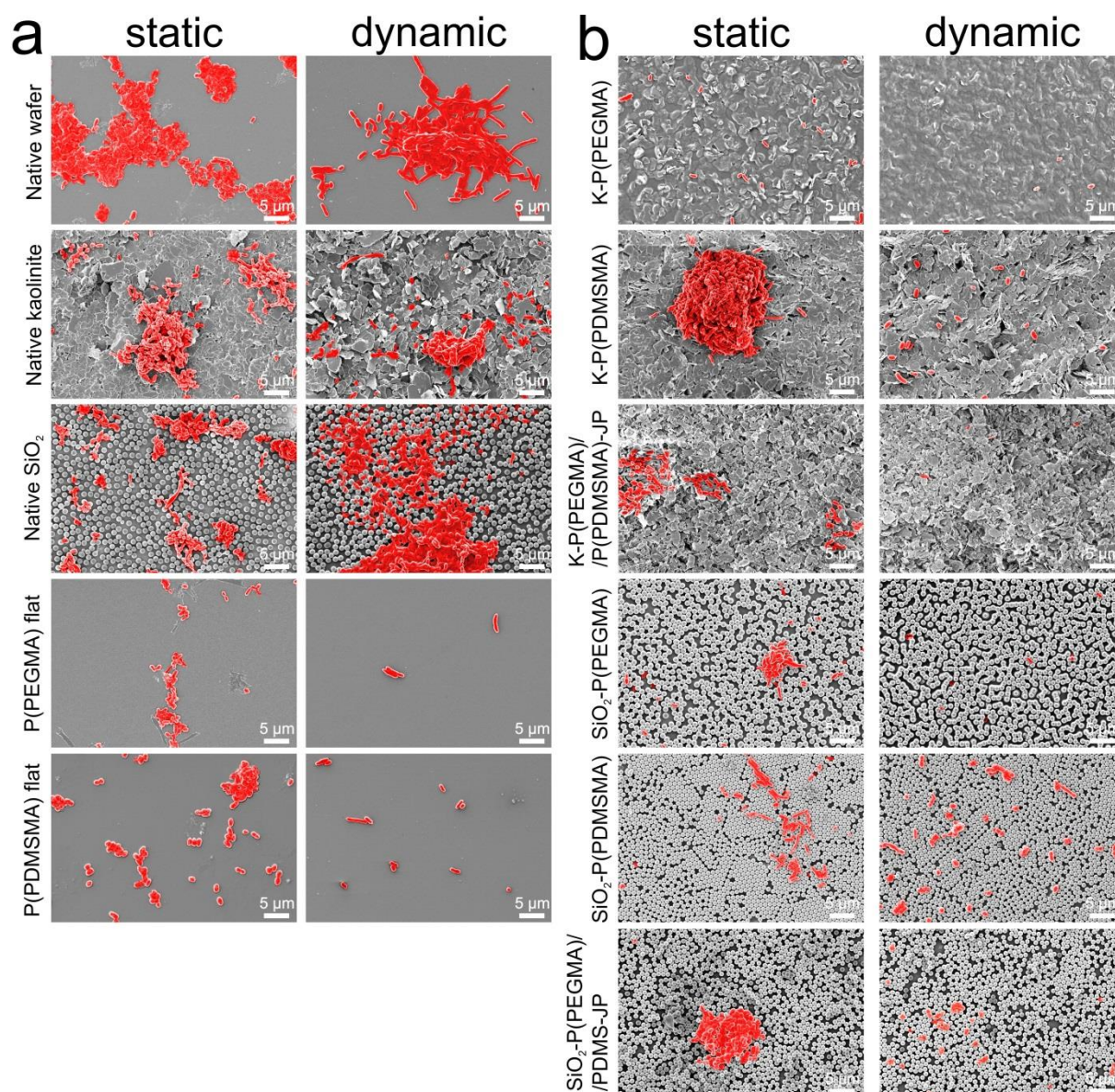


Figure R54. Representative false color SEM images of the (a) reference flat samples and coatings with native particles, and (b) of the respective modified particle-based (homogeneously coated and Janus) surfaces after the biofilm formation assay under static or dynamic conditions.

Both P(PDMSMA)-covered and Janus particle-based surfaces have prevented bacterial adhesion to a great extent compared to a control unmodified silicon wafer under static and dynamic conditions (**Figure R55**). However, while under dynamic conditions both of the surface types performed almost equally well, under static conditions SiO₂-based and kaolinite-based Janus particle layers exhibited a much better anti-fouling performance (-56 to -58% vs. -43 to -45%). If compared directly to the P(PDMSMA) particles layers, there are 24% less bacteria observed on the Janus particle-based surfaces in the case of SiO₂-P(PEGMA)/PDMS-JP, and 23% less bacteria in the case of K-P(PEGMA)/P(PDMSMA)-JP.

Eventually, this could lead to a universal application of such Janus particle-based surfaces under both low shear stress and high shear stress conditions.

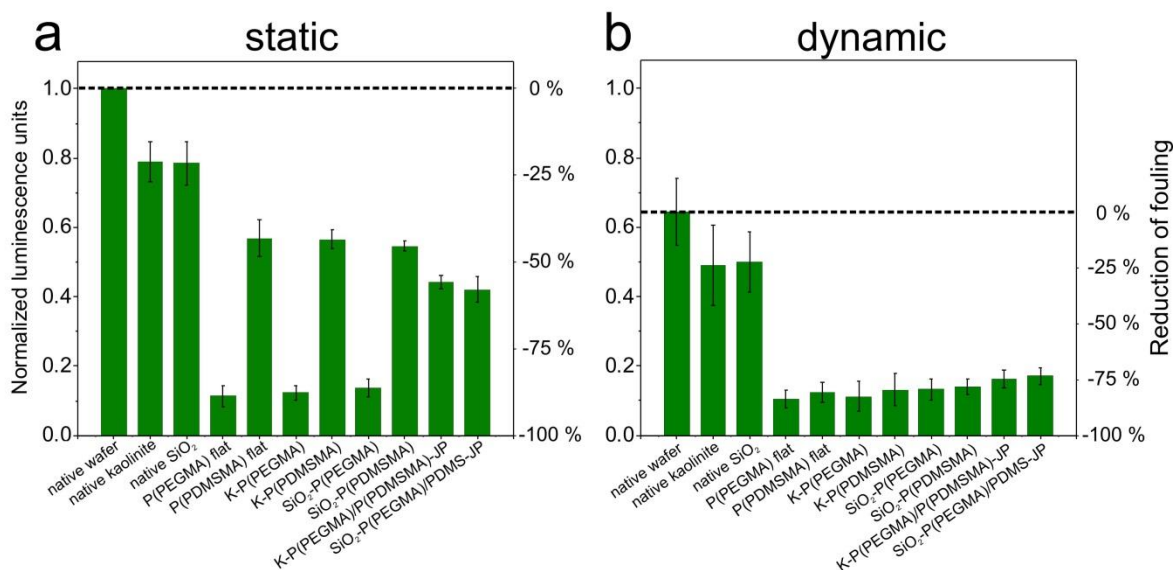


Figure R55. Anti-fouling and fouling-release performance of polymer-functionalized flat model and (Janus) particle-based surfaces. Marine, biofilm-forming bacterial cells were incubated for 24 hours with the samples under (a) static (45 rpm), or (b) dynamic (90 rpm) conditions. The amount of attached cells was quantified. Due to the significant variations between the independent experiments, all values were normalized against the negative control (native wafer, static conditions).

Chemically heterogeneous surfaces are already known as promising candidates for anti-fouling applications. However, amphiphilic block copolymers are most frequently used to create these soft surfaces with the size of the hydrophilic and hydrophobic patches on the nanometer scale. The preparation techniques of such surfaces are rather limited with respect to the large-scale industrial applications, and the coatings most probably will have limited robustness. Typically, *Ulva* spores are being used in the reported studies, making a direct comparison of our results with the literature difficult. We have utilized the *Cobetia marina* bacteria for the proof-of-principle investigation of our coating anti-fouling effects, whereas thousands of bacteria are present in seawater, indicating on the need for more extensive investigations.

The Janus particle-based surfaces in this study represented solid block copolymers with an interplay between chemical and topographical heterogeneity. Conclusively, it was found that the topographical aspect – the geometry of the Janus particle core – does not strongly influence the number of bacteria adhered to the surface, and both spherical as well as platelet-like Janus particles successfully reduced the adhesion of bacteria under both static and dynamic conditions. The difference between the mean RMS roughness values for spherical and platelet-like particle coatings is 50 nm, and it can be concluded that this difference is insufficient for the *Cobetia marina* bacteria to distinguish or respond. On the other hand, introducing chemical heterogeneity to the individual particles (JPs) led to their assembly into networks and, therefore, the formation of heterogeneous hydrophilic and hydrophobic domains on the (sub)micrometer scale from several hundreds of nanometers to several

micrometers. This resulted in the pronounced lowering of the bacterial adhesion under static, low shear stress conditions, if compared to pure hydrophobic P(PDMSMA)-modified as well as reference unmodified surfaces.

To the best of our knowledge, control of both chemical and topographical heterogeneity in the designed anti-fouling surfaces has not been addressed either in the previous works or in the literature in general. Moreover, we have pursued a systematic approach in our study and compared the anti-fouling performance of the bi-functional Janus particle-based surfaces with the corresponding mono-functional surfaces. Typically, analogous heterogeneous surfaces are only being compared to glass or pure PDMS elastomers, but not to their homogeneous counterparts. Therefore, we believe that this is the first study that demonstrates such systematic analysis of different heterogeneous surfaces as well as compares them to the homogeneous and the unmodified ones. Furthermore, the robust Janus particle-based surfaces developed in this work are a completely new type of anti-fouling coating, which can be easily prepared on a large scale.

4.4.2.2.4. Summary

In summary, we have used the hybrid hairy Janus particles for the first time as building blocks for robust multifunctional anti-fouling surfaces. The Janus particles used in this study comprised either a spherical silica particle core, or a platelet-like kaolinite particle core, and were grafted with the current anti-fouling ‘gold standards’ – P(PEGMA) and P(PDMSMA) polymers – at the opposite sides of the particles. The Janus particles serve as solid amphiphilic block copolymer prototypes that combine both chemical and topographical heterogeneity and have an impact on the final surface robustness. We have tested the anti-fouling performance of the Janus particle-based surfaces under application-relevant conditions using the marine, biofilm-forming bacterium *Cobetia marina*. Ultimately, we found that: (1) introducing chemical heterogeneity to the Janus particles allowed significant lowering of the bacterial adhesion under static conditions, if compared to pure hydrophobic P(PDMSMA)-modified as well as control native surfaces; (2) independently from the geometry of the Janus particles (spherical or platelet-like), the developed surfaces significantly reduced bacterial adhesion under dynamic conditions to the levels similar to homogeneous P(PEGMA)- and P(PDMSMA)-based surfaces; (3) the Janus particle-based surfaces were proven to be very robust, which facilitates their further application; (4) additionally, it was found that the adhered bacteria are mainly located on top of the topographical irregularities of the particle-based surfaces, which would presumably allow an easier removal of the undesirable bacteria accumulation during cleaning cycles in potential future applications. The kaolinite-based Janus particles represent a low-cost, alternative material that can easily be prepared on a large scale toward industrial applications. Moreover, the proposed Janus particles can be used to cover very large areas via simple spraying or solvent casting. Therefore, the developed Janus particle-based surfaces could be very promising as a novel type of robust, up-scalable anti-fouling coatings.

CHAPTER V

Summary & Conclusions

The present thesis embraces the topic of stimuli-responsive Janus particles: their design and the investigation of their self-assembly in bulk and at interfaces. Three issues have been addressed in the theoretical background and state-of-the-art section as well as in the results and discussion section: synthesis and design of the Janus particles, their (self-) assembly, and their possible applications. Challenges were pointed out in all three areas, indicating on the improvement possibilities, which were further developed.

In the first part of the work, two geometries of the Janus particles and the synthetic approaches for their fabrication were placed in focus: spherical and platelet-like. In the case of the spherical Janus particles, the possibility to easily tailor their Janus ratio was developed. The resulting hybrid Janus particles comprised a silica core and two kinds of polymer shells covering the surface of the core in different ratios. Additionally, a new methodology was employed to measure directly and in situ the position/contact angle of the prepared Janus particles at a water-oil interface. It could be concluded that having simply two different functionalities on a particle surface does not necessarily imply amphiphilic behavior: only in the case of large wettability contrasts our particles were in a true Janus regime. In the case of the platelet-like Janus particles, we have developed a completely new approach for their synthesis on a large scale through a reduced number of steps compared to the spherical Janus particles. For this purpose, we used a natural clay mineral kaolinite as a core material and grafted two kinds of polymer shells from the opposite sides of the core via simultaneous surface-initiated ATRPs in an emulsion. Two different monomers were located in the respective water or oil phase of the emulsion and the initiator-modified kaolinite particles assembled at the interfaces of the two phases, stabilizing the emulsion. Up to several grams of Janus particles could be synthesized in one batch, making this system relevant for technological applications.

In the second part of the work, the assembly behavior of various kinds of spherical Janus particles was investigated depending on their functionalities and the conditions of the surrounding media, such as pH, ionic strength, or solvent. Oppositely charged, uncharged amphiphilic, and charged amphiphilic Janus particles were prepared based on different responsive polymers and their aggregation behavior was tested. It was found that, under specific conditions, the Janus particles formed hierarchical chain-like structures in solutions, which were not observed in the case of the homogeneous particle mixtures. Such chain-like aggregates can be formed in a programmed manner and altered through changing the surrounding media conditions, such as pH or ionic strength. Therefore, the results of the self-assembly experiments indicate that the fundamental understanding of the Janus particle assembly mechanisms is crucial for the programmed formation of desired structures.

Moreover, the unique asymmetry of the Janus particles allows the formation of advanced structures inaccessible for their homogeneous analogues.

In the third part, two main directions were developed for the applications of the fabricated hybrid hairy Janus particles based on their exceptional properties and architectures. First, we utilized the enhanced interfacial activity of the Janus particles and demonstrated successful selective functionalization of amphiphilic Janus particles with metallic nanoparticles toward interfacial catalysis. The catalytic species were localized selectively in one hemisphere of the Janus particles, and the resulting catalysts showed high interfacial activity and efficient stabilization of oil-water emulsions that can be tuned by pH. A successful and effective reduction of two dyes, and a nitro compound with extremely low amounts of catalyst was conducted. Moreover, we have successfully performed a catalyzed reaction in the water phase of an emulsion stabilized by the Janus particles, showing their potential for interfacial catalysis. The Janus catalyst can be easily recovered after the reaction by centrifugation and reused again.

The second direction was based on the utilization of amphiphilic Janus particles as building blocks for functional structured surfaces. The developed surfaces were characterized and tested for two kinds of potential applications: as anti-icing or anti-fouling coatings. In the case of the anti-icing surfaces, a different mechanism of ice formation was observed on the Janus particles layers compared to the layers of homogeneous particles covered with the same polymers. Moreover, the ice adhesion values were extremely low on the Janus particle layers, indicating on the potential of such surfaces toward anti-icing applications. In the case of the anti-fouling surfaces, we systematically compared the anti-fouling performance of the Janus particle-based surfaces and compared them to the surfaces made of homogeneous particles covered with the same polymers and flat polymer-modified surfaces as well as unmodified particle-based surfaces and silicon wafers. We found that the Janus particle-based surfaces are robust under application-relevant conditions, and that they significantly reduce bacterial adhesion under static and dynamic shear stress conditions independent of their geometry: spherical or platelet-like. Therefore, the developed Janus particle-based surfaces could be very promising as a novel type of robust, up-scalable anti-fouling coatings.

Outlook

Research activities in the field of Janus particles have flourished in the past decade, indicating on the importance of the related investigations and novel kinds of asymmetric building blocks, ready to fulfill the requirement of multi-functionality in the field of materials science. Due to the numerous proposed synthetic strategies to produce Janus particles, it is now possible to acquire controlled functionalities and architectures at reasonable time and price expenses. However, the main challenge still remains the up-scalability of the developed approaches, delaying the application of Janus particles on an industrial scale. Therefore, the first point to consider in terms of future investigations is the optimization of the Janus particle synthetic procedures towards a large-scale, cheap and fast production. We have already addressed this point in the present work, proposing a new strategy for the fabrication of Janus particles on the basis of a natural clay mineral kaolinite and reducing the number of steps during the synthesis. Nevertheless, optimization needs to be carried out also in terms of the spherical Janus particle synthesis in order to minimize the efforts and the required number of steps. One way to do this would be to think of another strategy for the symmetry-breaking of the core particles instead of the Pickering emulsion approach.

Research concerning the self-assembly of the Janus particles has revealed a palette of diverse structures formed through different kinds of interactions between the asymmetric building blocks. Such structures have a great potential from the point of view of materials science, but there still remains the need for more fundamental investigations in order to translate the mechanisms of the Janus particle assembly toward the production of real materials. Programmed assembly is the key point for the future studies. The possibility to obtain the desired structures by tailoring the shapes and sizes of the building blocks, their chemistry and ratios, is of crucial importance for the future materials. In the present work, we have shown how different Janus particle architectures as well as the media conditions influence the assembly behavior of the Janus particles toward advanced linear structures. Another very interesting aspect here would be to investigate the programmed and reversible assembly of Janus particles with their homogeneous analogues.

In terms of applications, it is very beneficial to use the unique asymmetry inherent to the Janus particles, as it can result in special properties of the developed material. Typically, the enhanced interfacial activity of the Janus particles is in focus for their applications, leading to diverse successful attempts to use them as emulsion, foam, or polymer blend stabilizers. We took a step further and proposed an application of the Janus particles for interfacial catalysis. The next step in this field would be to test the simultaneous catalysis of several reactions at fluid/fluid interfaces.

Moreover, we have proposed a promising strategy for the application of Janus particles toward multi-functional coatings. The use of heterogeneous surfaces in terms of chemistry and/or topography is very advantageous for the future coating technology. Therefore, it is

crucial to fully understand the fundamental aspects of the coating preparation and of the Janus particle assembly in the final coatings as well as to develop even easier and more up-scalable techniques to design surfaces with controlled properties. Selective assembly of the Janus particles in the functional coatings is another important aspect for the future investigations, which would enhance their potential in the field of advanced materials.

Conclusively, this work has provided an extensive contribution on the topic of the Janus particle synthesis, their assembly, and applications, proposing different strategies to improve various aspects in these fields. Even though different solutions have been proposed, an area for improvement still lies in all three of the aforementioned topics. Considering the potential of the Janus particles, future extensive investigations on this topic are of great importance for different disciplines, such as materials and bio/life sciences.

References

1. A. Walther, M. Hoffmann and A. H. E. Müller, *Angew. Chem., Int. Ed.*, 2008, **47**, 711.
2. A. Walther, K. Matussek and A. H. E. Müller, *ACS Nano*, 2008, **2**, 1167.
3. M. Yoshida, K. H. Roh, S. Mandal, S. Bhaskar, D. Lim, H. Nandivada, X. Deng and J. Lahann, *Adv. Mater.*, 2009, **21**, 4920.
4. T. Nisisako, T. Torii, T. Takahashi and Y. Takizawa, *Adv. Mater.*, 2006, **18**, 1152.
5. J. N. Anker and R. Kopelman, *Appl. Phys. Lett.*, 2003, **82**, 1102.
6. J. R. Howse, R. A. L. Jones, A. J. Ryan, T. Gough, R. Vafabakhsh and R. Golestanian, *Phys. Rev. Lett.*, 2007, **99**, 048102.
7. M. Enquist and A. Arak, *Nature*, 1994, **372**, 169-172.
8. A. C. Little and B. C. Jones, *Proceedings of the Royal Society of London B: Biological Sciences*, 2003, **270**, 1759-1763.
9. A. Walther and A. H. E. Müller, *Chemical Reviews*, 2013, **113**, 5194-5261.
10. Z. Mao, H. Xu and D. Wang, *Advanced Functional Materials*, 2010, **20**, 1053-1074.
11. F. Li, D. P. Josephson and A. Stein, *Angewandte Chemie*, 2011, **50**, 360-388.
12. S. C. Glotzer and M. J. Solomon, *Nat Mater*, 2007, **6**, 557-562.
13. G. R. Yi, D. J. Pine and S. Sacanna, *J Phys Condens Matter*, 2013, **25**, 193101.
14. C. Casagrande, P. Fabre, E. Raphaël and M. Veyssié, *EPL (Europhysics Letters)*, 1989, **9**, 251.
15. P.-G. de Gennes, *Angewandte Chemie International Edition in English*, 1992, **31**, 842-845.
16. Web of Science. Thomson Reuters, <https://apps.webofknowledge.com>, Accessed 3 December 2015.
17. H. A. B. Wösten, *Annual Review of Microbiology*, 2001, **55**, 625-646.
18. M. B. Linder, G. R. Szilvay, T. Nakari-Setälä and M. E. Penttilä, *FEMS Microbiology Reviews*, 2005, **29**, 877-896.
19. M. A. Kostianen, G. R. Szilvay, D. K. Smith, M. B. Linder and O. Ikkala, *Angewandte Chemie International Edition*, 2006, **45**, 3538-3542.
20. P. A. Suci, S. Kang, M. Young and T. Douglas, *Journal of the American Chemical Society*, 2009, **131**, 9164-9165.
21. S. Semrau and T. Schmidt, *Soft Matter*, 2009, **5**, 3174-3186.
22. D. A. Christian, A. Tian, W. G. Ellenbroek, I. Levental, K. Rajagopal, P. A. Janmey, A. J. Liu, T. Baumgart and D. E. Discher, *Nat Mater*, 2009, **8**, 843-849.
23. C. J. Hawker, K. L. Wooley and J. M. J. Frechet, *Journal of the Chemical Society, Perkin Transactions 1*, 1993, 1287-1297.
24. K. L. Wooley, C. J. Hawker and J. M. J. Frechet, *Journal of the American Chemical Society*, 1993, **115**, 11496-11505.
25. V. Percec, D. A. Wilson, P. Leowanawat, C. J. Wilson, A. D. Hughes, M. S. Kaucher, D. A. Hammer, D. H. Levine, A. J. Kim, F. S. Bates, K. P. Davis, T. P. Lodge, M. L. Klein, R. H. DeVane, E. Aqad, B. M. Rosen, A. O. Argintaru, M. J. Sienkowska, K. Rissanen, S. Nummelin and J. Ropponen, *Science*, 2010, **328**, 1009-1014.
26. S. Zhang, H.-J. Sun, A. D. Hughes, R.-O. Moussodia, A. Bertin, Y. Chen, D. J. Pochan, P. A. Heiney, M. L. Klein and V. Percec, *Proceedings of the National Academy of Sciences*, 2014, **111**, 9058-9063.
27. S. Zhang, R.-O. Moussodia, H.-J. Sun, P. Leowanawat, A. Muncan, C. D. Nusbaum, K. M. Chelling, P. A. Heiney, M. L. Klein, S. André, R. Roy, H.-J. Gabis and V. Percec, *Angewandte Chemie International Edition*, 2014, **53**, 10899-10903.
28. X. Feng, D. Taton, E. Ibarboure, E. L. Chaikof and Y. Gnanou, *Journal of the American Chemical Society*, 2008, **130**, 11662-11676.
29. Z. Ge, J. Xu, J. Hu, Y. Zhang and S. Liu, *Soft Matter*, 2009, **5**, 3932-3939.
30. F. Ariura, M. Schappacher, R. Borsali and A. Deffieux, *React. Funct. Polym.*, 2009, **69**, 402.
31. J. Bolton, T. S. Bailey and J. Rzayev, *Nano Letters*, 2011, **11**, 998-1001.
32. I. K. Voets, A. de Keizer, P. de Waard, P. M. Frederik, P. H. H. Bomans, H. Schmalz, A. Walther, S. M. King, F. A. M. Leermakers and M. A. Cohen Stuart, *Angew. Chem., Int. Ed.*, 2006, **45**, 6673.
33. I. K. Voets, R. Fokink, T. Hellweg, S. M. King, P. de Waard, A. de Keizer and M. A. Cohen Stuart, *Soft Matter*, 2009, **5**, 999.
34. B. Fang, A. Walther, A. Wolf, Y. Xu, J. Yuan and A. H. E. Müller, *Angew. Chem., Int. Ed.*, 2009, **48**, 2877.
35. A. H. Gröschel, A. Walther, T. I. Löblich, J. Schmelz, A. Hanisch, H. Schmalz and A. H. E. Müller, *J. Am. Chem. Soc.*, 2012, **134**, 13850.

36. R. Erhardt, M. F. Zhang, A. Böker, H. Zettl, C. Abetz, P. Frederik, G. Krausch, V. Abetz and A. H. E. Müller, *J. Am. Chem. Soc.*, 2003, **125**, 3260.
37. R. Erhardt, A. Böker, H. Zettl, H. Kaya, W. Pyckhout-Hintzen, G. Krausch, V. Abetz and A. H. E. Müller, *Macromolecules*, 2001, **34**, 1069.
38. R. Saito, A. Fujita, A. Ichimura and K. Ishizu, *J. Polym. Sci., Part A: Polym. Chem.*, 2000, **38**, 2091.
39. Y. Liu, V. Abetz and A. H. E. Müller, *Macromolecules*, 2003, **36**, 7894.
40. A. Walther, M. Drechsler and A. H. E. Müller, *Soft Matter*, 2009, **5**, 385.
41. A. Wolf, A. Walther and A. H. E. Müller, *Macromolecules*, 2011, **44**, 9221.
42. N. Saito, Y. Kagari and M. Okubo, *Langmuir*, 2006, **22**, 9397.
43. T. Tanaka, M. Okayama, H. Minami and M. Okubo, *Langmuir*, 2010, **26**, 11732.
44. T. Higuchi, A. Tajima, H. Yabu and M. Shimomura, *Soft Matter*, 2008, **4**, 1302.
45. T. Higuchi, A. Tajima, K. Motoyoshi, H. Yabu and M. Shimomura, *Angew. Chem., Int. Ed.*, 2008, **47**, 8044.
46. A. Misra and M. W. Urban, *Macromol. Rapid Commun.*, 2010, **31**, 119.
47. J. G. Park, J. D. Forster and E. R. Dufresne, *J. Am. Chem. Soc.*, 2010, **132**, 5960.
48. K. H. Roh, D. C. Martin and J. Lahann, *Nat. Mater.*, 2005, **4**, 759.
49. S. Bhaskar, J. Hitt, S. W. L. Chang and J. Lahann, *Angew. Chem., Int. Ed.*, 2009, **48**, 4589.
50. S. Bhaskar, K. H. Roh, X. Jiang, G. L. Baker and J. Lahann, *Macromol. Rapid Commun.*, 2008, **29**, 1655.
51. Z. Nie, W. Li, M. Seo, S. Xu and E. Kumacheva, *J. Am. Chem. Soc.*, 2006, **128**, 9408.
52. R. K. Shah, J. W. Kim and D. A. Weitz, *Adv. Mater.*, 2009, **21**, 1949.
53. D. C. Pregibon, M. Toner and P. S. Doyle, *Science*, 2007, **315**, 1393.
54. D. Dendukuri, D. C. Pregibon, J. Collins, T. A. Hatton and P. S. Doyle, *Nat. Mater.*, 2006, **5**, 365.
55. H. Takei and N. Shimizu, *Langmuir*, 1997, **13**, 1865.
56. Q. Chen, S. C. Bae and S. Granick, *Nature*, 2011, **469**, 381-384.
57. S. Jiang and S. Granick, *Langmuir*, 2009, **25**, 8915.
58. L. Liu, M. Ren and W. Yang, *Langmuir*, 2009, **25**, 11048.
59. X. Y. Ling, I. Y. Phang, C. Acikgoz, M. D. Yilmaz, M. A. Hempenius, G. J. Vancso and J. Huskens, *Angew. Chem., Int. Ed.*, 2009, **48**, 7677.
60. S. H. Kim, S. Y. Lee and S. M. Yang, *Angew. Chem., Int. Ed.*, 2010, **49**, 2535.
61. C. C. Lin, C. W. Liao, Y. C. Chao and C. Kuo, *ACS Appl. Mater. Interfaces*, 2010, **2**, 3185.
62. S. Ye and R. L. Carroll, *ACS Appl. Mater. Interfaces*, 2010, **2**, 616.
63. M. D. McConnell, M. J. Kraeutler, S. Yang and R. J. Composto, *Nano Lett.*, 2010, **10**, 603.
64. S. U. Pickering, *Journal of the Chemical Society, Transactions*, 1907, **91**, 2001-2021.
65. L. Hong, S. Jiang and S. Granick, *Langmuir*, 2006, **22**, 9495-9499.
66. S. Jiang and S. Granick, *Langmuir*, 2008, **24**, 2438.
67. S. Jiang, M. J. Schultz, Q. Chen, J. S. Moore and S. Granick, *Langmuir*, 2008, **24**, 10073.
68. A. Perro, F. Meunier, V. Schmitt and S. Ravaine, *Colloids Surf., A*, 2009, **332**, 57.
69. S. Pradhan, L. Xu and S. Chen, *Adv. Funct. Mater.*, 2007, **17**, 2385.
70. R. Sardar, T. B. Heap and J. S. Shumaker-Parry, *J. Am. Chem. Soc.*, 2007, **129**, 5356.
71. H. Yu, M. Chen, P. M. Rice, S. X. Wang, R. L. White and S. Sun, *Nano Lett.*, 2005, **5**, 379.
72. K. D. Anderson, M. Luo, R. Jakubiak, R. R. Naik, T. J. Bunning and V. V. Tsukruk, *Chem. Mater.*, 2010, **22**, 3259.
73. B. Liu, C. Zhang, J. Liu, X. Qu and Z. Yang, *Chem. Commun.*, 2009, 3871.
74. B. Liu, W. Wei, X. Qu and Z. Yang, *Angew. Chem., Int. Ed.*, 2008, **47**, 3973.
75. S. Berger, A. Synytska, L. Ionov, K.-J. Eichhorn and M. Stamm, *Macromolecules*, 2008, **41**, 9669-9676.
76. B. M. Teo, S. K. Suh, T. A. Hatton, M. Ashokkumar and F. Grieser, *Langmuir*, 2011, **27**, 30.
77. C. Tang, C. Zhang, J. Liu, X. Qu, J. Li and Z. Yang, *Macromolecules*, 2010, **43**, 5114.
78. C. Zhang, B. Liu, C. Tang, J. Liu, X. Qu, J. Li and Z. Yang, *Chem. Commun.*, 2010, **46**, 4610.
79. S. Sacanna, L. Rossi and D. J. Pine, *J. Am. Chem. Soc.*, 2012, **134**, 6112.
80. R. F. Shepherd, J. C. Conrad, S. K. Rhodes, D. R. Link, M. Marquez, D. A. Weitz and J. A. Lewis, *Langmuir*, 2006, **22**, 8618.
81. B. Wang, B. Li, B. Zhao and C. Y. Li, *J. Am. Chem. Soc.*, 2008, **130**, 11594.
82. B. P. Binks and P. D. I. Fletcher, *Langmuir*, 2001, **17**, 4708-4710.
83. P. Pieranski, *Phys. Rev. Lett.*, 1980, **45**, 569.
84. Y. Hirose, S. Komura and Y. Nonomura, *The Journal of Chemical Physics*, 2007, **127**, 054707.
85. M. A. Fernandez-Rodriguez, M. A. Rodriguez-Valverde, M. A. Cabrerizo-Vilchez and R. Hidalgo-Alvarez, *Advances in Colloid and Interface Science*, 2015.
86. A. Walther, M. Drechsler, S. Rosenfeldt, L. Harnau, M. Ballauff, V. Abetz and A. H. E. Müller, *J. Am. Chem. Soc.*, 2009, **131**, 4720.

87. A. Walther, X. André, M. Drechsler, V. Abetz and A. H. E. Müller, *J. Am. Chem. Soc.*, 2007, **129**, 6187.
88. Q. Chen, J. K. Whitmer, S. Jiang, S. C. Bae, E. Luijten and S. Granick, *Science*, 2011, **331**, 199-202.
89. L. Hong, A. Cacciuto, E. Luijten and S. Granick, *Langmuir*, 2008, **24**, 621.
90. O. Cayre, V. N. Paunov and O. D. Velev, *Chem. Commun.*, 2003, **18**, 2296.
91. L. Hong, A. Cacciuto, E. Luijten and S. Granick, *Nano Letters*, 2006, **6**, 2510-2514.
92. D. Suzuki, S. Tsuji and H. Kawaguchi, *J. Am. Chem. Soc.*, 2007, **129**, 8088.
93. A. Goyal, C. K. Hall and O. D. Velev, *Phys. Rev. E*, 2008, **77**, 031401.
94. A. Goyal, C. K. Hall and O. D. Velev, *Soft Matter*, 2010, **6**, 480.
95. S. Gangwal, O. J. Cayre and O. D. Velev, *Langmuir*, 2008, **24**, 13312.
96. S. Gangwal, O. J. Cayre, M. Z. Bazant and O. D. Velev, *Phys. Rev. Lett.*, 2008, **100**, 058302.
97. L. Zhang and Y. Zhu, *Langmuir*, 2012, **28**, 13201.
98. S. K. Smoukov, S. Gangwal, M. Marquez and O. D. Velev, *Soft Matter*, 2009, **5**, 1285.
99. T. Isojima, S. K. Suh, J. B. Vander Sande and T. A. Hatton, *Langmuir*, 2009, **25**, 8292.
100. J. Yan, M. Bloom, S. C. Bae, E. Luijten and S. Granick, *Nature*, 2012, **491**, 578.
101. J. Yan, K. Chaudhary, S. Chul Bae, J. A. Lewis and S. Granick, *Nat Commun*, 2013, **4**, 1516.
102. J. Yan, S. C. Bae and S. Granick, *Advanced Materials*, 2015, **27**, 874-879.
103. D. Dendukuri, T. A. Hatton and P. S. Doyle, *Langmuir*, 2007, **23**, 4669.
104. L. T. Yan, N. Popp, S. K. Ghosh and A. Böker, *ACS Nano*, 2010, **4**, 913.
105. J. R. Link and M. J. Sailor, *Proc. Natl. Acad. Sci. U.S.A.*, 2003, **100**, 10607.
106. M. A. Bucaro, P. R. Kolodner, J. A. Taylor, A. Sidorenko, J. Aizenberg and T. N. Krupenkin, *Langmuir*, 2009, **25**, 3876.
107. S. Berger, L. Ionov and A. Synytska, *Advanced Functional Materials*, 2011, **21**, 2338-2344.
108. A. Synytska, R. Khanum, L. Ionov, C. Cherif and C. Bellmann, *ACS Appl. Mater. Interfaces*, 2011, **3**, 1216.
109. J. N. Anker, C. Behrend and R. Kopelman, *J. Appl. Phys.*, 2003, **93**, 6698.
110. C. J. Behrend, J. N. Anker, B. H. McNaughton and R. Kopelman, *J. Magn. Magn. Mater.*, 2005, **293**, 663.
111. *United States Pat.*, US5262098 A, 1993.
112. *United States Pat.*, US5344594 A, 1994.
113. N. K. Sheridan, E. A. Richley, J. C. Mikkelsen, D. Tsuda, J. M. Crowley, K. A. Oraha, M. E. Howard, M. A. Rodkin, R. Swidler and R. Sprague, *J. Soc. Inf. Disp.*, 1999, **7**, 141.
114. S. H. Kim, S. J. Jeon, W. C. Jeong, H. S. Park and S. M. Yang, *Adv. Mater.*, 2008, **20**, 4129.
115. R. A. Pavlick, S. Sengupta, T. McFadden, H. Zhang and A. Sen, *Angew. Chem., Int. Ed.*, 2011, **50**, 9374.
116. X. Ma, A. Jannasch, U.-R. Albrecht, K. Hahn, A. Miguel-López, E. Schäffer and S. Sánchez, *Nano Letters*, 2015, **15**, 7043-7050.
117. B. Jurado-Sánchez, S. Sattayasamitsathit, W. Gao, L. Santos, Y. Fedorak, V. V. Singh, J. Orozco, M. Galarnyk and J. Wang, *Small*, 2015, **11**, 499-506.
118. C. Xu, J. Xie, D. Ho, C. Wang, N. Kohler, E. G. Walsh, J. R. Morgan, Y. E. Chin and S. Sun, *Angew. Chem., Int. Ed.*, 2007, **47**, 173.
119. S. H. Hu and X. Gao, *J. Am. Chem. Soc.*, 2010, **132**, 7234.
120. A. Alexeev, W. E. Uspal and A. C. Balazs, *ACS Nano*, 2008, **2**, 1117.
121. K. Matyjaszewski, H. Dong, W. Jakubowski, J. Pietrasik and A. Kusumo, *Langmuir*, 2007, **23**, 4528-4531.
122. W. Stöber, A. Fink and E. Bohn, *Journal of Colloid and Interface Science*, 1968, **26**, 62-69.
123. A. Synytska, E. Svetushkina, D. Martina, C. Bellmann, F. Simon, L. Ionov, M. Stamm and C. Creton, *Langmuir*, 2012, **28**, 16444-16454.
124. P. W. Hawkes and J. C. H. Spence, *Science of Microscopy*, Springer-Verlag New York, 2007.
125. TESCAN, Cryo-SEM, <http://www.tescan.com/en/applications/life-sciences/cryo-sem>, Accessed 7 October 2015.
126. FEI, *An Introduction to Electron Microscopy*, FEI, 2010.
127. W. Probst, G. Benner, J. Bihl and E. Weimer, *Advanced Materials*, 1993, **5**, 297-300.
128. J. Kuntsche, J. C. Horst and H. Bunjes, *International Journal of Pharmaceutics*, 2011, **417**, 120-137.
129. Veeco, *A Practical Guide to SPM: Scanning Probe Microscopy*, Veeco Instruments Inc., 2005.
130. I. f. P. Universität Greifswald, AFM (Atomic Force Microscope), <http://www.physik.uni-greifswald.de/arbeitsgruppen/helm/methoden/afm-atomic-force-microscope.html>, Accessed 8 October 2015.
131. H.-J. Butt, B. Cappella and M. Kappl, *Surface Science Reports*, 2005, **59**, 1-152.
132. Veeco, *MultiMode SPM Instruction Manual*, Veeco Instruments Inc., 2004.
133. AZoNano, Fundamentals of Contact Mode and TappingMode Atomic Force Microscopy, <http://www.azonano.com/article.aspx?ArticleID=3010>, Accessed 8 October 2015.
134. D. B. Murphy, *Fundamentals of Light Microscopy and Electronic Imaging*, Wiley-Liss, Inc., USA, 2001.

135. M. Stamm, *Polymer Surfaces and Interfaces: Characterization, Modification and Applications*, Springer-Verlag Berlin Heidelberg, 2008.
136. W. Tscharnuter, *Photon Correlation Spectroscopy in Particle Sizing, Encyclopedia of Analytical Chemistry*, John Wiley & Sons Ltd, Chichester, 2000.
137. Wikipedia, Dynamic Light Scattering, https://en.wikipedia.org/wiki/Dynamic_light_scattering, Accessed 14 October 2015.
138. G. Bracco and B. Holst, *Surface Science Techniques*, Springer-Verlag Berlin Heidelberg, 2013.
139. H. G. Tompkins and E. A. Irene, *Handbook of Ellipsometry*, William Andrew, Inc., 2005.
140. L. Ionov, B. Zdyrko, A. Sidorenko, S. Minko, V. Klep, I. Luzinov and M. Stamm, *Macromolecular Rapid Communications*, 2004, **25**, 360-365.
141. B. P. Binks and P. D. I. Fletcher, *Langmuir*, 2001, **17**, 4708-4710.
142. R. Aveyard, *Soft Matter*, 2012, **8**, 5233-5240.
143. B. S. Binks and T. S. Horozov, eds., *Colloidal particles at liquid interfaces* Cambridge University Press, Cambridge, 2006.
144. Z. Nie, W. Li, M. Seo, S. Xu and E. Kumacheva, *Journal of the American Chemical Society*, 2006, **128**, 9408-9412.
145. C.-C. Lin, C.-W. Liao, Y.-C. Chao and C. Kuo, *ACS Applied Materials & Interfaces*, 2010, **2**, 3185-3191.
146. Z. He and I. Kretschmar, *Langmuir*, 2013, **29**, 15755-15761.
147. C. Casagrande, P. Fabre, E. Raphael and M. Veyssie, *Europhysics Letters*, 1989, **9**, 251-255.
148. T. Ondarcuhu, P. Fabre, E. Raphael and M. Veyssie, *Journal De Physique*, 1990, **51**, 1527-1536.
149. D. J. Adams, S. Adams, J. Melrose and A. C. Weaver, *Colloids and Surfaces A: Physicochemical and Engineering Aspects*, 2008, **317**, 360-365.
150. L. Isa, L. Falk, R. Wepf and E. Reimhult, *Nat. Comms.*, 2011, **2**, 438.
151. A. Synytska, A. Kirillova and L. Isa, *ChemPlusChem*, 2014, **79**, 656-661.
152. L. Ionov and S. Minko, *ACS Applied Materials & Interfaces*, 2012, **4**, 483-489.
153. N. Puretskiy, G. Stoychev, M. Stamm and L. Ionov, *ACS Appl. Mater. Interfaces*, 2010, **2**, 2944-2948.
154. L. Isa, *Chimia*, 2013, **67**, 231-235.
155. Y. Nonomura, S. Komura and K. Tsujii, *Langmuir*, 2004, **20**, 11821-11823.
156. F. Liang, K. Shen, X. Qu, C. Zhang, Q. Wang, J. Li, J. Liu and Z. Yang, *Angewandte Chemie International Edition*, 2011, **50**, 2379-2382.
157. S. Weiss, D. Hirsemann, B. Biersack, M. Ziadeh, A. H. E. Müller and J. Breu, *Polymer*, 2013, **54**, 1388-1396.
158. *Germany Pat.*, EP 2 902 103 A1, 2015.
159. G. Frens, *Nature Physical Science*, 1973, **241**, 20-22.
160. A. Kirillova, G. Stoychev, L. Ionov, K. J. Eichhorn, M. Malanin and A. Synytska, *ACS Appl Mater Interfaces*, 2014, **6**, 13106-13114.
161. Y. L. Lyubarskaya and A. A. Shestopalov, *ACS Applied Materials & Interfaces*, 2013, **5**, 7323-7329.
162. T. D. Clark, R. Ferrigno, J. Tien, K. E. Paul and G. M. Whitesides, *Journal of the American Chemical Society*, 2002, **124**, 5419-5426.
163. Y. Min, M. Akbulut, K. Kristiansen, Y. Golan and J. Israelachvili, *Nat Mater*, 2008, **7**, 527-538.
164. H. Xing, Z. Wang, Z. Xu, N. Y. Wong, Y. Xiang, G. L. Liu and Y. Lu, *ACS Nano*, 2012, **6**, 802-809.
165. A. Perro, E. Duguet, O. Lambert, J. C. Taveau, E. Bourgeat-Lami and S. Ravaine, *Angewandte Chemie*, 2009, **48**, 361-365.
166. Y.-S. Cho, G.-R. Yi, J.-M. Lim, S.-H. Kim, V. N. Manoharan, D. J. Pine and S.-M. Yang, *Journal of the American Chemical Society*, 2005, **127**, 15968-15975.
167. P. Datskos, D. A. Cullen and J. Sharma, *Angewandte Chemie*, 2015.
168. A. G. Vanakaras, *Langmuir*, 2006, **22**, 88-93.
169. B. Wang, B. Li, B. Dong, B. Zhao and C. Y. Li, *Macromolecules*, 2010, **43**, 9234-9238.
170. A. Kirillova, G. Stoychev, L. Ionov and A. Synytska, *Langmuir*, 2014, **30**, 12765-12774.
171. T. M. Ruhland, J. R. V. Lang, H. G. Alt and A. H. E. Müller, *European Journal of Inorganic Chemistry*, 2013, **2013**, 2146-2153.
172. D. E. Resasco, *Chinese Journal of Catalysis*, 2014, **35**, 798-806.
173. J. He, Y. Liu, T. C. Hood, P. Zhang, J. Gong and Z. Nie, *Nanoscale*, 2013, **5**, 5151-5166.
174. Z. W. Seh, S. Liu, S. Y. Zhang, M. S. Bharathi, H. Ramanarayan, M. Low, K. W. Shah, Y. W. Zhang and M. Y. Han, *Angewandte Chemie*, 2011, **50**, 10140-10143.
175. J. Hu, S. Zhou, Y. Sun, X. Fang and L. Wu, *Chemical Society reviews*, 2012, **41**, 4356-4378.
176. C. Wang, H. Yin, S. Dai and S. Sun, *Chemistry of Materials*, 2010, **22**, 3277-3282.
177. S. Crossley, J. Faria, M. Shen and D. E. Resasco, *Science*, 2010, **327**, 68-72.
178. J. Faria, M. P. Ruiz and D. E. Resasco, *Advanced Synthesis & Catalysis*, 2010, **352**, 2359-2364.

179. W. Lv, K. J. Lee, J. Li, T. H. Park, S. Hwang, A. J. Hart, F. Zhang and J. Lahann, *Small*, 2012, **8**, 3116-3122.
180. D. Rodríguez-Fernández and L. M. Liz-Marzán, *Particle & Particle Systems Characterization*, 2013, **30**, 46-60.
181. S. Pradhan, D. Ghosh and S. Chen, *ACS Appl Mater Interfaces*, 2009, **1**, 2060-2065.
182. Z. W. Seh, S. Liu, M. Low, S. Y. Zhang, Z. Liu, A. Mlayah and M. Y. Han, *Adv Mater*, 2012, **24**, 2310-2314.
183. A. Walther, M. Hoffmann and A. H. Muller, *Angewandte Chemie*, 2008, **47**, 711-714.
184. A. Kirillova, C. Schliebe, G. Stoychev, A. Jakob, H. Lang and A. Synytska, *ACS Applied Materials & Interfaces*, 2015, **7**, 21218-21225.
185. K. L. Kelly, E. Coronado, L. L. Zhao and G. C. Schatz, *The Journal of Physical Chemistry B*, 2003, **107**, 668-677.
186. M. Steffan, A. Jakob, P. Claus and H. Lang, *Catalysis Communications*, 2009, **10**, 437-441.
187. A. Tuchscherer, D. Schaarschmidt, S. Schulze, M. Hietschold and H. Lang, *Dalton Transactions*, 2012, **41**, 2738-2746.
188. A. Tuchscherer, D. Schaarschmidt, S. Schulze, M. Hietschold and H. Lang, *Inorganic Chemistry Communications*, 2011, **14**, 676-678.
189. Y. Lu, P. Spyra, Y. Mei, M. Ballauff and A. Pich, *Macromolecular Chemistry and Physics*, 2007, **208**, 254-261.
190. Q. Huang, W. Shen, Q. Xu, R. Tan and W. Song, *Materials Chemistry and Physics*, 2014, **147**, 550-556.
191. J. C. Love, L. A. Estroff, J. K. Kriebel, R. G. Nuzzo and G. M. Whitesides, *Chemical Reviews*, 2005, **105**, 1103-1170.
192. Z.-J. Jiang, C.-Y. Liu and L.-W. Sun, *The Journal of Physical Chemistry B*, 2005, **109**, 1730-1735.
193. S. Wunder, Y. Lu, M. Albrecht and M. Ballauff, *ACS Catalysis*, 2011, **1**, 908-916.
194. J. Cui, L. Gao, S. Yan, W. Zhang, Y. Li and L. Gao, *Synthesis and Reactivity in Inorganic, Metal-Organic, and Nano-Metal Chemistry*, 2014, **45**, 158-163.
195. Z. D. Pozun, S. E. Rodenbusch, E. Keller, K. Tran, W. Tang, K. J. Stevenson and G. Henkelman, *The Journal of Physical Chemistry C*, 2013, **117**, 7598-7604.
196. J. Lv, Y. Song, L. Jiang and J. Wang, *ACS Nano*, 2014, **8**, 3152-3169.
197. T. M. Schutzius, S. Jung, T. Maitra, P. Eberle, C. Antonini, C. Stamatopoulos and D. Poulikakos, *Langmuir*, 2015, **31**, 4807-4821.
198. P. Eberle, M. K. Tiwari, T. Maitra and D. Poulikakos, *Nanoscale*, 2014, **6**, 4874-4881.
199. A. J. Meuler, J. D. Smith, K. K. Varanasi, J. M. Mabry, G. H. McKinley and R. E. Cohen, *ACS Applied Materials & Interfaces*, 2010, **2**, 3100-3110.
200. P. Guo, Y. Zheng, M. Wen, C. Song, Y. Lin and L. Jiang, *Advanced Materials*, 2012, **24**, 2642-2648.
201. E. Celia, T. Darmanin, E. Taffin de Givenchy, S. Amigoni and F. Guittard, *Journal of Colloid and Interface Science*, 2013, **402**, 1-18.
202. M. He, J. Wang, H. Li and Y. Song, *Soft Matter*, 2011, **7**, 3993-4000.
203. P. W. Wilson, W. Lu, H. Xu, P. Kim, M. J. Kreder, J. Alvarenga and J. Aizenberg, *Physical Chemistry Chemical Physics*, 2013, **15**, 581-585.
204. S. Farhadi, M. Farzaneh and S. A. Kulinich, *Applied Surface Science*, 2011, **257**, 6264-6269.
205. Y. Wang, J. Xue, Q. Wang, Q. Chen and J. Ding, *ACS Applied Materials & Interfaces*, 2013, **5**, 3370-3381.
206. L. Boinovich, A. M. Emelyanenko, V. V. Korolev and A. S. Pashinin, *Langmuir: the ACS journal of surfaces and colloids*, 2014, **30**, 1659-1668.
207. S. A. Kulinich, S. Farhadi, K. Nose and X. W. Du, *Langmuir*, 2011, **27**, 25-29.
208. P. Kim, T.-S. Wong, J. Alvarenga, M. J. Kreder, W. E. Adorno-Martinez and J. Aizenberg, *ACS Nano*, 2012, **6**, 6569-6577.
209. M. Ruan, W. Li, B. Wang, B. Deng, F. Ma and Z. Yu, *Langmuir*, 2013, **29**, 8482-8491.
210. L. Cao, A. K. Jones, V. K. Sikka, J. Wu and D. Gao, *Langmuir*, 2009, **25**, 12444-12448.
211. L. Mishchenko, M. Khan, J. Aizenberg and B. D. Hatton, *Adv. Funct. Mater.*, 2013, **23**, 4577-4584.
212. K. Rykaczewski, S. Anand, S. B. Subramanyam and K. K. Varanasi, *Langmuir*, 2013, **29**, 5230-5238.
213. J. Chen, R. Dou, D. Cui, Q. Zhang, Y. Zhang, F. Xu, X. Zhou, J. Wang, Y. Song and L. Jiang, *ACS Applied Materials & Interfaces*, 2013, **5**, 4026-4030.
214. J. Chen, J. Liu, M. He, K. Li, D. Cui, Q. Zhang, X. Zeng, Y. Zhang, J. Wang and Y. Song, *Applied Physics Letters*, 2012, **101**, 111603.
215. S. Chernyy, M. Järn, K. Shimizu, A. Swerin, S. U. Pedersen, K. Daasbjerg, L. Makkonen, P. Claesson and J. Iruthayaraj, *ACS Appl. Mater. Interfaces*, 2014, **6**, 6487-6496.
216. R. Dou, J. Chen, Y. Zhang, X. Wang, D. Cui, Y. Song, L. Jiang and J. Wang, *ACS Applied Materials & Interfaces*, 2014, **6**, 6998-7003.
217. J. Chen, Z. Luo, Q. Fan, J. Lv and J. Wang, *Small*, 2014, **10**, 4693-4699.

218. A. Narayanan Krishnamoorthy, C. Holm and J. Smiatek, *The Journal of Physical Chemistry B*, 2014, **118**, 11613-11621.
219. A. S. Van Dyke and A. R. Betz, *The Effect of Mixed Hydrophilic and Hydrophobic Surfaces on Frost Nucleation and Growth*, San Diego, California, USA, 2013.
220. K. K. Varanasi, M. Hsu, N. Bhate, W. Yang and T. Deng, *Applied Physics Letters*, 2009, **95**, 094101.
221. S. A. Kulinich and M. Farzaneh, *Applied Surface Science*, 2009, **255**, 8153-8157.
222. S. A. Kulinich and M. Farzaneh, *Cold Regions Science and Technology*, 2011, **65**, 60-64.
223. J. Guadarrama-Cetina, A. Mongruel, W. González-Viñas and D. Beysens, *EPL (Europhysics Letters)*, 2013, **101**, 16009.
224. J. Guadarrama-Cetina, A. Mongruel, W. González-Viñas and D. Beysens, *EPL (Europhysics Letters)*, 2015, **110**, 56002.
225. S. Jung, M. K. Tiwari and D. Poulikakos, *Proceedings of the National Academy of Sciences*, 2012, **109**, 16073-16078.
226. X. Chen, R. Ma, H. Zhou, X. Zhou, L. Che, S. Yao and Z. Wang, *Sci. Rep.*, 2013, **3**.
227. J. Chanda, L. Ionov, A. Kirillova and A. Synytska, *Soft Matter*, 2015.
228. D. M. Yebra, S. Kiil and K. Dam-Johansen, *Progress in Organic Coatings*, 2004, **50**, 75-104.
229. D. Lindsay and A. von Holy, *The Journal of hospital infection*, 2006, **64**, 313-325.
230. R. F. Brady Jr, *Progress in Organic Coatings*, 1999, **35**, 31-35.
231. E. Almeida, T. C. Diamantino and O. de Sousa, *Progress in Organic Coatings*, 2007, **59**, 2-20.
232. S. Krishnan, C. J. Weinman and C. K. Ober, *Journal of Materials Chemistry*, 2008, **18**, 3405.
233. K. L. Prime and G. M. Whitesides, *Science*, 1991, **252**, 1164-1167.
234. K. L. Prime and G. M. Whitesides, *Journal of the American Chemical Society*, 1993, **115**, 10714-10721.
235. S. Krishnan, N. Wang, C. K. Ober, J. A. Finlay, M. E. Callow, J. A. Callow, A. Hexemer, K. E. Sohn, E. J. Kramer and D. A. Fischer, *Biomacromolecules*, 2006, **7**, 1449-1462.
236. A. Hucknall, S. Rangarajan and A. Chilkoti, *Advanced Materials*, 2009, **21**, 2441-2446.
237. S. Tugulu and H.-A. Klok, *Biomacromolecules*, 2008, **9**, 906-912.
238. N. Nath, J. Hyun, H. Ma and A. Chilkoti, *Surface Science*, 2004, **570**, 98-110.
239. H. Ma, J. Hyun, P. Stiller and A. Chilkoti, *Advanced Materials*, 2004, **16**, 338-341.
240. J. L. Dalsin, B.-H. Hu, B. P. Lee and P. B. Messersmith, *Journal of the American Chemical Society*, 2003, **125**, 4253-4258.
241. H. Lee, S. M. Dellatore, W. M. Miller and P. B. Messersmith, *Science (New York, N.Y.)*, 2007, **318**, 426-430.
242. J. L. Kerstetter and W. M. Gramlich, *J. Mater. Chem. B*, 2014, **2**, 8043-8052.
243. A. Olivier, F. Meyer, J.-M. Raquez, P. Damman and P. Dubois, *Progress in Polymer Science*, 2012, **37**, 157-181.
244. X. Zhu, S. Guo, D. Janczewski, F. J. Velandia, S. L. Teo and G. J. Vancso, *Langmuir*, 2014, **30**, 288-296.
245. C. S. Gudipati, J. A. Finlay, J. A. Callow, M. E. Callow and K. L. Wooley, *Langmuir*, 2005, **21**, 3044-3053.
246. J. Xu, D. A. Bohnsack, M. E. Mackay and K. L. Wooley, *Journal of the American Chemical Society*, 2007, **129**, 506-507.
247. C. J. Weinman, J. A. Finlay, D. Park, M. Y. Paik, S. Krishnan, H. S. Sundaram, M. Dimitriou, K. E. Sohn, M. E. Callow, J. A. Callow, D. L. Handlin, C. L. Willis, E. J. Kramer and C. K. Ober, *Langmuir*, 2009, **25**, 12266-12274.
248. H. S. Sundaram, Y. Cho, M. D. Dimitriou, C. J. Weinman, J. A. Finlay, G. Cone, M. E. Callow, J. A. Callow, E. J. Kramer and C. K. Ober, *Biofouling*, 2011, **27**, 589-602.
249. S. Krishnan, R. Ayothi, A. Hexemer, J. A. Finlay, K. E. Sohn, R. Perry, C. K. Ober, E. J. Kramer, M. E. Callow, J. A. Callow and D. A. Fischer, *Langmuir*, 2006, **22**, 5075-5086.
250. E. Martinelli, S. Agostini, G. Galli, E. Chiellini, A. Glisenti, M. E. Pettitt, M. E. Callow, J. A. Callow, K. Graf and F. W. Bartels, *Langmuir*, 2008, **24**, 13138-13147.
251. C. A. Amadei, R. Yang, M. Chiesa, K. K. Gleason and S. Santos, *ACS Appl Mater Interfaces*, 2014, **6**, 4705-4712.
252. W. van Zoelen, H. G. Buss, N. C. Ellebracht, N. A. Lynd, D. A. Fischer, J. Finlay, S. Hill, M. E. Callow, J. A. Callow, E. J. Kramer, R. N. Zuckermann and R. A. Segalman, *ACS Macro Letters*, 2014, **3**, 364-368.
253. L. Shen, J. Xie, J. Tao and J. Zhu, *J. Mater. Chem. B*, 2015, **3**, 1157-1162.
254. C. Leng, H. G. Buss, R. A. Segalman and Z. Chen, *Langmuir*, 2015, **31**, 9306-9311.
255. S. Bauer, M. P. Arpa-Sancet, J. A. Finlay, M. E. Callow, J. A. Callow and A. Rosenhahn, *Langmuir*, 2013, **29**, 4039-4047.
256. J. F. Destino, C. M. Gatley, A. K. Craft, M. R. Detty and F. V. Bright, *Langmuir*, 2015, **31**, 3510-3517.
257. M. Graham and N. Cady, *Coatings*, 2014, **4**, 37-59.
258. A. J. Scardino, J. Guenther and R. de Nys, *Biofouling*, 2007, **24**, 45-53.

259. J. F. Schumacher, M. L. Carman, T. G. Estes, A. W. Feinberg, L. H. Wilson, M. E. Callow, J. A. Callow, J. A. Finlay and A. B. Brennan, *Biofouling*, 2007, **23**, 55-62.
260. M. Kargar, A. Pruden and W. A. Ducker, *Journal of Materials Chemistry B*, 2014, **2**, 5962-5971.
261. K. A. Whitehead and J. Verran, *Food and Bioproducts Processing*, 2006, **84**, 253-259.
262. J. F. Schumacher, C. J. Long, M. E. Callow, J. A. Finlay, J. A. Callow and A. B. Brennan, *Langmuir*, 2008, **24**, 4931-4937.
263. X. Cao, M. E. Pettitt, F. Wode, M. P. Arpa Sancet, J. Fu, J. Ji, M. E. Callow, J. A. Callow, A. Rosenhahn and M. Grunze, *Advanced Functional Materials*, 2010, **20**, 1984-1993.
264. M. V. Graham, A. P. Mosier, T. R. Kiehl, A. E. Kaloyeros and N. C. Cady, *Soft Matter*, 2013, **9**, 6235.
265. W. Liu, X. Liu, J. Fangteng, S. Wang, L. Fang, H. Shen, S. Xiang, H. Sun and B. Yang, *Nanoscale*, 2014, **6**, 13845-13853.
266. S. Pechook, K. Sudakov, I. Polishchuk, I. Ostrov, V. Zakin, B. Pokroy and M. Shemesh, *J. Mater. Chem. B*, 2015, **3**, 1371-1378.
267. A. Beigbeder, P. Degee, S. L. Conlan, R. J. Mutton, A. S. Clare, M. E. Pettitt, M. E. Callow, J. A. Callow and P. Dubois, *Biofouling*, 2008, **24**, 291-302.
268. I. Banerjee, R. C. Pangule and R. S. Kane, *Adv Mater*, 2011, **23**, 690-718.
269. J. Satulovsky, M. A. Carignano and I. Szleifer, *Proceedings of the National Academy of Sciences of the United States of America*, 2000, **97**, 9037-9041.
270. G. Gunkel, M. Weinhart, T. Becherer, R. Haag and W. T. Huck, *Biomacromolecules*, 2011, **12**, 4169-4172.
271. K. M. Berntsson, H. Andreasson, P. R. Jonsson, L. Larsson, K. Ring, S. Petronis and P. Gatenholm, *Biofouling*, 2000, **16**, 245-261.
272. C. J. Galvin and J. Genzer, *Progress in Polymer Science*, 2012, **37**, 871-906.
273. W. J. Yang, D. Pranantyo, K. G. Neoh, E. T. Kang, S. L. Teo and D. Rittschof, *Biomacromolecules*, 2012, **13**, 2769-2780.
274. K. A. Pollack, P. M. Imbesi, J. E. Raymond and K. L. Wooley, *ACS Appl Mater Interfaces*, 2014, **6**, 19265-19274.
275. D. Park, C. J. Weinman, J. A. Finlay, B. R. Fletcher, M. Y. Paik, H. S. Sundaram, M. D. Dimitriou, K. E. Sohn, M. E. Callow, J. A. Callow, D. L. Handlin, C. L. Willis, D. A. Fischer, E. J. Kramer and C. K. Ober, *Langmuir*, 2010, **26**, 9772-9781.
276. H. S. Sundaram, Y. Cho, M. D. Dimitriou, J. A. Finlay, G. Cone, S. Williams, D. Handlin, J. Gatto, M. E. Callow, J. A. Callow, E. J. Kramer and C. K. Ober, *ACS Appl Mater Interfaces*, 2011, **3**, 3366-3374.
277. J. A. Finlay, S. Krishnan, M. E. Callow, J. A. Callow, R. Dong, N. Asgill, K. Wong, E. J. Kramer and C. K. Ober, *Langmuir*, 2008, **24**, 503-510.

Table of Abbreviations

AA	Ascorbic acid
AC	Alternating current
AFM	Atomic force microscopy
APS	3-Aminopropyltriethoxysilane
ARGET	Activators regenerated by electron transfer
ATP	Adenosine triphosphate
ATR-FTIR	Attenuated total reflectance Fourier transform infrared spectroscopy
ATRP	Atom transfer radical polymerization
BrIn	α -Bromoisobutyryl bromide
DCB	Dithionite-citrate-bicarbonate
DCM	Dichloromethane
DEA	2-Diethylaminoethyl methacrylate
DEP	Dielectrophoresis
DI	Deionized
DLS	Dynamic light scattering
DMAEMA	2-Dimethylaminoethyl methacrylate
DMF	<i>N,N</i> -dimethylformamide
DNA	Deoxyribonucleic acid
EBiB	Ethyl α -bromoisobutyrate
EDC	<i>N</i> -(3-Dimethylaminopropyl)- <i>N</i> '-ethylcarbodiimide hydrochloride
EDTA	Ethylenediaminetetraacetic acid
EDX	Energy dispersive X-ray spectroscopy
EFTEM	Energy-filtering transmission electron microscopy
EGFRA	Epidermal growth factor receptor antibody
EO	Ethylene oxide
EOY	Eosin Y
E-paper	Electronic paper
ETPTA	Ethoxylated trimethylolpropane triacrylate resin
FC	Fully covered
fcc	Face-centered cubic
FreSCa	Freeze-fracture shadow-casting
GPC	Gel permeation chromatography
GUVs	Giant unilamellar vesicles
HFBs	Hydrophobins
HPs	Homogeneous particles
IEP	Isoelectric point
JPs	Janus particles
JR	Janus ratio
LiDps	DNA-binding protein from <i>Listeria innocua</i>
LMA	Lauryl methacrylate
MagMOONs	Magnetically modulated optical nanoprobe
MCMs	Multicompartment micelles
MFFD	Microfluidic flow-focusing device
MMA	Methyl methacrylate
MOONs	Modulated optical nanoprobe
MUOH	11-Mercapto-1-undecanol
nBA	<i>n</i> -Butylacrylate
NHS	<i>N</i> -Hydroxysuccinimide
NIPAAm	<i>N</i> -isopropylacrylamide
NPs	Nanoparticles

OTS	<i>n</i> -Octadecanetrichlorosilane
P2MVP	Poly(<i>N</i> -methyl-2-vinyl pyridinium iodide)
P2VP	Poly(2-vinyl pyridine)
PAA	Poly(acrylic acid)
PAAm	Poly(acryl amide)
PAN	Polyacrylonitrile
PB	Polybutadiene
PDI	Polydispersity index
PDMAEMA	Poly(2-dimethylaminoethyl methacrylate)
PDMS	Polydimethylsiloxane
PDMSMA	Monomethacryloxypropyl terminated polydimethylsiloxane
PECAM	Platelet endothelial cell-adhesion molecule
PEG	Poly(ethylene glycol)
PEGMA	Poly(ethylene glycol) methyl ether methacrylate
PEO	Poly(ethylene oxide)
PFS	Pentafluorostyrene
PGMA	Poly(glycidyl methacrylate)
PI	Polyisoprene
PLA	Poly(lactide)
PLGA	Poly(lactide- <i>co</i> -glycolide)
PLMA	Poly(lauryl methacrylate)
PMAA	Poly(methacrylic acid)
PMDTA	<i>N,N,N',N'',N'''</i> -pentamethyldiethylenetriamine
PMMA	Poly(methyl methacrylate)
PNIPAAm	Poly(<i>N</i> isopropylacrylamide)
P(PDMSMA)	Poly(monomethacryloxypropyl terminated polydimethylsiloxane)
P(PEGMA)	Poly(poly(ethylene glycol) methyl ether methacrylate)
PS	Polystyrene
P(S-BIEM)	Poly(styrene-2-(2-bromoisobutyryloxy)ethyl methacrylate)
PtBA	Poly(<i>tert</i> -butyl acrylate)
PtBMA	Poly(<i>tert</i> -butyl methacrylate)
PtBS	Poly(4- <i>tert</i> -butoxystyrene)
RA	Reducing agent
SAM	Self-assembled monolayer
SANS	Small-angle neutron scattering
SBM	Polystyrene- <i>block</i> -polybutadiene- <i>block</i> -poly(methyl methacrylate)
SBT	Polystyrene- <i>block</i> -polybutadiene- <i>block</i> -poly(<i>tert</i> -butyl methacrylate)
SDS	Sodium dodecyl sulfate
SEM	Scanning electron microscopy
SI-ATRP	Surface-initiated atom transfer radical polymerization
Sn(II)	Tin(II) 2-ethylhexanoate
StAv	Streptavidin
tBA	<i>tert</i> -Butyl acrylate
TEM	Transmission electron microscopy
TEOS	Tetraethyl orthosilicate
TGA	Thermogravimetric analysis
THF	Tetrahydrofuran
TMSPA	Trimethoxysilylpropylacrylate
TPMA	Tris(2-pyridylmethyl)amine
UV	Ultraviolet
ZP	Zeta-potential

Table of Symbols

α	Angle parameterizing the relative areas of the polar and apolar domains of a Janus particle at an oil-water interface
A	Contact area of the ice cylinder on the substrate
β	Angle characterizing the immersion depth of a Janus particle at an oil-water interface
Γ	Grafting density
γ_{AO}	Interfacial tension of the Janus particle apolar domain/oil interface
γ_{AW}	Interfacial tension of the Janus particle apolar domain/water interface
γ_{HPO}	Interfacial tension of the homogeneous particle/oil interface
γ_{HPW}	Interfacial tension of the homogeneous particle/water interface
γ_{OW}	Interfacial tension between the oil and water phases
γ_{PO}	Interfacial tension of the Janus particle polar domain/oil interface
γ_{PW}	Interfacial tension of the Janus particle polar domain/water interface
$\Delta\theta$	Wettability contrast between the two portions of a Janus particle
D	Diameter
D_h	Hydrodynamic diameter
ϵ_0	Permittivity of the free space
ϵ_r	Permittivity of the liquid
E	Total surface free energy
$E_{ads.}$	Minimum surface energy of an adsorbed particle at an interface
$E_{des.}$	Desorption energy of a particle from an interface
$E_{ext.}$	External electric field intensity
E_{oil}	Surface energy of a particle located entirely in either the oil phase
E_{water}	Surface energy of a particle located entirely in either the water phase
ζ	Zeta potential
F	Force
F_c	Centrifugal force
f_{pol}	Polymer mass fraction according to TGA analysis
η	Viscosity of the liquid
h	Protrusion height of the particle from the frozen interface
H	Thickness of the polymer layer
h^*	Immersion degree of the particles into the wax droplets
θ	Particle contact angle
θ_a	Advancing contact angle
θ_A	Equilibrium contact angle of the apolar domain of the Janus particle adsorbed at an oil-water interface
$\theta_{average}$	Average contact angle of a Janus particle
θ_J	Angle corresponding to the Janus boundary
θ_P	Equilibrium contact angle of the polar domain of the Janus particle adsorbed at an oil-water interface
θ_r	Receding contact angle
k	Reaction rate constant
k_{app}	Apparent reaction rate constant
k_c	Spring constant of a cantilever
λ	Wavelength
L	Length
m	Mass
M_n	Number average molecular weight

M_w	Weight average molecular weight
v	Electrophoretic mobility
N	Number of particles forming a cluster
N_A	Avogadro's number
Q	Cross-sectional area
ρ	Density
R	Particle radius
S_{BET}	Surface area of the particles determined by BET measurements
τ	Ice adhesion strength
T	Temperature
T_2	Spin-spin relaxation time
T_g	Glass transition temperature
χ	Flory-Huggins interaction parameter
ω	Rotational speed
Z_c	Cantilever deflection
Z_p	Position of the piezo scanner normal to the surface

List of Publications

Journal Articles:

- Kirillova, A.; Ionov, L.; Roisman, I. V.; Synytska, A. Advanced Anti-Icing Surfaces Based on Hybrid Hairy Janus Particles, *submitted*
- Kirillova, A.; Schliebe, C.; Stoychev, G.; Jakob, A.; Lang, H.; Synytska, A. Hybrid Hairy Janus Particles Decorated with Metallic Nanoparticles for Catalytic Applications, *ACS Applied Materials & Interfaces* **2015**, *7*, 21218–21225.
- Chanda, J.; Ionov, L.; Kirillova, A.; Synytska, A. New Insight into Icing and De-icing Properties of Hydrophobic and Hydrophilic Structured Surfaces Based on Core-Shell Particles. *Soft Matter* **2015**, *11*, 9126–9134.
- Synytska, A.; Kirillova, A. Janus Particles with Polymer Shells. *European Patent Application* EP 2 902 103 A1, **2015**.
- Kirillova, A.; Stoychev, G.; Ionov, L.; Synytska, A. Self-Assembly Behavior of Hairy Colloidal Particles with Different Architectures: Mixed versus Janus. *Langmuir* **2014**, *30*, 12765–12774.
- Kirillova, A.; Stoychev, G.; Ionov, L.; Eichhorn K.-J.; Malanin, M.; Synytska, A. Platelet Janus Particles with Hairy Polymer Shells for Multifunctional Materials, *ACS Applied Materials & Interfaces* **2014**, *6*, 13106–13114.
- Synytska, A.; Kirillova, A.; Isa, L. Synthesis and Contact Angle Measurements of Janus Particles, *ChemPlusChem* **2014**, *79*, 656 – 661.

Contribution to conferences:

- Kirillova, A.; Marx, S.; Synytska, A. Hybrid Hairy Janus Particles: Controlled Design and Assembly (Poster). *European Polymer Federation Congress*, held in Dresden, Germany, 21 – 26 June **2015**.
- Kirillova, A.; Marx, S.; Synytska, A. Hybrid Hairy Janus Particles: Controlled Design and Assembly (Poster). *4th International Symposium Frontiers in Polymer Science*, held in Riva del Garda, Italy, 20 – 22 May **2015**.

- *Kirillova, A.; Marx, S.; Synytska, A. Stimuli-Responsive Janus Particles as Novel Building Blocks for Multifunctional Materials (Poster). 8th ECNP International Conference on Nanostructured Polymers and Nanocomposites*, held in Dresden, Germany, 16 – 19 September **2014**.
- *Kirillova, A.; Stoychev, G.; Synytska, A. Proof and Control of the “Janus Architecture” of Janus Particles Using Advanced Analytical Tools (Poster). 14th European Student Conference on Colloid and Interface Science (ESC)*, held in Potsdam, Germany, 10 – 13 June **2013**.
- *Kirillova, A.; Stoychev, G.; Synytska, A. Proof and Control of the “Janus Architecture” of Janus Particles Using Advanced Analytical Tools (Poster). 6th International Symposium on the Separation and Characterization of Natural and Synthetic Macromolecules*, held in Dresden, Germany, 6 – 8 February **2013**.
- *Kirillova, A.; Berger, S.; Puretskiy, N.; Stoychev, G.; Stamm, M.; Synytska, A. Smart Core-Shell Colloids with Chemical “Patchiness”: Janus Particles (Poster). 13th Dresden Polymer Discussion and 8th Max Bergmann Symposium*, held in Meißen, Germany, 1 – 4 April, **2012**.

Acknowledgements

Firstly, I would like to express my very great appreciation to Professor Manfred Stamm for his supervision and continuous support throughout this thesis process. I owe my deepest gratitude to my co-supervisor Dr. Alla Synytska for her scientific and personal guidance, motivation and encouragement, enthusiasm and immense knowledge. Her faith in me helped me in all the time of research and writing of this thesis. Without her extraordinary support this research work would hardly be imaginable.

I express my warmest gratitude to Professor Lucio Isa from ETH Zürich for our positive and productive collaboration as well as for providing us with valuable contact angle measurements on our Janus particles. I am very grateful to our collaborators from TU Chemnitz – Professor Heinrich Lang, Dr. Alexander Jacob, and Christian Schliebe – for helping us with the catalytic part of this work. My sincere appreciation also goes to Professor Carsten Werner and Dr. Jens Friedrichs from IPF for our fruitful collaboration on the topic of anti-fouling surfaces.

I am deeply grateful to my colleague Claudia Marschelke for her help in the lab as well as for her endless optimism and kind support. I would also like to thank my other labmates Jagannath Chanda, Sandra Marx, and Madeleine Müller for the positive and friendly atmosphere during lab work. I wish to thank the people from the Department of Polymer Interfaces, especially Anja Caspari for helping me with the electrokinetic measurements, and Dr. Astrid Drechsler for providing me with new knowledge in the field of atomic force microscopy.

I want to express my deep gratitude to Professor Leonid Ionov and his group for the beneficial scientific discussions and support during my thesis work. Especially I would like to thank my friends and colleagues Dr. Nikolay Puretskiy for his help in the lab during the early stages of my work, as well as Dr. Ivan Raguzin for the drawing of the beautiful 3D pictures included in this thesis.

I am sincerely grateful to my friend Dr. Georgi Stoychev for his valuable TEM and cryo-TEM measurements as well as for his great encouragement and trust in me, which has been a priceless support throughout the last years.

Finally, I would like to deeply thank my friends for always charging me with optimism and laughter. My very deep gratitude goes to my family: my parents, my grandmother, and my little sister for supporting me spiritually throughout this thesis and my life in general.

Versicherung

Hiermit versichere ich, dass ich die vorliegende Arbeit ohne unzulässige Hilfe Dritter und ohne Benutzung anderer als der angegebenen Hilfsmittel angefertigt habe; die aus fremden Quellen direkt oder indirekt übernommenen Gedanken sind als solche kenntlich gemacht. Die Arbeit wurde bisher weder im Inland noch im Ausland in gleicher oder ähnlicher Form einer anderen Prüfungsbehörde vorgelegt.

Dresden, __. __ 2015

Alina Kirillova

Erklärung

Hiermit erkläre ich, dass diese Arbeit unter wissenschaftlicher Betreuung von Herrn Prof. Dr. Manfred Stamm und Frau Dr. Alla Synytska in der Zeit von Juli 2012 bis Dezember 2015 am Leibniz-Institut für Polymerforschung Dresden e.V. angefertigt wurde.

Bislang haben keine weiteren Promotionsverfahren stattgefunden.

Hiermit erkenne ich die Promotionsordnung der Fakultät Mathematik und Naturwissenschaften der Technischen Universität Dresden vom 23.02.2011 in geänderter Fassung von 15.06.2011 und 18.06.2014 an.

Dresden, __. __ 2015

Alina Kirillova